Unconventional synthesis and properties of zeolitic imidazolate frameworks and 2D magnetic MOF

Javier López Cabrelles
Universitat de València
December, 2020

Supervised by Prof. Eugenio Coronado Miralles and
Dr. Guillermo Mínguez Espallargas
PhD Thesis in Nanoscience and Nanotechnology

Unconventional synthesis and properties of zeolitic imidazolate frameworks and 2D magnetic MOFs

VNIVERSITAT DE VALÈNCIA

Instituto de Ciencia Molecular (ICMol)

******

Memoria presentada por Javier López Cabrelles para aspirar al grado de Doctor en Nanociencia y Nanotecnología

******

Dirigida por:

Prof. Eugenio Coronado Miralles

Dr. Guillermo Mínguez Espallargas

Diciembre 2020

D. EUGENIO CORONADO MIRALLES, catedrático del Departamento de Química Inorgánica de la Universitat de València y D. GUILLERMO MÍNGUEZ ESPALLARGAS, doctor por la University of Sheffield y actualmente investigador del Instituto de Ciencia Molecular, de la Universitat de València.

CERTIFICAN:

Que la memoria presentada por D. Javier López Cabrelles con título "Unconventional synthesis and properties of zeolitic imidazolate frameworks and 2D magnetic MOFs" corresponde a su Tesis Doctoral y ha sido realizada bajo su dirección en el Instituto de Ciencia Molecular, autorizando mediante este escrito la presentación de la misma para optar al grado de Doctor.

En Paterna, a 14 de Diciembre de 2020.

Dr. Eugenio Coronado Miralles Dr. Guillermo Mínguez Espallargas

Agradecimientos

Han sido un total cinco años de tesis, pero al defender la tesis ya serán siete años en el ICMol. Así que, por suerte, este apartado se avecina algo extenso. Espero no dejarme a nadie por el camino. Gracias a todos por la mejor época que de momento me ha tocado vivir.

Los primeros agradecimientos son obviamente a mis padres, a quienes se lo debo todo. Ha sido toda una suerte contar con unos padres así, los cuales me dejan como "herencia" la mejor educación que podría haber recibido. Desde bien pequeño han estado ahí estimulando mis inquietudes por la química, separando arena y virutas metálicas con un imán, pasando por la música o los videojuegos, a los cuales les debo en gran parte esas ganas de investigar y explorar. En definitiva, si hoy estoy aquí terminando este trabajo, es gracias a los magníficos padres que tengo. Y gracias a mi hermano, por ser mi menos uno.

Agradecer a Eugenio Coronado Miralles por aceptarme ya en el trabajo fin de grado en el UIMM, confiar en que pudiese realizar la tesis y por todo lo que he aprendido sobre magnetismo, y más importante, a tener visión sobre las tendencias y lo importante de los trabajos.

A Guillermo Mínguez Espallargas, Guille, por todos los años bajo su tutela, día tras día, enseñándome prácticamente todo lo que he aprendido en este largo recorrido. Por la paciencia infinita con todas mis dudas y preguntas, y con mi inglés más que mejorable. El "título" que más me gusta y que lo resume todo, es que ha sido mi padre científico, y eso es para siempre.

Gracias a Samuel Mañas, por todo lo aprendido sobre ciencia, a trabajar de forma profesional y ser más que riguroso. Gracias a ti nuestros trabajos han sido mejores.

Gràcies a Josep, per donar-me l'oportunitat de realitzar l'estada al seu grup a l' ETH. Un plaer estar al grup d'una persona que admire, sense dubte un enorme científic, però encara millor persona, un exemple a seguir en tots els àmbits. Moltes gràcies també a la gent del seu grup que em va acollir, David, Alessandro, Carlos, Semih i James, amb els quals em vaig sentir molt a gust des del primer dia i me van ensenyar tot al laboratori.

A todos los colaboradores que han permitido que nuestro trabajo sea un poco mejor. A Iñigo por su paciencia infinita con los cristales más imposibles que le podíamos enviar, no ha fallado con ninguno, incluso nos llevamos alguna grata sorpresa con alguno. A P. Bereciartúa por las increíbles medidas de TEM. A A. R. Velamazán, por las medidas de neutrones. A J. C. Waerenborgh y B. J. C. Vieira por las medidas de Mössbauer. A D. Davidovikj, M. Šiškins, P. G. Steeneken, H. S. J. van der Zant y en especial a Martin Lee, por la increíble aplicación de los **MUV-1** como nanoresonadores. A S. Valencia, M. Palomino y F. Rey por las medidas de adsorción del **MUV-3**. A J. Romero y G. Abellán por las medidas de electrocatálisis y el nanocomposite derivado del **MUV-3**.

A todo el equipo técnico del UIMM e ICMol. Gracias a Chema y Gloria por las infinitas medidas magnéticas, con el dichoso canting. A Jose Usagre por toda la ayuda recibida con pedidos, pedidos urgentes, problemas técnicos y las charlas de pasillo. A Ángel y Cristian por estar dispuestos a ayudar de forma inmediata y eficiente. A Alejandra por estar ahí siempre

para solventar los problemas en el rayos-X de polvo. A Paco y Estrella por la ayuda con el papeleo del máster, tesis y estancia. A Manuel por la asistencia técnica en informática, sobre todo cuando te haces mayor y te dejan tener tu ordenador. A Ruth por la gran ayuda para solventar problemas, siendo seguramente la persona más eficiente y resolutiva del ICMol.

A Walter, por ser mi primer tutor en el lab cuando llegué, por perder el tiempo conmigo, por todas las charlas que tuvimos, el primer toque de profesionalidad y amistad que tuve en el lab, y por los partidos de futbito.

A los compañeros de máster, con los cuales pasé dos de los mejores años de mi vida, tanto en el laboratorio como en las visitas a San Vicent del Raspeig. En particular a los asiduos de la farreta, como Jesús (Yisus), Miguel, George, Ramón y Javi.

Gracias a los compañeros del ICMol y UIMM con los que he compartido muchos años, comidas, café, mañanas y tardes. Agradecer a Yan, Vero, Marc, Garín, Katia, Iván, Isaac, Eduardo, Roger, Marta, María, Mohanad. A Edurne per dur alegría i vida al lab. A Jose, por las largas conversaciones sobre videojuegos, consolas y la master race. A Manel, por ser un referente, un gran científico y persona, espero que volvamos a coincidir en algún otro momento. A Mónica, per tindre sempre paraules d'ànims i estar disposta ajudar, sobretot amb l'adsorció. A Miguel, por dejarse la vida peleando con crecer el **MUV-1**, y las buenas conversaciones que hemos tenido. A Natalia por ser un amor de persona, siempre preocupada por los demás y con ganas de ayudar. A los que venían al espectáculo del futbito, tanto el de antaño como el más reciente, con glorias

como José Jaime, Josep, Walter, Guille (hace eones), Gonzalo, Javi, Javi, Mario, Víctor, Isaac, Miguel, Carlos.

A Néstor, que, aunque pasaba de mí y me ignoraba al principio, limpiar la línea de uno de los primero POMs que hice nos acabó uniendo, siendo indispensable durante toda mi tesis. Gracias por ser un gran apoyo, pero sobretodo, por las infinitas risas y bromas que han hecho que esto sea mucho más llevadero, siendo la mayoría de veces, divertido venir a trabajar. Te echo de menos en el lab. Siempre nos quedará Zaragoza y Brest.

Gracias al grupete que por suerte hemos montado del lab, a Alejandro, Belén, Carmen, Javi, Euge, María, Mario, Víctor, Ana, Ramón y Luis. La etapa más dura, la etapa final, ha sido mucho más llevadera gracias a vosotros.

A Mario, per totes les vesprades de malitos jugant, rajant pel teamspeak, i les nits aguantant fins les sis per a que agafares el primer tren cap Alzira.

A Eugenia, el meu pilar fonamental, una amistat que en “poc” de temps s’ha fet imprescindible. La persona amb qui compartir les idees, sentiments i opinions, que sé que hem va a recolzar incondicionalment. Una amistat per sempre. T’estime.

A Carlos (Martí Gastaldo) por lo que comenzaron siendo conversaciones sobre videojuegos, han terminado siendo una muy buena amistad, más allá del ICMol un buen número de barbacoas, aperoles y conversaciones a la fresca en tu terraza. Muchas gracias.

A Javixu y Ramón, dos personajes también muy importantes en mi vida desde que empezó el periplo del ICMol. Muchas cenas, conversaciones, chupitos, resacas... Pero sobre todo mucho tiempo juntos, siempre riéndonos, hablando de ciencia y no ciencia, futuros inverosímiles, pero en los cuales siempre somos un equipo. De amigos.

A Luis, a Pirámide, Piramidón, que, aunque llegó de los últimos, ya es una persona importante para mí, en el día a día en el lab y fuera de él. Más que digno "sucesor", seguro que tu tesis deja a ésta a la altura del betún. Suerte estos años que te quedan, y espabila.

Hay mucha más gente de fuera del laboratorio que ha contribuido en mayor o menor medida a que este trabajo se realice. El apoyo de Carlos, my best friend, muchas veces ha sido necesario, aunque la tesis haya significado un corto periodo de tiempo en nuestra larga amistad. Jaime ha sido otro gran amigo que debido a que su labor también es elaborar una tesis en química, ha sido un gran confidente, tanto sobre ciencia como sobre la vida. Gracias a todos mis amigos de Xeraco, porque, aunque ahora los veranos son micro, son los que me hacen sentirme en casa. Vos vull molt a totes. Agradecer también a mis amigos de toda la vida, del "poble", que, a pesar de los altibajos, siempre están ahí. Y, por último, agradecer la acogida de mis amigos de enfermería, con los que he pasado innumerables buenos momentos, viajes, y he compartido gran parte del tiempo. Gracias a Willo conocí a ese magnífico grupo de personas, entre los cuales se encontraba Sílvia, que acabó convirtiéndose en la persona, para mí, más importante de estos últimos años, a quien le debo agradecer también muchas cosas. Y destacar a Pablo, con quien he vivido las historias más rocambolescas y

divertidas (gracias por descubrirnos Deseo), una persona que la necesito en mi vida.

Gracias a todos.

Summary

The work described in this thesis is motivated by the solvent-free synthesis of hybrid materials. These molecular compounds are based on azolates ligands and Fe(II) as metallic nodes. The sensibility of the Fe(II) species and facility to oxidizes to Fe(III) makes the solvent-free methodology based on ferrocene as metal source an important approach to expand the Fe(II) chemistry in materials science. This novel synthetic route can be applied to different metals and expand the synthesis to more metals such as Co(II), Zn(II) and Mn(II).

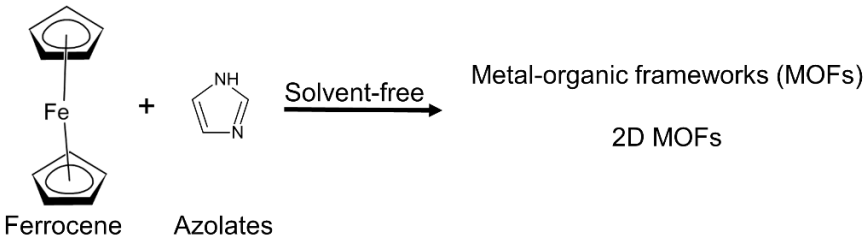

Chapter 1 offers a general introduction to hybrid materials based on molecules, as coordination polymers and metal-organic frameworks. The introduction is focused on zeolitic imidazolate frameworks and layered molecular materials, after a historical review of these metal-organic frameworks. Chapter 2 presents the synthesis of the iron ZIF-8 analogue (the **MUV-3**), using a solvent-free synthesis. This material was an elusive compound owing to the facility of the Fe(II) to oxidize to Fe(III) in the classic synthetic routes. In Chapter 3 it is shown a mixed-ligand approach to improve the water stability of SOD zeolitic imidazolate frameworks, using bulkier ligands to prevent the etching of water molecules. Chapter 4 presents a novel methodology to grow ZIF-8 in a controlled manner as a

film onto a glass substrate, based on microfluidic techniques. This technique permits the study of the crystal growth and the control of different parameters such as diffusion and time.

In Chapter 5 it is shown the first example of a high-quality 2D material based on a molecular compound (the **MUV-1**) thanks to its great stability and robustness. Its high quality permits to study and confirm its chemical composition and its crystallinity. Chapter 6 presents the goodness of the molecular materials, showing the easy implementation of several functionalities in a pre-synthetic approach, preserving all the properties and crystallinity. Chapter 7 shows the versatility of the **MUV-1** family, thanks to the tunability of the magnetic properties changing the metallic nodes of the systems maintaining the crystal structure. Finally, in Chapter 8 it is shown two different approaches to expand the synthesis of layered molecular materials to achieve 2D robust molecular materials such as the **MUV-1**.

The work described in this dissertation has given rise to the following publications:

"*Isoreticular two-dimensional magnetic coordination polymers prepared through pre-synthetic ligand functionalization*". J. López-Cabrelles, S. Mañas-Valero, I. J. Vitórica-Yrezábal, P. J. Bereciartua, J. A. Rodríguez-Velamazán, J. C. Waerenborgh, B. J. C. Vieira, D. Davidovikj, P. G. Steeneken, H. S. J. van der Zant, G. Mínguez Espallargas, E. Coronado. *Nature Chemistry*, **2018**, *10*, 1001

"*Solvent-free synthesis of ZIFs: a route towards the elusive Fe(II) analogue of ZIF-8*". J. Lopez-Cabrelles; J. Romero, G. Abellán, M. Giménez-

Marqués; M. Palomino, S. Valencia, F. Rey, G. Mínguez Espallargas. *JACS*, **2019**, *141*, 7173

"*Molecular 2D materials: a facile route to tune magnetic properties*". J. López-Cabrelles, S. Mañas-Valero, I. J. Vitórica-Yrezábal, M. Siskins, P. G. Steeneken, H. S. J. van der Zant, G. Mínguez Espallargas, E. Coronado. *Submitted*.

"*Microfluidic synthesis for metal-organic frameworks*". J. López-Cabrelles, C. Franco, A. Sorrenti, G. Mínguez Espallargas, J. Puigmartí-Luis. *In preparation*.

"*Solvent-free synthesis of ligand-mixed ZIFs*". J. Lopez-Cabrelles; E. Miguel-Casañ, E. Andres-Garcia, G. Minguez Espallargas. *In preparation*

Also, Javier López Cabrelles contributed to other works during the PhD:

"*Two Consecutive Magneto-Structural Gas–Solid Transformations in Non-Porous Molecular Materials*". J. Miguel-Donet, J. López-Cabrelles, N. Calvo Galve, E. Coronado, G. Mínguez Espallargas. *Chem. Eur. J.* **2018**, *24*, 12426.

"*Cation influence in adsorptive propane/propylene separation in ZIF-8 (SOD) topology"*. E. Andres-Garcia, J. López-Cabrelles, L. Oar-Arteta, B. Roldan-Martinez, M. Cano-Padilla, J. Gascon, G. Mínguez Espallargas, F. Kapteijn. *Chem. Eng. J.* **2019**, *371*, 848–856

"*2D magnetic MOFs with micron-lateral size by liquid exfoliation".* L. Leon-Alcaide, J. López-Cabrelles, G. Mínguez Espallargas, E. Coronado. *Chem Commun.* **2020**, *56*, 7657-7660

And these works have been presented as oral contribution by Javier López Cabrelles in (most relevant selection):

"*Surface tunability in magnetic layered MOFs*". J. López-Cabrelles; S. Mañas-Valero; G. Mínguez Espallargas; E. Coronado. *XXXVI Reunión Bienal de la RSEQ,* **2017**, Sitges (Spain).

"*Solvent-free synthesis of iron(II) ZIF-8 analogue: a single precursor for a bifunctional oxygen electrocatalyst*". J. López-Cabrelles; J. Romero; G. Abellán; G. Mínguez Espallargas. *43rd International Conference on Coordination Chemistry*, **2018**, Sendai (Japan).

"*Defect-free functionalized magnetic 2D coordination polymers*". J. López-Cabrelles; S. Mañas-Valero; G. Mínguez Espallargas; E. Coronado. *POLYMAT Spotlight*, **2018**, San Sebastian (Spain).

"*Solvent-free synthesis of magnetic two-dimensional coordination polymers*". J. López-Cabrelles; S. Mañas-Valero; G. Mínguez Espallargas; E. Coronado. *Multifunctional, Hybrid and nanomaterials*, **2019**, Sitges (Spain).

"*Chemical versatility in two-dimensional coordination polymers*". J. López-Cabrelles; S. Mañas-Valero; G. Mínguez Espallargas; E. Coronado, *EuroMof 2019*, **2019**, Paris (France).

Table of Contents

Chapter 1

Introduction

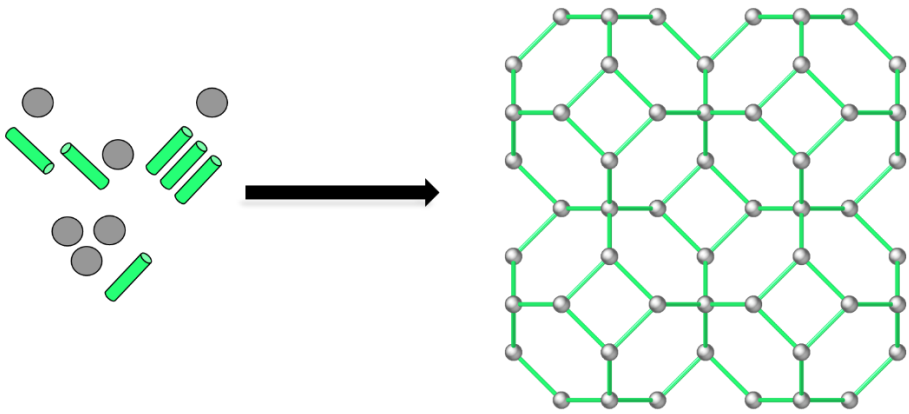

1.1 Coordination polymers and metal-organic frameworks

Along the XX century, inorganic and organic chemistry developed coordination chemistry around molecules: metal complexes, organometallics, and supramolecular chemistry,[1] although also some coordination classic polymers were discovered during these years such as Prussian blues[2] or Hoffman clathrates.[3] Coordination chemistry is based on a dative bond, the coordination bond, which is a class of acid-base Lewis interaction where metallic atoms act like Lewis acids and ligands as Lewis bases (Figure 1.1a). These metallic complexes can form a discrete entity (0D). However, in a repeated structure like the very known organic polymers, they can form chains with an extension in one dimension (1D), or construct more complicated frameworks with repetition of the motifs in two or three dimensions (2D and 3D) (Figure 1.1b). This class of materials, based on molecular complexes, has attracted the interest of different fields, and has played an important role in the growth of important areas such as molecular magnetism.[4]

However, the interest in extended metal-organic materials was initiated exploded in the 1980s with the publication of two seminal works by B. Hoskins and R. Robson in which they envisioned the possibility of designing frameworks with potential voids in their structures. In 1989, B. Hoskins and R. Robson reported the use of the four connected ligand 4,4,',4'',4'''-tetracyanotetraphenylmethane in combination with Cu(I), synthetising for the first time a metal-organic crystalline material in which 2/3 of the volume was occupied by solvent, being only 1/3 of the volume occupied by the framework (Figure 1.2a). This meant that this material

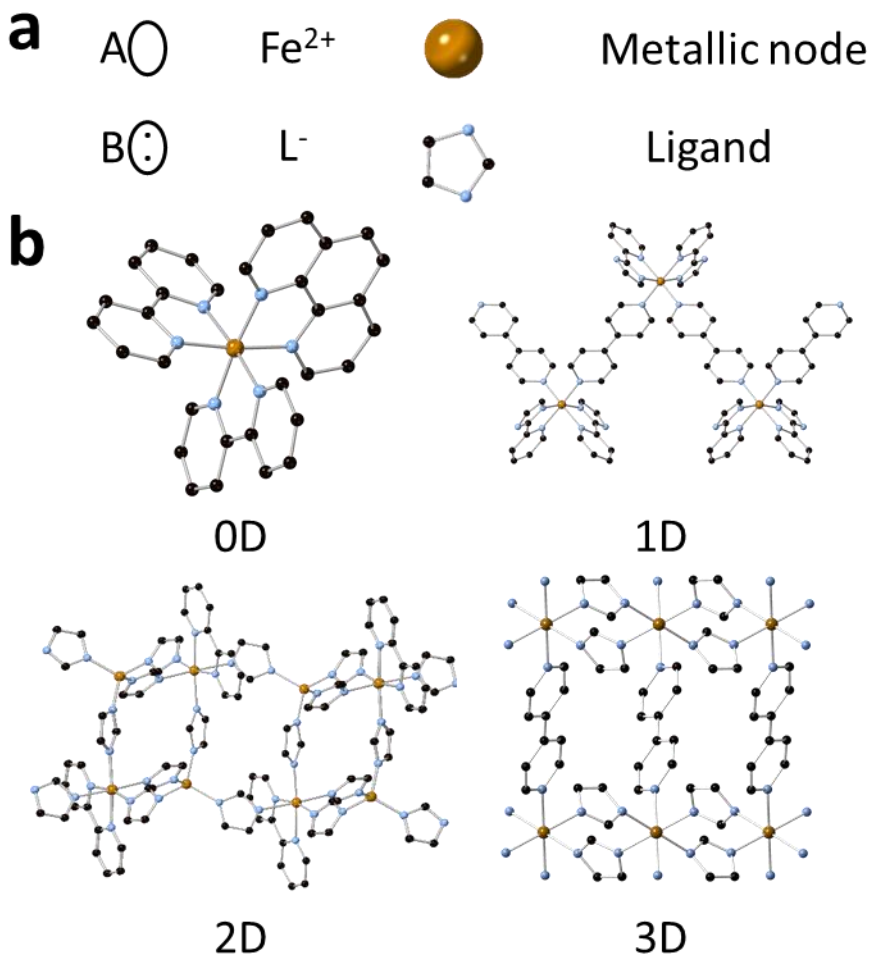

Figure 1.1 a) Coordination compounds are composed by Lewis acids (metal cation) and Lewis bases (ligand neutral/anion). c) Coordination compounds can organize in complexes (0D), chains (1D), or extended compounds (3D and layered materials).

possesed potential voids similar to those found in other known porous solids, such as zeolites,[5,6] but made from both organic and inorganic

moieties. In other words, this was the first example of a 3D hybrid framework, composed by an organic part, the 4-connected ligand, and an inorganic moiety, the metallic node, presenting cavities of 3,200 $Å^3$. This is considered to be the beginning of a new field that has attracted much interest in the past 30 years, and is the focus of this thesis: metal-organic frameworks, or MOFs.[7,8]

A few years later, in 1995, O. Yaghi and co-workers contributed to this new trend in coordination chemistry with a novel porous hybrid network and coining the term metal-organic framework (MOF).[9] The same year and only few months later, they published a MOF based in trimesic acid coordinated to Co(II) as metallic nodes. The octahedral environment was completed with pyridines, forming an interdigitated layered framework with channels full of different solvents, which for the first time were proved to be interexchanged, thus showing the first application of these porous systems (Figure 1.2b). However, this MOF collapsed upon evacuation, limiting their use in other applications.[10]

In another part of the world, almost at the same time, in 1997, S. Kitagawa and co-workers synthesized a different three-dimensional framework based in 4,4'-bipyridine, nitrate and M(II) (Co, Ni, Zn), with small cavities and channels. This was the result of a complex structure based in the arrangement of 1D chains forming planes (2D structure) and originating a "tongue-and-groove" like 3D structure (Figure 1.2c). This material was experimentally shown to be able to sorb O_2 (0.8 mmol/g), CH_4 (2.3 mmol/g) and N_2 (0.8 mmol/g) gas molecules in type I isotherms at 1-36 bar and 298 K. Thus, this was the first example of gas adsorption under

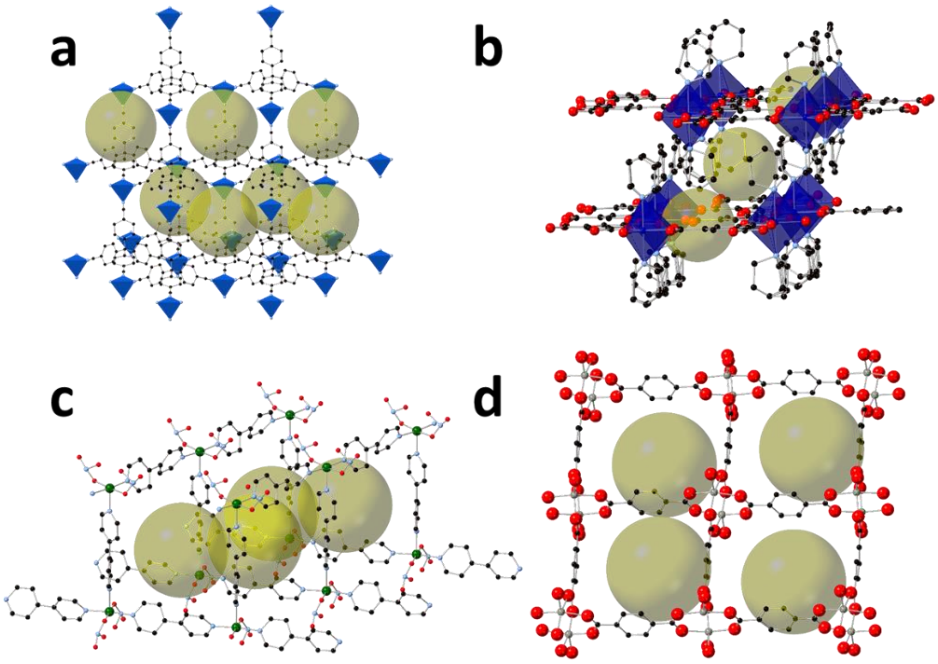

Figure 1.2 Three of the first metal-organic frameworks with potential voids and the first MOF with los pressures isotherms. a) Cu(I) centers in a tetrahedral environment connected by four-connected organic ligands. b) Co(II) centers in an octahedral environment connected by carboxylates (trimesic) and completing the coordination sphere with pyridines. c) Ni(II) centers connected by 4,4'bipyridines completing the coordination sphere with nitrates anions. d) Crystal structure composed by terephtalic birdges between Zn(II) paddlewheel nodes.

high pressures in coordination polymers, with a behaviour characteristic of microporous materials.[11]

In 1998, Yaghi's group presented the first experiments demonstrating the reversibility of the gas sorption process and permanent microporosity in a open framework, using a Zn(II) paddle-wheel material connected by terephthalic organic ligands (Figure 1.2d).[12] They measured the N_2 and CO_2 isotherms at 78 K and 195 K, respectively, at low pressures and reveling a type I isotherms for both gasses.

During the 90's, G. Ferey contributed with the application of the hydrothermal synthesis, characteristic of microporous inorganic compounds such as phospahetes or oxyfluorinated materials,[13] to synthtized hybrid networks.[14,15] However, is not until the publication of the MIL-47 material in 2002, a microporous hybrid compound constructed by V(III) and terephthalate ligand with a breathing behaviour,[16] when they start to developed their MOFs chemistry.

Nevertheless, these hybrid networks so far prepared had the common problem of a poor thermal stability, especially in comparison with the very robust zeolites. A significant breakthrough was then achieved, which consisted in the synthesis of the first example of a high thermal stable metal-organic framework (MOF), denoted **MOF-5**, by O. Yaghi and co-workers in 1999. This MOF is formed by Secondary Building Units (SBU), each composed by four Zn(II) as metallic nodes, connected between them by an O atom. This tetranuclear units are bridged by terephthalate ligand, forming a 3D structure of **pcu** topology (Figure 1.3a).[17] This concept of secondary building units (SBUs), i.e. metallic clusters of different geometries, offer multiple options from reticular design based in the connectivity to construct more stable and easier to be substituted metallic

clusters.[18,19] However, despite being stable until 410 ºC, **MOF-5** degrades upon exposure to water, thus limiting its applicability.

Furthermore, the enormous interest woken up in the coordination field was due to the similarity with the zeolites, besides adding the possibility to design flexible materials thanks to the organic nature of ligands and the huge number of possibilities to combine metals and ligands.[20] The combination of inorganic and organic parts opened the door to develop and design a vast number of compounds and applications.[18] In fact, many new structures started to be published every year,[21–23] with an exponential growth that still has not reached its maximum. Making an exhaustive description of all the MOFs is unfeasible, as there are almost 100,000 MOFs reported to date. In this part of the introduction we will present a personal list of the most important and representative MOFs in the early years, in order to understand the evolution of the field (Figure 1.4).

One of the most-studied MOFs was reported in 1999 few months before the publication of **MOF-5**. D. Williams and co-workers synthesized a material denoted **HKUST-1** (HKUST is the acronym Hong Kong University of Science and Technology), a novel network constructed by trimesate as organic part and a bimetallic Cu(II) unit forming a paddlewheel SBU as the metallic node. The coordination environment is completed with apical water molecules (Figure 1.3b).[24] **HKUST-1** presents thermal stability (240 °C) and, contrast to zeolites, offers the possibility of removing the water molecules from the SBU unit, opening the door to chemically functionalizable frameworks. For these reasons, it is commonly used as a model MOF in novel applications or synthetic routes.

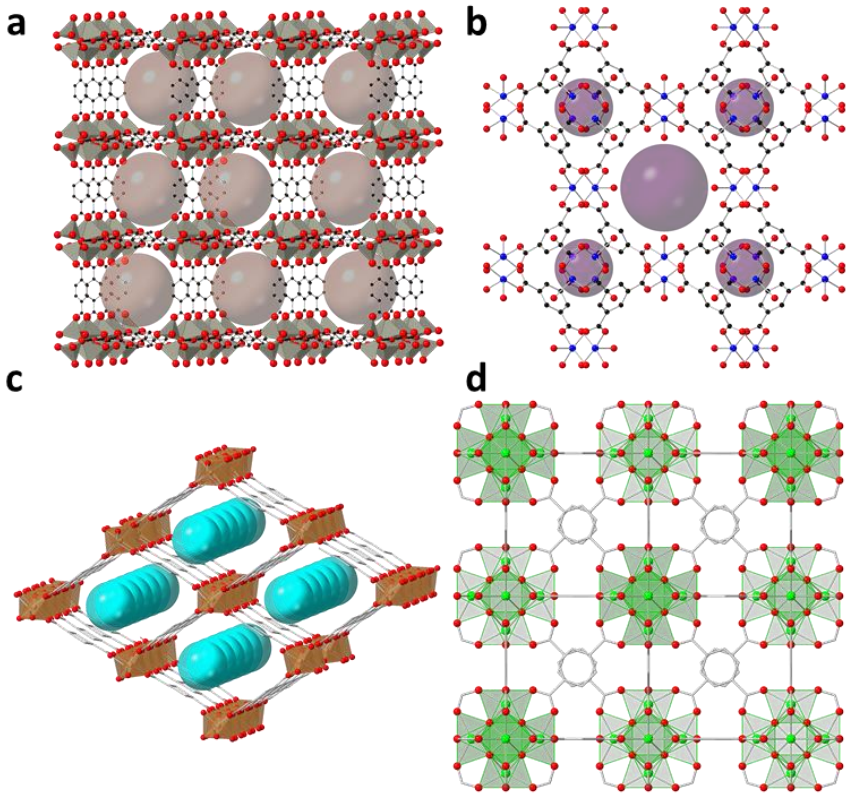

Figure 1.3 Crystal structure of most used metal-organic frameworks. **MOF-5** composed by Zn (II) SBUs and terephthalic acid (a), **HKUST-1** composed by Cu (II) paddle-wheel SBUs and trimesic acid (b), **MIL-53** composed by Cr (III) and terephthalic acid (c) and **UiO-66** composed by Zr (IV) SBUs and terephthalic acid (d).

In parallel, and once the isolation of some stable MOFs was achieved, the combination of these hybrid networks with the presence of pores and cavities opened the door to explore potential applications. The high interest in these materialsc came from the presence of SBUs with the possibility of

unsaturated coordination position or removable coordinated solvent molecules and the interaction of guest with the organic linker.[25–27]

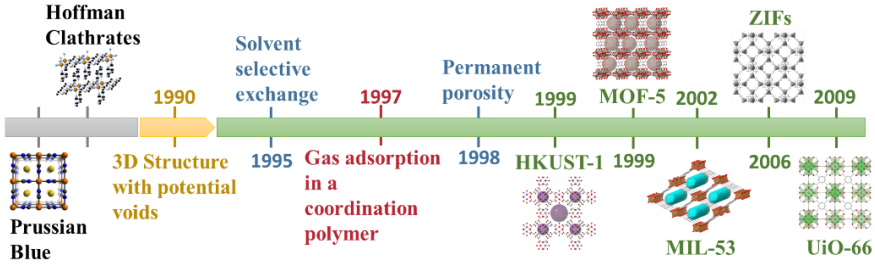

Figure 1.4 Scheme of the achievements and materials in porous coordination polymers and MOFs in the early years.

The first of these applications is the interaction with gases, such as gas storage, gas capture and gas separation.[28] CO_2 capture and separation are one of the most important applications for industry and prevention of climatic change, and for these reasons is a very studied application in porous materials.[29] The hybrid nature of MOFs or also called porous coordination polymers (PCPs), makes them perfect candidates to solve this problem, and many examples on CO_2 separation can be found in the literature from different approximations, such as using unsaturated metal SBUs (for a stronger interaction with the gas), using ligands with functional groups (for a strong interaction with the gas molecules, e.g. amines),[30] or pillared layered compounds based in SiF_6^{2-}.[31]

Nevertheless, a common problem of MOFs after the removal of the guest is the collapse of the framework. That occurred often in the first generation of MOFs. For this reason, some research groups focused on robust MOFs (second generation), which do not collapse upon evacuation

of the pores. The third generation of MOFs brings a novel concept, flexible MOFs, making these hybrid networks more responsive to external stimuli.[32] The most simple concept in flexible networks, such as breathing, consists on a displacement of the atoms of the framework that is accompanied by a unit cell volume change due to the incorporation of a guest. Another possibility is swelling, a gradual enlargement of the MOF unit cell. These flexible behaviours were present in very-known MOFs, as **MIL-53**[33] and **MIL-88**.[34] However, the phenomenon of gas adsorption can be complicated even more when a flexible network is present. The design of novel flexible MOFs shows interesting phenomena such as the negative gas sorption, displayed by **DUT-49**, a work developed by S. Kaskel's group.[35,36] The flexible network is nowadays an important challenge to understand better the gas sorption phenomenon.

Returning to the search of significant early MOFs, a few years after the synthesis of **HKUST-1**, in 2002, Ferey's group at the Institut Lavoisier in France reported the first examples of the combination of carboxylates and M(III). Until that moment, the metallic nodes based on M(II) centers dominated the MOFs field. Ferey and co-workers developed a series of Cr-based MOFs, such as **MIL-53,** composed by octahedral Cr(III) centers connected by terephthalic linkers (Figure 1.3c), and **MIL-101,** based in trimers of Cr(III) as SBUs bridged by terephthalic, presenting high gas adsorption capacities with surface areas around 5,900 m^2g^{-1} showing the huge possibilities to host not only gases, but also large molecules.[33,37] **MIL-101** presents a giant unit cell volume, around 380,000 $Å^3$, and pore sizes between 25-29 Å in diameter. Their huge capacity to host guest molecules

was demonstrated through the incorporation of a enormous polyoxo salt, the Keggin $K_7PW_{11}O_4$ polyoxometalate, with a van der Waals radius of 13.1 Å. The huge cavities opened the door to encapsulate drugs and higher molecules for biomedical applications and drug delivery.[38]

After several years of discovering novel MOFs, with a considerable number of structures, applications became more common. However, the instability against water was a problem, primarily due to the lability of M(II)-carboxylate –the most present chemical composition in MOFs to the date–. For this reason, MOFs stability in water became a hot topic and the chemistry of MOFs expanded looking for SBUs beyond the metals of the first transition series. Rational and reticular design are two important tools to develop new materials, and in the race to achieve stable MOFs, there are important chemical concepts to make easier this achievement. The introduction of this thesis began with the example of Lewis acid/base, and in this theory, the concepts of "hard" and "soft" play an important role to construct stable MOFs. Carboxylates are hard Lewis bases, and form strong bonds with hard Lewis acids, i.e. metals with high oxidation states, such as Cr(III) in the mentioned **MIL-101**. But there are also higher oxidation states avaible in other transition metals, such as Ti(IV) or Zr(IV). On the other hand, azolates are soft Lewis bases that, in combination of Co(II), Zn(II), Ni(II) or Fe(II), form strong bonds. Two examples of these strategies will be briefly discussed.[39]

The first example, based in hard Lewis acids/bases, was reported in 2009. K. Lillerud and co-workers designed a metallic cluster composed by six Zr(IV), four O^{2-} and four OH^{-}, which were interconnected with

terephthalates, yielding a 3D material denoted **UiO-66** (Figure 1.3d). This MOF was proved to be resistant to water, DMF, benzene and acetone.[40] They also used similar linkers increasing the length with the number of aromatic rings, achieving isoreticular MOFs with extended structures, denoted **UiO-67** and **UiO-68**.The use of hard Lewis acids and oxo-ligands for constructing stable SBUs, such as Ti(IV) or Zr(IV), was popularized since the publication of this work.

In contrast to the examples described so far, there are also alternatives to carboxylate ligands. Nitrogen-based ligands, such as azolates, can offer an stable alternative using M(II), being the second example of a stable MOF based in soft Lewis acids/bases. Replicating the structure and topologies of zeolites, looking for analogous systems with high chemical and thermal stability, one of the most important subclasses of MOFs was born in 2006: zeolitic imidazolate frameworks (ZIFs). Imitating the angle of bonding in zeolites, Yaghi's group developed a huge family of materials based in imidazole derivate.[41] The relevance of this important family of compounds to this thesis deserves a specific section (section 1.2).

In the recent years, the number of MOF structures has continued to grow. However, the applications and emerging concepts have taken more relevance than in the first years, where were focused on synthesis of MOFs.[42] The accessible cavities in the structures of different MOFs permits to expand the applications of these materials beyond those involving gas interactions (capture, separation, storage). In fact, the pores can act as microreactors and make MOFs an exciting platform as heterogeneous catalyst.[43,44]

The change in dimensionality and size is a challenging recent topic. Most of the porous frameworks are 3D networks. However, the exfoliation of hybrid materials (layered compounds) was known ten years ago. Also the isolation of coordination materials as nanoparticles ir thin films. These are an interesting tools for the development of several applications, such as electronics,[45,46] magnetism[4] or membranes,[47] which seeks to explore the 2D world, in for example, SURMOFs, 2D MOFs or 2D nanosheets. [48]

Another recent area of interest deals with the combination of flexibility, rigididity and periodic lattice arragments, which permits to explore and study mechanical stress and novel properties, such as the unusual metamaterials. This class of materials presents exotic properties and behaviours, such as negative thermal expansion, negative Poisson's ratio or negative linear compression.[49]

Finally, the emerging concepts in MOFs have evolved to a new generation of MOFs (4^{th} generation). The main characteristic of these compounds is the lose of long-range order, becoming liquids or glasses. To the date, the MOFs field has grown closely with crystallography and crystalline materials. However, this noncrystalline family of compounds can offer different properties and functionalities, such as the classic noncrystalline materials in other families (metals, polymers and ceramics).

This thesis is focused mainly on Fe(II) azolates and other 3d metals (Co, Mn, Zn) in combination with imidazole derivate. For this reason, the following section will present in detail one of the most important subclasses of MOFs based in imidazole: Zeolitic Imidazolate Frameworks.

1.2 Zeolitic imidazolate frameworks

In the part of "famous" MOFs developed in the first years, Zeolitic Imidazolate Frameworks (ZIFs) have been mentioned as an important subclass of MOFs. ZIFs are composed by imidazole (and derivatives) and monometallic nodes with tetrahedral environment (in this case the SBU is formed by only one metallic atom) (Figure 1.5a). The main characteristic of these compounds is that similar topologies are similar to inorganic zeolites. This is due to the coordination angle of imidazole, which is similar those of to that of Si-O (Figure 1.5b). Although there are earlier examples of imidazolate-based fameworks,[50–52] some with zeolite-like topologies,[53–56] this subclass of MOFs were synthesized and popularized by Yaghi and co-workers in 2006 due to the high chemical and thermal stability.[41] In that work, twelve structures were reported based on imidazole, 2-methylimidazole (2meimH) and benzimidazoles (bimH), and Zn(II) and Co(II) as metallic cations (denoted from **ZIF-1** to **ZIF-12**). One important MOF of this type is $Zn(2meim)_2$, also known as **ZIF-8**.

The synthesis of ZIFs opened the possibility to imitate inorganic topologies through molecular chemistry, bringing some advantages such as broad functionalization and chemical variety. These MOFs provide the same distribution of channels and windows as zeolites due to the crystal location of the metal and ligands. For example, **ZIF-8** ($Zn(2\text{-}meim)_2$) has the sodalite topology (**SOD**), which consist of a ring of 4 and 6 members, and 0D channels (voids). This material crystallized in the cubic crystalline

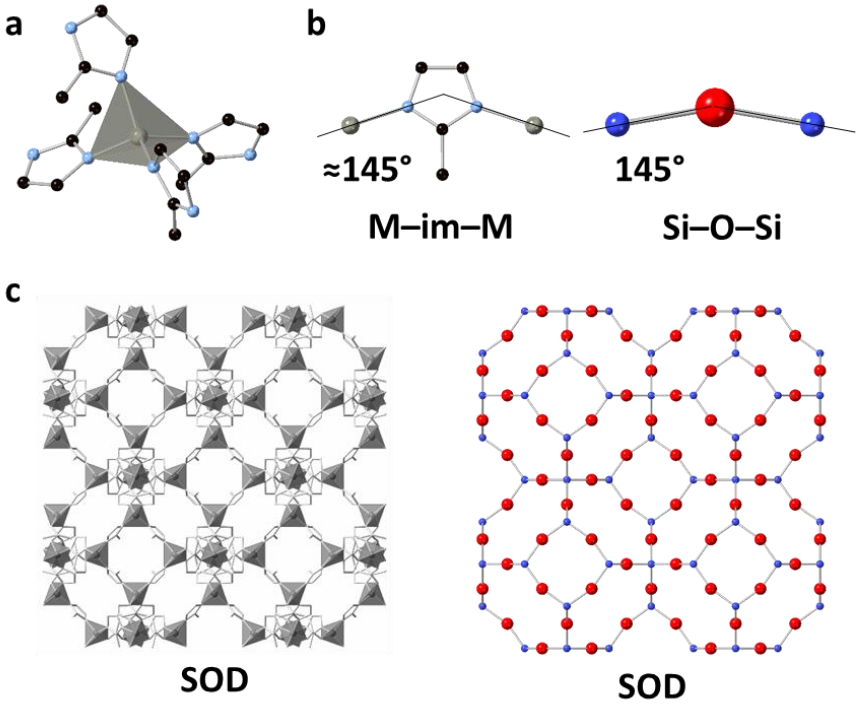

Figure 1.5 a) The tetrahedral environment of Zn(II) in ZIFS. b) The similitude of coordination angle in ZIFs with zeolites. c) The SOD topology in zeolites (right) composed by Si (blue) and oxygen (red) and SOD topology in ZIFs (left).

system and, when compared with a zeolite with **SOD** topology, it can be clearly appreciated the same type of framework (i.e. isoreticular framework) (Figure 1.5c).

The versatility of these materials arise from the easy functionalization of imidazole in different position. As a result, a huge range of imidazole derivates are available to construct ZIFs (Figure 1.6). In addition, the high

number of metals (mainly 3d metals) that can be incorporated in the structure allows to tune the properties of ZIFs.

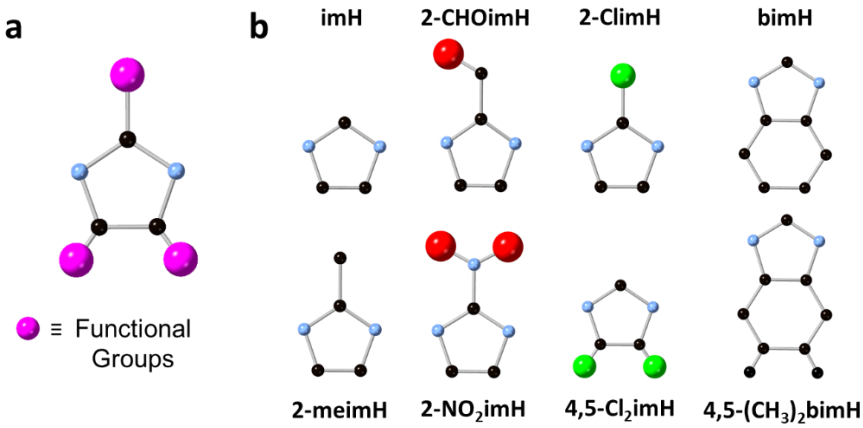

Figure 1.6 a) Positions for possible functional groups in imidazole derivate. b) Some examples of different imidazole derivate which can form ZIFs.

Polymorphism also plays an important role in the vast number of ZIFs, owing to the different networks accessible with the same cation and ligand. For example, the combination of 2meimH with Co(II) (**ZIF-67**), Zn(II) (**ZIF-8**), Mg(II), Mn(II) or Cd(II) (**CdIF-1**) can produce a crystalline porous material with **SOD** topology network,[41,57–60] although it is also possible to obtain networks with *kat* and *dia* topologies (dense polymorphs) depending on the synthetic routes[61] (Figure 1.7). This example is extensible to other ligands. For example, the combination of bimH with Zn(II) and Co(II) can yield **ZIF-7** and **ZIF-9**, which are porous solids with **SOD** topology, but through different synthetic methodologies other topologies such as **RHO** can also be synthetized (in **ZIF-11**),[41] or even layered structures[62] (Figure 1.7). The topologies are not exclusive for a specific

ligand, and one topology can be accessible by many different linkers. For example, **RHO** topology can be constructed by bimH (**ZIF-11**)[41] or with 2-ethylimidazole (**MAF-6**).[55] **SOD** topology is the most common in ZIFs, obtainable by at least 6 imidazoles,[41,57,63] not only by direct synthesis, but also by ligand exchanges.[64]

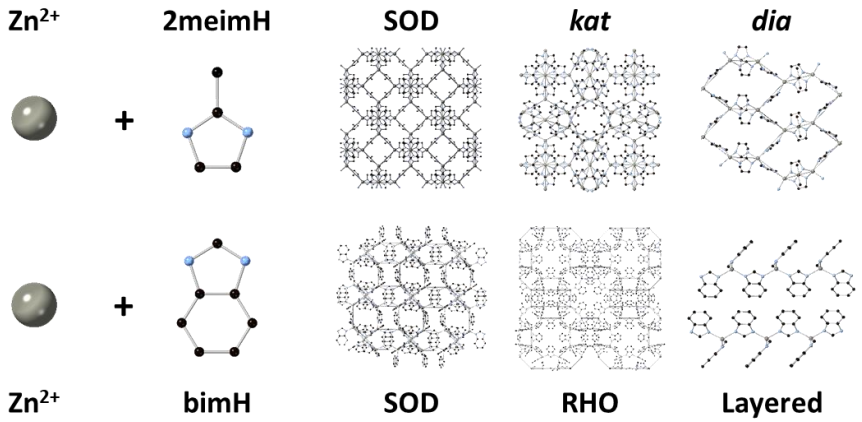

Figure 1.7 The different topologies achievable by the assembly of 2-meimH and Zn^{2+} in $Zn(meim)_2$ (Top) and the assembly of bimH and Zn^{2+} in $Zn(bim)_2$ (below).

Among all the reported ZIFs, the most studied is **ZIF-8** due to its facile synthesis and its high chemical (despite its water instability) and thermal stability. **ZIF-8** crystallizes in a cubic crystalline system and typically forms big single crystals with a rhombohedral morphology (Figure 1.8). Nonetheless, a huge range of different shapes can be obtained by chemical etching.[65] **ZIF-8** is a model material used to develop new techniques in processability and synthetic methodologies, and has been applied in many different areas such as gas separation,[66–68] membranes,[69–

[71] thin films,[72] drug delivery,[73,74] nanorobotics,[75,76] catalysis[77,78] and water splitting (Figure 1.8).[79–82]

The possibility to use different metals opens the window to tune some properties due to the changes in the network flexibility, changing the gas preference between **ZIF-8** (Zn) and **ZIF-67** (Co).[67] **ZIF-67** is a very well known material, which has been widely used to prepare carbon derived materials for water splitting.[83,84]

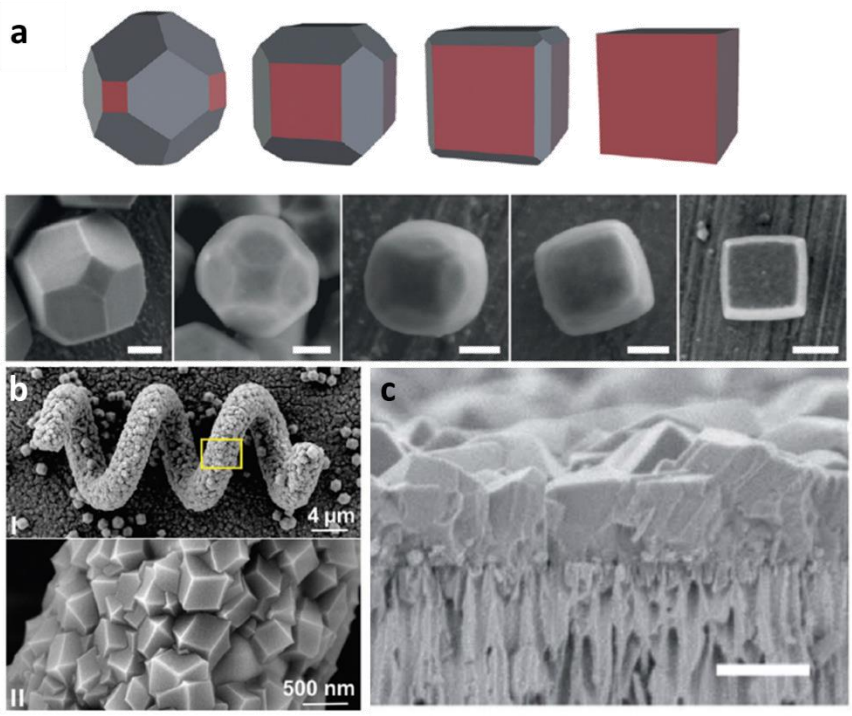

Figure 1.8 a) Different morphologies for **ZIF-8**. b) MOF-Bots covered by crystals of **ZIF-8**. c) Membranes based in thin films of **ZIF-8** for gas separation. Adapted from references 65,71 and 75.

The manganese and magnesium analogues of **ZIF-8** present only a small difference in the total gas sorption and structural instability. These small changes in the gas sorption can be attributed to the small difference in the crystal cell parameters or a different gate opening behavior.[58,59] The gate opening phenomenon is a two-step gas adsorption due to the effect of the pressure in the framework because of the flexibility of the imidazolate bond and M(II) nodes. The structural changes in **ZIF-8** were studied at high pressures (14 700 bar), where the imidazolate linker rotate a little bit and change the window aperture to the pore (Figure 1.9a).[85] The adsorption of molecules with higher molecular diameter than the six ring pore window suggests a structural change at more "current" pressures for gas adsorption. D. Fairen-Jimenez and co-workers studied these structural changes in **ZIF-8** during the N_2 adsorption and calculated the theoretical adsorption for the known **ZIF-8** crystal structure and the crystal **ZIF-8** structure at high pressures. These results were can sustent with a two-step gas adsorption of **ZIF-8** caused by a structural change involving the rotation of the imidazolate linker during the gas adsorption, which allows for better packing of N_2 molecules inside the cavity and close to the four-ring window. [86–88] Note that although the original discovery of ZIFs was based on zeolite like topologies there are also imidazole-metal compounds without zeolite topologies. In fact, novel topologies have been found nowadays, not present in zeolites. Thus, the line between ZIFs and imidazolate-based materials is somewhat unclear. One example of this is the layered $Zn_2(bim)_4$ synthesized by Peng and co-workers for building molecular sieving membranes.[62,89] The layered structure gives novel

possibilities and applications on MOFs and CPs and the complexity of this group of materials makes us change section.

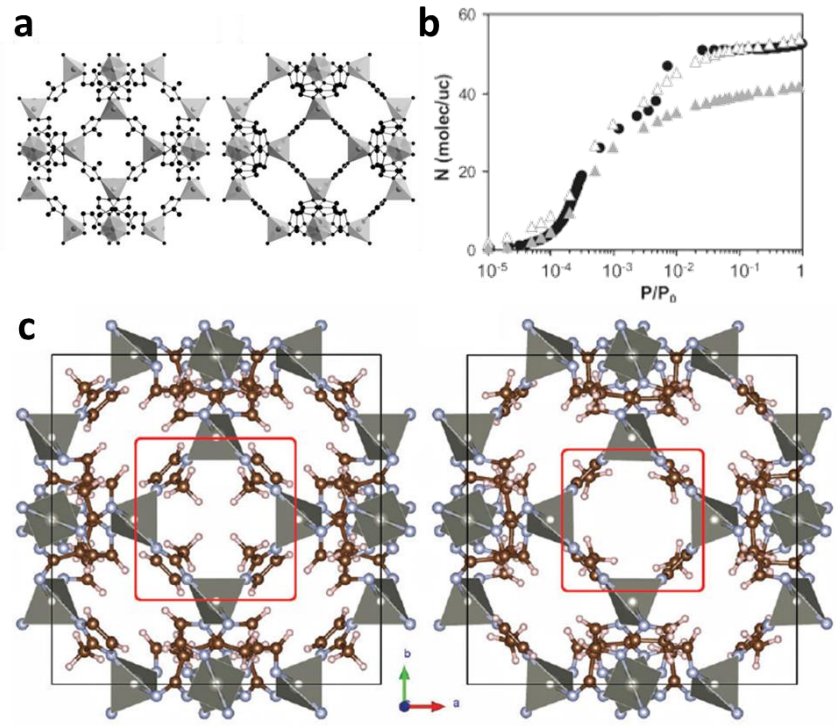

Figure 1.9 a) Different orientation of 2meimH in the crystal structure at atmospheric pressure (left) or high pressure (right) b) Different gas adsorption behavior for the high/atmospheric/experiment pressure. c) Crystal structure in detail before (left) and after (right) the gas adsorption showing the gate opening phenomenon. Adapted from references 85, 86 and 88.

1.3 Layered materials and two-dimensional materials

The existence and knowledge of layered inorganic materials date back to 1960s,[90] but it was not until the isolation of **graphene**[91] that this class of materials were popularized.[92] Graphite is a 3D material composed of an infinite number of stacked layers of carbon atoms bonded covalently, which are assembled by weak van der Waals (vdW) interactions. When one layer is isolated, **graphene** is obtained, which is a two-dimensional material (2D material) (Figure 1.10a). For example, the electronic conductivity changes from a gap semiconductor in bulk to a zero-gap semiconductor in the 2D limit.[91] The interest in graphene is due to the rise of novel properties related to the low dimensionality. One of the hottest fields now in physics is the magic angle between two layers of graphene, which can give rise to superconductivity.[93–95] Beyond graphene, other layered inorganic materials separated by weak vdW forces, which can be exfoliated down to the monolayer.[96] The resulting 2D materials exhibit different behaviors, such as **insulator** (h-BN),[97] **semiconductor** (2H-MoS_2, black phosphorous),[98,99] **metallic** (1T-MoS_2),[100] and **superconductor** (Mo_2C, 2H-$NbSe_2$ or 2H-TaS_2).[101–103] In this context, the most elusive property has been the **magnetism** (V_5S_8, $FePS_3$, $Cr_2Ge_2Te_3$ or CrI_3).[104–107] Thus, ferromagnetism in the 2D limit was reported for the first time in 2017, although it should be noted that these inorganic 2D materials are unstable at ambient conditions (Figure 1.11b).

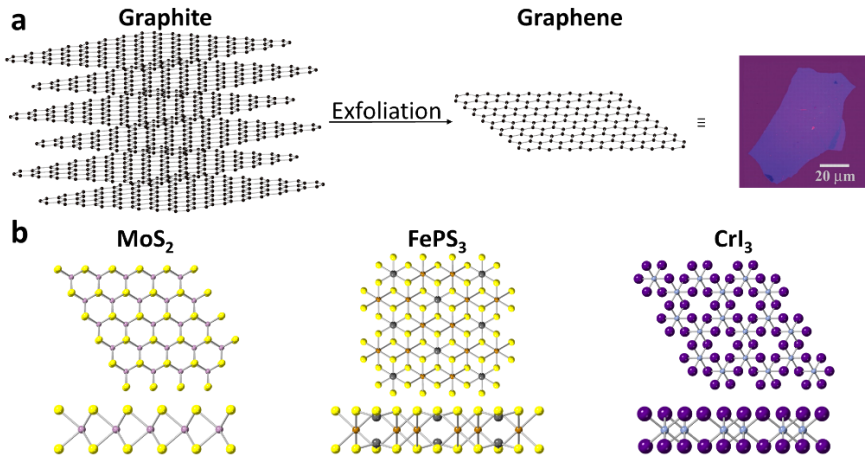

Figure 1.10 a) Crystal structure of graphite and the exfoliation to obtain graphene monolayer with a lateral size around 40 µm. b) Examples of layered and 2D inorganic materials presenting different properties such as semicundoctors (2H-MoS_2) or magnetic materials ($FePS_3$ and CrI_3).

The 2D world is in constant evolution and there are two uncovered main goals. First, magnetic properties were under search to study the influence of dimensionality over the magnetism in these materials. The recent discovery of ferromagnetism in monolayers,[106,107] has encouraged to seek more magnetic and stable materials.

Second, chemical functionalization of 2D materials is another topicfield of great interest. In the absence of convincing achievements in functionalization of 2D materials, novel approaches are required. The functionalization permits to tune, for example, the electronic properties a given material, or modify its surface behavior to incorporate these materials in devices, or improve their processability.[108] The chemical stability of "archetypal" inorganic 2D materials (graphene, MoS_2, etc) difficults their

functionalization and randomize the position of the introduced function over defects. At this point, novel materials are required to take advantage of the properties of the 2D material while making easier their functionalization and tunability.

The measurement of the physical properties of a 2D material (such as magnetism) often requires a clean exfoliation. For this reason, the cleavage of layered materials is usually done by micromechanical exfoliation using the Scotch tape method (Figure 1.11a). However, one big disadvantage of this technique is that it requires large single crystals to be exfoliated. This methodology consists of exfoliating the crystals of the layered material putting the oriented crystals in a strip of Scotch tape and with different clean strip, the layers go separating in cycles. However, for purposes, such as functionalization or chemical applications, the quality of the flakes can be lower and an exfoliation process assisted by solvents becomes appropriate. This method allows to obtain high quantities of 2D materials (Figure 11b).[109]

Owing to these limitations, coordination chemistry can offer alternatives to classical inorganic materials, thanks to the possibility to exploit chemical design and reticular chemistry. In metal-organic frameworks and coordination polymers, several examples of layered materials were reported since the 90s. For example, coordination polymers based in oxalate mixed-metal assemblies were first published by Okawa and co-workers in 1992,[111] and vastly developed afterwards.[112] This family of compounds was synthesized with bulky countercations (for example,

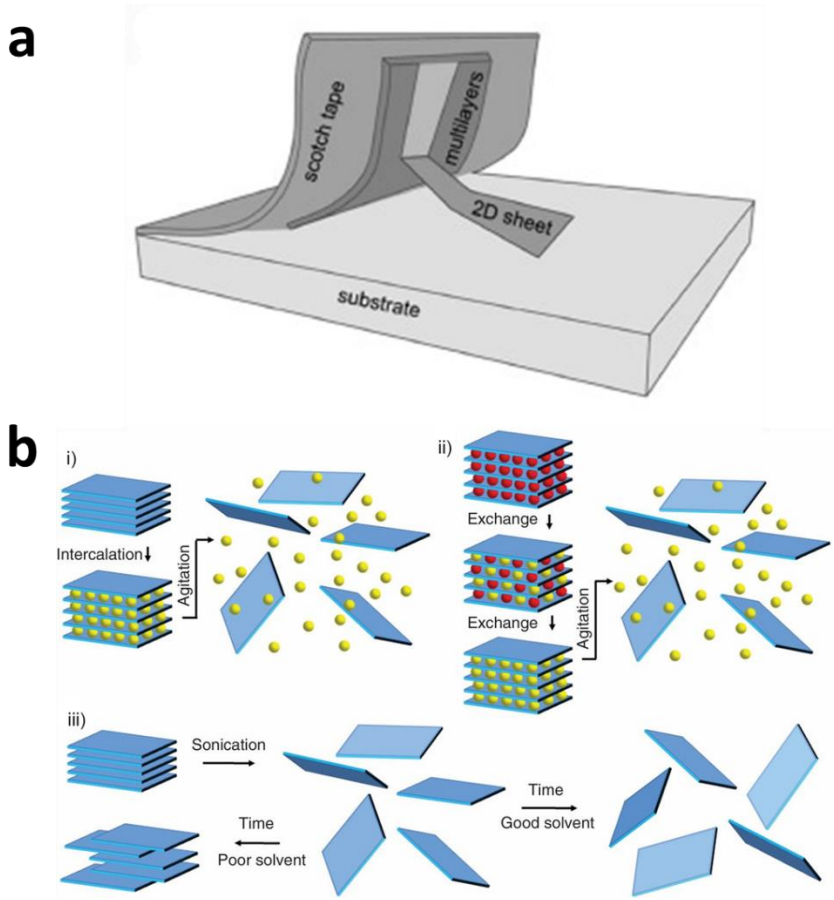

Figure 1.11 a) Different strategies for liquid exfoliation in 2D materials. b) Scotch tape methodology for dry exfoliation of 2D crystals. Adapted from references 109 and 110.

tetrabutylammonium, TBA) to counterbalance the negative charge of the layers. The bulky nature of the counteraction and ots design influences the layered growth of the material. Very similar are the anilate families,[113] based in benzoquinones ligands, and with similar properties and layered structure.[114] The interest in these compounds is primarily based on the

magnetic properties and the combination of other functionalities such as metal conductivity(multifunctionality).[112,115] Normally, the obtained materials are polycrystalline or small single crystals, and the charged nature of the layers difficult their exfoliation by micromechanical methods.[116] However, few examples of liquid exfoliation of anilate-based coordination polymers have been reported.[116,117]

A recent example of interesting layered material was published by K. Pedersen and co-workers based in pyrazine ligand and $CrCl_2$.[118] This combination forms a layered MOF with conductive and magnetic properties. At room temperature, this material presents high conductivity due to the hopping-based transport mechanism. Pyrazine acts like redox-active ligand, combining their π orbitals with d orbitals from Cr. This mechanism delocalizes the electrons and explains the conductive behavior. At low temperatures (around 55 K), the electron from the pyrazine radical and the Cr electrons coupling in ferromagnetic ordering, obtaining an uncompensated magnetic moment at low temperatures. This approximation using a redox-active strategy to design conductive materials at room temperatures and magnetic materials at low temperatures is a promising chemical design to synthesize functional MOF for electronics applications.

For the purpose to obtain 2D molecular materials, the first option is the top-down exfoliation of layered materials. For this approach, it is necessary that CPs and MOFs have weak interaction between the layers and after the exfoliation the possibility to stabilize these 2D MOFs. For that, the most common technique is the liquid assisted exfoliation (wet methodology).[119,120] However, exist some examples of micromechanical

exfoliation (dry methodology). This technique is the cleanest and most used for physical measurements owing to the high quality flakes obtained by this method. The counterpart is the small quantity obtained of the exfoliated material and the requirement of big and robust crystals (uncommon in coordination chemistry). Before the presentation of the work developed in this thesis (Chapters 5 and 6), only one attempt to micromechanically exfoliate a coordination polymer was described in the literature.[116] In this case, some flakes of the compound could be exfoliated, although due to the fragility of the crystals, the flakes were partially destroyed. In addition, the thinner flakes were too small in lateral dimensions, and monolayers of the material could not be found (Figure 1.12a). However, small micosheets present 2 nm thickness, corresponding to bilayers. Recently, after publishing the work described at the Chapter 5, S. Tongay and co-workers published an example of chemical design to form a layered MOF to facilitate the exfoliation process by micromechanical exfoliation and bottom-up approaches (thin films).[121] They use the MOF-2 layered strcuture[12] composed originally by Zn paddle-wheel unit in a pyramidal square base environment connected by benzenedicarboxylate (BDC) (one H_2O molecule complete the coordination sphere) (Figure 1.12b). In their chemical design, they used a two-phase synthesis to control the crystal growth and the interlayer hydrogen bonds using pyridine as a coordinating monodentate ligand (Figure 1.12b). The replacement of the water molecules by pyridines changes the hydrogen bonds between layers by weak van der Waals forces, facilitating the exfoliation process, obtaining monolayers.

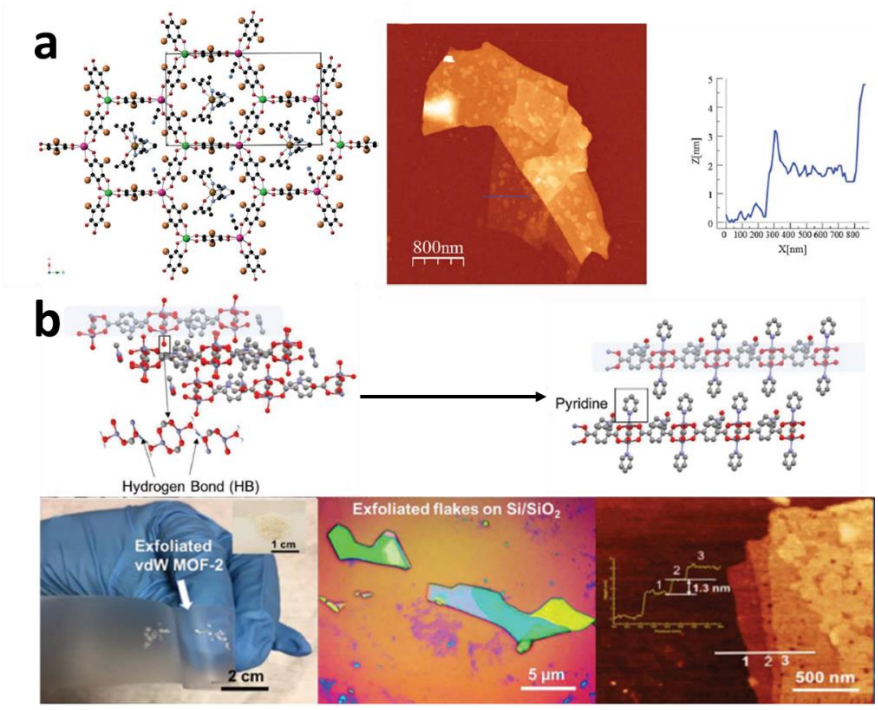

Figure 1.12 a) Layered crystal structure of anilate compounds (left), AFM image, and their thickness (middle and right, respectively). b) Scotch tape exfoliation for the MOF-2 (left) and AFM image and their thickness (middle and right, respectively). Modified from references 116 and 121.

For the most used methodology, the liquid assisted exfoliation, the first example was developed by F. Zamora and co-workers in 2010, using Cu coordination polymers composed by isocotinic ligand and bromine atoms ($[Cu_2Br(IN)_2]$, IN = isocotinate).[122] The copper cations are in a paddle wheel environment, coordinated by two oxygen atoms from two different carboxylates groups, two nitrogen atoms from two isocotinato, and a bromine atom bonded to the two copper atoms from the paddle wheel unit (Figure 1.13a). The layered nature of the coordinated compound and

the similitude to graphite, suggested to the authors to use the sonication bath such as the mechanical force to exfoliate this Cu CP. They deposited the sonicated solution on Highly Oriented Pyrolitic Graphite (HOPG) as a substrate, and characterized the exfoliated flakes by a common technique in this field, atomic force microscopy (AFM), to measure the thickness and lateral size of the exfoliated material. In this study, they isolated monolayers with a thickness of around 0.5 nm (monolayer) with lateral sizes around 500 nm (Figure 1.13b). However, the chemical composition and crystallinity were not confirmed in the exfoliated material. This observed size, around 500 nm or less, is known as nanosheets, the most common obtained material by this exfoliation methodology.

In this direction, one of the best examples of layered MOFs and their exfoliation[62] is a compound based in bimH and Zn(II). This is a great example of the preparation of a layered material, its exfoliation, and characterization after the exfoliation process. In this work, Peng and co-workers used $[Zn_2(bim)_4]$ as a layered precursor, a material composed by Zn(II) metallic nodes in a tetrahedral environment, connected by benzimidazolate bridges, where the benzene ring are oriented to the surface of the layers and Zn nodes are in the inner part of the layers (Figure 1.14a). These layers interact with weak van der Waals interactions facilitating the exfoliation process. The single crystals of $[Zn_2(bim)_4]$ have a clear layered morphology checked by Scanning Electron Microscopy (SEM) (Figure 1.14b) and a high crystallinity measured by X-ray powder diffraction (XRPD) (Figure 1.14c). Before this work, the chemical and structural properties of the exfoliated 2D molecular materials were typically not

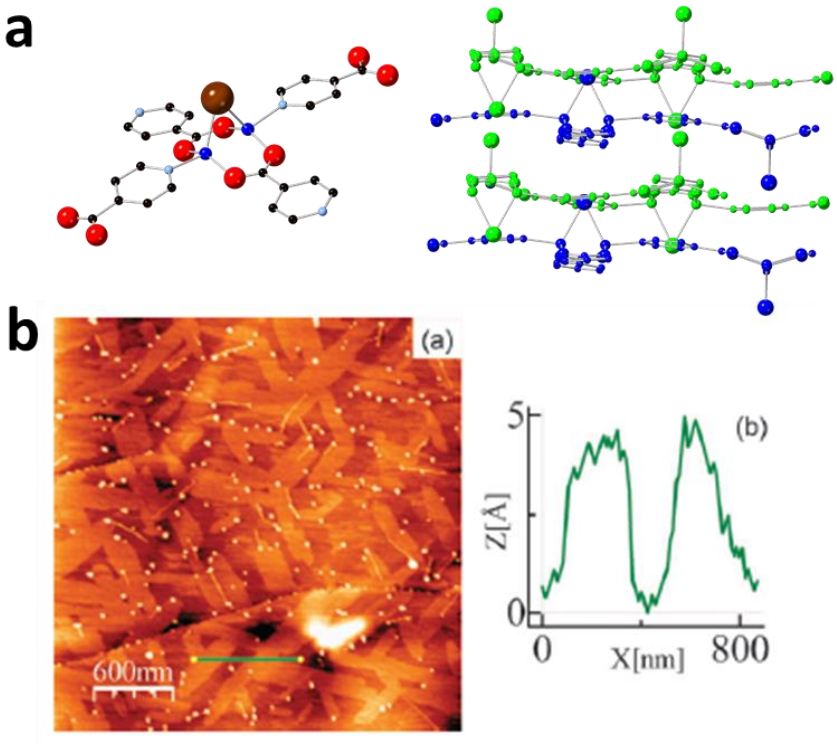

Figure 1.13 a) The coordination environment of the Cu paddlewheel and the crystalline layered structure of the Cu CP b) AFM measurement of monolayers from the exfoliated Cu CP. Modified from reference 122.

measured, which is an important aspect to compare with classical 2D inorganic materials and their application and correlation between properties and crystal structure. AFM studies were the sole experimental technique applied to the exfoliated flakes, and although this is very appropriate to show the topography of the flakes, it does not demonstrate the chemical and structural integrity retained in the 2D molecular materials from the bulk precursor.

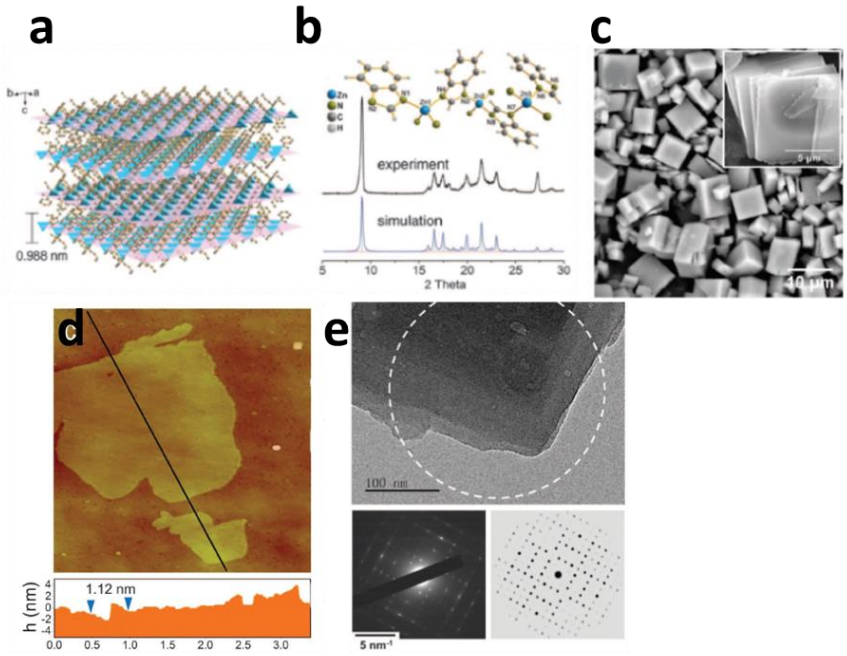

Figure 1.14 a) Architecture of the layered MOF precursor. The *ab* planes are highlighted in purple to better illustrate the layered structure. b) Powder XRD patterns of Zn_2 (bim)$_4$. The top trace is the experimental pattern, whereas the bottom trace is the pattern simulated based on the single-crystal data c) SEM image of as-synthesized Zn_2(bim)$_4$ crystals. The inset image shows the typical flake-like morphology of Zn_2(bim)$_4$ crystals. d) Tappingmode AFM topographical image of Zn_2(bim)$_4$ nanosheets on a silicon wafer. The height profile of the nanosheets along the black lines was marked in the image. e) SAED pattern (white circle) shows the diffraction from (hk0) planes within a few-layered nanosheet. A simulated SAED pattern of Zn_2(bim)$_4$ nanosheet down the *c* axis is also shown. Adapted from reference 62.

At this point, Peng and co-workers decided to use a modification of the classical liquid exfoliation using a softer methodology to prevent the damage of the in-plane MOF structure. They used a wet ball-milled at low speed before the sonication process to help the solvent induce the separation of the layers. They checked a list of solvents and determined the combination of methanol and propanol as the best option.

After the exfoliation process, they characterized the nanosheets by AFM to show the thickness and lateral size of the exfoliated material (monolayers around 1 nm thick and lateral sizes around 2 μm). Nevertheless, the most important characterization here is the High-Resolution Transmission Electron Microscopy (HRTEM). With this technique it is possible to measure the crystallinity of the nanosheet by Selected Area Electron Diffraction (SAED) to demonstrate the same crystal structure to the nanosheets and the precursor bulk material (Figure 1.14). They used these nanosheets to make membranes to separate H_2/CO_2 due to the size of the pore aperture between these two molecules.

The interest in membranes using 2D nanosheets is huge and there are a lot of research not only looking for novel systems, but also trying to develop new synthetic routes to control the crystal growth in two-dimensions. Based on the same system such as Peng and co-workers, Zhang and co-workers develop a controlled synthesis of $[Zn_2(bim)_4]$ based in ZnO nanoparticles assisted by ammonia solutions.[123] With this technique they synthesized crystalline nanosheets of around 500 nm in lateral size and 20 nm thickness. The approximation to the 2D world seems worse than Peng's work, even if this bottom-up technique opens the door to explore different

applications such as a crystal growth on substrates to form thin films, which are difficult to achieve with a top-down technique.

Foster's group has experience in chemical design of layered CP and MOFs to fabricate nanosheets for catalysis applications.[124–126] Their work is normally based in paddle-wheel systems with 1,4 dicarboxylate ligands functionalized in the positions 2,5 to make easier the exfoliation process, change the wettability of the nanosheets. They study the exfoliation process to maximize the number of nanosheets changing exfoliation parameters such as temperature, sonication times, solvent, and centrifugation (like in inorganic compounds)[109,127].

The first example of chemical design to grow freestanding 2D MOF nanosheets (bottom-up approach) is the work developed by J. Gascon, X. Llabrés i Xamena and co-workers[128] on a carboxylate-based MOF, Cu(BDC), consisting of Cu paddle wheel metallic nodes bridged by benzenedicarboxylate (BDC). They used a three-phase synthesis that favors the growth of a layered structure in the interface. In the top solution, $Cu(NO_3)_2$, acetonitrile and dimethylformamide (DMF); in the middle, acetonitrile and DMF to prevent a quick mix of phases; and at bottom a solution of the ligand, BDC, acetonitrile and DMF (Figure 1.15a). Adjusting the reaction parameters it was possible to prepare nanosheets with 1 μm lateral size and 10 nm thickness. They used these nanosheets to make MOF-polymer composites for gas separation due to the unsaturated coordination environment of the metallic nodes.

The groups of X. Feng and R. Dong used the interfacial method (at the interface between to solvents) controlling the reaction times to

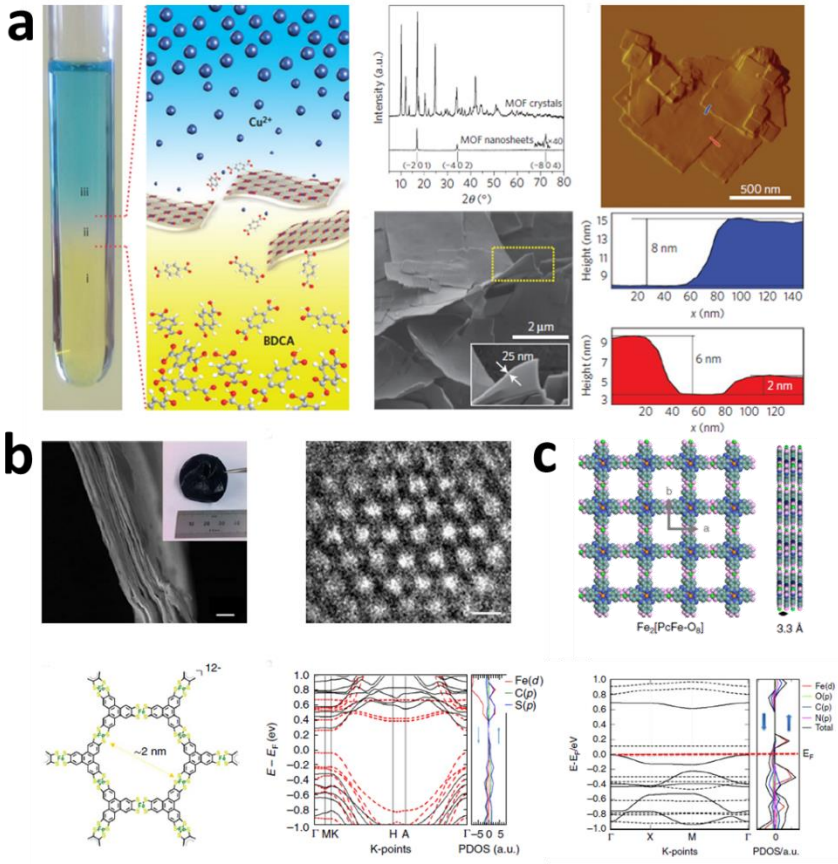

Figure 1.15 a) Synthetic procedure for the Cu-BDC thin MOF and their characterization. b) Fe(II,III) with hexathioltriphenylenes MOF. c) Fe(II,III) and porphyrins MOF. Adapted from references 128–130.

synthesize other 2D MOFs as free standing films (oriented microcrystals with around 100 nm lateral size). They used planar ligands such as triphenylenes and porphyrins to construct Fe(II)/Fe(III) MOFs with semiconducting and magnetic properties (Figure 1.15b).[129,130] The combination of Fe(II,III) with hexathioltriphenylenes gives a hexagonal lattice where Fe is in a square planar coordination environment. These work

permitted to study the electronic models in MOFs and the band structures to help to understand the conductive mechanisms in hybrid materials. The synthetic methodology helped also to integrate these materials into devices thanks to the formation of films of these compounds.

Is also possible to use three-dimensional networks to organize them in two-dimensional lattices. Ameloot and co-workers are developing vapour-phase depositions and chemical vapour depositions of mainly ZIFs[72,131] and some carboxylic MOFs,[132] achieving microcrystals organized as films on surfaces, with huge extensions (>10 μm) and thickness around 90 nm. The solvent-free methodology open the door to integrate these systems on chips and make them compatible for physical measurements.

The 2D world in molecular materials such as MOFs and CPs is dominated by the production of nanosheets by liquid approaches, by top-down methods (exfoliation). The similitude of some layered coordination polymers with graphene and related 2D materials makes 2D MOF an interesting field to explore due to the possibilities through chemical design and vast options in coordination chemistry, more limited in classical inorganic compounds. The key point is the develop robust and interesting molecular materials and cleaner methodologies to produce 2D MOF compatible with physical measurements.

1.4 References

(1) Lehn, J. M. Supramolecular Chemistry. *Science* **1993**, *260* (5115), 1762–1763.

(2) Buser, H. J.; Ludi, A.; Schwarzenbach, D.; Petter, W. The Crystal Structure of Prussian Blue: $Fe_4[Fe(CN)_6]3\cdot xH_2O$. *Inorg. Chem.* **1977**, *16* (11), 2704–2710.

(3) POWELL, H. M.; RAYNER, J. H. Clathrate Compound Formed by Benzene with an Ammonia–Nickel Cyanide Complex. *Nature* **1949**, *163* (4145), 566–567.

(4) Coronado, E. Molecular Magnetism: From Chemical Design to Spin Control in Molecules, Materials and Devices. *Nat. Rev. Mater.* **2019**.

(5) Hoskins, B. F.; Robson, R. Infinite Polymeric Frameworks Consisting of Three Dimensionally Linked Rod-like Segments. *J. Am. Chem. Soc.* **1989**, *111* (15), 5962–5964.

(6) Hoskins, B. F.; Robson, R. Design and Construction of a New Class of Scaffolding-like Materials Comprising Infinite Polymeric Frameworks of 3D-Linked Molecular Rods. A Reappraisal of the Zinc Cyanide and Cadmium Cyanide Structures and the Synthesis and Structure of the Diamond-Rela. *J. Am. Chem. Soc.* **1990**, *112* (4), 1546–1554.

(7) Kitagawa, S.; Kitaura, R.; Noro, S. Functional Porous Coordination Polymers. *Angew. Chemie - Int. Ed.* **2004**, *43* (18), 2334–2375.

(8) Férey, G. Hybrid Porous Solids: Past, Present, Future. *Chem. Soc. Rev.* **2008**, *37* (1), 191–214.

(9) Yaghi, O. M.; Li, H. Hydrothermal Synthesis of a Metal-Organic Framework Containing Large Rectangular Channels. *J. Am. Chem. Soc.* **1995**, *117* (41), 10401–10402.

(10) Yaghi, O. M.; Li, G.; Li, H. Selective Binding and Removal of Guests in a Microporous Metal–Organic Framework. *Nature* **1995**, *378* (6558), 703–706.

(11) Kondo, M.; Yoshitomi, T.; Matsuzaka, H.; Kitagawa, S.; Seki, K. Three-Dimensional Framework with Channeling Cavities for Small Molecules:{$[M_2(4, 4'\text{-}Bpy)_3(NO_3)_4]\cdot xH_2O$}n(M = Co, Ni, Zn). *Angew. Chemie Int. Ed. English* **1997**, *36* (16), 1725–1727.

(12) Li, H.; Eddaoudi, M.; Groy, T. L.; Yaghi, O. M. Establishing Microporosity in Open Metal−Organic Frameworks: Gas Sorption Isotherms for Zn(BDC) (BDC = 1,4-Benzenedicarboxylate). *J. Am. Chem. Soc.* **1998**, *120* (33), 8571–8572.

(13) Cavellec, M.; Grenèche, J. M.; Férey, G. Oxyfluorinated Open Framework Compounds. XVIII Dehydration of Single Crystals of the Iron Phosphate ULM-12 or $[Fe_4(PO_4)_4F_3(H_2O)_3,N_2C_6H_{14}]$ with an Open Structure, Structural Determination and Magnetic Study of the Dehydrated Phase(ULM-19). *Microporous Mesoporous Mater.* **1998**, *20* (1–3), 45–52.

(14) Livage, C.; Egger, C.; Nogues, M.; Férey, G. Hybrid Open Frameworks (MIL-n). Part 5 Synthesis and Crystal Structure of MIL-9: A New Three-Dimensional Ferrimagnetic Cobalt(II) Carboxylate with a Two-Dimensional Array of Edge-Sharing Co Octahedra with 12-Membered Rings. *J. Mater. Chem.* **1998**, *8* (12), 2743–2747.

(15) Serpaggi, F.; Férey, G. Hybrid Open Frameworks (MIL-n). Part 6 Hydrothermal Synthesis and X-Ray Powder Ab Initio Structure Determination of MIL-11, a Series of Lanthanide Organodiphosphonates with Three-Dimensional Networks, $Ln^{III}H[O_3P(CH_2)NPO_3]$ (N=1-3). *J. Mater. Chem.* **1998**, *8* (12), 2749–2755.

(16) Barthelet, K.; Marrot, J.; Riou, D.; Férey, G. A Breathing Hybrid Organic-Inorganic Solid with Very Large Pores and High Magnetic Characteristics. *Angew. Chemie - Int. Ed.* **2002**, *41* (2), 281–284.

(17) Li, H.; Eddaoudi, M.; O'Keeffe, M.; Yaghi, O. M. Design and Synthesis of an Exceptionally Stable and Highly Porous Metal-Organic Framework. *Nature* **1999**, *402* (6759), 276–279.

(18) Yaghi, O. M.; M, O. K.; Ockwig, N. W.; Chae, H. K.; Eddaoudi, M.; Kim, J. Reticular Synthesis and the Design of New Materials. *Nature* **2003**, *423* (6941), 705–714.

(19) Ockwig, N. W.; Delgado-Friedrichs, O.; O'Keeffe, M.; Yaghi, O. M. Reticular Chemistry: Occurrence and Taxonomy of Nets and Grammar for the Design of Frameworks. *Acc. Chem. Res.* **2005**, *38* (3), 176–182.

(20) Zhou, H. C.; Long, J. R.; Yaghi, O. M. Introduction to Metal-Organic Frameworks. *Chem. Rev.* **2012**, *112* (2), 673–674.

(21) Moghadam, P. Z.; Li, A.; Wiggin, S. B.; Tao, A.; Maloney, A. G. P.; Wood, P. A.; Ward, S. C.; Fairen-Jimenez, D. Development of a Cambridge Structural Database Subset: A Collection of Metal-Organic Frameworks for Past, Present, and Future. *Chem. Mater.* **2017**, *29* (7), 2618–2625.

(22) Li, A.; Bueno-Perez, R.; Wiggin, S.; Fairen-Jimenez, D. Enabling Efficient Exploration of Metal–Organic Frameworks in the Cambridge Structural Database. *CrystEngComm* **2020**.

(23) Moghadam, P. Z.; Li, A.; Liu, X.-W.; Bueno-Perez, R.; Wang, S.-D.; Wiggin, S. B.; Wood, P. A.; Fairen-Jimenez, D. Targeted Classification of Metal–Organic Frameworks in the Cambridge Structural Database (CSD). *Chem. Sci.* **2020**, *11* (32), 8373–8387.

(24) Chui, S. S. Y. A Chemically Functionalizable Nanoporous Material [Cu3(TMA)2(H2O)3]N. *Science* **1999**, *283* (5405), 1148–1150.

(25) Horike, S.; Shimomura, S.; Kitagawa, S. Soft Porous Crystals. *Nat. Chem.* **2009**, *1* (9), 695–704.

(26) Furukawa, H.; Cordova, K. E.; O'Keeffe, M.; Yaghi, O. M. The Chemistry and Applications of Metal-Organic Frameworks. *Science* **2013**, *341* (6149), 1230444–1230444.

(27) Ricco, R.; Pfeiffer, C.; Sumida, K.; Sumby, C. J.; Falcaro, P.; Furukawa, S.; Champness, N. R.; Doonan, C. J. Emerging Applications of Metal–Organic Frameworks. *CrystEngComm* **2016**, *18* (35), 6532–6542.

(28) Li, H.; Wang, K.; Sun, Y.; Lollar, C. T.; Li, J.; Zhou, H.-C. Recent Advances in Gas Storage and Separation Using Metal–Organic Frameworks. *Mater. Today* **2018**, *21* (2), 108–121.

(29) Sumida, K.; Rogow, D. L.; Mason, J. A.; McDonald, T. M.; Bloch, E. D.; Herm, Z. R.; Bae, T.-H.; Long, J. R. Carbon Dioxide Capture in Metal–Organic Frameworks. *Chem. Rev.* **2012**, *112* (2), 724–781.

(30) Vaidhyanathan, R.; Iremonger, S. S.; Dawson, K. W.; Shimizu, G. K. H. An Amine-Functionalized Metal Organic Framework for Preferential CO2 Adsorption at Low Pressures. *Chem. Commun.* **2009**, No. 35, 5230.

(31) Nugent, P.; Belmabkhout, Y.; Burd, S. D.; Cairns, A. J.; Luebke, R.; Forrest, K.; Pham, T.; Ma, S.; Space, B.; Wojtas, L.; Eddaoudi, M.; Zaworotko, M. J. Porous Materials with Optimal Adsorption Thermodynamics and Kinetics for CO2 Separation. *Nature* **2013**, *495* (7439), 80–84.

(32) Schneemann, A.; Bon, V.; Schwedler, I.; Senkovska, I.; Kaskel, S.; Fischer, R. A. Flexible Metal-Organic Frameworks. *Chem. Soc. Rev.* **2014**, *43* (16), 6062–6096.

(33) Millange, F.; Serre, C.; Férey, G. Synthesis, Structure Determination and Properties of MIL-53as and MIL-53ht: The First Criii Hybrid Inorganic–Organic Microporous Solids: $Cr^{iii}(OH)\cdot\{O_2C–C_6H_4–CO_2\}\cdot\{HO_2C–C_6H_4–CO_2H\}$xElectronic Supplementary Information (ESI) Available: Crystal Data, Atomic C. *Chem. Commun.* **2002**, *601* (8), 822–823.

(34) Mellot-Draznieks, C.; Serre, C.; Surblé, S.; Audebrand, N.; Férey, G. Very Large Swelling in Hybrid Frameworks: A Combined Computational and Powder Diffraction Study. *J. Am. Chem. Soc.* **2005**, *127* (46), 16273–16278.

(35) Krause, S.; Bon, V.; Senkovska, I.; Stoeck, U.; Wallacher, D.; Többens, D. M.; Zander, S.; Pillai, R. S.; Maurin, G.; Coudert, F. X.; Kaskel, S. A Pressure-Amplifying Framework Material with Negative Gas Adsorption Transitions. *Nature* **2016**, *532* (7599), 348–352.

(36) Krause, S.; Evans, J. D.; Bon, V.; Senkovska, I.; Iacomi, P.; Kolbe, F.; Ehrling, S.; Troschke, E.; Getzschmann, J.; Többens, D. M.; Franz, A.; Wallacher, D.; Yot, P. G.;

Maurin, G.; Brunner, E.; Llewellyn, P. L.; Coudert, F. X.; Kaskel, S. Towards General Network Architecture Design Criteria for Negative Gas Adsorption Transitions in Ultraporous Frameworks. *Nat. Commun.* **2019**, *10* (1).

(37) Ferey, G. A Chromium Terephthalate-Based Solid with Unusually Large Pore Volumes and Surface Area. *Science* **2005**, *309* (5743), 2040–2042.

(38) Giménez-Marqués, M.; Hidalgo, T.; Serre, C.; Horcajada, P. Nanostructured Metal-Organic Frameworks and Their Bio-Related Applications. *Coord. Chem. Rev.* **2016**, *307*, 342–360.

(39) Yuan, S.; Feng, L.; Wang, K.; Pang, J.; Bosch, M.; Lollar, C.; Sun, Y.; Qin, J.; Yang, X.; Zhang, P.; Wang, Q.; Zou, L.; Zhang, Y.; Zhang, L.; Fang, Y.; Li, J.; Zhou, H. C. Stable Metal–Organic Frameworks: Design, Synthesis, and Applications. *Adv. Mater.* **2018**, *30* (37), 1–35.

(40) Cavka, J. H.; Jakobsen, S.; Olsbye, U.; Guillou, N.; Lamberti, C.; Bordiga, S.; Lillerud, K. P. A New Zirconium Inorganic Building Brick Forming Metal Organic Frameworks with Exceptional Stability. *J. Am. Chem. Soc.* **2008**, *130* (42), 13850–13851.

(41) Park, K. S.; Ni, Z.; Côté, A. P.; Choi, J. Y.; Huang, R.; Uribe-Romo, F. J.; Chae, H. K.; O'Keeffe, M.; Yaghi, O. M. Exceptional Chemical and Thermal Stability of Zeolitic Imidazolate Frameworks. *Proc. Natl. Acad. Sci. U. S. A.* **2006**, *103* (27), 10186–10191.

(42) Thomas, A. Much Ado about Nothing – a Decade of Porous Materials Research. *Nat. Commun.* **2020**, *11* (1), 11–13.

(43) Fujita, M.; Washizu, S.; Ogura, K.; Kwon, Y. J. Preparation, Clathration Ability, and Catalysis of a Two-Dimensional Square Network Material Composed of Cadmium(II) and 4, 4′-Bipyridine. *J. Am. Chem. Soc.* **1994**, *116* (3), 1151–1152.

(44) Bavykina, A.; Kolobov, N.; Khan, I. S.; Bau, J. A.; Ramirez, A.; Gascon, J. Metal–Organic Frameworks in Heterogeneous Catalysis: Recent Progress, New Trends, and Future Perspectives. *Chem. Rev.* **2020**, *120* (16), 8468–8535.

(45) Xie, L. S.; Skorupskii, G.; Dincă, M. Electrically Conductive Metal–Organic Frameworks. *Chem. Rev.* **2020**, *120* (16), 8536–8580.

(46) Rubio-Giménez, V.; Tatay, S.; Martí-Gastaldo, C. Electrical Conductivity and Magnetic Bistability in Metal-Organic Frameworks and Coordination Polymers: Charge Transport and Spin Crossover at the Nanoscale. *Chem. Soc. Rev.* **2020**, *49* (15), 5601–5638.

(47) Peng, Y.; Yang, W. 2D Metal-Organic Framework Materials for Membrane-Based Separation. *Adv. Mater. Interfaces* **2020**, *7* (1), 1901514.

(48) Duan, J.; Li, Y.; Pan, Y.; Behera, N.; Jin, W. Metal-Organic Framework Nanosheets: An

Emerging Family of Multifunctional 2D Materials. *Coord. Chem. Rev.* **2019**, *395*, 25–45.

(49) Coudert, F. X.; Evans, J. D. Nanoscale Metamaterials: Meta-MOFs and Framework Materials with Anomalous Behavior. *Coord. Chem. Rev.* **2019**, *388*, 48–62.

(50) Rettig, S. J.; Storr, A.; Summers, D. A.; Thompson, R. C.; Trotter, J. Transition Metal Azolates from Metallocenes . 2 . Synthesis , X-Ray Structure , and Magnetic Properties of a Three-Dimensional Polymetallic Iron (II) Imidazolate Complex , a Low-Temperature Weak Ferromagnet. *Society* **1997**, *7863* (Ii), 8675–8680.

(51) Rettig, S. J.; Storr, A.; Summers, D. A.; Thompson, R. C.; Trotter, J. Iron(II) 2-Methylimidazolate and Copper(II) 1,2,4-Triazolate Complexes: Systems Exhibiting Long-Range Ferromagnetic Ordering at Low Temperatures. *Can. J. Chem.* **1999**, *77* (4), 425–433.

(52) Sánchez, V.; Storr, A.; Thompson, R. C. Magnetic and Structural Studies on 1,3-Diazolate Complexes of Cobalt(II) — The Characterization of Three New Cobalt(II) Molecule-Based Magnets. *Can. J. Chem.* **2002**, *80* (2), 133–140.

(53) Masciocchi, N.; Bruni, S.; Cariati, E.; Cariati, F.; Galli, S.; Sironi, A. Extended Polymorphism in Copper(II) Imidazolate Polymers: A Spectroscopic and XRPD Structural Study. *Inorg. Chem.* **2001**, *40* (23), 5897–5905.

(54) Tian, Y. Q.; Cai, C. X.; Ji, Y.; You, X. Z.; Peng, S. M.; Lee, G. H. [Co5(Im)10·2MB]∞: A Metal-Organic Open-Framework with Zeolite-like Topology. *Angew. Chemie - Int. Ed.* **2002**, *41* (8), 1384–1386.

(55) Huang, X.-C.; Lin, Y.-Y.; Zhang, J.-P.; Chen, X.-M. Ligand-Directed Strategy for Zeolite-Type Metal–Organic Frameworks: Zinc(II) Imidazolates with Unusual Zeolitic Topologies. *Angew. Chemie Int. Ed.* **2006**, *45* (10), 1557–1559.

(56) HUANG, X.; Zhang, J.; Chen, X. $[Zn(Bim)_2] \cdot (H_2O)1.67$: A Metal-Organic Open-Framework with Sodalite Topology. *Chinese Sci. Bull.* **2003**, *48* (15), 1531–1534.

(57) Banerjee, R.; Phan, A.; Wang, B.; Knobler, C.; Furukawa, H.; O'Keeffe, M.; Yaghi, O. M. High-Throughput Synthesis of Zeolitic Imidazolate Frameworks and Application to CO2 Capture. *Science* **2008**, *319* (5865), 939–943.

(58) Horike, S.; Kadota, K.; Itakura, T.; Inukai, M.; Kitagawa, S. Synthesis of Magnesium ZIF-8 from $Mg(BH_4)_2$. *Dalt. Trans.* **2015**, *44* (34), 15107–15110.

(59) Kadota, K.; Sivaniah, E.; Bureekaew, S.; Kitagawa, S.; Horike, S. Synthesis of Manganese ZIF-8 from $[Mn(BH_4)_2 \cdot 3THF] \cdot NaBH_4$. *Inorg. Chem.* **2017**, *52334* (4), 8744–8747.

(60) Tian, Y.-Q.; Yao, S.-Y.; Gu, D.; Cui, K.-H.; Guo, D.-W.; Zhang, G.; Chen, Z.-X.; Zhao,

D.-Y. Cadmium Imidazolate Frameworks with Polymorphism, High Thermal Stability, and a Large Surface Area. *Chem. - A Eur. J.* **2010**, *16* (4), 1137–1141.

(61) Katsenis, A. D.; Puškarić, A.; Štrukil, V.; Mottillo, C.; Julien, P. A.; Užarević, K.; Pham, M. H.; Do, T. O.; Kimber, S. A. J.; Lazić, P.; Magdysyuk, O.; Dinnebier, R. E.; Halasz, I.; Friščić, T. In Situ X-Ray Diffraction Monitoring of a Mechanochemical Reaction Reveals a Unique Topology Metal-Organic Framework. *Nat. Commun.* **2015**, *6*.

(62) Peng, Y.; Li, Y.; Ban, Y.; Jin, H.; Jiao, W.; Liu, X.; Yang, W. Metal-Organic Framework Nanosheets as Building Blocks for Molecular Sieving Membranes. *Science* **2014**, *346* (6215), 1356–1359.

(63) Yaghi, O. M.; Furukawa, H.; Morris, W.; Doonan, C. J.; Banerjee, R. Crystals as Molecules: Postsynthesis Covalent Functionalization of Zeolitic Imidazolate Frameworks. *J. Am. Chem. Soc.* **2008**, *130* (38), 12626–12627.

(64) Karagiaridi, O.; Lalonde, M. B.; Bury, W.; Sarjeant, A. a.; Farha, O. K.; Hupp, J. T. Opening ZIF-8: A Catalytically Active Zeolitic Imidazolate Framework of Sodalite Topology with Unsubstituted Linkers. *J. Am. Chem. Soc.* **2012**, *134* (45), 18790–18796.

(65) Avci, C.; Ariñez-Soriano, J.; Carné-Sánchez, A.; Guillerm, V.; Carbonell, C.; Imaz, I.; Maspoch, D. Post-Synthetic Anisotropic Wet-Chemical Etching of Colloidal Sodalite ZIF Crystals. *Angew. Chemie - Int. Ed.* **2015**, *54* (48), 14417–14421.

(66) Venna, S. R.; Carreon, M. A. Highly Permeable Zeolite Imidazolate Framework-8 Membranes for CO 2/CH4 Separation. *J. Am. Chem. Soc.* **2010**, *132* (1), 76–78.

(67) Andres-Garcia, E.; López-Cabrelles, J.; Oar-Arteta, L.; Roldan-Martinez, B.; Cano-Padilla, M.; Gascon, J.; Mínguez Espallargas, G.; Kapteijn, F. Cation Influence in Adsorptive Propane/Propylene Separation in ZIF-8 (SOD) Topology. *Chem. Eng. J.* **2019**, *371* (March), 848–856.

(68) Krokidas, P.; Castier, M.; Moncho, S.; Brothers, E.; Economou, I. G. Molecular Simulation Studies of the Diffusion of Methane, Ethane, Propane, and Propylene in ZIF-8. *J. Phys. Chem. C* **2015**, *119* (48), 27028–27037.

(69) Yao, J.; Wang, H. Zeolitic Imidazolate Framework Composite Membranes and Thin Films: Synthesis and Applications. *Chem. Soc. Rev.* **2014**, *43* (13), 4470–4493.

(70) Zhu, H.; Liu, D. The Synthetic Strategies of Metal–Organic Framework Membranes, Films and 2D MOFs and Their Applications in Devices. *J. Mater. Chem. A* **2019**, *7* (37), 21004–21035.

(71) Hao, J.; Babu, D. J.; Liu, Q.; Chi, H. Y.; Lu, C.; Liu, Y.; Agrawal, K. V. Synthesis of High-Performance Polycrystalline Metal-Organic Framework Membranes at Room

Temperature in a Few Minutes. *J. Mater. Chem. A* **2020**, *8* (16), 7633–7640.

(72) Stassen, I.; Styles, M.; Grenci, G.; Van Gorp, H.; Vanderlinden, W.; De Feyter, S.; Falcaro, P.; De Vos, D.; Vereecken, P.; Ameloot, R. Chemical Vapour Deposition of Zeolitic Imidazolate Framework Thin Films. *Nat. Mater.* **2016**, *15* (3), 304–310.

(73) He, L.; Pang, K.; Liu, W.; Tian, Y.; Chang, L.; Liu, X.; Zhao, M.; Liu, Y.; Li, Y.; Jiang, X.; Song, R.; Liu, Y. Core-Shell Noble-Metal@zeolitic-Imidazolate-Framework Nanocarriers with High Cancer Treatment Efficiency in Vitro. *J. Mater. Chem. B* **2019**, *7* (7), 1050–1055.

(74) Astria, E.; Thonhofer, M.; Ricco, R.; Liang, W.; Chemelli, A.; Tarzia, A.; Alt, K.; Hagemeyer, C. E.; Rattenberger, J.; Schroettner, H.; Wrodnigg, T.; Amenitsch, H.; Huang, D. M.; Doonan, C. J.; Falcaro, P. Carbohydrates@MOFs. *Mater. Horizons* **2019**, *6* (5), 969–977.

(75) Wang, X.; Chen, X. Z.; Alcântara, C. C. J.; Sevim, S.; Hoop, M.; Terzopoulou, A.; de Marco, C.; Hu, C.; de Mello, A. J.; Falcaro, P.; Furukawa, S.; Nelson, B. J.; Puigmartí-Luis, J.; Pané, S. MOFBOTS: Metal–Organic-Framework-Based Biomedical Microrobots. *Adv. Mater.* **2019**, *31* (27), 2–8.

(76) Terzopoulou, A.; Hoop, M.; Chen, X. Z.; Hirt, A. M.; Charilaou, M.; Shen, Y.; Mushtaq, F.; del Pino, A. P.; Logofatu, C.; Simonelli, L.; de Mello, A. J.; Doonan, C. J.; Sort, J.; Nelson, B. J.; Pané, S.; Puigmartí-Luis, J. Mineralization-Inspired Synthesis of Magnetic Zeolitic Imidazole Framework Composites. *Angew. Chemie - Int. Ed.* **2019**, *58* (38), 13550–13555.

(77) Murillo, B.; Zornoza, B.; De La Iglesia, O.; Téllez, C.; Coronas, J. Chemocatalysis of Sugars to Produce Lactic Acid Derivatives on Zeolitic Imidazolate Frameworks. *J. Catal.* **2016**, *334*, 60–67.

(78) Luo, Z.; Chaemchuen, S.; Zhou, K.; Verpoort, F. Ring-Opening Polymerization of l-Lactide to Cyclic Poly(Lactide) by Zeolitic Imidazole Framework ZIF-8 Catalyst. *ChemSusChem* **2017**, *10* (21), 4135–4139.

(79) Zhao, J.; Quan, X.; Chen, S.; Liu, Y.; Yu, H. Cobalt Nanoparticles Encapsulated in Porous Carbons Derived from Core-Shell ZIF67@ZIF8 as Efficient Electrocatalysts for Oxygen Evolution Reaction. *ACS Appl. Mater. Interfaces* **2017**, *9* (34), 28685–28694.

(80) He, F.; Chen, G.; Zhou, Y.; Yu, Y.; Li, L.; Hao, S.; Liu, B. ZIF-8 Derived Carbon (C-ZIF) as a Bifunctional Electron Acceptor and HER Cocatalyst for g-C3N4: Construction of a Metal-Free, All Carbon-Based Photocatalytic System for Efficient Hydrogen Evolution. *J. Mater. Chem. A* **2016**, *4* (10), 3822–3827.

(81) Mukhopadhyay, S.; Debgupta, J.; Singh, C.; Kar, A.; Das, S. K. A Keggin Polyoxometalate Shows Water Oxidation Activity at Neutral PH: POM@ZIF-8, an Efficient and Robust Electrocatalyst. *Angew. Chemie - Int. Ed.* **2018**, *57* (7), 1918–1923.

(82) Han, H.; Karlicky, F.; Pitchaimuthu, S.; Shin, S. H. R.; Chen, A. Highly Ordered N-Doped Carbon Dots Photosensitizer on Metal–Organic Framework-Decorated ZnO Nanotubes for Improved Photoelectrochemical Water Splitting. *Small* **2019**, *15* (40), 1–7.

(83) Xia, B. Y.; Yan, Y.; Li, N.; Wu, H. Bin; Lou, X. W.; Wang, X. A Metal–Organic Framework-Derived Bifunctional Oxygen Electrocatalyst. *Nat. Energy* **2016**, *1* (1), 15006.

(84) Gadipelli, S.; Zhao, T.; Shevlin, S. A.; Guo, Z. Switching Effective Oxygen Reduction and Evolution Performance by Controlled Graphitization of a Cobalt–Nitrogen–Carbon Framework System. *Energy Environ. Sci.* **2016**, *9* (5), 1661–1667.

(85) Moggach, S. A.; Bennett, T. D.; Cheetham, A. K. The Effect of Pressure on ZIF-8: Increasing Pore Size with Pressure and the Formation of a High-Pressure Phase at 1.47 GPa. *Angew. Chemie - Int. Ed.* **2009**, *48* (38), 7087–7089.

(86) Fairen-Jimenez, D.; Moggach, S. A.; Wharmby, M. T.; Wright, P. A.; Parsons, S.; Düren, T. Opening the Gate: Framework Flexibility in ZIF-8 Explored by Experiments and Simulations. *J. Am. Chem. Soc.* **2011**, *133* (23), 8900–8902.

(87) Fairen-Jimenez, D.; Galvelis, R.; Torrisi, A.; Gellan, A. D.; Wharmby, M. T.; Wright, P. A.; Mellot-Draznieks, C.; Düren, T. Flexibility and Swing Effect on the Adsorption of Energy-Related Gases on ZIF-8: Combined Experimental and Simulation Study. *Dalt. Trans.* **2012**, *41* (35), 10752.

(88) Casco, M. E.; Cheng, Y. Q.; Daemen, L. L.; Fairen-Jimenez, D.; Ramos-Fernández, E. V.; Ramirez-Cuesta, A. J.; Silvestre-Albero, J. Gate-Opening Effect in ZIF-8: The First Experimental Proof Using Inelastic Neutron Scattering. *Chem. Commun.* **2016**, *52* (18), 3639–3642.

(89) Yang, Q.-F.; Cui, X.-B.; Yu, J.-H.; Lu, J.; Yu, X.-Y.; Zhang, X.; Xu, J.-Q.; Hou, Q.; Wang, T.-G. A Series of Metal–Organic Complexes Constructed from in Situ Generated Organic Amines. *CrystEngComm* **2008**, *10* (11), 1534.

(90) Wilson, J. A.; Yoffe, A. D. The Transition Metal Dichalcogenides Discussion and Interpretation of the Observed Optical, Electrical and Structural Properties. *Adv. Phys.* **1969**, *18* (73), 193–335.

(91) Novoselov, K. S. Electric Field Effect in Atomically Thin Carbon Films. *Science* **2004**, *306* (5696), 666–669.

(92) Geim, A. K.; Novoselov, K. S. The Rise of Graphene. *Nat. Mater.* **2007**, *6* (3), 183–191.

(93) Uri, A.; Grover, S.; Cao, Y.; Crosse, J. A.; Bagani, K.; Rodan-Legrain, D.; Myasoedov, Y.; Watanabe, K.; Taniguchi, T.; Moon, P.; Koshino, M.; Jarillo-Herrero, P.; Zeldov, E. Mapping the Twist-Angle Disorder and Landau Levels in Magic-Angle Graphene. *Nature* **2020**, *581* (7806), 47–52.

(94) Cao, Y.; Fatemi, V.; Fang, S.; Watanabe, K.; Taniguchi, T.; Kaxiras, E.; Jarillo-Herrero, P. Unconventional Superconductivity in Magic-Angle Graphene Superlattices. *Nature* **2018**, *556* (7699), 43–50.

(95) Cao, Y.; Rodan-Legrain, D.; Rubies-Bigorda, O.; Park, J. M.; Watanabe, K.; Taniguchi, T.; Jarillo-Herrero, P. Tunable Correlated States and Spin-Polarized Phases in Twisted Bilayer–Bilayer Graphene. *Nature* **2020**, *583* (7815), 215–220.

(96) Ferrari, A. C.; Bonaccorso, F.; Fal'ko, V.; Novoselov, K. S.; Roche, S.; Bøggild, P.; Borini, S.; Koppens, F. H. L.; Palermo, V.; Pugno, N.; Garrido, J. A.; Sordan, R.; Bianco, A.; Ballerini, L.; Prato, M.; Lidorikis, E.; Kivioja, J.; Marinelli, C.; Ryhänen, T.; Morpurgo, A.; Coleman, J. N.; Nicolosi, V.; Colombo, L.; Fert, A.; Garcia-Hernandez, M.; Bachtold, A.; Schneider, G. F.; Guinea, F.; Dekker, C.; Barbone, M.; Sun, Z.; Galiotis, C.; Grigorenko, A. N.; Konstantatos, G.; Kis, A.; Katsnelson, M.; Vandersypen, L.; Loiseau, A.; Morandi, V.; Neumaier, D.; Treossi, E.; Pellegrini, V.; Polini, M.; Tredicucci, A.; Williams, G. M.; Hee Hong, B.; Ahn, J.-H.; Min Kim, J.; Zirath, H.; van Wees, B. J.; van der Zant, H.; Occhipinti, L.; Di Matteo, A.; Kinloch, I. A.; Seyller, T.; Quesnel, E.; Feng, X.; Teo, K.; Rupesinghe, N.; Hakonen, P.; Neil, S. R. T.; Tannock, Q.; Löfwander, T.; Kinaret, J. Science and Technology Roadmap for Graphene, Related Two-Dimensional Crystals, and Hybrid Systems. *Nanoscale* **2015**, *7* (11), 4598–4810.

(97) Dean, C. R.; Young, a F.; Meric, I.; Lee, C.; Wang, L.; Sorgenfrei, S.; Watanabe, K.; Taniguchi, T.; Kim, P.; Shepard, K. L.; Hone, J. Boron Nitride Substrates for High-Quality Graphene Electronics. *Nat. Nanotechnol.* **2010**, *5* (10), 722–726.

(98) Mak, K. F.; Lee, C.; Hone, J.; Shan, J.; Heinz, T. F. Atomically Thin MoS2: A New Direct-Gap Semiconductor. *Phys. Rev. Lett.* **2010**, *105* (13), 136805.

(99) Li, L.; Yu, Y.; Ye, G. J.; Ge, Q.; Ou, X.; Wu, H.; Feng, D.; Chen, X. H.; Zhang, Y. Black Phosphorus Field-Effect Transistors. *Nat. Nanotechnol.* **2014**, *9* (5), 372–377.

(100) Acerce, M.; Voiry, D.; Chhowalla, M. Metallic 1T Phase MoS2 Nanosheets as Supercapacitor Electrode Materials. *Nat. Nanotechnol.* **2015**, *10* (4), 313–318.

(101) Xu, C.; Wang, L.; Liu, Z.; Chen, L.; Guo, J.; Kang, N.; Ma, X. L.; Cheng, H. M.; Ren, W. Large-Area High-Quality 2D Ultrathin Mo2C Superconducting Crystals. *Nat. Mater.*

2015, *14* (11), 1135–1141.

(102) El-Bana, M. S.; Wolverson, D.; Russo, S.; Balakrishnan, G.; Paul, D. M.; Bending, S. J. Superconductivity in Two-Dimensional $NbSe_2$ Field Effect Transistors. *Supercond. Sci. Technol.* **2013**, *26*, 125020.

(103) Navarro-Moratalla, E.; Island, J. O.; Mañas-Valero, S.; Pinilla-Cienfuegos, E.; Castellanos-Gomez, A.; Quereda, J.; Rubio-Bollinger, G.; Chirolli, L.; Silva-Guillén, J. A.; Agraït, N.; Steele, G. A.; Guinea, F.; van der Zant, H. S. J.; Coronado, E. Enhanced Superconductivity in Atomically Thin TaS2. *Nat. Commun.* **2016**, *7*, 11043.

(104) Hardy, W. J.; Yuan, J.; Guo, H.; Zhou, P.; Lou, J.; Natelson, D. Thickness-Dependent and Magnetic-Field-Driven Suppression of Antiferromagnetic Order in Thin V_5S_8 Single Crystals. *ACS Nano* **2016**, *10* (6), 5941–5946.

(105) Lee, J.-U.; Lee, S.; Ryoo, J. H.; Kang, S.; Kim, T. Y.; Kim, P.; Park, C.-H.; Park, J.; Cheong, H. Ising-Type Magnetic Ordering in Atomically Thin FePS 3. *Nano Lett.* **2016**, *16* (12), 7433–7438.

(106) Gong, C.; Li, L.; Li, Z.; Ji, H.; Stern, A.; Xia, Y.; Cao, T.; Bao, W.; Wang, C.; Wang, Y.; Qiu, Z. Q.; Cava, R. J.; Louie, S. G.; Xia, J.; Zhang, X. Discovery of Intrinsic Ferromagnetism in Two-Dimensional van Der Waals Crystals. *Nature* **2017**, *546* (7657), 265–269.

(107) Huang, B.; Clark, G.; Navarro-Moratalla, E.; Klein, D. R.; Cheng, R.; Seyler, K. L.; Zhong, Di.; Schmidgall, E.; McGuire, M. A.; Cobden, D. H.; Yao, W.; Xiao, D.; Jarillo-Herrero, P.; Xu, X. Layer-Dependent Ferromagnetism in a van Der Waals Crystal down to the Monolayer Limit. *Nature* **2017**, *546* (7657), 270–273.

(108) Bottari, G.; Ángeles Herranz, M.; Wibmer, L.; Volland, M.; Rodríguez-Pérez, L.; Guldi, D. M.; Hirsch, A.; Martín, N.; D'Souza, F.; Torres, T. Chemical Functionalization and Characterization of Graphene-Based Materials. *Chem. Soc. Rev.* **2017**, *46* (15), 4464–4500.

(109) Nicolosi, V.; Chhowalla, M.; Kanatzidis, M. G.; Strano, M. S.; Coleman, J. N. Liquid Exfoliation of Layered Materials. *Science* **2013**, *340* (6139), 1226419.

(110) Gao, E.; Lin, S. Z.; Qin, Z.; Buehler, M. J.; Feng, X. Q.; Xu, Z. Mechanical Exfoliation of Two-Dimensional Materials. *J. Mech. Phys. Solids* **2018**, *115*, 248–262.

(111) Tamaki, H.; Zhong, Z. J.; Matsumoto, N.; Kida, S.; Koikawa, M.; Achiwa, N.; Hashimoto, Y.; Okawa, H. Design of Metal-Complex Magnets. Syntheses and Magnetic Properties of Mixed-Metal Assemblies $\{NBu_4[MCr(Ox)_3]\}_x$ (NBu^{4+} = Tetra(n-Butyl)Ammonium Ion; Ox_2- = Oxalate Ion; M = Mn^{2+}, Fe^{2+}, Co^{2+}, Ni^{2+}, Cu^{2+}, Zn^{2+}). *J.*

Am. Chem. Soc. **1992**, *114* (18), 6974–6979.

(112) Clemente-León, M.; Coronado, E.; Martí-Gastaldo, C.; Romero, F. M. Multifunctionality in Hybrid Magnetic Materials Based on Bimetallic Oxalate Complexes. *Chem. Soc. Rev.* **2011**, *40* (2), 473.

(113) Kitagawa, S.; Kawata, S. Coordination Compounds of 1,4-Dihydroxybenzoquinone and Its Homologues. Structures and Properties. *Coord. Chem. Rev.* **2002**, *224* (1–2), 11–34.

(114) Atzori, M.; Benmansour, S.; Mínguez Espallargas, G.; Clemente-León, M.; Abhervé, A.; Gómez-Claramunt, P.; Coronado, E.; Artizzu, F.; Sessini, E.; Deplano, P.; Serpe, A.; Mercuri, M. L.; Gómez García, C. J. A Family of Layered Chiral Porous Magnets Exhibiting Tunable Ordering Temperatures. *Inorg. Chem.* **2013**, *52* (17), 10031–10040.

(115) Coronado, E.; Galán-Mascarós, J. R. Hybrid Molecular Conductors. *J. Mater. Chem.* **2005**, *15* (1), 66–74.

(116) Abhervé, A.; Mañas-Valero, S.; Clemente-León, M.; Coronado, E. Graphene Related Magnetic Materials: Micromechanical Exfoliation of 2D Layered Magnets Based on Bimetallic Anilate Complexes with Inserted $[Fe^{III}(Acac_2\text{-Trien})]^+$ and $[Fe^{III}(Sa_2\text{-Trien})]^+$. *Chem. Sci.* **2015**, *2*, 4665–4673.

(117) Benmansour, S.; Abhervé, A.; Gómez-Claramunt, P.; Vallés-García, C.; Gómez-García, C. J. Nanosheets of Two-Dimensional Magnetic and Conducting Fe(II)/Fe(III) Mixed-Valence Metal-Organic Frameworks. *ACS Appl. Mater. Interfaces* **2017**, *9* (31), 26210–26218.

(118) Pedersen, K. S.; Perlepe, P.; Aubrey, M. L.; Woodruff, D. N.; Reyes-Lillo, S. E.; Reinholdt, A.; Voigt, L.; Li, Z.; Borup, K.; Rouzières, M.; Samohvalov, D.; Wilhelm, F.; Rogalev, A.; Neaton, J. B.; Long, J. R.; Clérac, R. Formation of the Layered Conductive Magnet $CrCl_2(Pyrazine)_2$ through Redox-Active Coordination Chemistry. *Nat. Chem.* **2018**, *10* (10), 1056–1061.

(119) Rodríguez-San-Miguel, D.; Amo-Ochoa, P.; Zamora, F. MasterChem: Cooking 2D-Polymers. *Chem. Commun.* **2016**, *52* (22), 4113–4127.

(120) Peng, Y.; Yang, W. 2D Metal-Organic Framework Materials for Membrane-Based Separation. *Adv. Mater. Interfaces* **2020**, *7* (1), 1901514.

(121) Shen, Y.; Shan, B.; Cai, H.; Qin, Y.; Agarwal, A.; Trivedi, D. B.; Chen, B.; Liu, L.; Zhuang, H.; Mu, B.; Tongay, S. Ultimate Control over Hydrogen Bond Formation and Reaction Rates for Scalable Synthesis of Highly Crystalline VdW MOF Nanosheets with Large Aspect Ratio. *Adv. Mater.* **2018**, *30* (52), 1–8.

(122) Amo-Ochoa, P.; Welte, L.; González-Prieto, R.; Sanz Miguel, P. J.; Gómez-García, C. J.;

Mateo-Martí, E.; Delgado, S.; Gómez-Herrero, J.; Zamora, F. Single Layers of a Multifunctional Laminar Cu(I,II) Coordination Polymer. *Chem. Commun. (Camb).* **2010**, *46* (19), 3262–3264.

(123) Li, Y.; Lin, L.; Tu, M.; Nian, P.; Howarth, A. J.; Farha, O. K.; Qiu, J.; Zhang, X. Growth of ZnO Self-Converted 2D Nanosheet Zeolitic Imidazolate Framework Membranes by an Ammonia-Assisted Strategy. *Nano Res.* **2018**, *11* (4), 1850–1860.

(124) Foster, J. A.; Henke, S.; Schneemann, A.; Fischer, R. A.; Cheetham, A. K. Liquid Exfoliation of Alkyl-Ether Functionalised Layered Metal-Organic Frameworks to Nanosheets. *Chem. Commun.* **2016**, *52* (69), 10474–10477.

(125) Ashworth, D. J.; Cooper, A.; Trueman, M.; Al-Saedi, R. W. M.; Smith, L. D.; Meijer, A. J. H. M.; Foster, J. A. Ultrasonic Exfoliation of Hydrophobic and Hydrophilic Metal–Organic Frameworks To Form Nanosheets. *Chem. - A Eur. J.* **2018**, *24* (68), 17986–17996.

(126) Nicks, J.; Zhang, J.; Foster, J. A. Tandem Catalysis by Ultrathin Metal-Organic Nanosheets Formed through Post-Synthetic Functionalisation of a Layered Framework. *Chem. Commun.* **2019**, *55* (60), 8788–8791.

(127) Backes, C.; Szydłowska, B. M.; Harvey, A.; Yuan, S.; Vega-Mayoral, V.; Davies, B. R.; Zhao, P.; Hanlon, D.; Santos, E. J. G.; Katsnelson, M. I.; Blau, W. J.; Gadermaier, C.; Coleman, J. N. Production of Highly Monolayer Enriched Dispersions of Liquid-Exfoliated Nanosheets by Liquid Cascade Centrifugation. *ACS Nano* **2016**, *10* (1), 1589–1601.

(128) Rodenas, T.; Luz, I.; Prieto, G.; Seoane, B.; Miro, H.; Corma, A.; Kapteijn, F.; Llabrés i Xamena, F. X.; Gascon, J. Metal–Organic Framework Nanosheets in Polymer Composite Materials for Gas Separation. *Nat. Mater.* **2015**, *14* (1), 48–55.

(129) Dong, R.; Han, P.; Arora, H.; Ballabio, M.; Karakus, M.; Zhang, Z.; Shekhar, C.; Adler, P.; Petkov, P. S.; Erbe, A.; Mannsfeld, S. C. B.; Felser, C.; Heine, T.; Bonn, M.; Feng, X.; Cánovas, E. High-Mobility Band-like Charge Transport in a Semiconducting Two-Dimensional Metal–Organic Framework. *Nat. Mater.* **2018**, *17* (11), 1027–1032.

(130) Yang, C.; Dong, R.; Wang, M. M.; Petkov, P. St.; Zhang, Z.; Wang, M. M.; Han, P.; Ballabio, M.; Bräuninger, S. A.; Liao, Z.; Zhang, J.; Schwotzer, F.; Zschech, E.; Klauss, H.-H. H.; Cánovas, E.; Kaskel, S.; Bonn, M.; Zhou, S.; Heine, T.; Feng, X. A Semiconducting Layered Metal-Organic Framework Magnet. *Nat. Commun.* **2019**, *10* (1), 1–9.

(131) Stassin, T.; Stassen, I.; Marreiros, J.; Cruz, A. J.; Verbeke, R.; Tu, M.; Reinsch, H.;

Dickmann, M.; Egger, W.; Vankelecom, I. F. J.; De Vos, D. E.; Ameloot, R. Solvent-Free Powder Synthesis and MOF-CVD Thin Films of the Large-Pore Metal-Organic Framework MAF-6. *Chem. Mater.* **2020**, *32* (5), 1784–1793.

(132) Stassin, T.; Rodríguez-Hermida, S.; Schrode, B.; Cruz, A. J.; Carraro, F.; Kravchenko, D.; Creemers, V.; Stassen, I.; Hauffman, T.; De Vos, D.; Falcaro, P.; Resel, R.; Ameloot, R. Vapour-Phase Deposition of Oriented Copper Dicarboxylate Metal-Organic Framework Thin Films. *Chem. Commun.* **2019**, *55* (68), 10056–10059.

Chapter 2

The elusive Fe (II) ZIF-8 analogue

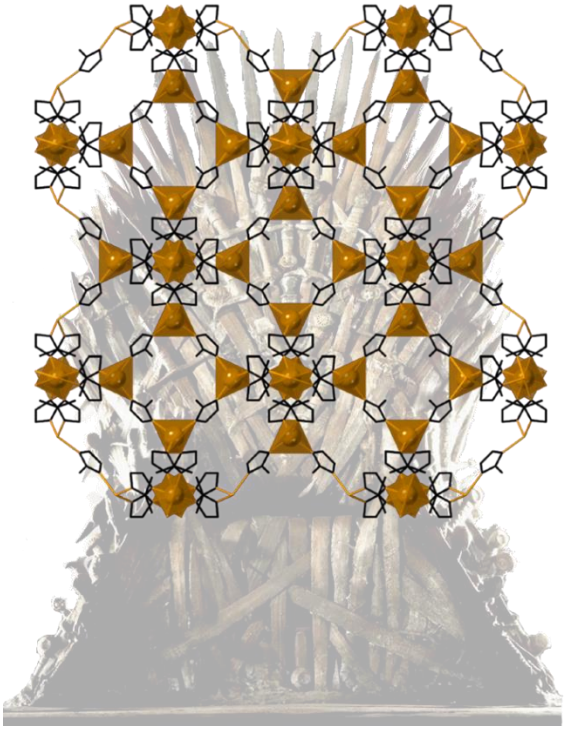

2.1 Introduction

An interesting feature of MOFs is the possibility of modifying the metal content whilst retaining the same structure, thus offering a unique opportunity to tune their physical properties. This is exemplified by the extensive family M-MOF-74, with formula M_2(dobdc) ($dobdc^{4-}$ = 2,5-dioxidobenzene-1,4-dicarboxylate), which can be prepared for an ample range of metals, such as Mg, Mn, Fe, Co, Ni, Cu, and Zn, or combination of these,[1] showing different properties. Indeed, whereas Mg-MOF-74 is optimum for CO_2 capture,[2] Fe-MOF-74 is suitable for alkane/alkene separation.[3,4] In the subclass of MOF known as zeolitic imidazolate frameworks, or ZIFs, which are composed by imidazolate derivatives and divalent metals, it is also possible to obtain the same topology with different metal cations. For example, the most renown ZIF, denoted ZIF-8, with SOD topology,[5,6] is formed by 2-methylimidazole (2meimH) and Zn(II), but can also be obtained with other divalent metals such as Co(II),[7] Cd(II),[8] Mg(II),[9] or Mn(II),[10] resulting in five isostructural porous materials (Figure 2.1). In these cases, it has also been shown that metal cation can influence physical properties such as gas sorption,[11] due to the different flexibility of the frameworks. However, the iron analogue, i.e. Fe(2meim)$_2$, formed exclusively by Fe(II) centers, has been elusive, despite the vast number of potential applications of this solid. Indeed, the incorporation of Fe(II) in a structure like ZIF-8 is interesting not only due to the applications in catalysis, or in environmental and biomedical fields due to the low toxicity of this cation,[12] but also from a fundamental point of view as it can serve to understand the gas sorption and gate opening phenomena in this type of materials. Considering energy-related applications, pyrolysis of MOFs has

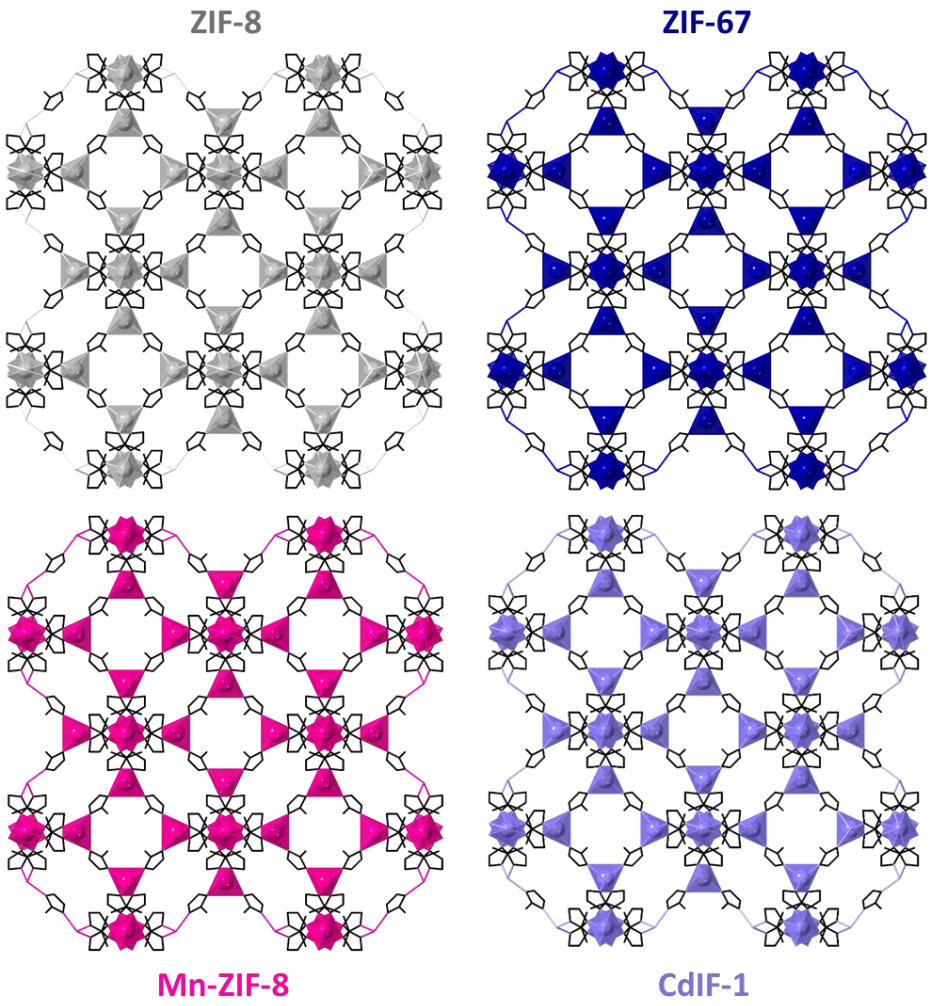

Figure 2.1 Crystal structure of the different isostructural $M^{2+}(2meim)_2$ SOD topology. The related magnesium compound CIF is not available.

been shown to be an effective pathway for the formation of carbon derived materials with unique properties, with a strong influence of porosity and metal nature of the MOF in the quality of these carbon derived materials.[13,14] ZIF-8 has been extensively studied for these applications,

with exceptional electrochemical catalytic activity due to its high N-content and high porosity. Fe-based ZIFs, in which Fe(II) is present as the metal nodes, will allow to preserve the porosity while incorporating this interesting metal in the structure. Together with a high nitrogen content, it can be a great candidate as a precursor for energy related applications.[15,16]

However, only a few examples of iron azolates are known. These are dense coordination polymers.[17,18] The scarcity of Fe(II) as metallic nodes in MOFs is due to its facility to oxidize to Fe(III) during the synthetic conditions.[19] The usual synthetic procedures for synthesizing MOFs (and ZIFs) require high temperatures or solvents like dimethylformamide (DMF),[6] alcohols (methanol, ethanol)[20] or water,[21] which favor the oxidation of Fe^{2+} to Fe^{3+}. Thus, an alternative synthetic route is required for synthesizing Fe(II) MOFs. This Chapter presents a general approach for the preparation of Fe(II)-based ZIFs in the absence of solvents, with the successful formation of the Fe(II)-analogue of ZIF-8, published in Journal of the American Chemical Society.[22]

2.2 Results and discussion

Synthesis of MUV-3. Solvent-free synthesis is an option to obtain Fe(II)-based MOF as demonstrated by Storr and Thompson with Fe(II)-based coordination polymers 25 years ago. More recently, Ameloot and co-workers have developed a special case of chemical vapor deposition to synthesize ZIF-8 based in the use of ZnO as precursor. 2meimH is evaporated and reacts with the previously deposited ZnO.[23] Mechanochemical synthesis of ZIFs has also been explored; for example, Friščić and co-workers developed a synthetic route assisted by solvent and

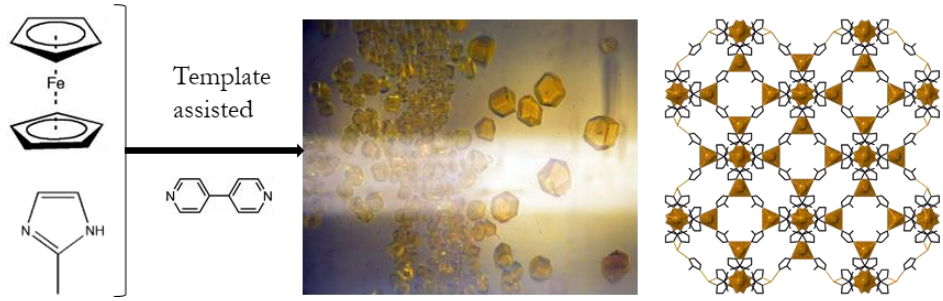

Figure 2.2. Synthetic route to form **MUV-3** single-crystals.

salts to obtain different phases of particular ZIFs such as the three different possible phases obtained by the combination of Zn and 2-ethylimidazole.[24] The problem of these solvent-free techniques is the absence of single crystals of the desired MOF. Furthermore, there is a strong limitation by the metal sources, since not all oxides or derived salts of all metals work under solvent-free conditions. In the example of Fe(II), the use of oxides is very limited as the common oxidation state is Fe(III).

The common routes are not compatible with the synthesis of Fe-ZIF-8. For that, we developed a compatible synthetic route with Fe(II), adapting a previously described method for the preparation of non-porous iron azolates.[17,18] For the first time, this solvent-free synthesis is compatible with Fe(II) to obtain a porous crystalline material denoted **MUV-3** (MUV: Materials of the University of Valencia). The reaction of ferrocene and 2meimH at 150 °C under vacuum in a sealed ampule, in the presence of 4,4-bipyridine (acting as a template), results after 96 h in the formation of yellow single-crystals of **MUV-3** in a quantitative manner (Figure 2.2).

Structural, magnetic and spectroscopic characterization unambiguously reveals the formation of the desired material. The good

quality of the crystals permitted crystal structure determination by single-crystal X-ray diffraction despite the fact that the synthesis is carried out in the absence of solvents.

Single-crystal X-ray diffraction analysis of the as-synthesized material reveals that the yellow crystals are isostructural to ZIF-8 (a = 17.1656(2) Å; space group $I\bar{4}3m$). Structure solution shows that each iron atom is coordinated to four nitrogen atoms from four 2meimH ligands (Fe—N distance of 2.032(1) Å and Fe···Fe distances of 6.069(1) Å), with voids of 2580 $Å^3$ in size, which are accessible through windows of 3.3 Å, similar to ZIF-8 (Figure 2.3a).

Table 2.1 Crystallographic data of $M(meim)_2$ compounds.

	ZIF-8	**ZIF-67**	**Mn-ZIF-8**	**CdIF-1**	**MUV-3**
a (Å)	16.99	16.96	17.52	18.12	17.16
M(II)-N (Å)	1.98	1.98	2.06	2.2	2.03

The pores of the as-synthetized single crystals contain residual electron density in the voids (estimated to be 494 electrons), which can be attributed to starting material, template and/or cyclopentadiene resulting from the reaction.

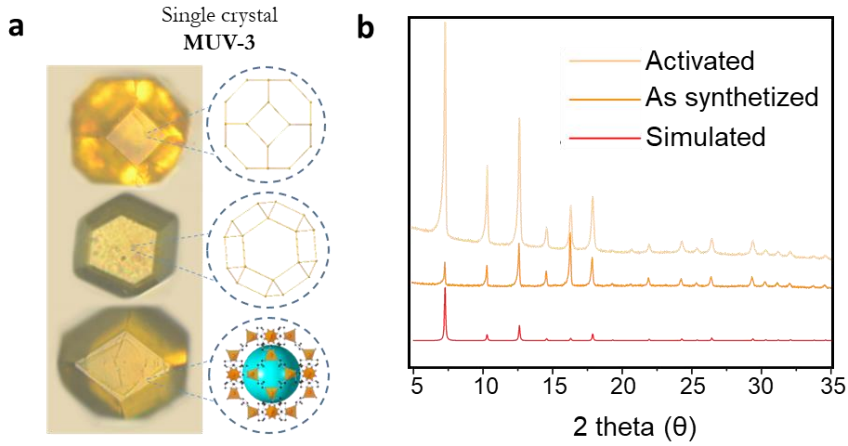

Figure 2.3 a) The different crystal faces of **MUV-3**. Key: Fe, orange tetrahedra; C, black balls; N, blue balls; the blue sphere (diameter of 11 Å) represents the empty space of the structure; hydrogen atoms have been omitted for clarity. b) X-ray powder diffraction patterns of **MUV-3** to check the activation process. In red, theoretical powder pattern of **MUV-3**; in orange, as-synthetized; and in peach, the activated material. Note the change in the intensity of the peaks upon activation.

In fact, the as-synthetized bulk material presents different peak intensities in the experimental X-ray powder diffraction (XRPD) pattern as compared with the simulated one (Figure 2.3b), and also thermogravimetric analysis (TGA) reveals a 20 % weight loss at 200 ºC (Figure 2.4a). A thorough activation process was therefore performed, which consisted in washing several times with dry acetonitrile for 48 h and subsequent overnight heating at 150 ºC under vacuum. This yields an activated form of **MUV-3**, as demonstrated by XRPD (Figure 2.3b).

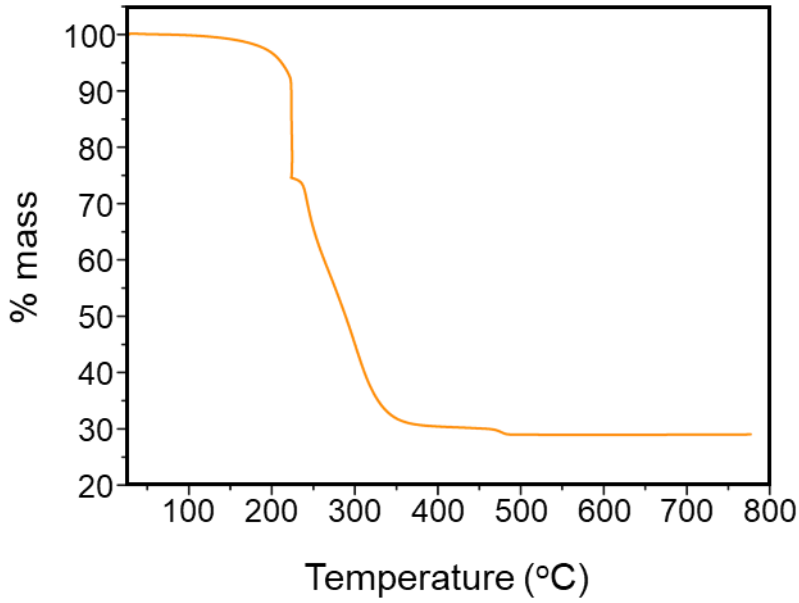

Figure 2.4 a) Thermal gravimetric analysis (TGA) of as-synthetized bulk crystals of **MUV-3** at a heating rate of 20 ºC min^{-1}.

The Fe-N-C-N-Fe pathway permits the magnetic exchange between the metallic cations. Magnetic measurements indicate the presence of strong antiferromagnetic metal-metal interactions between the Fe(II) centres occurring through the imidazolate bridges. In the magnetic susceptibility plot (Figure 2.5b), it can be seen the increase of χ with the temperature to achieve a maximum value at 23.3 K, indicating the antiferromagnetic ordering between the iron centres. The temperature dependence of the magnetic susceptibility in the high temperature range (T > 50 K) can be fitted by the Curie-Weiss law, $\chi_m = C/(T-\Theta)$, with a Curie constant C = 5.4 $emu \cdot mol^{-1} \cdot K$ and a negative Curie-Weiss temperature Θ = –138 K (Figure 2.5c). The strong antiferromagnetic nature **MUV-3** is

confirmed by the weak M vs. H linear signal, which is much below the expected saturation value (Figure 2.5d).

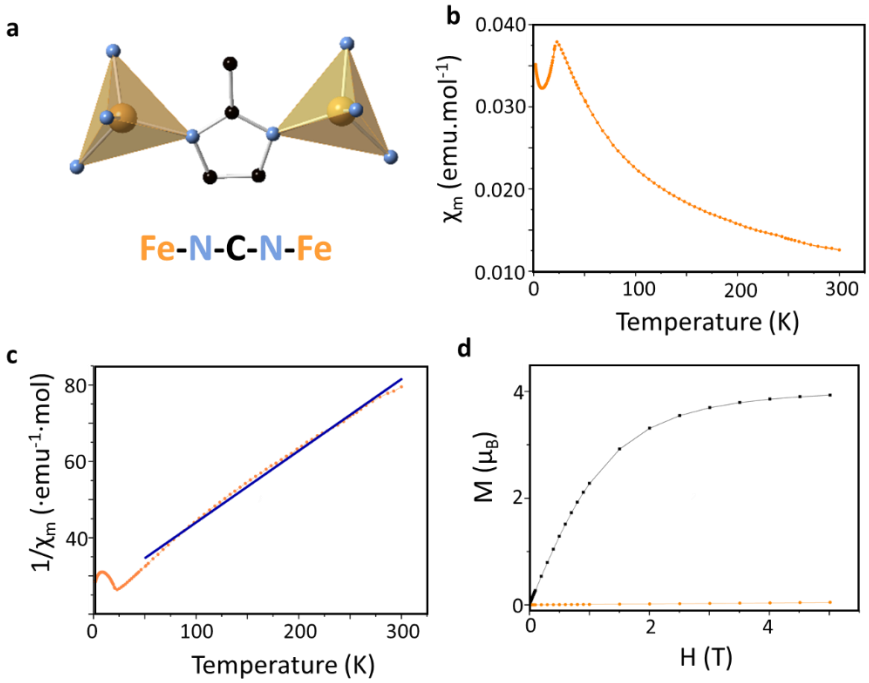

Figure 2.5 a) Pathway for the magnetic exchange coupling. b) Magnetic susceptibility plot showing the antiferromagnetic interactions and antiferromagnetic ordering at low temperature between Fe(II) centers. c) The temperature dependence of the magnetic susceptibility in the high temperature range. The blue line represents the fit to the Curie-Weiss law. d) Magnetization at 2 K of **MUV-3**; the black line represents the Brillouin function for S = 2.

Only one morphology was found for **MUV-3** crystals, being highly distorted truncated rhombohedra (Figure 2.6), similar to one of the possible morphologies founded in ZIF-8 morphologies.[25] This difference in the

crystal growth can be due to the template effect during the synthesis discussed later in the text. Although we have not managed to control the morphology of the crystals, we have been successful in the control of crystal size. In fact, changing the reaction times it is also possible to obtain smaller crystals, below 50 μm, for times below 12 hours (Figure 2.6b).

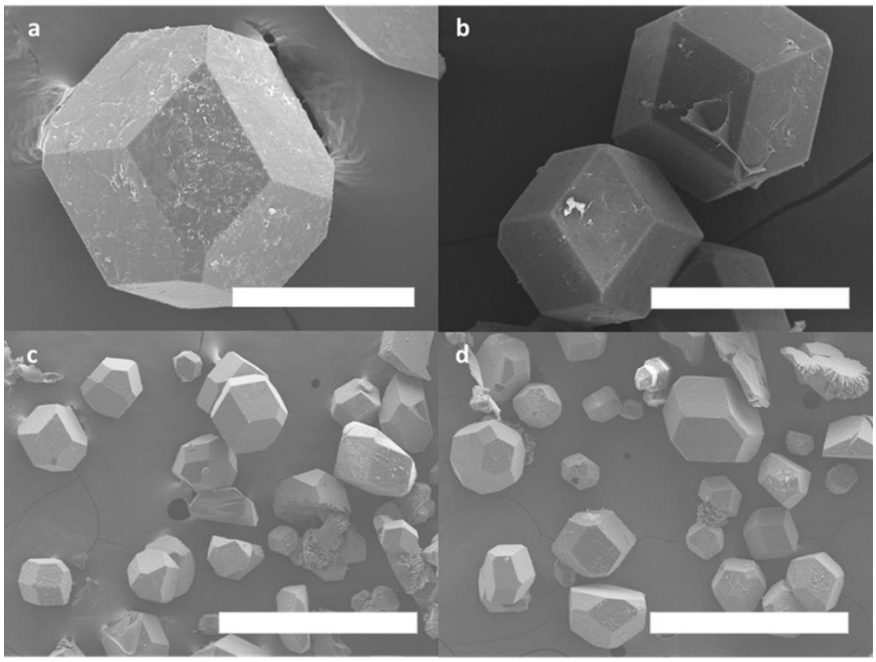

Figure 2.6. SEM image of the as-synthesized material, showing the morphology of **MUV-3**. Figures 2.4a, 2.4c and 2.4d show images of crystals from 72 hours of reaction revealing a crystal size of approx. 100 μm. Figure 2.4b shows an image of crystals from 8 h reaction, revealing a crystal size of approx. 50 μm.

In contrast to ZIF-8, **MUV-3** is quite sensitive to humidity in air (Figure 2.7a), as has also been observed in Mg-ZIF-8 and Mn-ZIF-8. Nevertheless, time-resolved XRPD study indicates that **MUV-3** is stable

for a few hours in air before it starts to decompose. The stability in dry air drastically improves, pointing out humidity as the main stability issue (Figure 2.7b). Despite this moisture-sensitivity, the compound is stable for months in inert (N_2 or Ar) atmospheres.

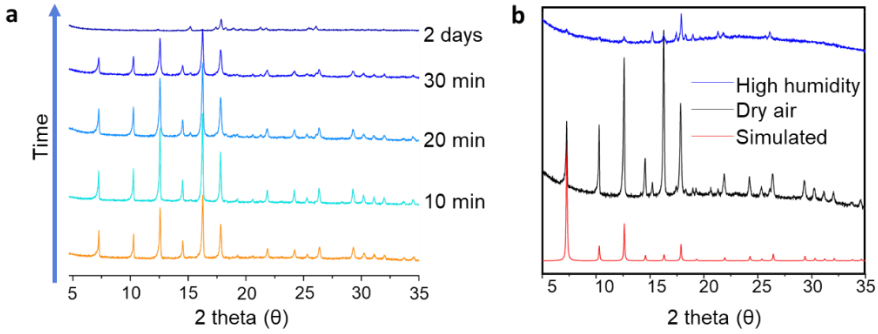

Figure 2.7 a) Test of stability in air with X-ray powder diffraction of **MUV-3** at different times in air atmosphere. b) Test of stability in air with X-ray powder diffraction of **MUV-3** under dry air and vapor water atmosphere. In red, theoretical powder pattern of **MUV-3**; in black, **MUV-3** after 4 hours exposure at dry air atmosphere; in blue, **MUV-3** after 1 hour exposure to humid air atmosphere.

Remarkably, the use of 4,4'-bipyridine as template is essential for the exclusive formation of **MUV-3**; in its absence, the dense polymer $Fe(2meim)_2$ $0.13(FeCp)_2$, (**FeDCP**), is instead obtained (Figure 2.8). The importance of a template in other type of solvent-free reaction (specifically mechanochemical reactions) was established by Friščić and co-workers, who showed that the presence of NH_4^+ affects the thermodynamic/kinetic product in Zn-based ZIFs.[24]

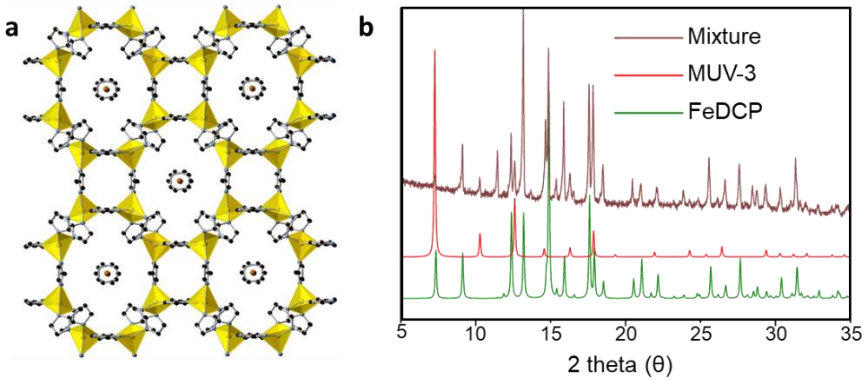

Figure 2.8 a) Crystal structure of the dense polymer, $Fe(meim)_2 0.13(FeCp_2)$. b) Template effect of 4,4-bipyridine in the solvent-free synthesis of **MUV-3**. In green, theoretical pattern of the dense coordination polymer **FeDCP**; in red the theoretical pattern of **MUV-3**; and in brown for the mixture of compounds obtained without presence of template.

We hypothesized that the presence of 4,4'-bipyridine blocks some of the coordination positions of the iron centres, thus affecting the kinetics of the crystal growth. We have screened an extensive number of templates, primarily based on pyridines, in order to examine the importance of pK_{HA}, the physical state of the template in the reaction conditions, the steric hindrance of the template and its coordination ability, establishing the importance of the latter two (see Table 2.1). We have observed that pyridine and 4-aminopyridine do not act as template, resulting in the formation of both porous **MUV-3** and the dense **FeDCP**. We hypothesize that the nitrogen atom of the pyridine interacts with the iron blocking the coordination and directing the structure formation to the porous material. If the pyridine has a small substituted group (or none), it does not block the

coordination of the Fe and does not act as a template (as observed with pyridine and 4-aminopyridine). If a bulky group is used in the 2 position, as in the case of 2-bromopyridine, it blocks the interaction of the pyridine nitrogen with the iron; therefore, in this case the templating effect is also absent (Figure 2.9).

Table 2.2 List of different molecules used as templates in the solvent-free synthesis of **MUV-3**.

Template	Physical state at the reaction	pK_{HA}	Exclusive formation of **MUV-3**
pyridine	Gas	5.14	No
2-chloropyridine	Gas-liquid	0.72	Yes
3- chloropyridine	Gas	2.84	Yes
4-aminopyridine	Liquid	8.96	No
2,2-bipyridyl	Liquid	4.3	Yes
4,4-dimethyl-2,2-dipyridyl	Liquid	-	Yes
1,2-bis(4-pyridyl)ethane	Liquid	-	Yes
1,4-diazabicyclo[2.2.2]octane	Liquid	8.8	Yes
3,5-lutidine	Gas-liquid	-	Yes
2-ethylpirydine	Gas	5.83	Yes
2-bromopyridine	Liquid	0.9	No
3-bromopyridine	Liquid	2.84	Yes

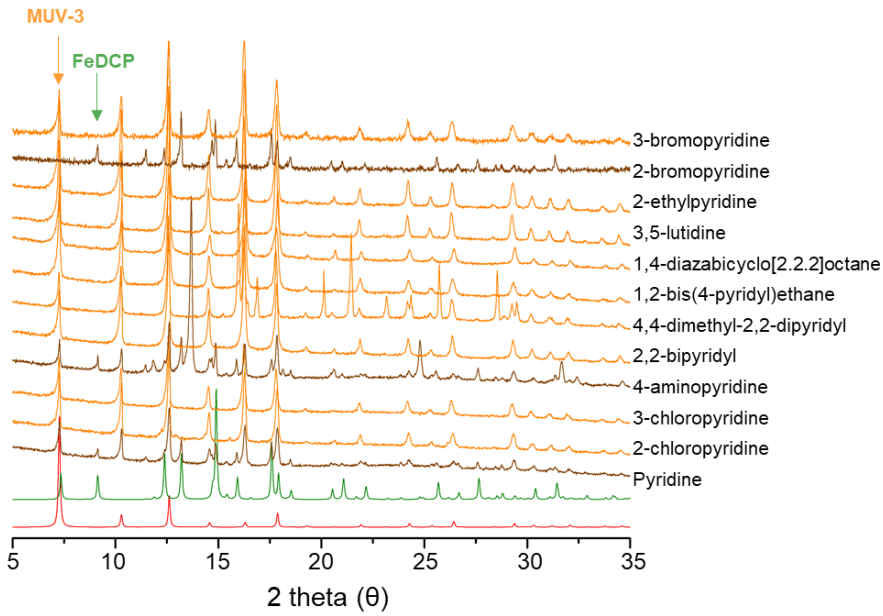

Figure 2.9 Template effect in the solvent free synthesis of **MUV-3** with different molecules. In red, the theoretical pattern of **MUV-3**; in green, theoretical pattern of dense coordination polymer **FeDCP**. Orange represent the pure phase synthesis of **MUV-3**, and brown color represents the mixture of phases after the synthesis using different the different templates (each indicated on the right). The arrows at the top indicate the most characteristic peaks for **MUV-3** and the iron dense coordination polymer (**FeDCP**) and serve to analyse the effect of the template. In the case of 4,4-dimethyl-2,2-dipyridyl we can also observe the diffraction peaks corresponding to the template.

Gas sorption. The porous nature of **MUV-3** was assessed by N_2 and CO_2 sorption. Activation of **MUV-3** prior to measurement was achieved by treating the washed material at 150 ºC under vacuum overnight. Figure 2.10a displays a characteristic two-step N_2 adsorption isotherm, with a

plateau at 260 $cm^3 \cdot g^{-1}$, which is reminiscent to that of the analogous ZIF-8 and ZIF-67 materials. Such a similar structural response upon sorption is attributed to the flexibility of the ligands. The obtained accessible surface area was calculated using the Brunauer–Emmett–Teller (BET) model, obtaining a value of 960 $m^2 \cdot g^{-1}$, which is significantly lower to that of ZIF-8 (*ca.* 1400 $m^2 \cdot g^{-1}$) likely due to the presence of organic molecules remaining in the pores. The CO_2 sorption at 298 K, shown in Figure 2.10b, reveals a total uptake of 2.9 $mmol \cdot g^{-1}$ at 18 bar.

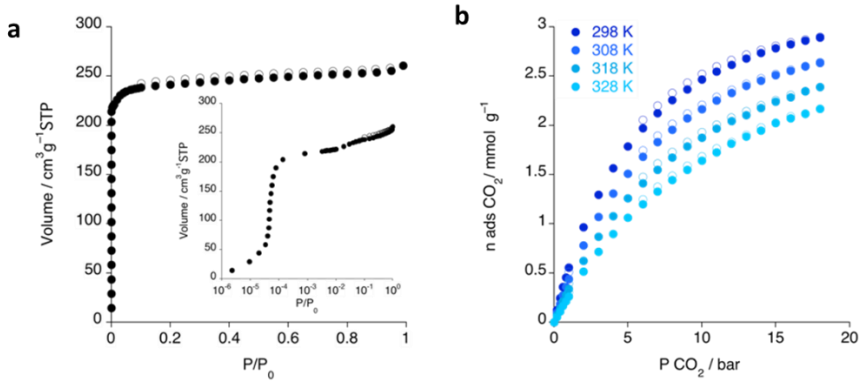

Figure 2.10 a) N_2 sorption (solid circle) and desorption (open circle) of **MUV-3** at 77 K. Inset: semilog plot revealing the two-step adsorption resulting from the flexibility of **MUV-3**. b) CO_2 sorption (solid circle) and desorption (open circle) isotherms at different temperatures.

Furthermore, we examined the sorption capacity of **MUV-3** towards the biologically active NO gas.

Between gas-framework interactions and catalytic properties is the use of MOFs to solve the problem with chemical warfare agents and toxic industrial chemicals.[26] For example, toxics NOx produced by coal, automobile and agricultural activities there is an important problem. In

particular, nitric oxide (NO) is a highly toxic gas, similar to CO and interesting to biological applications. The use of Fe-based MOF with unsaturated coordination sites is the most common approach for chemisorption of NO.[27–31] For example, in a Fe(II) substituted MOF-5, NO coordinate to Fe centers and disproportionate to different species of NO_x (Figure 2.11a) demonstrated by in situ infrared DRIFTS experiments.[30] Another example is the use of the well know Fe-based **MOF-74**, Fe_2(dobdc), with unsaturated coordination sites and the possibility to redox actives sites due to the possibility to access to Fe(III) (Figure 2.11b).[28] The latest example is based in the high stable Ti-MOF (MIP-177), where the activated compound exposed to NO gas is replacing a coordinated OH^- molecule to form NO_2^- and when is introduced in body fluid, molecules of water replace the NO_2^- molecules (Figure 2.11c).[32]

MUV-3 present Fe(II) centres in a tetrahedral environment, which can be amplified to interact with NO molecules. For this reason, and the Fe(II) and 2meimH biocompatibility it was thought as a good candidate to NO adsorption.

These experiments were performed at the Instituto de Tecnología Química (ITQ) of the Polytechnic Universtiy of Valencia, with the group of Prof. Fernando Rey. **MUV-3** material was subjected to NO volumetric adsorption at 273 K, presenting a total uptake of 2.1 $mmol \cdot g^{-1}$ at 1 bar (Figure 2.12), which corresponds to *ca*. 0.45 NO molecules per Fe(II) site. This suggests an incomplete NO loading, which is in agreement with the absence of a saturated plateau at 1 bar. This sorption value is lower than the

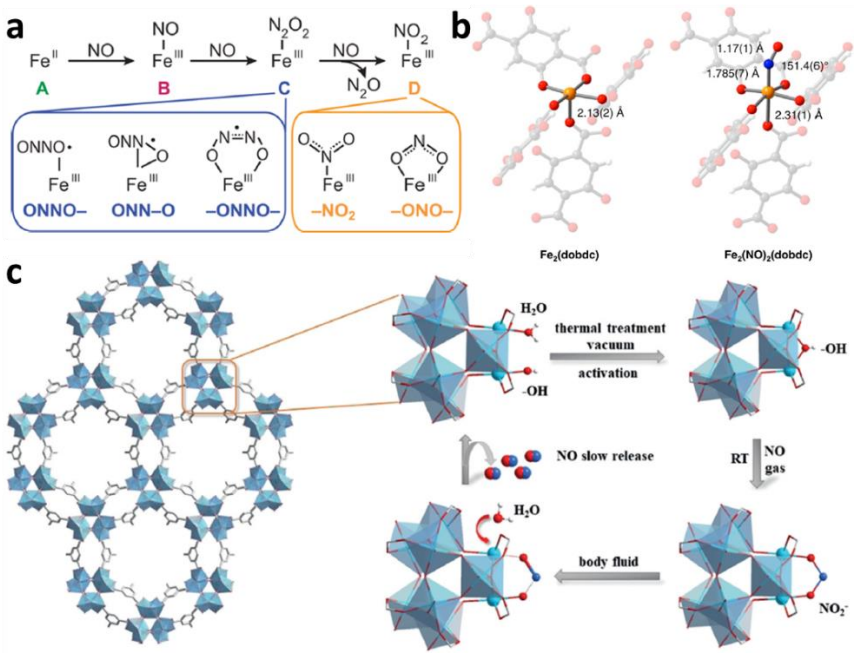

Figure 2.11 a) Mechanism of the transformation of NO in other nitrogen oxides in **MOF-5** substituted by Fe(II) cations.b) Metal open sites in Fe-MOF-74 enhancing the interaction with NO.c) Mechanism to trap and realize NO by Ti (IV) MOFs. Adapted from references 28, 30 and 32.

exceptional storage capacity of the M-MOF-74 materials (up to 7 mmol·g^{-1}), and similar to that of HKUST-1 (3 mmol·g^{-1}),[23] both of them presenting a high density of open metal sites. However, in sharp contrast to M-MOF-74, which shows a similar NO sorption regardless of the metal centre, **MUV-3** has a significantly different behavior to its isostructural Zn analogue (i.e. ZIF-8). As shown in Figure 2.12 the behavior of both **MUV-3** and ZIF-8 is analogous at low pressures (< 0.15 bar), with a slow progressive loading of NO, which can be attributed to physisorption. Upon further pressure increase, the amount of NO adsorbed by **MUV-3** rises

sharply between 0.15 and 0.23 bar, which is not observed for ZIF-8. This is attributed to a "gate opening" effect caused by the chemisorption of NO molecules to the Fe(II) centers, unprecedented in MOFs, which typically show a constant NO sorption, even when using flexible MOFs such as MIL-88 and MIL-53.

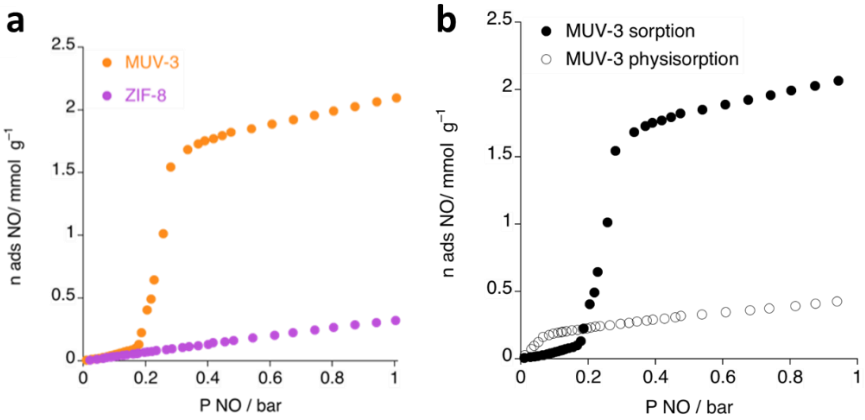

Figure 2.12 a) NO sorption of **MUV-3** (orange) and ZIF-8 (violet) at 273 K. b) NO sorption of **MUV-3** at 273 K, showing the first cycle of sorption (filled circles) and the second cycle of sorption (empty circles).

The NO chemisorption is evidenced by IR spectroscopy, which reveals the appearance of characteristic vibration of coordinated NO species (ν_{N-O} 1720 and 1790 cm^{-1}, see Figure 2.13a) after exposing **MUV-3** to NO, which are absent in ZIF-8 (Figure 2.13b). In addition, upon vacuum treatment of the NO loaded **MUV-3** and re-exposure to NO, we observe only a small sorption that can be attributed exclusively to physisorption (Figure 2.12b), indicating that the coordinated NO molecules are retained in the structure. Interestingly, at low pressures (< 0.2 bar) the amount of adsorbed NO is larger than that observed in the first sorption

cycle, indicating that the **NO-MUV-3** (i.e. **MUV-3** with chemisorbed NO) remains in the open form.

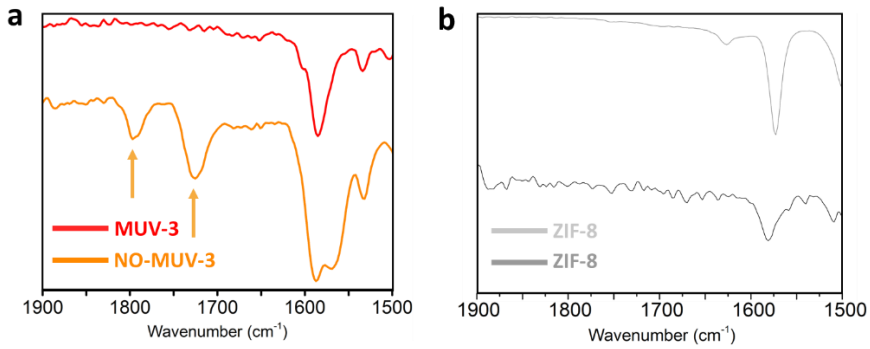

Figure 2.13 a) Infrarred spectra of **MUV-3** before (red) and after (orange) exposure to NO at room temperature and ambient pressure. The arrows indicate the appearance of characteristic vibration of coordinated NO species b) Infrared spectra of ZIF-8 before (gray) and after (dark gray) exposure to NO.

Generalization of the solvent-free synthesis. The solvent-free approach here described can be expanded to the preparation of other isostructural metal analogues to **MUV-3**, which opens the door to reach a variety of mixed-metal structures[33] or mixed-ligand structures.[34]. Thus, using other metal sources compatible with chemical vapor deposition (CVD) techniques such as $Zn(TMHD)_2$ [TMHD = bis(2,2,6,6-tetramethyl-3,5-heptanedionato)], ZnO or cobaltocene, we could also obtain ZIF-8 and ZIF-67 (Figure 2.14). However, contrary to the preparation of **MUV-3**, no template is required for the formation of ZIF-8 or ZIF-67.

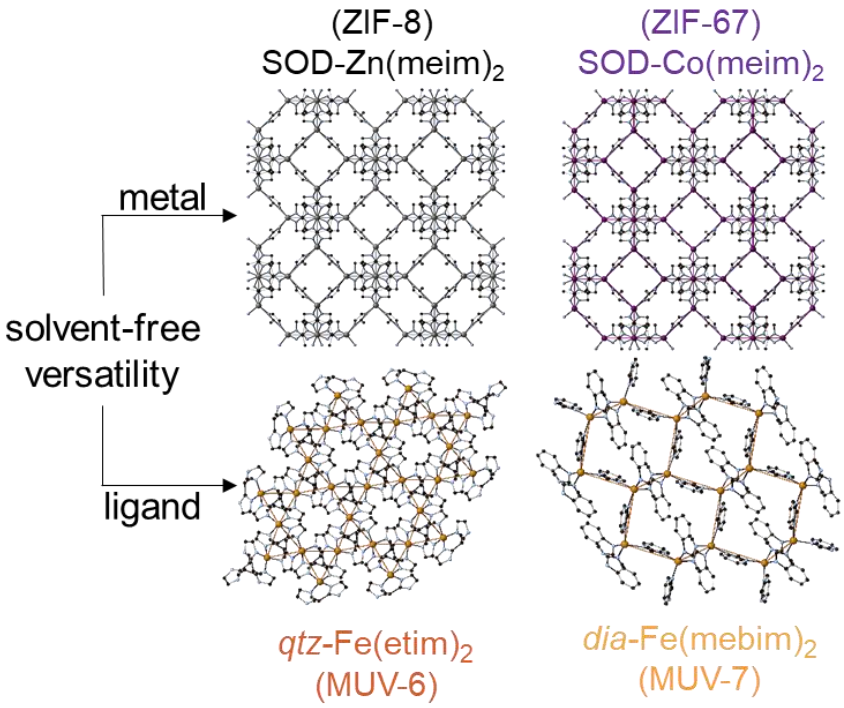

Figure 2.14 Expansion of the solvent-free methodology to prepare isostructural metal analogues to **MUV-3**, ZIF-8 (shown in black) and ZIF-67 (shown in purple), represented with the with SOD topology, and different topologies of other iron(II)-ZIFs obtained with the same solvent-free methodology (**MUV-6** and **MUV-7**, shown in dark orange and light orange respectively).

Furthermore, the use of different imidazolate ligands allows the preparation of other unprecedented Fe(II)-ZIFs with different topologies, such as Fe(etim)$_2$ (etimH = 2-ethylimidazole), with *qtz* topology (denoted **MUV-6**), and Fe(mebim)$_2$ (mebimH = 2-methylbenzylimidazole), with *dia* topology (denoted **MUV-7**) (Figure 2.16). This highlights the relevance of

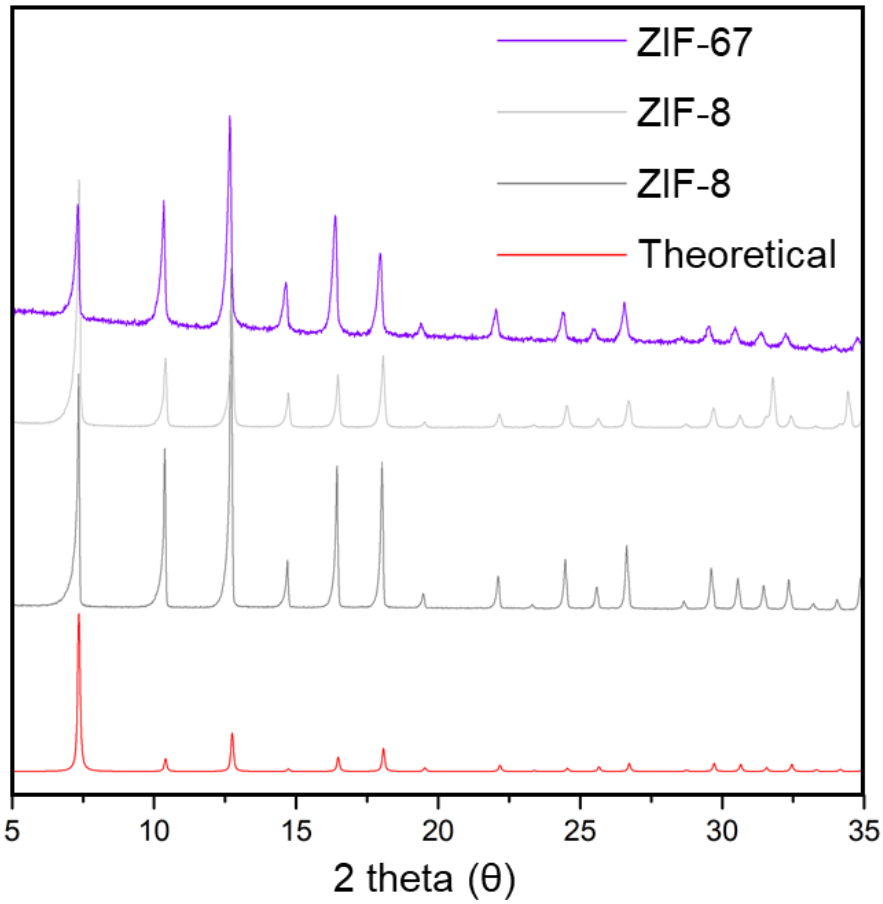

Figure 2.15 X-ray powder diffraction of ZIF-8 and ZIF-67 synthetized by solvent-free method. In red, theoretical powder pattern of ZIF-8; in dark grey, ZIF-8 synthetized using bis(2,2,6,6-tetramethyl-3,5-heptanedionato) zinc(II); in grey, ZIF-8 synthetized using ZnO; in purple, ZIF-67 synthetized using cobaltocene.

the methodology here described. These ligands in combination of Zn(II) or Co(II) can give several structures. In the case of etimH, the most thermodynamic topology is the dense polymorph, in this case, the *qtz*

topology. The alternatives (RHO and ANA topology), present cavities and porosity.[35]

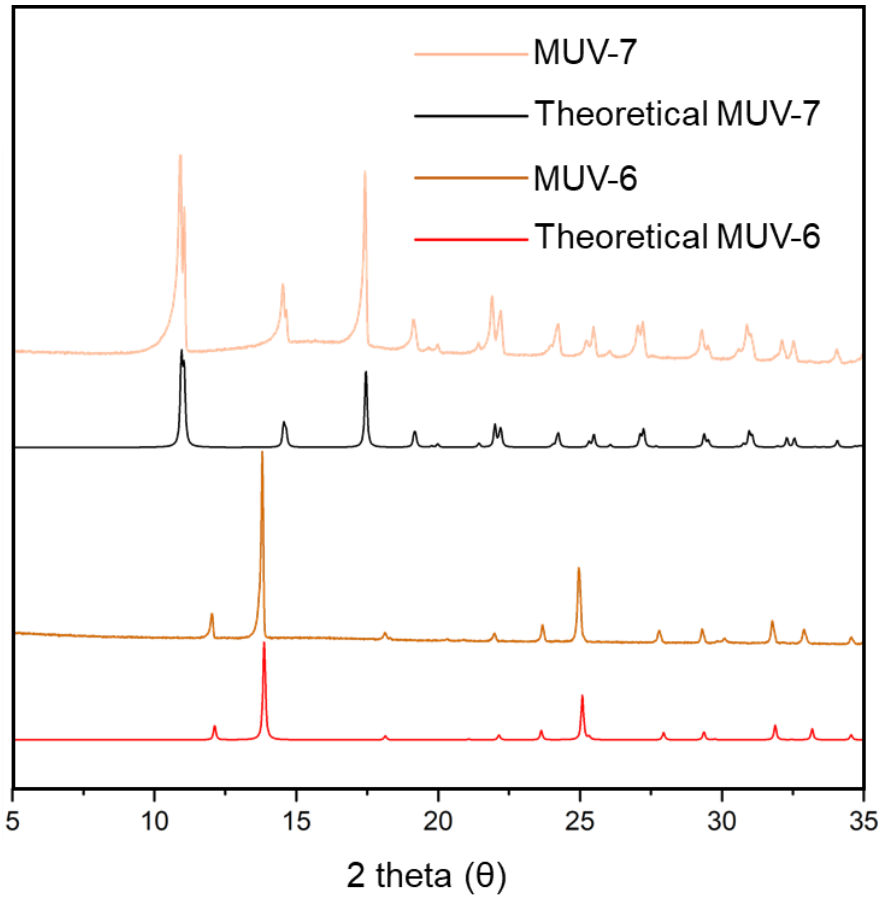

Figure 2.16 X-ray powder diffraction of **MUV-6** and **MUV-7** synthetized by solvent-free method (in orange and clear orange, respectively) and the theoretical powder pattern of **MUV-6** and **MUV-7** (in red and black, respectively).

With mebimH does not exist any pure ligand ZIF structure due to the bulky nature of the ligand. But the *dia* topology exist as polymorph of ZIF-

8 and ZIF-67, and also is the most thermodynamic topology for this combination.

2.3 Conclusions

In summary, we have presented the solvent-free synthesis of the highly interesting iron(II) analogue of ZIF-8, **MUV-3**, inaccessible through conventional preparation routes, thus paving the way for exploring many applications. The presence of a template is crucial for the facile synthesis of phase pure single crystals of **MUV-3**, which show a gate opening behaviour analogous to that of ZIF-8. However, its behaviour towards NO sorption is completely different due to the presence of Fe(II) centres, revealing a chemisorption of the NO molecules to the metal centres. The synthetic procedure here presented, using ferrocene as the source of iron, is also compatible with the chemical vapor deposition (CVD) techniques commonly used in microelectronics and recently shown to be effective with MOFs,[23] thus facilitating its applicability. This green alternative to synthetize ZIFs is also possible to apply for other already known as ZIF-8 and ZIF-67, and presents the opportunity to explore novel ZIF phases and materials.

2.4 Methods

All reagents were commercially available and used without further purification.

Synthesis of MUV-3. Ferrocene (30 mg, 0.16 mmol), 4,4-bipyridine (50 mg, 0.32 mmol), or an alternative template and 2-methylimidazole (25 mg, 0.30 mmol) were combined and sealed under vacuum in a layering tube (4

mm diameter). The mixture was heated at 150 °C for 4 days to obtain yellow crystals suitable for X-ray single-crystal diffraction. The product was allowed to cool to room temperature, and the layering tube was then opened. The unreacted precursors were extracted with acetonitrile and benzene, and **MUV-3** was isolated as yellow crystals (yield 20 %). Phase purity was established by X-ray powder diffraction.

Synthesis of ZIF-8 and ZIF-67. Cobaltocene (for ZIF-67, 30 mg, 0.16 mmol), ZnO (for ZIF-8, 13 mg, 0.16 mmol) or bis(2,2,6,6-tetramethyl-3,5-heptanedionato) zinc(II) (for ZIF-8, 69 mg, 0.16 mmol) and 2-methylimidazole (25 mg, 0.30 mmol) were combined and sealed under vacuum in a layering tube (4 mm diameter). The mixtures were heated at 150 °C for 4 days to obtain purple powder (ZIF-67) or white powder (ZIF-8). The products were allowed to cool to room temperature, and the layering tubes were then opened. The unreacted precursors were extracted with acetonitrile and benzene. Phase purity was established by X-ray powder diffraction.

Synthesis of MUV-6 and MUV-7. Ferrocene (30 mg, 0.16 mmol), 2-ethylimidazole (29 mg, 0.30 mmol, for the preparation of *qtz*-[Fe(etim)$_2$], **MUV-6**) or 2-methylbenzimidazole (40 mg, 0.30 mmol, for the preparation of *dia*-[Fe(mebim)$_2$], **MUV-7**) were combined and sealed under vacuum in a layering tube (4 mm diameter). The mixtures were heated at 150 °C (**MUV-6**) and 250 °C (**MUV-7**) for 4 days to obtain pale yellow crystals suitable for X-ray single-crystal diffraction. The products were allowed to cool to room temperature, and the layering tube were then opened. The unreacted precursors were extracted with acetonitrile and benzene, and

MUV-6 or **MUV-7** were isolated as pale yellow crystals. Phase purity was established by X-ray powder diffraction.

X-ray powder diffraction. Polycrystalline samples of **MUV-3**, **MUV-6**, **MUV-7,** ZIF-8 and ZIF-67 (prepared by solvent-free synthesis) were lightly ground in an agate mortar and pestle and used to fill 0.5 mm borosilicate capillaries that were mounted and aligned on an Empyrean PANalytical powder diffractometer, using Cu Kα radiation (λ = 1.54056 Å). Three repeated measurements were collected at room temperature (2θ = 2−40 °) and merged in a single diffractogram for each sample, with sharp and intense peaks denoting the high crystallinity of the material (Figure 2.3).

Single Crystal diffraction. Single crystals of **MUV-3, MUV-6** and **MUV-7** were mounted on cryoloops using a viscous hydrocarbon oil to coat the crystals. X-ray data were collected at 120 K on a Supernova diffractometer equipped with a graphite-monochromated Enhance (Mo) X-ray Source (λ = 0.71073 Å). The program CrysAlisPro, Oxford Diffraction Ltd., was used for unit cell determinations and data reduction. Empirical absorption correction was performed using spherical harmonics, implemented in the SCALE3 ABSPACK scaling algorithm. Crystal structures were solved and refined against all F^2 values by using the SHELXTL and Olex2 suite of programs.[36,37] Non-hydrogen atoms were refined anisotropically and hydrogen atoms were placed at calculated positions (riding model). Solvent mask protocol in Olex 2 was implemented to account with the remaining electrondensity corresponding to disordered molecules of starting material

in **MUV-3**. A total of 494 electrons were found un-accounted in the model (in a cavity of 2580 $Å^3$ in size).

Thermogravimetric analysis. Thermogravimetric analyzed of **MUV-3**, **MUV-6**, **MUV-7,** ZIF-8 and ZIF-67 were carried out with a TA instruments TGA 550 apparatus in the 25–500 °C temperature range under a $5°C \cdot min^{-1}$ scan rate and a N_2 flow of 40 $mL \cdot min^{-1}$.

Scanning electronic microscopy. Scanning Electronic Micrographs images were recorded in a Hitachi S-4800 at different times of reaction. Synthesis length below 12 hours yields crystals of around 50 μm, whereas synthesis length longer than 12 hours yields crystals of around 100 μm size.

Magnetic measurements. The magnetic structure and the presence of Fe(II) was characterized by magnetic measurements. Variable-temperature (2−300 K) direct current (dc) magnetic susceptibility measurements were carried out in applied fields of 0.1 T and variable field magnetization measurements up to 5 T at 2 K.

Gas Sorption. Nitrogen isotherms were measured using a TRIFLEX apparatus (Micromeritics) at −196 °C. The sample was transferred from a sealed ampoule to the sample holder inside a glove box. Before the analysis, 50 mg of the thoroughly washed **MUV-3** were degassed at 150 °C and $\sim 5 \times 10^{-6}$ bar overnight. The BET surface area was calculated by using the Brunauer−Emmett−Teller equation, and micropore volume was calculated by the t-plot method.

The high-pressure CO_2 adsorption isotherms were measured in a gravimetric sorption analyzer IGA-100 (Hiden Isochema). 50 mg of

adsorbent were placed in a sample holder and before measurement, the sample was degassed 3 hours at 100 °C under vacuum. CO_2 adsorption isotherms were acquired at 25, 35, 45 and 55 °C.

The NO adsorption isotherms were collected in a Micromeritics ASAP 2010 apparatus. In the first experiment, 200 mg of fresh **MUV-3** were placed in the sample holder and activated at 100 ºC under vacuum overnight. Then, the isotherm was measured at 0 ºC up to 1 bar. In order to distinguish between physisorption and chemisoption, a second isotherm was measured on the same sample but degassing at room temperature, assuming that only the physisorbed molecules were removed.

Infrared spectra. IR were recorded in a Platinum-ATR diamond Bruker spectrometer in the 4000−350 cm^{-1} range using powdered samples.

2.5 References

(1) Wang, L. J.; Deng, H.; Furukawa, H.; Gándara, F.; Cordova, K. E.; Peri, D.; Yaghi, O. M. Synthesis and Characterization of Metal–Organic Framework-74 Containing 2, 4, 6, 8, and 10 Different Metals. *Inorg. Chem.* **2014**, *53* (12), 5881–5883.

(2) Caskey, S. R.; Wong-Foy, A. G.; Matzger, A. J. Dramatic Tuning of Carbon Dioxide Uptake via Metal Substitution in a Coordination Polymer with Cylindrical Pores. *J. Am. Chem. Soc.* **2008**, *130* (33), 10870–10871.

(3) Bloch, E. D.; Queen, W. L.; Krishna, R.; Zadrozny, J. M.; Brown, C. M.; Long, J. R. Hydrocarbon Separations in a Metal-Organic Framework with Open Iron(II) Coordination Sites. *Science* **2012**, *335* (6076), 1606–1610.

(4) Queen, W. L.; Hudson, M. R.; Bloch, E. D.; Mason, J. A.; Gonzalez, M. I.; Lee, J. S.; Gygi, D.; Howe, J. D.; Lee, K.; Darwish, T. A.; James, M.; Peterson, V. K.; Teat, S. J.; Smit, B.; Neaton, J. B.; Long, J. R.; Brown, C. M. Comprehensive Study of Carbon Dioxide Adsorption in the Metal–Organic Frameworks M $_2$ (Dobdc) (M = Mg, Mn, Fe, Co, Ni, Cu, Zn). *Chem. Sci.* **2014**, *5* (12), 4569–4581.

(5) Huang, X.-C.; Lin, Y.-Y.; Zhang, J.-P.; Chen, X.-M. Ligand-Directed Strategy for Zeolite-Type Metal–Organic Frameworks: Zinc(II) Imidazolates with Unusual Zeolitic Topologies. *Angew. Chemie Int. Ed.* **2006**, *45* (10), 1557–1559.

(6) Park, K. S.; Ni, Z.; Côté, A. P.; Choi, J. Y.; Huang, R.; Uribe-Romo, F. J.; Chae, H. K.; O'Keeffe, M.; Yaghi, O. M. Exceptional Chemical and Thermal Stability of Zeolitic Imidazolate Frameworks. *Proc. Natl. Acad. Sci. U. S. A.* **2006**, *103* (27), 10186–10191.

(7) Banerjee, R.; Phan, A.; Wang, B.; Knobler, C.; Furukawa, H.; O'Keeffe, M.; Yaghi, O. M. High-Throughput Synthesis of Zeolitic Imidazolate Frameworks and Application to CO2 Capture. *Science* **2008**, *319* (5865), 939–943.

(8) Tian, Y.-Q.; Yao, S.-Y.; Gu, D.; Cui, K.-H.; Guo, D.-W.; Zhang, G.; Chen, Z.-X.; Zhao, D.-Y. Cadmium Imidazolate Frameworks with Polymorphism, High Thermal Stability, and a Large Surface Area. *Chem. - A Eur. J.* **2010**, *16* (4), 1137–1141.

(9) Horike, S.; Kadota, K.; Itakura, T.; Inukai, M.; Kitagawa, S. Synthesis of Magnesium ZIF-8 from Mg(BH $_4$) $_2$. *Dalt. Trans.* **2015**, *44* (34), 15107–15110.

(10) Kadota, K.; Sivaniah, E.; Bureekaew, S.; Kitagawa, S.; Horike, S. Synthesis of Manganese ZIF - 8 from [Mn(BH_4)$_2$ · 3THF] · $NaBH_4$. **2017**, *52334* (4), 8–11.

(11) Andres-Garcia, E.; López-Cabrelles, J.; Oar-Arteta, L.; Roldan-Martinez, B.; Cano-Padilla, M.; Gascon, J.; Mínguez Espallargas, G.; Kapteijn, F. Cation Influence in Adsorptive Propane/Propylene Separation in ZIF-8 (SOD) Topology. *Chem. Eng. J.* **2019**,

371 (March), 848–856.

(12) Giménez-Marqués, M.; Hidalgo, T.; Serre, C.; Horcajada, P. Nanostructured Metal-Organic Frameworks and Their Bio-Related Applications. *Coord. Chem. Rev.* **2016**, *307*, 342–360.

(13) Kaneti, Y. V.; Tang, J.; Salunkhe, R. R.; Jiang, X.; Yu, A.; Wu, K. C. W.; Yamauchi, Y. Nanoarchitectured Design of Porous Materials and Nanocomposites from Metal-Organic Frameworks. *Adv. Mater.* **2017**, *29* (12), 1604898.

(14) Cao, X.; Tan, C.; Sindoro, M.; Zhang, H. Hybrid Micro-/Nano-Structures Derived from Metal–Organic Frameworks: Preparation and Applications in Energy Storage and Conversion. *Chem. Soc. Rev.* **2017**, *46* (10), 2660–2677.

(15) Zhao, D.; Shui, J.-L.; Chen, C.; Chen, X.; Reprogle, B. M.; Wang, D.; Liu, D.-J. Iron Imidazolate Framework as Precursor for Electrocatalysts in Polymer Electrolyte Membrane Fuel Cells. *Chem. Sci.* **2012**, *3* (11), 3200.

(16) Lee, J. S. M.; Sarawutanukul, S.; Sawangphruk, M.; Horike, S. Porous Fe-N-C Catalysts for Rechargeable Zinc-Air Batteries from an Iron-Imidazolate Coordination Polymer. *ACS Sustain. Chem. Eng.* **2019**, *7* (4), 4030–4036.

(17) Rettig, S. J.; Storr, A.; Summers, D. A.; Thompson, R. C.; Trotter, J. Iron(II) 2-Methylimidazolate and Copper(II) 1,2,4-Triazolate Complexes: Systems Exhibiting Long-Range Ferromagnetic Ordering at Low Temperatures. *Can. J. Chem.* **1999**, *77* (4), 425–433.

(18) Rettig, S. J.; Storr, A.; Summers, D. A.; Thompson, R. C.; Trotter, J. Transition Metal Azolates from Metallocenes. 2. Synthesis, X-Ray Structure, and Magnetic Properties of a Three-Dimensional Polymetallic Iron(II) Imidazolate Complex, a Low-Temperature Weak Ferromagnet. *J. Am. Chem. Soc.* **1997**, *119* (37), 8675–8680.

(19) Fernandez-Bartolome, E.; Santos, J.; Khodabakhshi, S.; Mcormick, L. J.; Teat, S. J.; De Pipaon, C. S.; Galan-Mascarós, J. R.; Martín, N.; Sanchez Costa, J. A Robust and Unique Iron(II) Mosaic-like MOF. *Chem. Commun.* **2018**, *54* (44), 5526–5529.

(20) Cravillon, J.; Münzer, S.; Lohmeier, S. J.; Feldhoff, A.; Huber, K.; Wiebcke, M. Rapid Room-Temperature Synthesis and Characterization of Nanocrystals of a Prototypical Zeolitic Imidazolate Framework. *Chem. Mater.* **2009**, *21* (8), 1410–1412.

(21) Pan, Y.; Liu, Y.; Zeng, G.; Zhao, L.; Lai, Z. Rapid Synthesis of Zeolitic Imidazolate Framework-8 (ZIF-8) Nanocrystals in an Aqueous System. *Chem. Commun.* **2011**, *47* (7), 2071–2073.

(22) López-Cabrelles, J.; Romero, J.; Abellán, G.; Giménez-Marqués, M.; Palomino, M.;

Valencia, S.; Rey, F.; Mínguez Espallargas, G. Solvent-Free Synthesis of ZIFs: A Route toward the Elusive Fe(II) Analogue of ZIF-8. *J. Am. Chem. Soc.* **2019**, *141* (17), 7173–7180.

(23) Stassen, I.; Styles, M.; Grenci, G.; Van Gorp, H.; Vanderlinden, W.; De Feyter, S.; Falcaro, P.; De Vos, D.; Vereecken, P.; Ameloot, R. Chemical Vapour Deposition of Zeolitic Imidazolate Framework Thin Films. *Nat. Mater.* **2016**, *15* (3), 304–310.

(24) Beldon, P. J.; Fábián, L.; Stein, R. S.; Thirumurugan, A.; Cheetham, A. K.; Friščić, T. Rapid Room-Temperature Synthesis of Zeolitic Imidazolate Frameworks by Using Mechanochemistry. *Angew. Chemie Int. Ed.* **2010**, *49* (50), 9640–9643.

(25) Avci, C.; Ariñez-Soriano, J.; Carné-Sánchez, A.; Guillerm, V.; Carbonell, C.; Imaz, I.; Maspoch, D. Post-Synthetic Anisotropic Wet-Chemical Etching of Colloidal Sodalite ZIF Crystals. *Angew. Chemie - Int. Ed.* **2015**, *54* (48), 14417–14421.

(26) Islamoglu, T.; Chen, Z.; Wasson, M. C.; Buru, C. T.; Kirlikovali, K. O.; Afrin, U.; Mian, M. R.; Farha, O. K. Metal-Organic Frameworks against Toxic Chemicals. *Chem. Rev.* **2020**.

(27) Xiao, B.; Wheatley, P. S.; Zhao, X.; Fletcher, A. J.; Fox, S.; Rossi, A. G.; Megson, I. L.; Bordiga, S.; Regli, L.; Thomas, K. M.; Morris, R. E. High-Capacity Hydrogen and Nitric Oxide Adsorption and Storage in a Metal−Organic Framework. *J. Am. Chem. Soc.* **2007**, *129* (5), 1203–1209.

(28) Bloch, E. D.; Queen, W. L.; Chavan, S.; Wheatley, P. S.; Zadrozny, J. M.; Morris, R.; Brown, C. M.; Lamberti, C.; Bordiga, S.; Long, J. R. Gradual Release of Strongly Bound Nitric Oxide from $Fe_2(NO)_2$ (Dobdc). *J. Am. Chem. Soc.* **2015**, *137* (10), 3466–3469.

(29) McKinlay, A. C.; Eubank, J. F.; Wuttke, S.; Xiao, B.; Wheatley, P. S.; Bazin, P.; Lavalley, J.-C.; Daturi, M.; Vimont, A.; De Weireld, G.; Horcajada, P.; Serre, C.; Morris, R. E. Nitric Oxide Adsorption and Delivery in Flexible MIL-88(Fe) Metal–Organic Frameworks. *Chem. Mater.* **2013**, *25* (9), 1592–1599.

(30) Brozek, C. K.; Miller, J. T.; Stoian, S. A.; Dincă, M. NO Disproportionation at a Mononuclear Site-Isolated Fe^{2+} Center in Fe^2 -MOF-5. *J. Am. Chem. Soc.* **2015**, *137* (23), 7495–7501.

(31) McKinlay, A. C.; Xiao, B.; Wragg, D. S.; Wheatley, P. S.; Megson, I. L.; Morris, R. E. Exceptional Behavior over the Whole Adsorption−Storage−Delivery Cycle for NO in Porous Metal Organic Frameworks. *J. Am. Chem. Soc.* **2008**, *130* (31), 10440–10444.

(32) Pinto, R. V.; Wang, S.; Tavares, S. R.; Pires, J.; Antunes, F.; Vimont, A.; Clet, G.; Daturi, M.; Maurin, G.; Serre, C.; Pinto, M. L. Tuning Cellular Biological Functions Through the

Controlled Release of NO from a Porous Ti-MOF. *Angew. Chemie - Int. Ed.* **2020**, *59* (13), 5135–5143.

(33) Xiao, Y.; Hong, A. N.; Hu, D.; Wang, Y.; Bu, X.; Feng, P. Solvent-Free Synthesis of Zeolitic Imidazolate Frameworks and the Catalytic Properties of Their Carbon Materials. *Chem. – A Eur. J.* **2019**, *25* (71), 16358–16365.

(34) Marreiros, J.; Van Dommelen, L.; Fleury, G.; Oliveira-Silva, R.; Stassin, T.; Iacomi, P.; Furukawa, S.; Sakellariou, D.; Llewellyn, P. L.; Roeffaers, M.; Ameloot, R. Vapor-Phase Linker Exchange of the Metal–Organic Framework ZIF-8: A Solvent-Free Approach to Post-synthetic Modification. *Angew. Chemie* **2019**, *131* (51), 18642–18646.

(35) Akimbekov, Z.; Katsenis, A. D.; Nagabhushana, G. P.; Ayoub, G.; Arhangelskis, M.; Morris, A. J.; Friščić, T.; Navrotsky, A. Experimental and Theoretical Evaluation of the Stability of True MOF Polymorphs Explains Their Mechanochemical Interconversions. *J. Am. Chem. Soc.* **2017**, *139* (23), 7952–7957.

(36) Dolomanov, O. V.; Bourhis, L. J.; Gildea, R. J.; Howard, J. A. K.; Puschmann, H. OLEX2 : A Complete Structure Solution, Refinement and Analysis Program. *J. Appl. Crystallogr.* **2009**, *42* (2), 339–341.

(37) Sheldrick, G. M. Crystal Structure Refinement with SHELXL. *Acta Crystallogr. Sect. C Struct. Chem.* **2015**, *71* (1), 3–8.

Chapter 3

Mixed-ligand SOD ZIFs

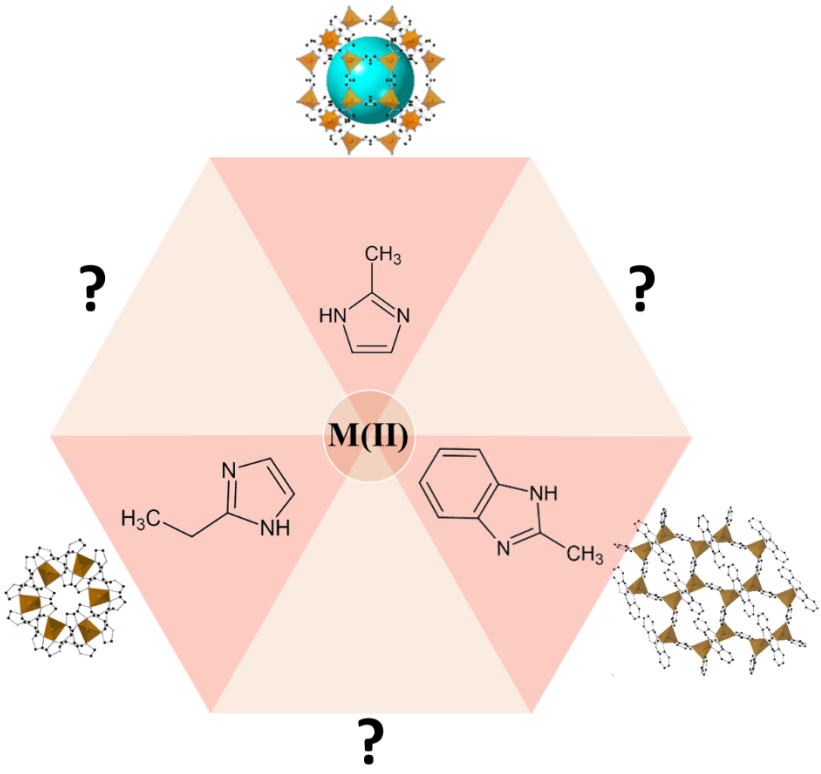

3.1 Introduction

One of the most important aspects in metal-organic frameworks (MOFs), from an application point of view, concerns their thermal and chemical stability.[1] As has been shown in Chapter 1, one successful approach for the formation of stable MOFs consists on the combination of soft Lewis acids with soft Lewis bases, being zeolitic imidazolate frameworks (ZIFs) an example of such approximation.[2] However, "chemical stability" is a very broad concept, and we will focus on the stability in water, whose presence in many of the industrial processes is ubiquitous.[3,4]

The problem of the stability of **MUV-3**, the Fe-based ZIF-8 analogue material, *i.e.* $Fe(2mim)_2$, is caused by the presence of water (Chapter 2, Figure 2.7). This also occurs in the Mn(II)[5] and Mg(II)[6] related materials. Their high sensibility to water is problematic for possible applications, such as bio-applications or gas separation,[7–9] where this novel MOF could potentially be very interesting. Thus, the improvement of its water stability can help with the development and applicability.

Initial studies of the stability of ZIFs were performed using $Zn(2mim)_2$, also known as ZIF-8, a porous crystalline material with SOD zeolite topology, which has been used in membrane applications, where water stability is an important characteristic.[10] Different authors reported its high stability in water based in the crystallinity retention after being exposed to boiling water, which was demonstrated with X-ray powder diffraction.[2,11] Nevertheless, these results have been questioned by other authors, who have shown a degradation of the material with time (Figure

3.1).[12,13] These different points of view onto the water stability in ZIFs have been rationalized analyzing the ratio between ZIF-8 vs water. Specifically, the formation of ZIF-8 in solution results from an equilibrium of different $Zn(2mim)_x$ clusters, whose formation depends strongly on the concentration of 2mimH and Zn^{2+}.[14] Thus, when ZIF-8 is exposed to water, it is partially dissolved and, depending on the ratio ZIF-8 vs water, the dissolution is a major phenomenon or only partial. For small quantities of water (in relation with ZIF-8), the equilibrium between the dissolution and formation of ZIF-8 is almost unaffected (large amounts of solid are present and only a minor amount is dissolved). This, combined with the high crystallinity of ZIF-8, prevents the observation of dissolution through X-ray powder diffraction. However, in this case it is more instructive to analyze the solution instead of the solid, with the aim of detecting the presence of ligand or Zn^{2+}, which could be achieved with NMR and ICP.

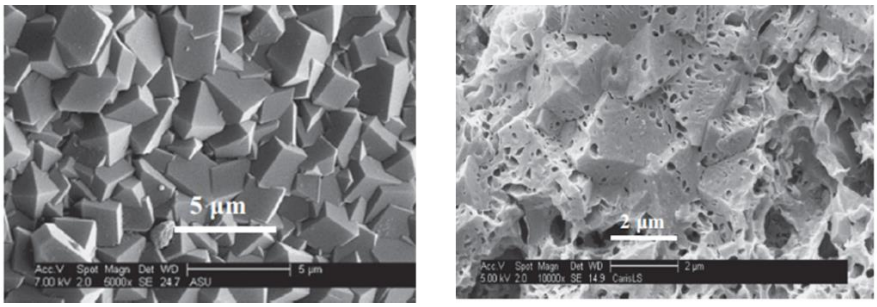

Figure 3.1 A ZIF-8 membrane (left) immersed in pure water 72 hours (right). Adapted from reference 13.

Despite these results for the water stability of ZIF-8, the hydrophobic nature of this material is also tested. In fact, water isotherms of ZIF-8 show its hydrophobic behavior.[15] In that work, led by F-X. Coudert, a type V

isotherm was observed for water adsorption on ZIF-8, characteristic of hydrophobic microporous materials.[16] The water sorption was also checked with other ZIFs of different hydrophilicity, such as ZIF-7 (sod-Zn(bim)$_2$), ZIF-65 (sod-Zn(2-NO$_2$im)$_2$), ZIF-65(rho-Zn(2-NO$_2$im)$_2$), ZIF-90 (sod-Zn(2-CHOim)$_2$), ZIF-Cl (sod-Zn(2-Clim)$_2$) and SALEM-2 (sod-Zn(im)$_2$). This study emphasized the importance of the functional group, topology, and geometry. ZIF-8 has micropores with narrow windows, and alkyl/aromatic framework (2mimH ligand). The methyl group located in the 2nd position can be substituted by –Cl, –NO$_2$, –H or –CHO groups. For similar groups, such as –H or –Cl, the hydrophobicity is analogous. The inclusion of polar groups, such as –NO$_2$ or –CHO to enhance the interaction of the framework with water molecules, has an important influence. In ZIF-65 the hydrophobicity is decreased, but still remains as a hydrophobic framework. However, for ZIF-90, the –CHO group induces a significant change in the interaction between the framework and water, transforming the framework to a hydrophilic system. Regarding the effects of the topology, the different distribution of windows and different sizes have an effect on the steps during the adsorption, owing to the different related sites and accessibility with a major affinity for water molecules. Finally, the geometry is also important, as can be seen upon comparison between ZIF-8 (2mim) and ZIF-7 (bim), both having SOD topology. It was expected a higher hydrophobicity for ZIF-7, but, on the contrary, ZIF-7 is hydrophilic. This is because of a small distortion of the ideal SOD topology, presenting two different distorted hexagonal windows. The crystal system for ZIF-8 is founded on a cubic system, meanwhile for ZIF-7 is a trigonal crystal system. To summarize, the functional groups have a huge importance in the

wettability of the material, albeit more parameters can play important roles and, in some cases, the incorporation of aromatic/alkyl groups is not enough to improve the hydrophobicity.

The post-synthetic methodology to exchange the organic linker is the most used technique to tune the properties owing to the similar coordination angle for all imidazole derivatives, thus helping the exchange while preserving the structure. This allows to achieve non-accessible ZIFs via direct synthesis. For instance, W. Yang and co-workers developed a strategy to improve the hydrothermal stability of ZIF-8 exchanging the 2-methylimidazole by 5,6-dimethylbenzimidazole, a larger organic ligand, through a shell-ligand-exchange-reaction (SLER).[17] Whereas in a previous work based in the solvent-assisted linker exchange (SALE), the ligand exchange is complete,[18] Yang's group exchange the linkers only partially, just from the surface, improving their hydrophobicity and retaining the crystal structure of ZIF-8.

Nonetheless, very recently it has been developed a novel linker exchange procedure based on a solvent-free approximation, namely the vapor phase linker exchange (VPLE).[19] In this work, Ameloot's group exposes ZIF-8 to vapors of an imidazole derivative which forms ZIFs with **sod** topology, such as ZIF-7 ($Zn(bim)_2$), ZIF-65 ($Zn(2\text{-}NO_2im)_2$), ZIF-90 ($Zn(2\text{-}CHOim)_2$), ZIF-71 ($Zn(4,5\text{-}Cl_2im)_2$) and SALEM-2 ($Zn(im)_2$). For ZIF-90, a near complete conversion is obtained (88 %), but for other ligands, the percentage is minor: 68 %, 44 % and 37% for $2\text{-}NO_2$imH, bimH and $4,5\text{-}Cl_2$imH, respectively. In the case of imH the **sod** structure is not achieved, in contrast to what is obtained by SALE[18] Nevertheless, this

approximation is a great alternative to avoid solvents and opens the door to the use of this methodology in pre-formed thin films.

In this Chapter, owing to the incompatibility of **MUV-3**, the iron analogue of ZIF-8 presented in Chapter 2, with post-synthetic methodologies using common solvents, a direct synthesis approach to enhance its stability. Will be discussed to improve the "defense" of **MUV-3** against water**,** an increase of the alkyl/aromatic rests of the organic part has been investigated in order to favor the steric hindrance, thus preventing the entrance of water molecules.

One of the most common ways to enhance water stability behavior is the inclusion of fluorinated groups or alkyl chains in a metal-organic framework.[20] However, the inclusion of these functional groups maintaining the desired topology is a huge challenge, as their incorporation is typically accompanied by a change in the topology. An alternative approach consists on the use of similar ligands (from a molecular structure point of view), but employing slightly bulkier substituents (ethyl group instead of methyl group) to difficult the entrance of water molecules. In addition, to prevent crystal distortion as observed in ZIF-7, a mixed-ligand strategy can circumvent these issues resulting in a combination of retaining the desired topology and the introduction of a bulkier ligand.

Post-synthetic methodologies such as SALE or SLER involve the use of different solvent, which is incompatible with **MUV-3** as it results in a mixture of iron oxides and amorphous materials. Consequently, another strategy was developed based on a pre-synthetic process. Taking as a model the **MUV-3**, bulkier organic ligands will be chosen, although most similar

possible to 2mimH, to construct mixed-ligand materials, preserving the SOD topology with the least possible distortions (Figure 3.2).

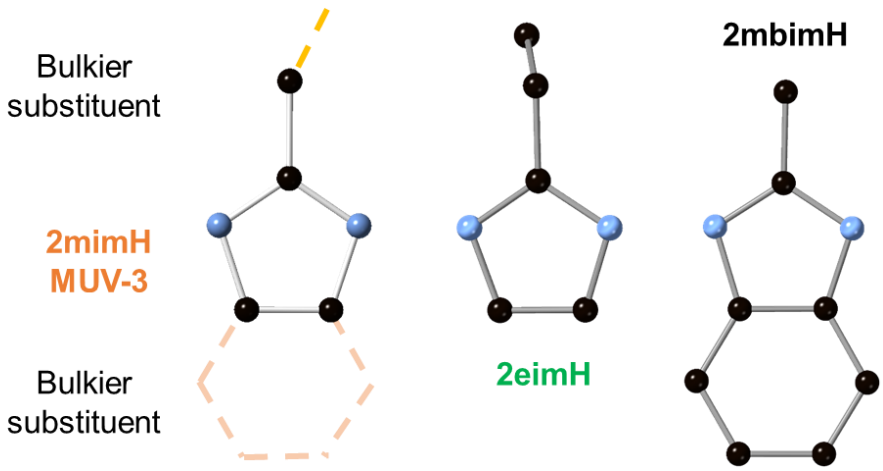

Figure 3.2 MUV-3 is constructed by 2mimH. To use bulkier ligands 2eimH and 2mbimH were selected owing to their bigger organic rests at 2nd and 4th-5th positions.

The incorporation of 2-ethylimidazole (2eimH) and 2-methylbenzimidazole (2mbimH) in the SOD topology is a challenge, as the crystal structures based solely in 2eimH or 2mbimH have different topologies. Specifically, three different crystal structures can be obtained with the 2eimH ligand in combination with Co(II) and Zn(II) as metallic nodes, namely RHO-M(2eim)$_2$, ANA-M(2eim)$_2$ and ***qtz***-M(2eim)$_2$, also known as MAF-6, MAF-5 and MAF-32, respectively (MAF = metal-azolates frameworks).[21,22] The RHO and ANA polymorphs are porous materials with zeolite topologies. However, the ***qtz*** polymorph is a dense coordination polymer (Figure 3.3). When using Fe(II) instead of Co(II) or

Zn(II), the dense ***qtz*** polymorph can be obtained, as shown in Chapter 2, denoted **MUV-6**.

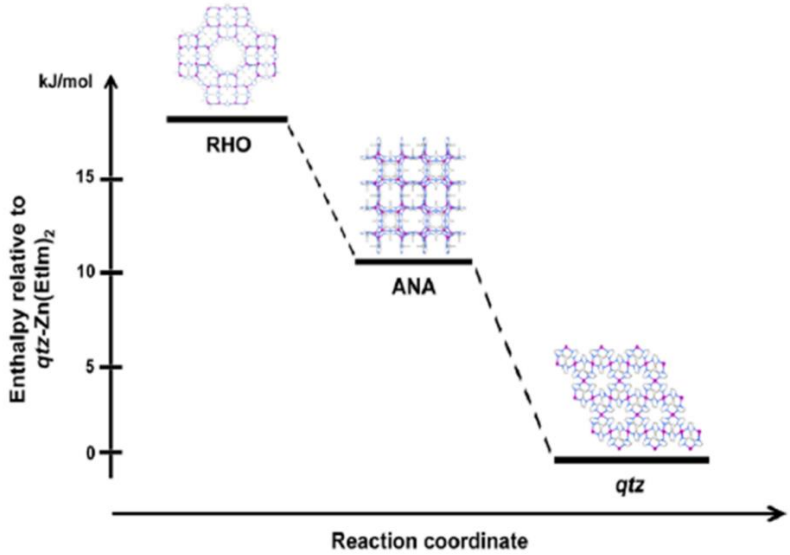

Figure 3.3 The achievable polymorph of $Zn(2eim)_2$ and their respective energy enthalpies. Adapted from reference 21.

Interestingly, there are no reports of any material with exclusively 2mbimH as a ligand in a combination with Co(II) or Zn(II), most probably owing to its bulky nature. However, two mixed-ligand structures were published by the groups of S. Qiu and O. Yaghi using 2mbimH. The first has a formula $Zn_4(2mbim)_3(bim)_5$, a mixed compound with GIS topology called JUC-160 (Jilin University China) (Figure 3.4a).[23] The bulky groups make it stable in different solvents such as benzene and apparently, water (although this was only checked by X-ray powder diffraction). Also, owing to the bulky groups, JUC-160 does not allow N_2 gas molecules entering in the pores, while the smaller CO_2 molecules can be physisorbed, which

allows the calculation of a BET value of around 210 m^2/g. The second material results from a combination of 5-methylbenzimidazole and 2mbimH with Zn(II), of formula $Zn(2mbim)_{0.28}(2mbim)_{1.72}$, published by O. Yaghi and co-workers.[24] This material does not possess a zeolite topology, but rather it has a novel topology, undescribed before for porous materials, and denoted **ykh** (Figure 3.4b). Similar to what has been observed with **MUV-6**, it is possible to construct an extended CP based in Fe(II) centers and 2mbimH, described in Chapter 2, which is a dense polymorph with ***dia*** topology (**MUV-7**).

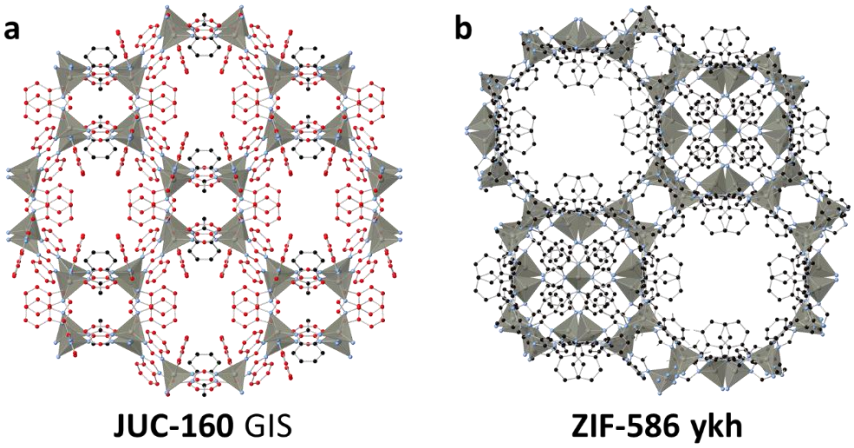

Figure 3.4 a) Crystal structure of **JUC-160** with zeolite topology GIS. b) Crystal structure of **ZIF-586** with **ykh** topology.

3.2 Results and discussion

Synthesis of mixed-ligands sod-Fe(II) structures. Three different mixed-ligand compounds have been prepared combining two ligands with ferrocene at 150°C, using a 1:1 mixture of ligands: 2mimH and 2mbimH results in **MUV-3-mimb**, 2eimH and 2mbimH results in **MUV-3-eimb**,

and 2mimH and 2eimH results in mixture of **MUV-6** and an unknown material. In the case of **MUV-3-mimb** and **MUV-3-eimb** large single-crystals have been isolated, suitable to single-crystal diffraction. Structural analysis of **MUV-3-eimb** reveals that both compounds are isoreticular with **MUV-3**. They present SOD topology and similar crystal cell parameters, with *a* = 17.2998(2) Å and Fe—N distance of 2.043(1) Å (Figure 3.5), slightly bigger than **MUV-3** (*a* = 17.1656(2) Å). The 2mbim ligands have an occupancy of 0.3, what suggest a ligand ratio of 70:30 between 2mim/2eim: 2mbim.

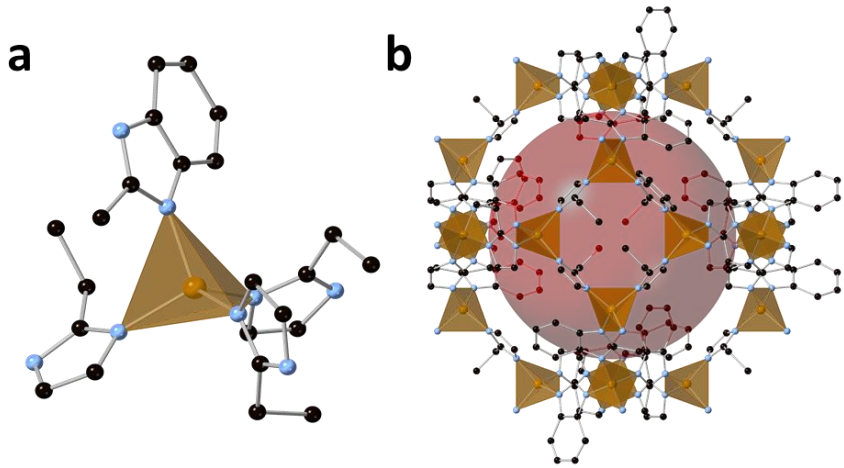

Figure 3.5 a) Coordination environment of the Fe(II) atoms in **MUV-3-eimb**. b) Crystal structure of **MUV-3-eimb** showing SOD topology.

Table 3.1 Fe-N bonds distances in the different Fe(II)-azolates-based materials.

	MUV-3	**MUV-3-eimb**	**MUV-6**	**MUV-7**
Fe–N	2.0342 Å	2.0426 Å	2.0554–2.1787 Å	2.0404–2.0479 Å

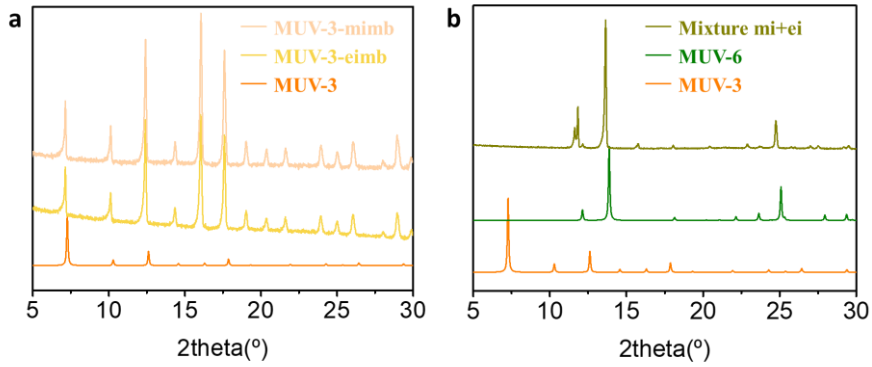

Figure 3.6 a) X-ray powder diffractograms of **MUV-3-mimb** (peach color) and **MUV-3-eimb** (yellow color) in comparison to **MUV-3** (orange color), showing the isoreticularity between them. b) X-ray powder diffractograms of 2mimH/2eimH mixture and the theoretical of **MUV-6** and **MUV-3**.

The phase purity and the presence of only one crystal structure were determined by X-ray powder diffraction (XRPD). This technique confirms the homogeneity of the crystals obtained during the synthesis and allows to determine possible segregation of phases, a common scenario when using mixtures of ligands. **MUV-3-eimb** and **MUV-3-mimb** present XRPD patterns which match perfectly with the **MUV-3** diffractogram (Figure 3.6a). However, the mixture 2mimH/2eimH gives two different crystalline materials, **MUV-6** compound and an unidentified phase (Figure 3.6b).

The ratio between the ligands was confirmed by ^{1}H NMR spectroscopy. For this purpose, the samples of **MUV-3-eimb** and **MUV-3-mimb** were digested in D_2O and deuterated trifluoroacetic acid for the comparison with the pure organic spectra (Figure 3.7). The synthetic used

ratio in the synthesis was 50% for each ligand. However, the experimental ratio is around 65% for the 2eimH and 2mimH versus 2mbimH (Figure 3.8). This percentage can be increased to 70-75% (maximum) of 2eimH and 2mimH by increasing the ratio in the synthesis. Nevertheless, the ratio cannot decrease under 65% for 2eimH and 2mimH using lower synthetic ratios of 2eimH and 2mimH. In these cases, the quantity of crystals decreases and presents the same ligand ratio than the 50% ligand synthetic ratio (around 65%). The hypothesis and explanation can be the necessary ratio for construct the mixed-ligand SOD material is around 65% for 2eimH-2mimH, and when this ratio is decreased, the 2eimH-2mimH acts as the limiting reagent.

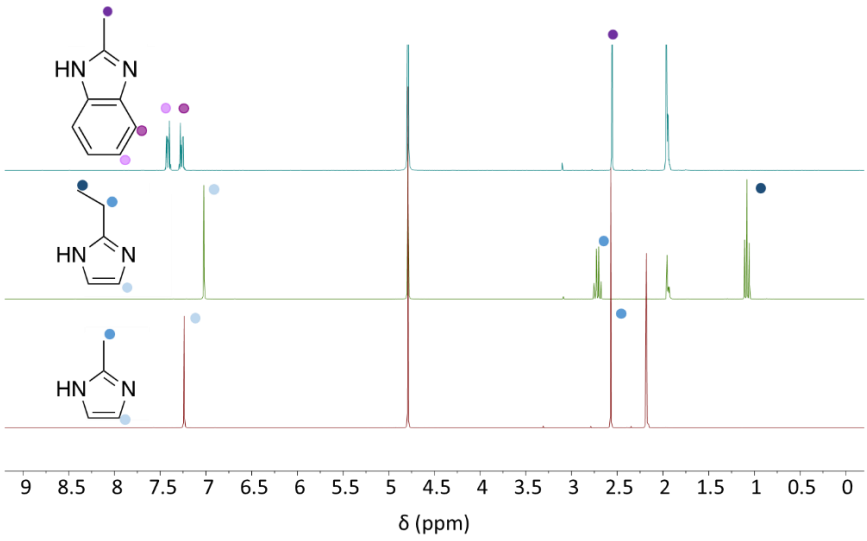

Figure 3.7 NMR spectra of the pure organic ligands used to construct the mixed-ligand **MUV-3** family.

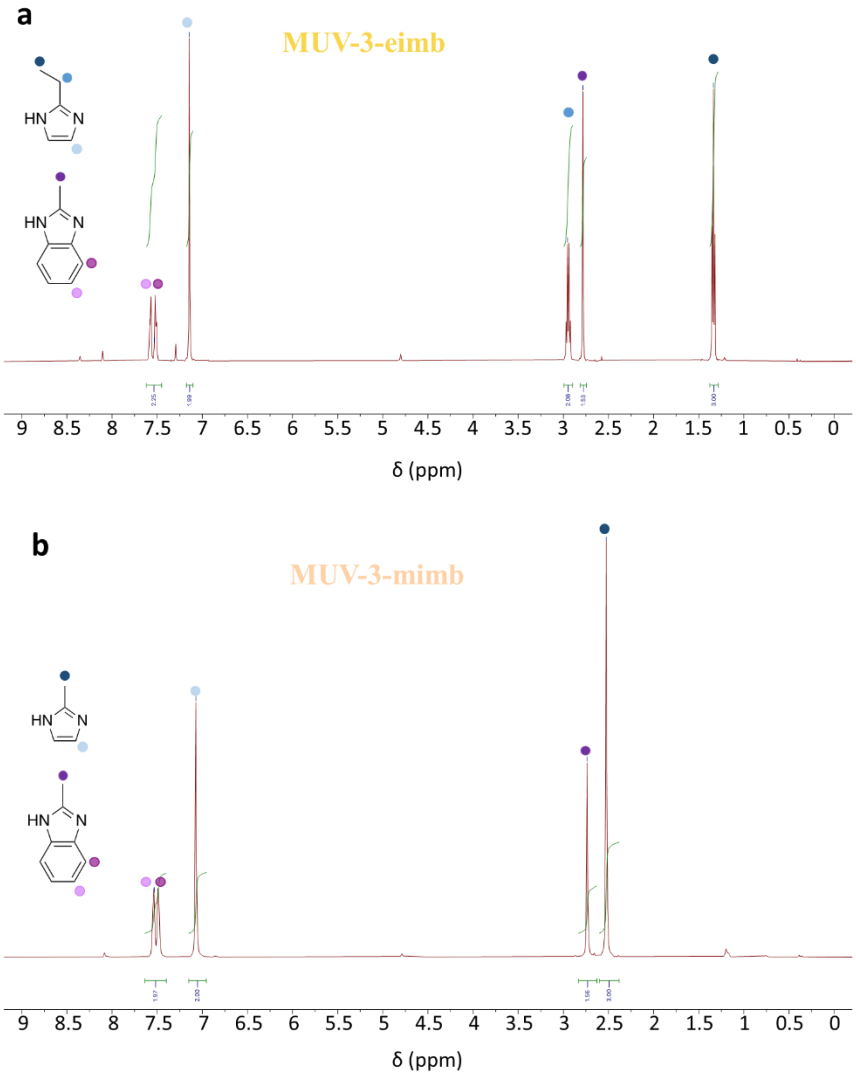

Figure 3.8 NMR spectra of **MUV-3-eimb** and **MUV-3-mimb**. Clearly identified the H atoms from each ligand. Colored circles help to localized its corresponding chemical shifts of the protons.

The confirmed mixed-ligand structures present higher thermal stability in comparison to **MUV-3**. The pure 2mim SOD compound starts to decompose around 200°C, and the related mixed-ligand isoreticular materials begin to decompose around 350°C. Thus, the incorporation of 2mbimH in the **MUV-3** structure stabilizes thermally the compound. This improvement of the thermal stability is similar to the Fe(II) related dense materials, such as **MUV-6** and **MUV-7** (Figure 3.9).

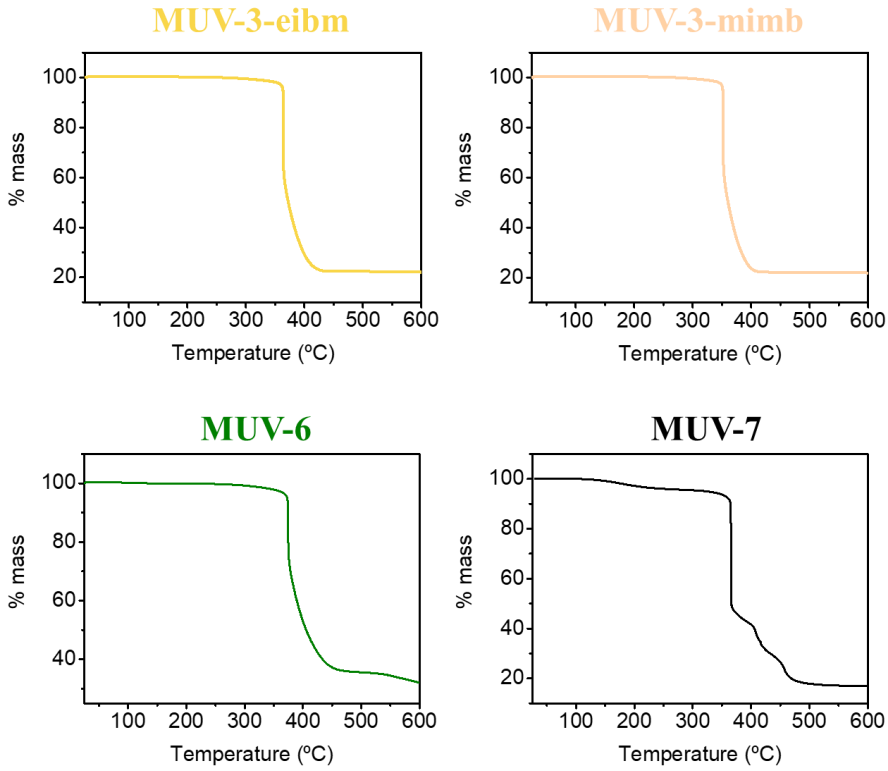

Figure 3.9 Thermogravimetric analysis of **MUV-6**, **MUV-7, MUV-3-mimb** and **MUV-3-eimb** in nitrogen gas at a heating rate of 20 ºC min^{-1}.

The ligand composition and its chemical structure are slightly different for the **MUV-3** mixed-ligand compounds. However, the Fe···Fe pathway is very similar, with a similar magnetic exchange between the metallic nodes in **MUV-3-eimb** and **MUV-3-mimb**. The measurements of the magnetic properties indicate the presence of strong antiferromagnetic metal-metal interactions between the Fe(II), as also observed in **MUV-3** (Figure 3.10). There is an increase in χ upon cooling down to achieve maximum value at 17-15 K, indicating antiferromagnetic ordering. However, the Neél temperature for the mixed-ligand compounds has a lower value than the **MUV-3** (23 K) and the dense **MUV-6** (34 K) and **MUV-7** (39 K) (Table 3.2). Despite the differences in the crystal structure, the tetrahedral environment of the Fe(II) in **MUV-6** and **MUV-7** is similar to the **MUV-3** and the mixed-ligand family. The presence of a single peak in the magnetic measurements indicates a single crystalline phase, discarding the combination of two different phases or domains.* This fact is also in accordance with the XRPD studies. In addition, the ordering temperature of the mixed-ligand materials is closer to **MUV-3**, the isoreticular compound, although different enough to appreciate a distortion on the structure and magnetic properties owing to the combination of ligands.

*If the composition of the **MUV-3-eimb** and **MUV-3-mimb** were based on the combination of only one ligand domains, two different signals in the magnetic measurements should be appreciated.

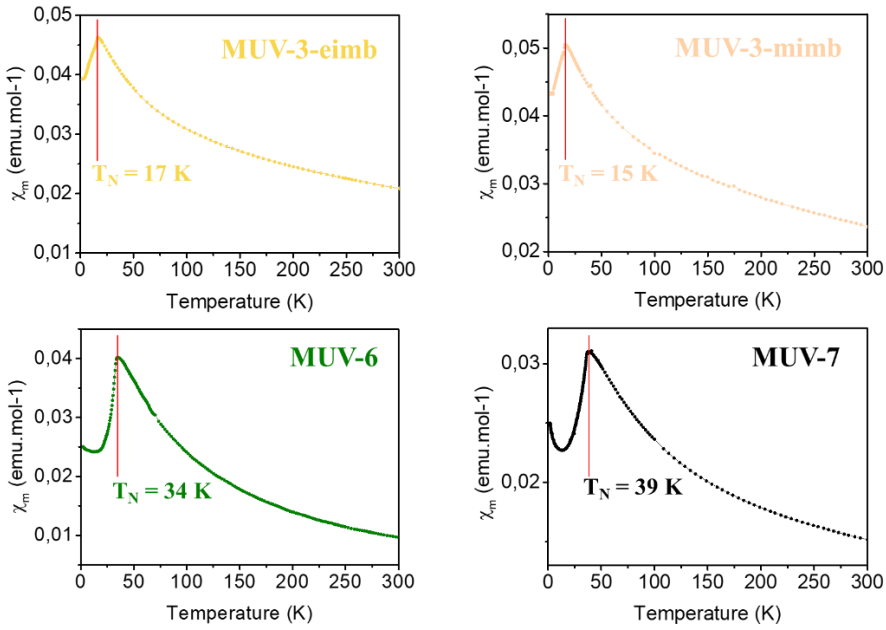

Figure 3.10 Magnetic susceptibility plot showing the antiferromagnetic interactions and antiferromagnetic ordering at low temperature between Fe(II) centers in **MUV-3-eimb, MUV-3-mimb**, **MUV-6** and **MUV-7.**

Table 3.2 T_N for the **MUV-3** family and Fe(II) related azolates.

	MUV-3	**MUV-6**	**MUV-7**	**MUV-3-eimb**	**MUV-3-mimb**
T_N	23 K	34 K	39 K	17 K	15 K

These **MUV-3-mimb** and **MUV-3-eimb** compounds also present different crystal morphology in front of **MUV-3**. The study of the shape of the crystals by scanning electron microscopy (SEM) shows truncated rhombohedral particles. However, the surface of these crystals presents holes and defects with very defined geometries (Figure 3.11). These holes or defects are observed in defective MOFs, especially in mixed-ligand

compounds. This class of materials favor the appearance of these imperfections.[25]

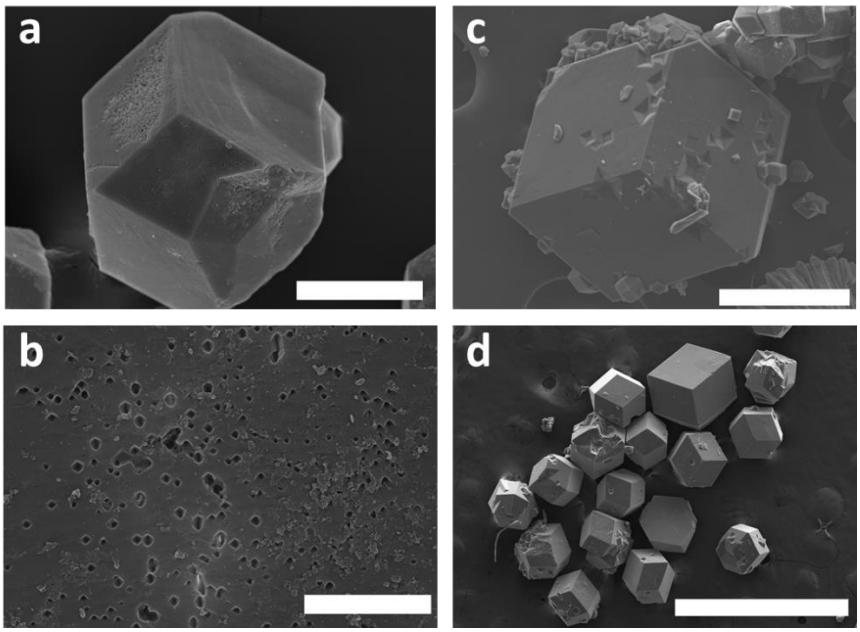

Figure 3.11 a) A single crystal of **MUV-3-mimb** with rhombohedral morphology and holes at the surface. Scale bar 50 μm b) Zoom of the surface of the crystal (a), with rhombohedral holes. Scale bar 5 μm c) A single-crystal of **MUV-3-eimb** with geometric holes. Scale bar 200 μm. d) A representative sample of **MUV-3-eimb** crystals. Scale bar 1 mm.

Furthermore, it is possible to achieve novel materials using the solvent-free approach through Fe(II) chemistry (Figure 3.12). The strategy of mixed-linker synthesis results useful to incorporate bulkier ligands such as 2-methylbenzimidazole and 2-ethylimidazolate. However, the improvement of stability at open atmosphere is only slightly enhanced,

from couple of hours[26] for **MUV-3** to 2 days for the mixed-ligand materials (Figure 3.13).

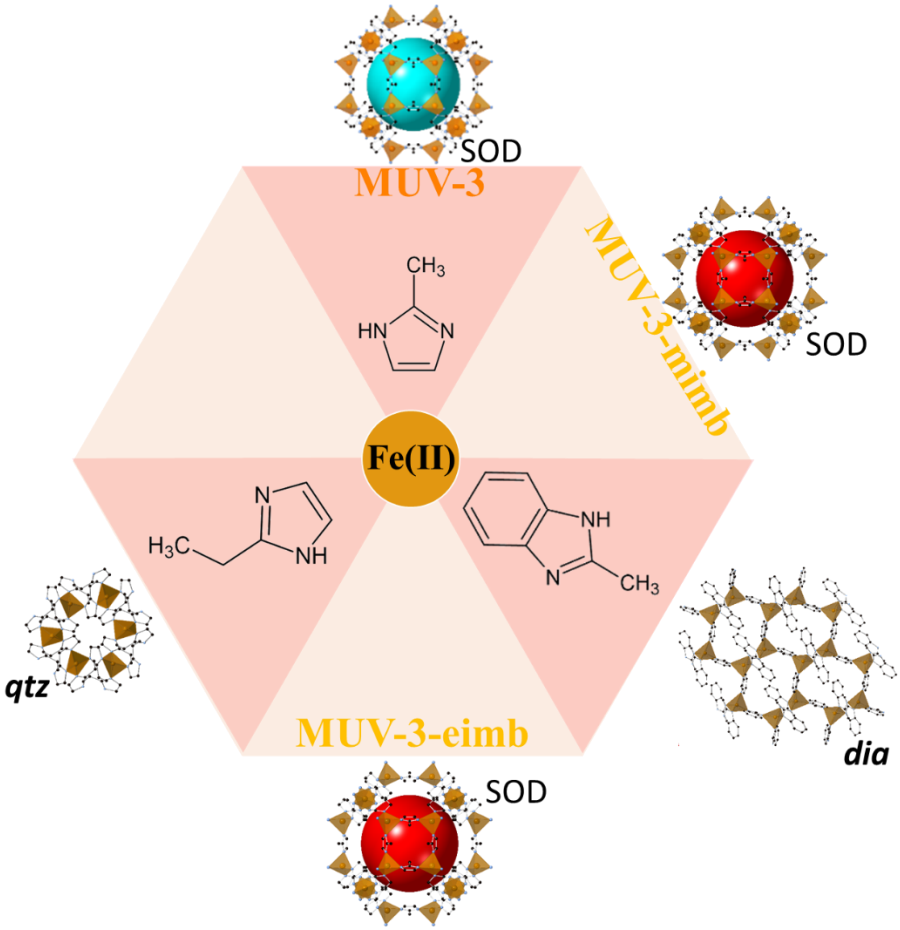

Figure 3.12 Scheme of the different achievable crystal structures combining Fe(II) and the three imidazoles: 2mimH, 2eimH and 2mbimH.

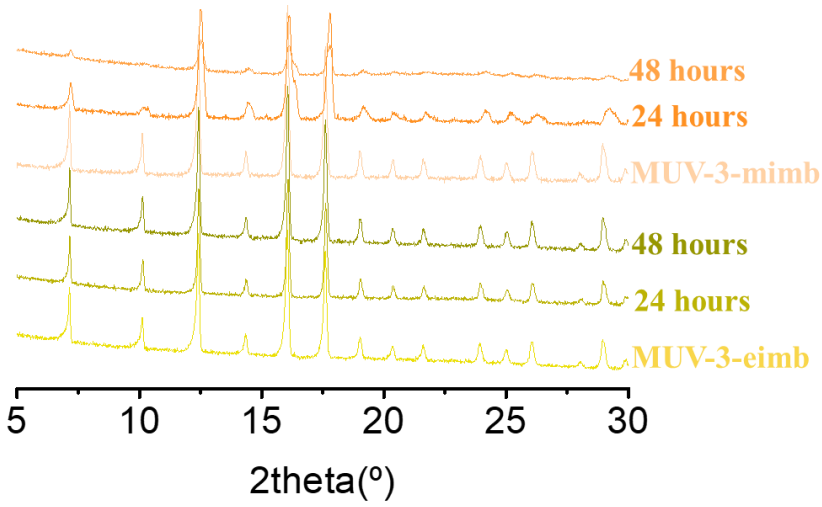

Figure 3.13 X-ray powder diffraction after 24 and 48 hours of exposition at air atmosphere.

Expanding the mixed-ligand strategy. This pre-synthetic strategy can be extended to Zn(II) and Co(II), which will serve to study the impact of the incorporation of these ligands in classical more stable ZIFs.

The water stability of ZIF-8 is an important point, as has been discussed during the introduction to this Chapter. For this reason, it can be interesting to transport the SOD mixed-ligand synthesis to Zn(II) and Co(II), to check the influence in their chemical stability and properties. In addition, the solvent-free methodology has been demonstrated as a useful technique in Chapter 2, synthesizing also Zn(II) and Co(II) materials like ZIF-8 and ZIF-67.

Therefore, the same synthetic strategy was used to obtain the Zn(II) and Co(II) counterparts of **MUV-3-mimb** and **MUV-3-eimb.** Cobaltocene and ZnO were the metal sources for the synthesis, and purple/white powders were obtained for the Co(II)/Zn(II) derivatives. Phase purity was checked by X-ray powder diffraction, showing high crystallinity and a single phase as in the Fe(II) compounds (Figure 3.14). However, the crystal sizes of the Co(II) and Zn(II) analogues were not suitable for single-crystal studies (as also occurred with ZIF-8 and ZIF-67 obtained by solvent-free methodologies).

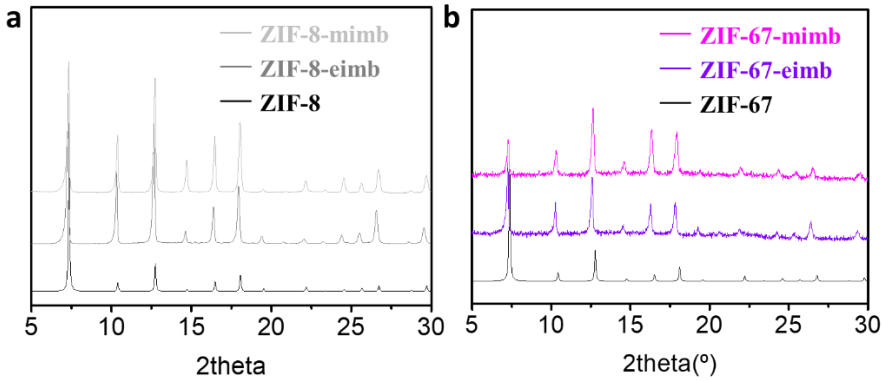

Figure 3.14 a) X-ray powder diffractograms of **ZIF-8-mimb** (clear gray) and **ZIF-8-eimb** (dark gray) in comparison of **ZIF-8** (black color), showing the isoreticularity between them. b) X-ray powder diffractograms of **ZIF-67-mimb** (magenta) and **ZIF-67-eimb** (violet) in comparison of **ZIF-8** (black), showing the isoreticularity between them.

The possible crystal structures that can be obtained with Zn(II) or Co(II) in combination with 2eimH have been discussed previously.

However, the possibilities of the solvent-free synthesis for that combination, and the results using 2mbimH were not explored. Thus, it can be interesting to know the accessible phases through solvent-free synthesis with those linkers to understand better the phase distributions. This can also serve to compare with Fe(II) compounds, owing to the major possible phases with 2eimH in Zn(II) and Co(II) compounds.

For the Zn(II) and 2mbimH combination, it was found an unknown crystal structure, unidentified at the moment, different to the known SOD and ***dia*** topologies. Using the 2eimH linker, the expected ***qtz*** structure matches perfectly with the synthesized material (Figure 3.15). In the case of Co(II), in the first case with 2mbimH ligand, the obtained material results in an amorphous compound. However, for the 2eimH, the resulting compound is a mixture of two very known crystals structures, MAF-5 and MAF-6, two porous coordination polymers with ANA and RHO zeolite topologies (Figure 3.15). If the synthetic parameters are changed, different polymorphs can be obtained, such as the ***dia*** topology with Co(II) or the MAF-6 with Zn(II).

After checking the different phases achievable by solvent-free synthesis, and discarding the possibility of the obtaining SOD topology by pure structures based in 2eimH or 2mbimH, the ligand composition of the ligand-mixed materials was checked by ^{1}H NMR to see the percentage in the structure. For the eimb compound, the ratio between ligands is similar to the Fe(II) compound, around 60%-75% for the 2eim linker, depending

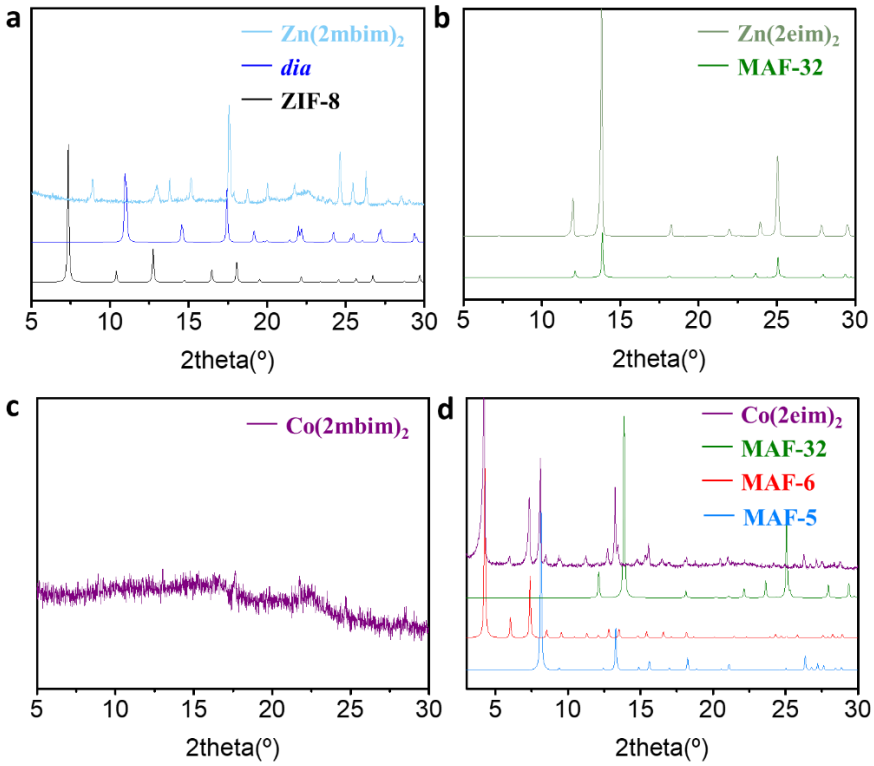

Figure 3.15 a) X-ray powder diffraction of $Zn(2mbim)_2$, showing an unknown structure. b) X-ray powder diffraction of $Zn(2eim)_2$ presenting the ***qtz*** topology. c) X-ray powder diffraction of $Co(2mbim)_2$ showing an amorphous material. d) X-ray powder diffraction of $Co(2eim)_2$, is a mixture of two very known structures, MAF-5 (ANA) and MAF-6 (RHO).

on the synthesis ratio. However, for the mimb mixture, there are some differences between these compounds and the Fe(II) materials. The ratio in the Zn(II) and Co(II) compounds with 2mim can oscillate between 50% and 80%, preserving the phase purity, using different linker ratio in the synthesis (Figures 3.16-3.17). Unfortunately, this higher range in the linker

ratio for ZIF-8 and ZIF-67 cannot be explained, and more experiments are required. Nonetheless, the different framework flexibility between MUV-3, ZIF-8 and ZIF-67 may play a role in the accommodation of the 2mbim bulky ligand inside the structure.

The differences in the thermal stability, checked by thermogravimetric analysis, are only present in the Zn(II) derivatives. Figure 3.18 shows 8% and 20 % mass loss for **ZIF-8-eimb** and **ZIF-8-mimb**, respectively. This may be due to the presence of solvent and an easier removal, owing to a different framework breathing behavior between Zn(II) and Co(II) networks. Between the Zn(II) derivatives. The difference in the loss mass observed in the two Zn(II) derivatives can be attributed to the more accessible pores thanks to the less bulky ligand, 2mim. For Co(II), it is also possible to appreciate a mass loss in the **ZIF-67-mimb** (around 6 %). The Zn(II) derivatives are stable up to 400 °C, while Co(II) derivatives are stable up to 340 °C. These results are comparable to those observed in Fe(II) frameworks. However, these mixed-ligand compounds are a little bit less stable than the isoreticular compounds based in pure 2mim (ZIF-8 and ZIF-67).

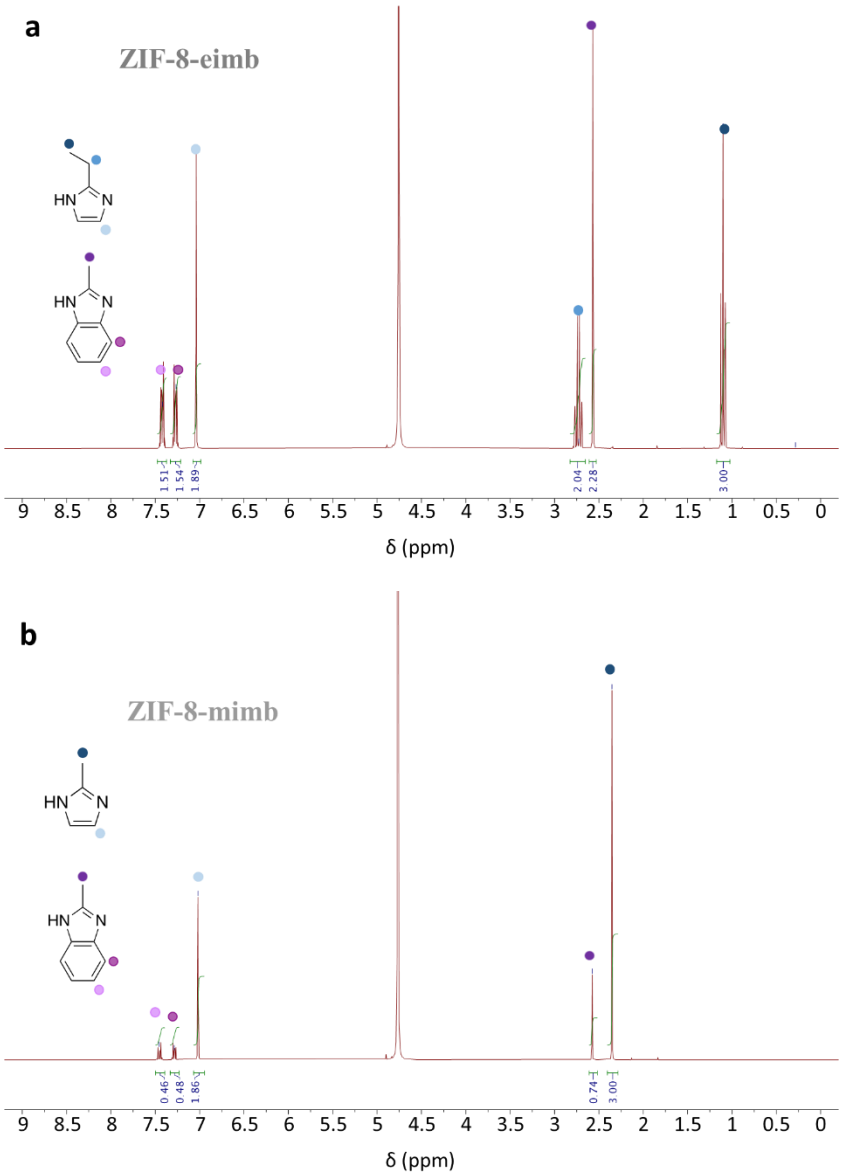

Figure 3.16 NMR spectra of **ZIF-8-eimb** and **ZIF-8-mimb.**

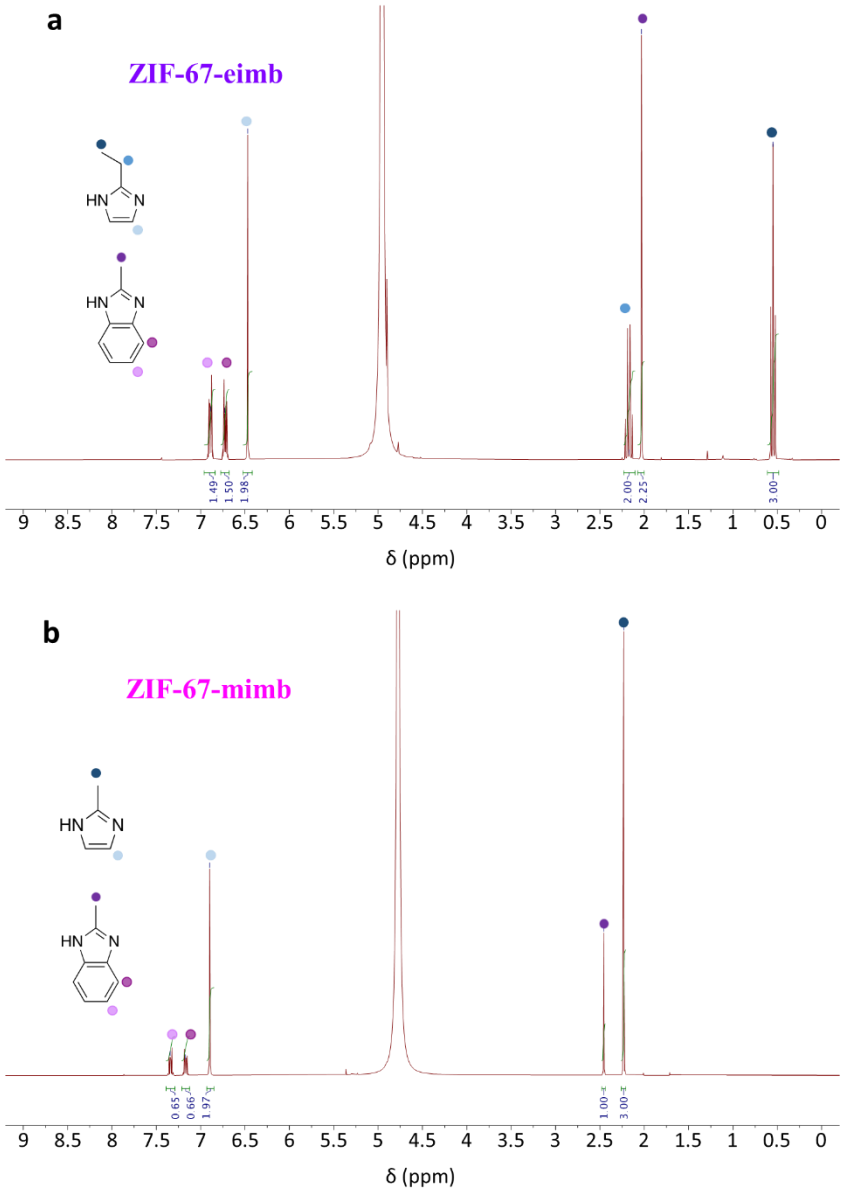

Figure 3.17 NMR spectra of **ZIF-67-eimb** and **ZIF-67-mimb.**

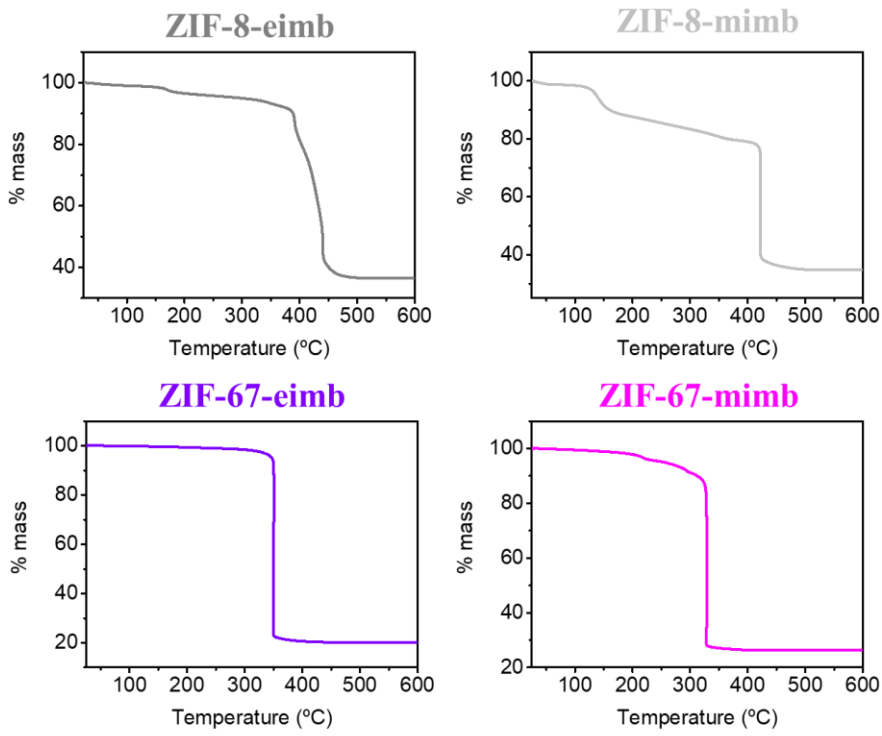

Figure 3.18 Thermogravimetric analysis of the mixed-ligand derivatives of Zn(II) and Co(II).

The Co(II) compounds can present magnetic exchange through the same pathway, Co-im-Co, such as the Fe(II) networks. However, Zn(II) is a d^{10} cation in a tetrahedral environment, i.e. with no unpaired electrons, and therefore cannot present magnetic ordering. The magnetic behavior of **ZIF-67-eimb** and **ZIF-67-mimb** is very similar to the Fe(II) compounds discussed previously (Figure 3.19). There exist antiferromagnetic interactions between Co(II) centers, and at low temperatures, around 16–18 K, they are ordered in the antiferromagnetic phase. This antiferromagnetic behavior is typical in Co(II) azolates.[27,28] The only

presence of one magnetic signal corroborates the presence of only one phase per compound.

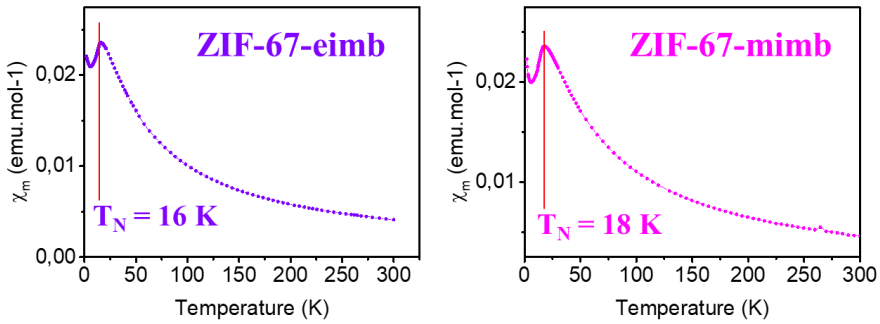

Figure 3.19 Magnetic susceptibility plot showing the antiferromagnetic interactions between Co(II) centers and antiferromagnetic ordering at low temperature in the **ZIF-67 eimb** and **ZIF-67-mimb** materials.

The crystal size and quality of these isoreticular materials in comparison to the Fe(II) frameworks are lower. The scanning electron microscopy images show the smaller sizes of the crystals and less defined morphologies for the four compounds (Figure 3.20).

Water stability. One of the objectives was to check the impact of the mixed-ligand structure in the chemical stability owing to the inclusion of the bulkier linkers. For that, a water stability experiment was designed similar to the reported and discussed during the introduction. 12 mg of the four obtained materials were introduced in 20 ml (0.06 weight % of ZIF) of water under continuous stirring for 48 hours. To check the instability of ZIF-8 under the same conditions, some samples of ZIF-8 and ZIF-67 were prepared by solvent-free conditions. Figure 3.21 shows the appearance of

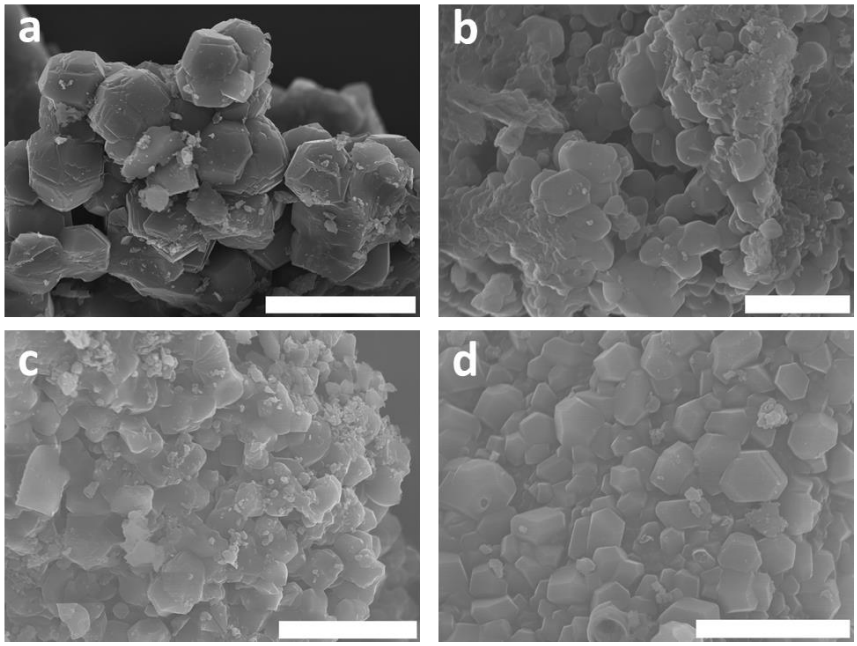

Figure 3.20 a) Crystals of **ZIF-8-eimb** with defined morphology. Scale bar 20 μm. b) Crystals of **ZIF-8-mimb** with defined morphology, similar to ZIF-8. Scale bar 5 μm. c) Crystals of **ZIF-67-eimb**. Scale bar 20 μm. d) Crystals of **ZIF-67-eimb** with similar morphology to ZIF-67. Scale bar 10 μm.

another unknown phase in the ZIF-8 diffractogram, such as the mentioned work in the introduction.[12] Some works identify this phase as $Zn(OH)(NO_3)(H_2O)$.[29] However, in this experiment there are no NO_3^- ions present, due to the solvent-free nature of the synthesis, using ZnO as a metallic source. ZIF-67 seems to retain the crystal structure without the appearance of any additional phase. The four mixed-ligand structures present the same diffractogram as that observed before the water treatment.

The Zn(II) compounds seem to be more stable than the ZIF-8, and no extra peak is observed.

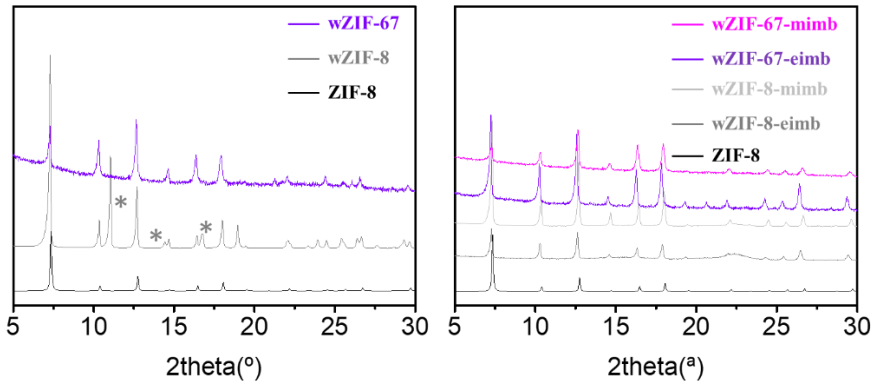

Figure 3.21 a) X-ray powder diffraction of ZIF-8 and ZIF-67 after 48 hours in water solution. The asterisk indicates the extra peaks of the unknown phase. b) X-ray powder diffraction of **ZIF-67-mimb, ZIF-67-eimb, ZIF-8-mimb** and **ZIF-8-eimb** after 48 hours in water solution.

However, X-ray diffraction does not reveal possible etching of the ligands owing to the instability in water. Still, this can be detected by H^1 NMR spectroscopy. Thus, upon 48-hours immersion in D_2O, under continuous stirring, water samples were analyzed by H^1 NMR spectroscopy (Figures 3.22–3.23). The comparison between ZIF-8/ZIF-67 and the mixed ligand ZIFs shows less etching of the material for the same time immersed in water. For a quantitative comparison, known volumes of the D_2O (from the ZIFs water immersed) were analyzed with an internal standard, $(CH_3)_4NCl$, with known concentration, as recent reported works.[30] The characteristics peaks from the different methyl groups were identify and the areas were normalized to quantify the linker ratios and concentration in the

original water stability studies. For ZIF-8 and ZIF-67 were founded a 48 % and 21 % of 2mimH in the D_2O, respective to the maximum possible molar ratio. For ZIF-eimb compounds, very similar percentages were found, 46 % for Zn(II) compound and 27 % for the Co(II) compound. However, for the ZIF-mimb series, lower percentages of ligands were found in the D_2O, 38 % for the Zn(II) material and 16% for the Co(II) material. Despite the major hydrophobicity and steric hindrance, the eimb mixtures present higher percentages of etching than the mimb series.

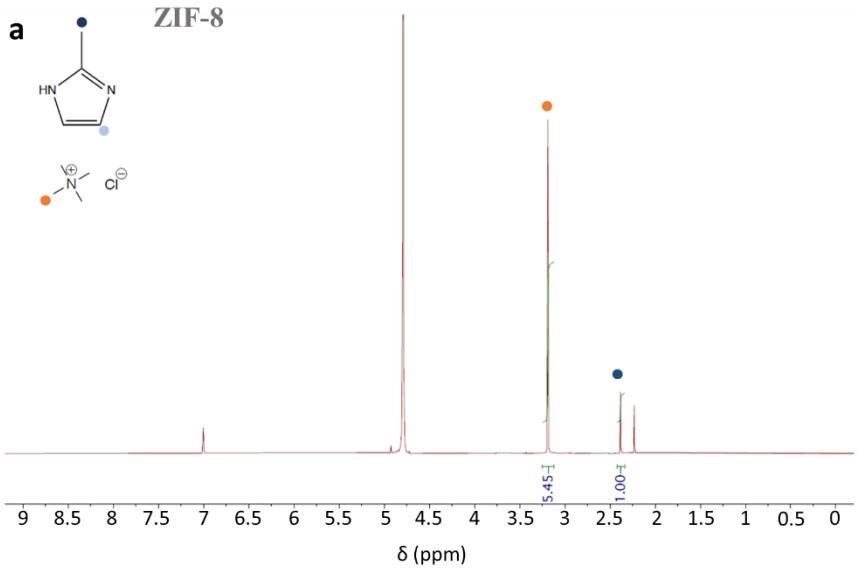

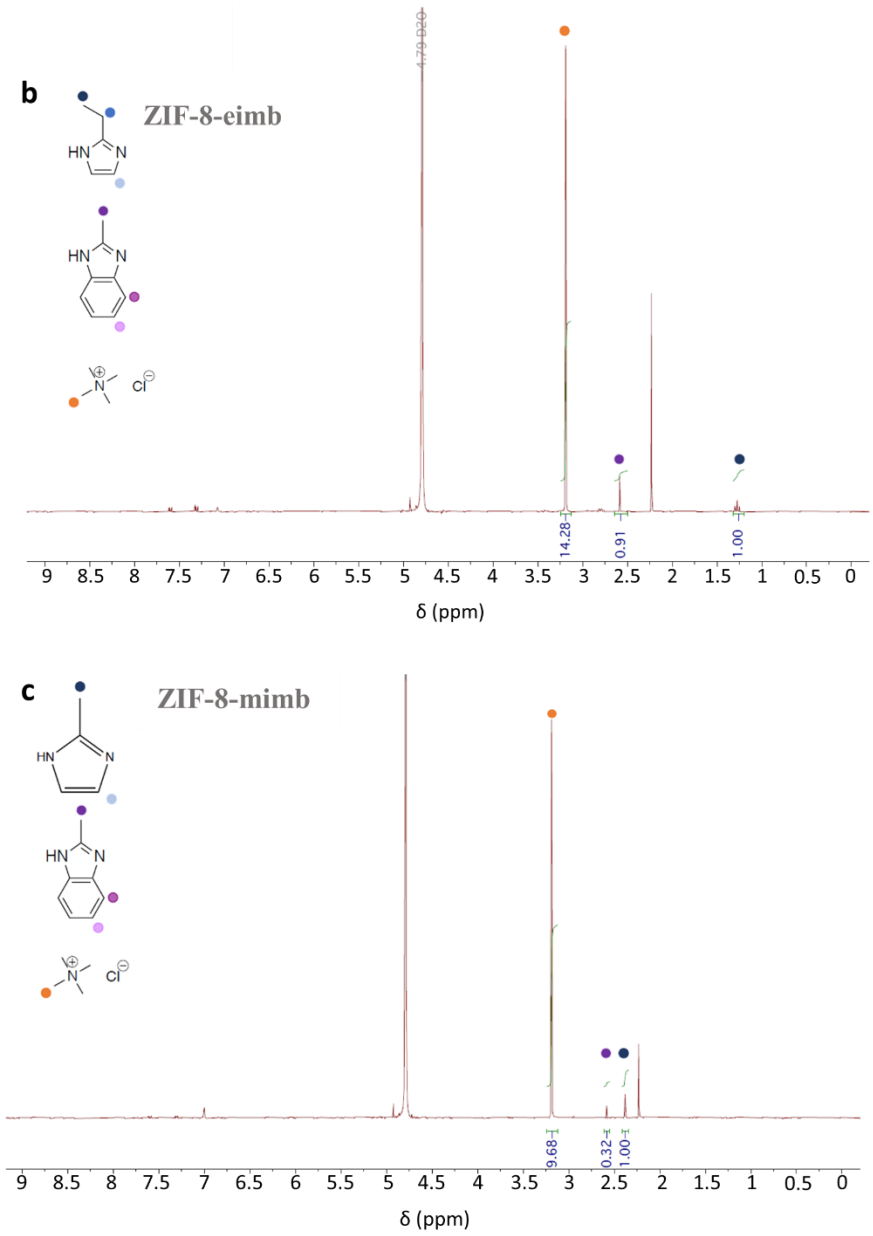

Figure 3.22 NMR spectra of **ZIF-8** (a), **ZIF-8-eimb** (b) and **ZIF-8-mimb** (c).

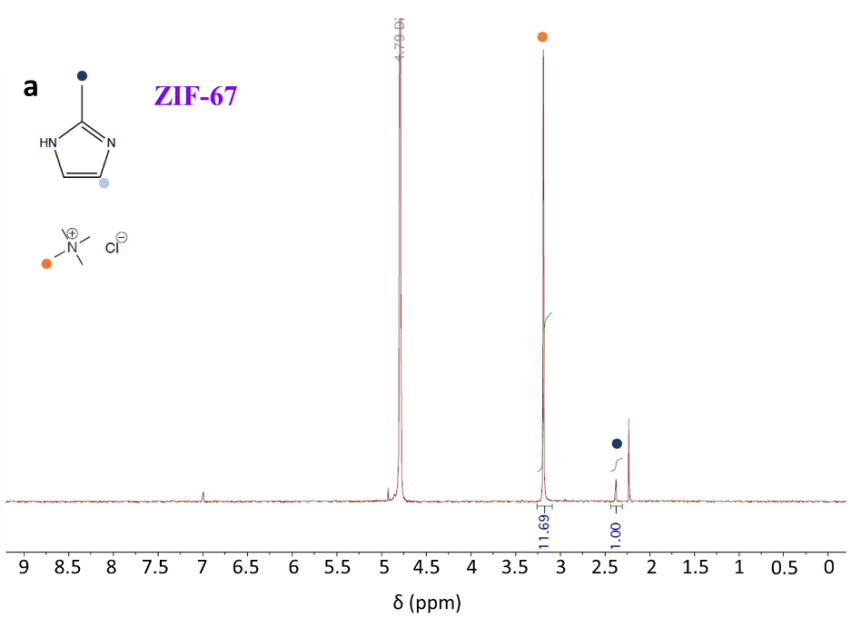
a
ZIF-67
HN
N
Cl
4.79
11.69
1.00
9 8.5 8 7.5 7 6.5 6 5.5 5 4.5 4 3.5 3 2.5 2 1.5 1 0.5 0
δ (ppm)

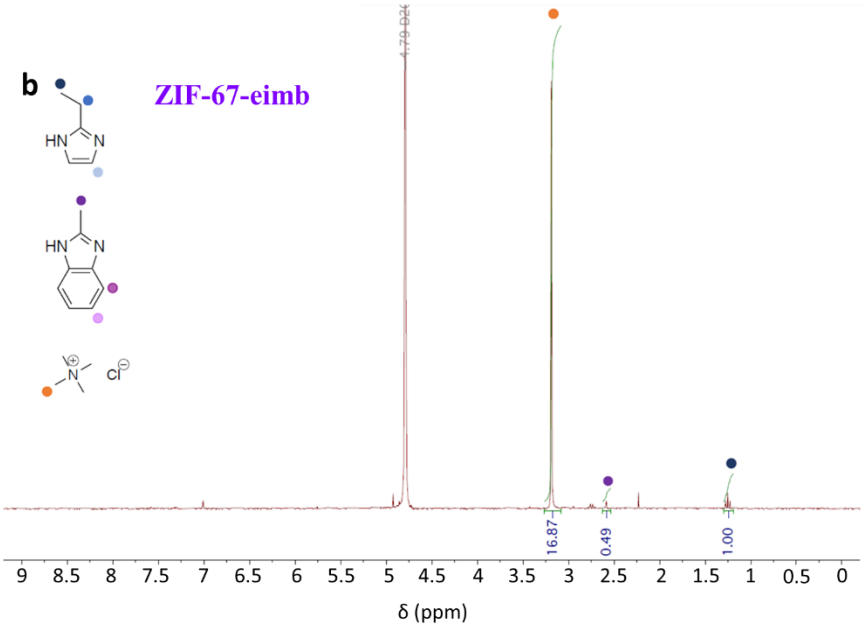
b
ZIF-67-eimb
HN
N
Cl
4.79
16.87
0.49
1.00
9 8.5 8 7.5 7 6.5 6 5.5 5 4.5 4 3.5 3 2.5 2 1.5 1 0.5 0
δ (ppm)

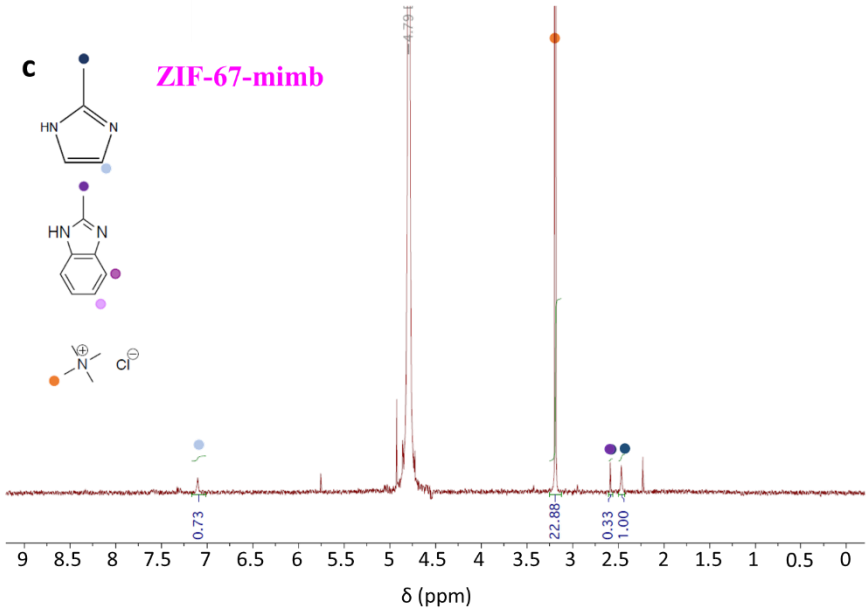

Figure 3.23 NMR spectra of **ZIF-67** (a), **ZIF-67-eimb** (b) and **ZIF-67-mimb** (c).

It is possible to extend the synthesis of **MUV-3-mix** to Co(II) and Zn(II) derivatives. This mixture of linkers and the solvent-free methodology permit to achieve novel SOD crystalline compounds and expand the ZIFs family (Figures 3.24-3.25) with higher water stability.

The crystal structure, phase purity, thermal and chemical stability are clear for all the mixed-ligand ZIFs compounds. However, the porous nature of these materials is required to be studied. N_2 sorption shows a common inability for the six materials to adsorb N_2. Nonetheless, the CO_2 sorption measurements at 298 K (Figure 3.26) confirm the presence of porosity in the Zn(II) and Co(II) derivatives. The total uptakes for the four compounds

are near to the 10 % in mass for **ZIF-8-mimb**, and and lower (4-2 %) for the rest of compounds.

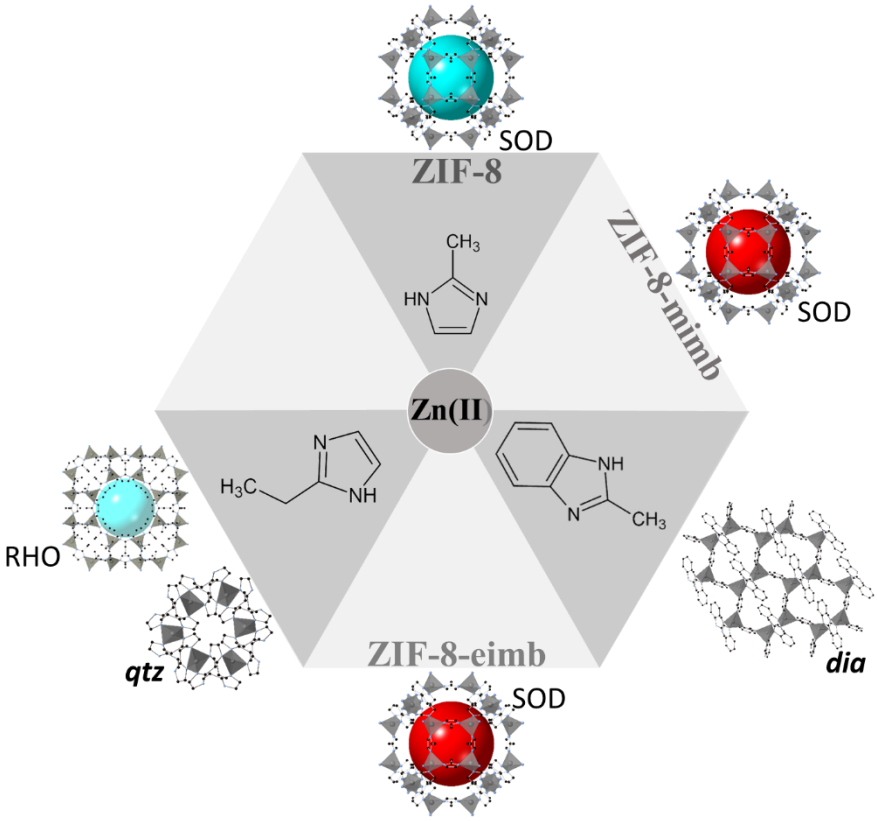

Figure 3.24 Scheme of the different achievable crystal structures combining Zn(II) and the three imidazoles: 2mimH, 2eimH and 2mbimH.8

These values are lower than those obtained for ZIF-8.[31] In comparison with the thermogravimetric data, the total uptake trend in these four materials is in good agreement with the observed for the loss mass. The **ZIF-8-mimb**

is the material exhibiting the highest loss mass and the most accessible porosity.

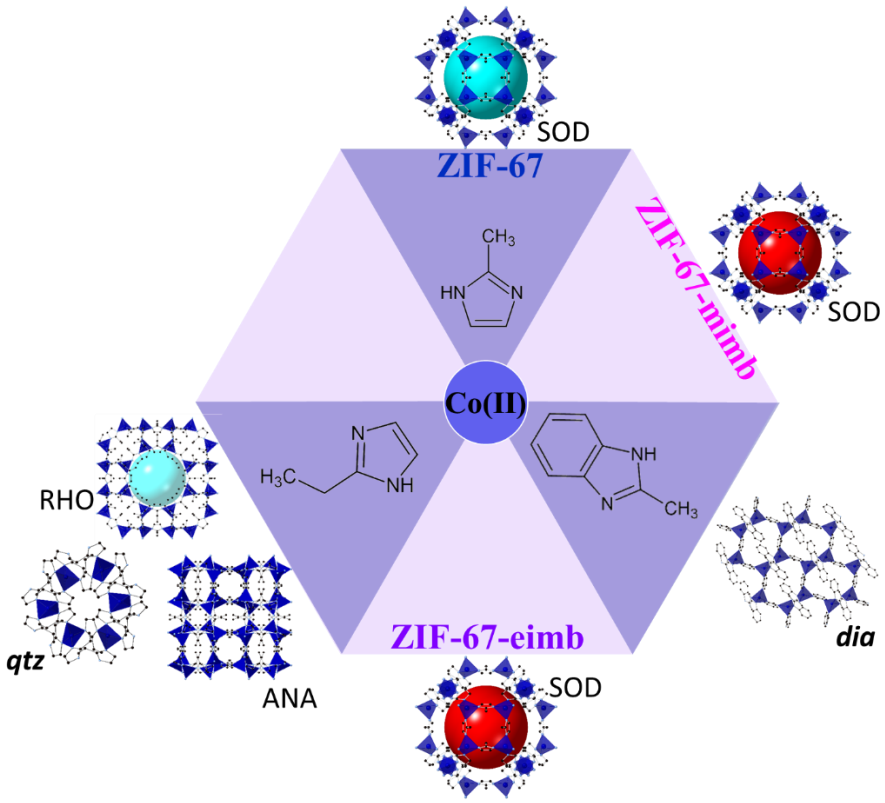

Figure 3.25 Scheme of the different achievable crystal structures combining Co(II) and the three imidazoles: 2mimH, 2eimH and 2mbimH.

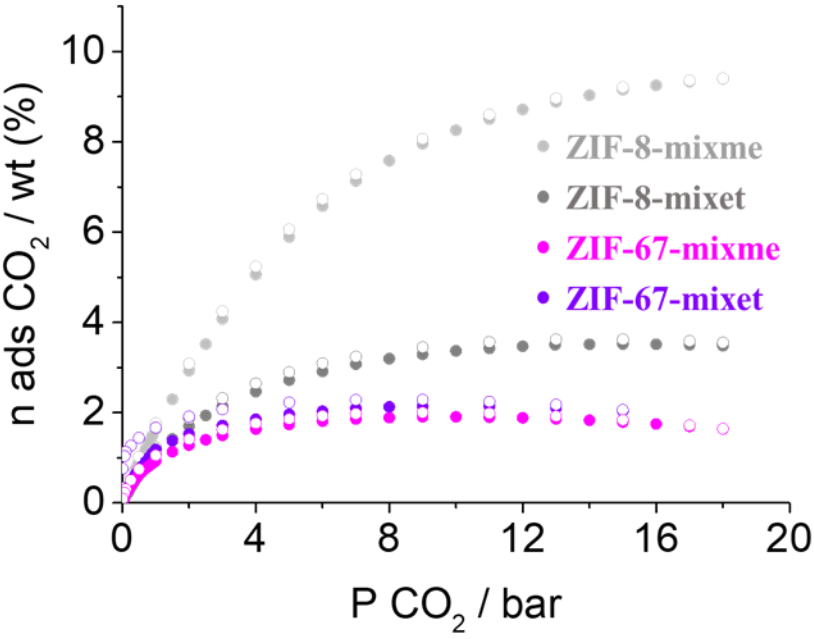

Figure 3.26 CO2 sorption (solid circle) and desorption (open circle) isotherms at 298 K for the four mixed-ligand ZIFs derivatives.

3.3 Conclusions

The solvent-free synthesis offers a platform with high versatility and applicability to expand the ZIFs family. The mixed-ligand approach has been used as a method to find novel zeolite-like materials. In combination with the solvent-free synthetic route, this approach permits to explore novel crystal structure beyond to Fe(II) derivate, enabling the incorporation of bulkier ligands. The strategy to insert bulky groups in a sodalite topology has been extended to other metals, such as Zn(II) and Co(II). Overall, the incorporation of bulkier ligands had allowed to study the water stability of these novel ZIFs. This work opens the door to investigate novel ZIFs and a

combination of them in a green route owing to the absence of solvent during the synthesis.

3.4 Methods

All reagents were commercially available and used without further purification.

Synthesis of MUV-3-mix. Ferrocene (30 mg, 0.16 mmol) and a combination of 2-methylimidazole, 2-ethylimidazole and/or 2-methylbenzimidazole (0.10-0.24 mmol per reactant) were combined and sealed under vacuum in a layering tube (4 mm diameter). The mixture was heated at 150 °C for 4 days to obtain yellow crystals suitable for X-ray single-crystal diffraction. The product was allowed to cool to room temperature, and the layering tube was then opened. The unreacted precursors were extracted with acetonitrile and benzene, and **MUV-3-mix** was isolated as yellow crystals (yield 20 %). Phase purity was established by X-ray powder diffraction.

Synthesis of ZIF-8-mix and ZIF-67-mix. Cobaltocene (for ZIF-67-mix, 30 mg, 0.16 mmol) or ZnO (for ZIF-8-mix, 13 mg, 0.16 mmol) and a combination of 2-methylimidazole, 2-ethylimidazole and/or 2-methylbenzimidazole (0.10-0.24 mmol per reactant) were combined and sealed under vacuum in a layering tube (4 mm diameter). The mixtures were heated at 150 °C for 4 days to obtain purple powder (ZIF-67-mix) or white powder (ZIF-8-mix). The products were allowed to cool to room temperature, and the layering tubes were then opened. The unreacted

precursors were extracted with acetonitrile and benzene. Phase purity was established by X-ray powder diffraction.

X-ray powder diffraction. Polycrystalline samples of **MUV-3-eimb**, **MUV-3-mimb, ZIF-8-eimb**, **ZIF-8-mimb, ZIF-67-eimb**, **ZIF-67-mimb,** $Zn(2eim)_2$, $Zn(2mbim)_2$, $Co(2eim)_2$, $Co(2mbim)_2$, ZIF-8 and ZIF-67 (prepared by solvent-free synthesis) were lightly ground in an agate mortar and pestle and used to fill 0.5 mm borosilicate capillaries that were mounted and aligned on an Empyrean PANalytical powder diffractometer, using Cu Kα radiation (λ = 1.54056 Å). Two repeated measurements were collected at room temperature (2θ = 2−40 °) and merged in a single diffractogram for each sample, with sharp and intense peaks denoting the high crystallinity of the material.

Single Crystal diffraction. Single crystals of **MUV-3-eimb** and **MUV-3-mimb** were mounted on cryoloops using a viscous hydrocarbon oil to coat the crystals. X-ray data were collected at 120 K on a Supernova diffractometer equipped with a graphite-monochromated Enhance (Mo) X-ray Source (λ = 0.71073 Å). The program CrysAlisPro, Oxford Diffraction Ltd., was used for unit cell determinations and data reduction. Empirical absorption correction was performed using spherical harmonics, implemented in the SCALE3 ABSPACK scaling algorithm. Crystal structures were solved and refined against all F^2 values by using the SHELXTL and Olex2 suite of programs.[32,33] Non-hydrogen atoms were refined anisotropically and hydrogen atoms were placed at calculated positions (riding model).

Thermogravimetric analysis. Thermogravimetric analyzed of **MUV-3-eimb**, **MUV-3-mimb, ZIF-8-eimb**, **ZIF-8-mimb, ZIF-67-eimb**, **ZIF-67-mimb, MUV-6** and **MUV-7** were carried out with a TA instruments TGA 550 apparatus in the 25–650 °C temperature range under a 20°C·min^{-1} scan rate and a N_2 flow of 40 mL·min^{-1}.

Scanning electronic microscopy. Scanning Electronic Micrographs images were recorded in a Hitachi S-4800.

Magnetic measurements. The magnetic structure and the presence of Fe(II) and Co(II) were characterized by magnetic measurements. Variable-temperature (2−300 K) direct current (dc) magnetic susceptibility measurements were carried out in applied fields of 0.1 T.

NMR studies. NMR spectra were recorded on Bruker DRX-500 spectrometer.

Water stability experiments. 12 mg of several materials (**ZIF-8-eimb**, **ZIF-8-mimb, ZIF-67-eimb**, **ZIF-67-mimb,** ZIF-8 and ZIF-67) were immersed in 20 ml of water under permanent stirring for 48 hours. After this time, the water was evaporated in an oven at 40 °C. The obtained powder was checked by X-ray powder diffraction. For the D_2O studies, 1.2 mg of the different ZIFs were used and 2 ml of D_2O. A solution of 3.4 mg of $(CH_3)_4NCl$ in 2 ml of D_2O was used as internal standard.

Gas Sorption. The high-pressure CO_2 adsorption isotherms were measured in a gravimetric sorption analyzer IGA-100 (Hiden Isochema). 50 mg of adsorbent was placed in a sample holder and before measurement, the

sample was degassed 3 hours at 100 °C under vacuum. CO_2 adsorption isotherms were acquired at 25 °C.

3.5 References

(1) Furukawa, H.; Cordova, K. E.; O'Keeffe, M.; Yaghi, O. M. The Chemistry and Applications of Metal-Organic Frameworks. *Science (80-.).* **2013**, *341* (6149), 1230444–1230444.

(2) Park, K. S.; Ni, Z.; Côté, A. P.; Choi, J. Y.; Huang, R.; Uribe-Romo, F. J.; Chae, H. K.; O'Keeffe, M.; Yaghi, O. M. Exceptional Chemical and Thermal Stability of Zeolitic Imidazolate Frameworks. *Proc. Natl. Acad. Sci. U. S. A.* **2006**, *103* (27), 10186–10191.

(3) Qian, Q.; Asinger, P. A.; Lee, M. J.; Han, G.; Mizrahi Rodriguez, K.; Lin, S.; Benedetti, F. M.; Wu, A. X.; Chi, W. S.; Smith, Z. P. MOF-Based Membranes for Gas Separations. *Chem. Rev.* **2020**.

(4) Yang, L.; Qian, S.; Wang, X.; Cui, X.; Chen, B.; Xing, H. Energy-Efficient Separation Alternatives: Metal–Organic Frameworks and Membranes for Hydrocarbon Separation. *Chem. Soc. Rev.* **2020**, 5359–5406.

(5) Kadota, K.; Sivaniah, E.; Bureekaew, S.; Kitagawa, S.; Horike, S. Synthesis of Manganese ZIF-8 from $[Mn(BH_4)_2 \cdot 3THF] \cdot NaBH_4$. *Inorg. Chem.* **2017**, *52334* (4), 8744–8747.

(6) Horike, S.; Kadota, K.; Itakura, T.; Inukai, M.; Kitagawa, S. Synthesis of Magnesium ZIF-8 from $Mg(BH_4)_2$. *Dalt. Trans.* **2015**, *44* (34), 15107–15110.

(7) Giménez-Marqués, M.; Hidalgo, T.; Serre, C.; Horcajada, P. Nanostructured Metal-Organic Frameworks and Their Bio-Related Applications. *Coord. Chem. Rev.* **2016**, *307*, 342–360.

(8) Astria, E.; Thonhofer, M.; Ricco, R.; Liang, W.; Chemelli, A.; Tarzia, A.; Alt, K.; Hagemeyer, C. E.; Rattenberger, J.; Schroettner, H.; Wrodnigg, T.; Amenitsch, H.; Huang, D. M.; Doonan, C. J.; Falcaro, P. Carbohydrates@MOFs. *Mater. Horizons* **2019**, *6* (5), 969–977.

(9) Pimentel, B. R.; Parulkar, A.; Zhou, E. K.; Brunelli, N. A.; Lively, R. P. Zeolitic Imidazolate Frameworks: Next-Generation Materials for Energy-Efficient Gas Separations. *ChemSusChem* **2014**, *7* (12), 3202–3240.

(10) Shekhah, O.; Chernikova, V.; Belmabkhout, Y.; Eddaoudi, M. Metal–Organic Framework Membranes: From Fabrication to Gas Separation. *Crystals* **2018**, *8* (11), 412.

(11) Pan, Y.; Liu, Y.; Zeng, G.; Zhao, L.; Lai, Z. Rapid Synthesis of Zeolitic Imidazolate Framework-8 (ZIF-8) Nanocrystals in an Aqueous System. *Chem. Commun.* **2011**, *47* (7), 2071–2073.

(12) Zhang, H.; Zhao, M.; Lin, Y. S. Stability of ZIF-8 in Water under Ambient Conditions.

Microporous Mesoporous Mater. **2019**, *279* (December 2018), 201–210.

(13) Zhang, H.; Liu, D.; Yao, Y.; Zhang, B.; Lin, Y. S. Stability of ZIF-8 Membranes and Crystalline Powders in Water at Room Temperature. *J. Memb. Sci.* **2015**, *485*, 103–111.

(14) Yeung, H. H. M.; Sapnik, A. F.; Massingberd-Mundy, F.; Gaultois, M. W.; Wu, Y.; Fraser, D. A. X.; Henke, S.; Pallach, R.; Heidenreich, N.; Magdysyuk, O. V.; Vo, N. T.; Goodwin, A. L. Control of Metal-Organic Framework Crystallization by Metastable Intermediate Pre-Equilibrium Species. *Angew. Chem. Int. Ed.* **2019**, *58* (2), 566–571.

(15) Ortiz, A. U.; Freitas, A. P.; Boutin, A.; Fuchs, A. H.; Coudert, F. X. What Makes Zeolitic Imidazolate Frameworks Hydrophobic or Hydrophilic? The Impact of Geometry and Functionalization on Water Adsorption. *Phys. Chem. Chem. Phys.* **2014**, *16* (21), 9940–9949.

(16) Thommes, M.; Kaneko, K.; Neimark, A. V.; Olivier, J. P.; Rodriguez-Reinoso, F.; Rouquerol, J.; Sing, K. S. W. Physisorption of Gases, with Special Reference to the Evaluation of Surface Area and Pore Size Distribution (IUPAC Technical Report). *Pure Appl. Chem.* **2015**, *87* (9–10), 1051–1069.

(17) Liu, X.; Li, Y.; Ban, Y.; Peng, Y.; Jin, H.; Bux, H.; Xu, L.; Caro, J.; Yang, W. Improvement of Hydrothermal Stability of Zeolitic Imidazolate Frameworks. *Chem. Commun.* **2013**, *49* (80), 9140–9142.

(18) Karagiaridi, O.; Lalonde, M. B.; Bury, W.; Sarjeant, A. a.; Farha, O. K.; Hupp, J. T. Opening ZIF-8: A Catalytically Active Zeolitic Imidazolate Framework of Sodalite Topology with Unsubstituted Linkers. *J. Am. Chem. Soc.* **2012**, *134* (45), 18790–18796.

(19) Marreiros, J.; Van Dommelen, L.; Fleury, G.; Oliveira-Silva, R.; Stassin, T.; Iacomi, P.; Furukawa, S.; Sakellariou, D.; Llewellyn, P. L.; Roeffaers, M.; Ameloot, R. Vapor-Phase Linker Exchange of the Metal–Organic Framework ZIF-8: A Solvent-Free Approach to Post-synthetic Modification. *Angew. Chem. Int. Ed.* **2019**, *131* (51), 18642–18646.

(20) Jayaramulu, K.; Geyer, F.; Schneemann, A.; Kment, Š.; Otyepka, M.; Zboril, R.; Vollmer, D.; Fischer, R. A. Hydrophobic Metal–Organic Frameworks. *Adv. Mater.* **2019**, *31* (32), 1–31.

(21) Akimbekov, Z.; Katsenis, A. D.; Nagabhushana, G. P.; Ayoub, G.; Arhangelskis, M.; Morris, A. J.; Friščić, T.; Navrotsky, A. Experimental and Theoretical Evaluation of the Stability of True MOF Polymorphs Explains Their Mechanochemical Interconversions. *J. Am. Chem. Soc.* **2017**, *139* (23), 7952–7957.

(22) Bhadra, B. N.; Seo, P. W.; Khan, N. A.; Jhung, S. H. Hydrophobic Cobalt-Ethylimidazolate Frameworks: Phase-Pure Syntheses and Possible Application in

Cleaning of Contaminated Water. *Inorg. Chem.* **2016**, *55* (21), 11362–11371.

(23) Huang, L.; Xue, M.; Song, Q.; Chen, S.; Pan, Y.; Qiu, S. Carbon Dioxide Selective Adsorption within a Highly Stable Mixed-Ligand Zeolitic Imidazolate Framework. *Inorg. Chem. Commun.* **2014**, *46*, 9–12.

(24) Yang, J.; Zhang, Y. B.; Liu, Q.; Trickett, C. A.; Gutiérrez-Puebla, E.; Monge, M. Á.; Cong, H.; Aldossary, A.; Deng, H.; Yaghi, O. M. Principles of Designing Extra-Large Pore Openings and Cages in Zeolitic Imidazolate Frameworks. *J. Am. Chem. Soc.* **2017**, *139* (18), 6448–6455.

(25) Fang, Z.; Bueken, B.; De Vos, D. E.; Fischer, R. A. Defect-Engineered Metal-Organic Frameworks. *Angew. Chem. Int. Ed.* **2015**, *54* (25), 7234–7254.

(26) López-Cabrelles, J.; Romero, J.; Abellán, G.; Giménez-Marqués, M.; Palomino, M.; Valencia, S.; Rey, F.; Mínguez Espallargas, G. Solvent-Free Synthesis of ZIFs: A Route toward the Elusive Fe(II) Analogue of ZIF-8. *J. Am. Chem. Soc.* **2019**, *141* (17), 7173–7180.

(27) Tian, Y. Q.; Cai, C. X.; Ren, X. M.; Duan, C. Y.; Xu, Y.; Gao, S.; You, X. Z. The Silica-Like Extended Polymorphism of Cobalt(II) Imidazolate Three-Dimensional Frameworks: X-Ray Single-Crystal Structures and Magnetic Properties. *Chem. - A Eur. J.* **2003**, *9* (22), 5673–5685.

(28) Sánchez, V.; Storr, A.; Thompson, R. C. Magnetic and Structural Studies on 1,3-Diazolate Complexes of Cobalt(II) — The Characterization of Three New Cobalt(II) Molecule-Based Magnets. *Can. J. Chem.* **2002**, *80* (2), 133–140.

(29) Zhang, Y.; Jia, Y.; Li, M.; Hou, L. Influence of the 2-Methylimidazole/Zinc Nitrate Hexahydrate Molar Ratio on the Synthesis of Zeolitic Imidazolate Framework-8 Crystals at Room Temperature. *Sci. Rep.* **2018**, *8* (1), 1–7.

(30) Stassin, T.; Stassen, I.; Marreiros, J.; Cruz, A. J.; Verbeke, R.; Tu, M.; Reinsch, H.; Dickmann, M.; Egger, W.; Vankelecom, I. F. J.; De Vos, D. E.; Ameloot, R. Solvent-Free Powder Synthesis and MOF-CVD Thin Films of the Large-Pore Metal-Organic Framework MAF-6. *Chem. Mater.* **2020**, *32* (5), 1784–1793.

(31) Pérez-Pellitero, J.; Amrouche, H.; Siperstein, F. R.; Pirngruber, G.; Nieto-Draghi, C.; Chaplais, G.; Simon-Masseron, A.; Bazer-Bachi, D.; Peralta, D.; Bats, N. Adsorption of CO2, CH4, and N2 on Zeolitic Imidazolate Frameworks: Experiments and Simulations. *Chem. - A Eur. J.* **2010**, *16* (5), 1560–1571.

(32) Dolomanov, O. V.; Bourhis, L. J.; Gildea, R. J.; Howard, J. A. K.; Puschmann, H. OLEX2 : A Complete Structure Solution, Refinement and Analysis Program. *J. Appl.*

Crystallogr. **2009**, *42* (2), 339–341.

(33) Sheldrick, G. M. Crystal Structure Refinement with SHELXL. *Acta Crystallogr. Sect. C Struct. Chem.* **2015**, *71* (1), 3–8.

Chapter 4

In-flow ZIF lithography

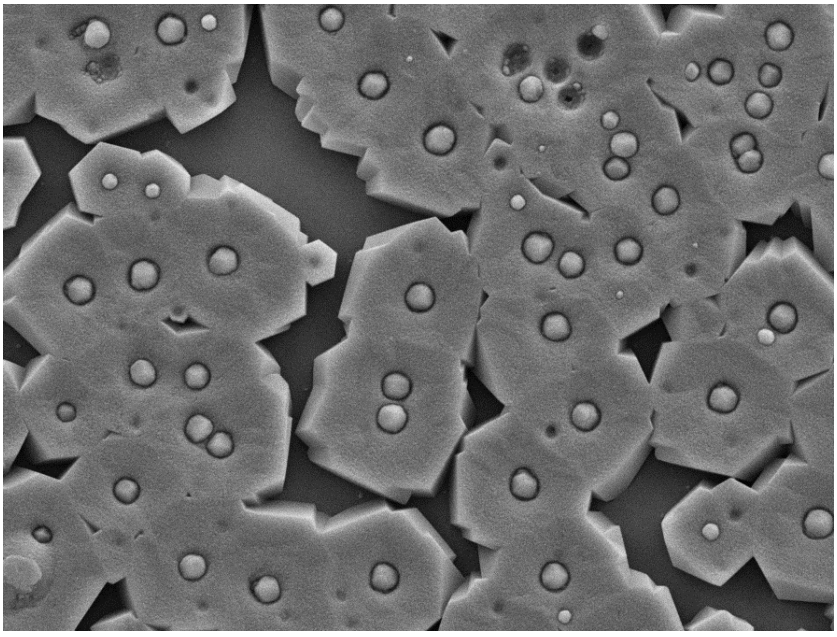

4.1 Introduction

The hybrid composition of Metal-Organic Frameworks (MOFs) promotes the synthesis of a vast number of novel structures, owing to the enormous variety of organic ligands and metallic clusters. This large amount of new structures provides countless candidates to select materials and applications.[1] Nevertheless, despite this sharp increase in the number of structures there is a lack of knowledge about some fundamental and critical stages in MOF chemistry, such as assembly, crystallization, crystal growth or polymorphism.[2] Most of the synthetic techniques used for MOF formation are based in equilibrium regimes, where the typically controlled parameters are temperature, concentration, pressure and atmosphere. However, the diffusion through the media, necessary for the formation of the material, is an uncontrolled process. In fact, most of the reactions occur in convective current systems.

Nonetheless, in nature, most of the chemical processes occur in-flow and out of the equilibrium. Thus, the factor of mass transport can play an important role in a chemical reaction and the assembly of molecules in materials. In fact, this was proved for the first time in 1896 by R. Liesegang, who managed to control mass transport through the diffusion of reactants in a gel. Specifically, he studied the periodic precipitation (PP) of certain pairs of inorganic salts such as $AgNO_3/K_2Cr_2O_7$ in a gel matrix. A droplet of salt moves and reacts with another salt present in the gel, and that provokes periodic bands of a precipitate ($Ag_2Cr_2O_7$ in this case), known nowadays as “Liesengang rings” (Figure 4.1a). The reaction between the ions happens equal to a classic environment, and the product is also formed,

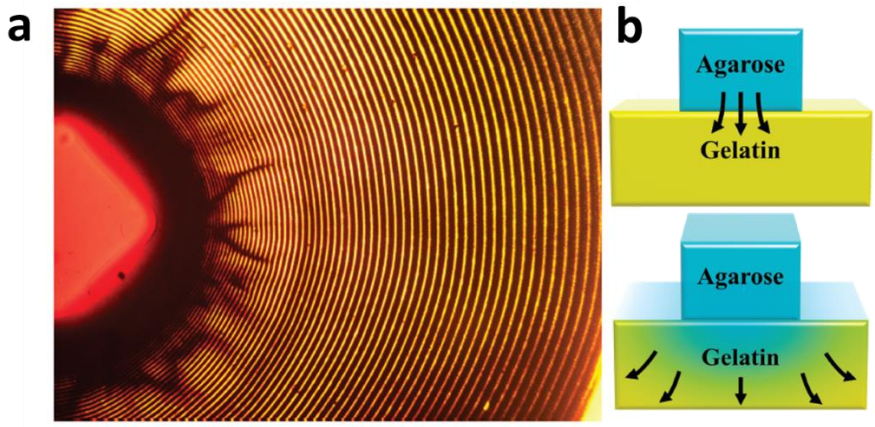

Figure 4.1 a) Classical Liesegang rings of insoluble $Ag_2Cr_2O_7$, the bands in this picture are all thinner than a human hair. b) Small block of agarose gel soaked with model substance A (in blue) is placed onto a larger block of pure gelatin. Substance A is diffused from agarose to the gelatin. Adapted from reference 3.

but the periodic precipitation is exclusive to the "extraordinary" reaction matrix. The PP is due to the control of the diffusion through the media, a different condition versus the classical reaction in solution in a vial (in a convective regime). Nature uses similar reaction-diffusion systems, albeit obviously much more sophisticated, to build structures and patterns, which find diverse applications, from cell regulatory processes to control of the crystal growth on a micro-nano scale.[3]

The study of the simplest model of migration, the diffusion (Figure 4.1b), in a chemical reaction, is called reaction-diffusion (RD). The RD is present in nature in many ways, both in animated and inanimated systems. Examples in animated systems are the control in cells of the intracellular

oscillations of Ca^{2+}, and the Turing-like mechanism of the skin patterns in zebras. In inanimate systems, RD is also present in minerals (garnet, augite…) or cave stalactites controlling the crystal formation.[3]

The application of RD to multifunctional molecule-based materials can be interesting from different points: a) The control of diffusion and the reaction out of convective currents can help to understand fundamental issues of assemblies and crystal growth. b) This reaction across space and time can lead to interesting non-equilibrium species not achievable by classic methods. For these reasons, the study of the formation of MOFs by RD systems can be useful not only from a fundamental point of view, but also for applications.

This combination of RD and MOFs is quite challenging and novel, and only a few examples have been previously reported. A recent work developed by the group of M. Hmadeh explored the formation of **ZIF-8** and **ZIF-67** in an agar gel matrix containing the metallic cation (Zn^{2+} or Co^{2+}) upon addition of a solution of 2-methylimidazole (2meimH) (Figure 4.2).[4] The 2meimH diffuses through the gel and reacts with the metallic cations creating new diffusing species, denoted [ZIF (aq)], which nucleate when exceeds a certain concentration. When the supersaturation wave is important (early stages), *nucleation* dominates the process, and small crystals are thus obtained. On the contrary, when the supersaturated wave is less important, *growth* dominates the process, and larger crystals are thus obtained. The size distribution is not linear and depends on the coupling between RD and nucleation/growth kinetics.

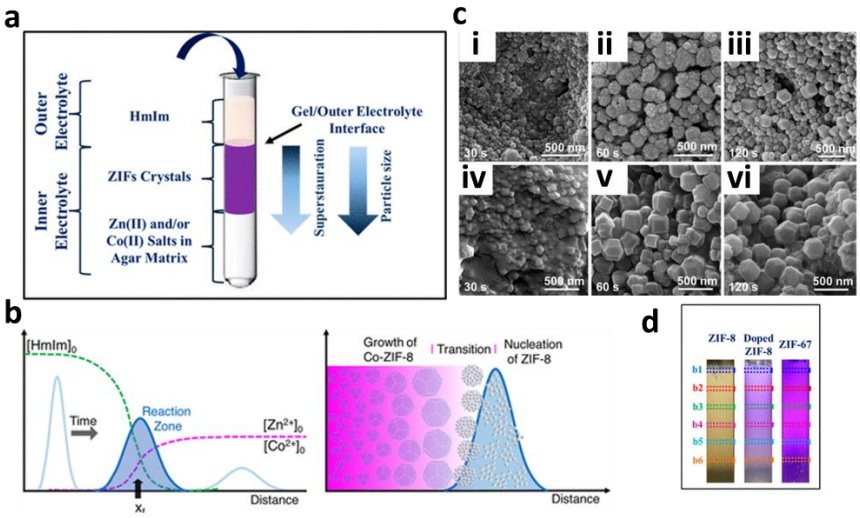

Figure 4.2 a) Schematic representation of the ZIFs synthesis via the reaction-diffusion framework. b) The theoretical basis of the reaction-diffusion framework (RDF). (left) Diffusion profiles of 2meimH and Zn^{2+}/Co^{2+}. (right) Nucleation of pure **ZIF-8** leading to nanospheroids takes place within the reaction zone. Transition to multisized Co-doped polyhedra with a gradient of composition takes place in its wake c) Nucleation and growth kinetics of ZIFs dodecahedrons. SEM images of the **ZIF-8** crystals after 30 (i), 60 (ii), and 120 s (iii) and of ZIF-67 crystals after 30 (iv), 60 (v), and 120 s (vi) of reaction at the interface region. d) Formation of the **ZIF-8**, Co-doped **ZIF-8**, and ZIF-67 crystals in the tubular reactor where the extracted bands are indicated as *bn.* Modified from reference 4.

The authors also checked the particle size by HSEM and observed bigger crystals far away from the most saturated in 2meimH zone. Besides, in the intermediate location, the preorganization of small nanocrystals has

been observed before the formation of the classic rhombic dodecahedral shaped crystals.

Another recent example is the work of B. A. Grzybowski and co-workers with the archetype MOF HKUST-1 as a model, whose shape can be tuned using RD systems.[5] This MOF is formed by trimesic acid and Cu paddle-wheel units disposed in a 3D network. Thus, they used a hydrogel composed of agarose to control the diffusion of $Cu(NO_3)_2$, trimesic acid, and triethylamine (a modulator), observing the formation of bands across the gel matrix. The first three bands show different species, but from the fourth band, formation of HKUST-1 is observed. Interestingly, different

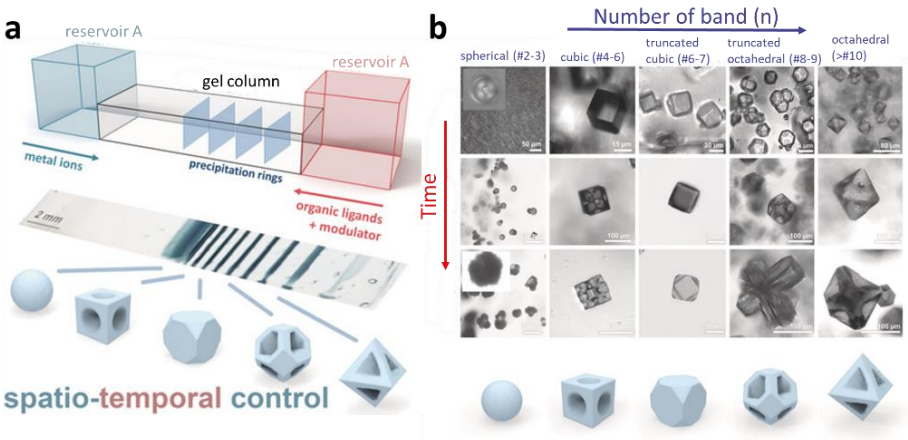

Figure 4.3 a) Schematic representation of the synthetic system and the obtained bands of HKUST-1. b) Evolution of MOF-crystal morphology in space and in time. Confocal microscopy images of crystals observed in consecutive PP bands (horizontal axis) and also changing in time (vertical axis). Modified from reference 5.

morphologies can be achieved depending on the modulator concentration.

The first band where HKUST-1 is formed has a relatively low concentration of triethylamine, favoring a spherical morphology. In the next bands, where the concentration of the modulator is increased, different crystal growths are favored due to the effect of the coordination of triethylamine to the Cu(II) centers, resulting in very distinct morphologies (Figure 4.3).

These examples show the powerful tool of the RD systems for MOFs synthesis, and the theoretical and practical use of control of diffusion. Nevertheless, this technique has also some limitations, such as the solubility in water for the ligand and metal sources due to the hydrogel nature, the temperature application during the synthesis (limited to room temperature) and a real control over the diffusion.

The possibilities offered by combining RD and MOFs are very promising. For this reason, we decided to start a collaboration with an expert group in RD and microfluidics, Josep Puigmarti group, at the ETH Zurich (Switzerland). The group of J. Puigmartí has wide experience in the interface between microfluidics and materials,[6–8] studying the formation of kinetic products only achievable by microfluidics systems,[9] controlling the formation of covalent organic frameworks nanoparticles[10] or the crystal growth of MOF.[11] I made a 3-month placement between April and June of 2019 at their laboratory to study the influence of RD in zeolitic imidazolate frameworks (ZIFs) formation under novel characteristics such as continuous-flow and liquid-solid interfaces.

Microfluidic systems are good platforms to study crystallization and assembly processes as they offer several advantages to the classical synthetic routes such as turbulent-free conditions (as RD systems) and

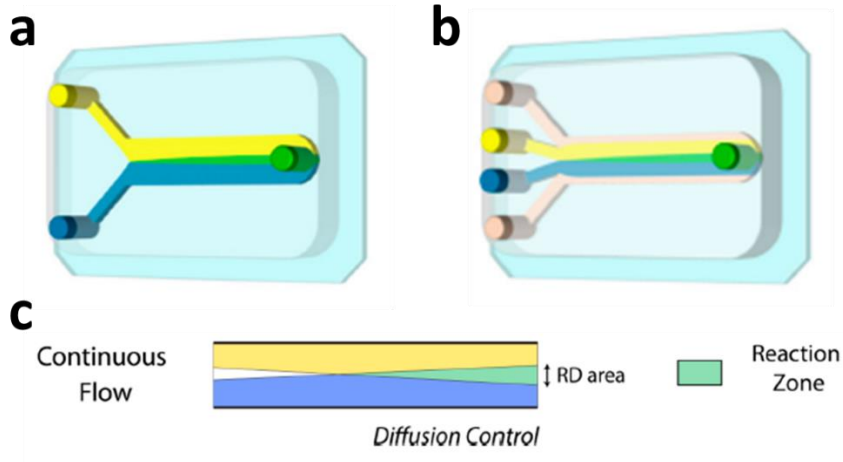

Figure 4.4 a-b) Schematic illustrations of (a) two laminar co-flowing streams and (b) a flow-focusing microfluidic set-up with two sheath flows (or hydrodynamic focusing). c) Mixing of reactants is only accomplished through molecular diffusion. Note that the latter is a unique method for establishing an effective reaction-diffusion (RD) area, just like the ones present in nature. In the figure, the yellow and blue colors indicate reactants, the white color the pure solvent area, and in green. Adapted from reference 7.

excellent control of mass and heat transport. Among the different possibilities offered by microfluidics, we are going to focus on continuous-flow platforms. Continuous-flow platforms present some interesting characteristics similar to the RD examples in gel systems, such as the slow mixing of the reactants due to the molecular diffusion inside the microfluidic channel. In addition, this prevents the chaotic advection. Continuous-flow devices work under laminar flow conditions, which allow spatial and temporal control of reactants through the RD. This system,

depicted in Figure 4.4, consists of a microfluidic chip with a series of different channels where reactants and solvents can flow in a controlled manner. In contrast to gel systems, the RD is more precise thanks to the flow rate ratio (FRR) during the synthesis. The FRR is defined as the ratio between the sheath and reagent flows.

A novel system developed by Puigmartí and co-workers was the "in-flow MOF lithography". This technique consists of a combination of a Y-shaped microfluidic chip and a glass substrate coated by a metallic oxide (Figure 4.5a). In their work, they used Cu_2O to show the formation of the well-known HKUST-1 (Figure 4.5b). In the channels of the chip, the ligand (trimesic acid) and ethanol flow through the chip and react with the Cu_2O. The acidic nature of the mixture etches the oxide and they hypothesized that the presence of oxygen in solution oxidizes Cu^+ to Cu^{2+} which reacts with the ligand to form the MOF. They used an unreacted flow channel with only solvent (ethanol), which diffused to the channel containing the ligand, observing the formation of MOF in the initial areas for the ligand flow channel and the RD along the channel (Figure 4.5c).

Microfluidic platforms offer novel perspectives to control the assembly and reaction in MOFs and hybrid materials fields. The versatility of continuous-flow platforms allows understanding better the crystal growth and explore new applications and processability, such as the direct growth over a substrate. This Chapter describes the influence of different techniques on the growth of MOFs, in particular **ZIF-8**, based in RD systems from simple diffusion through a gel and another system more

sophisticated based on continuous-flow devices.

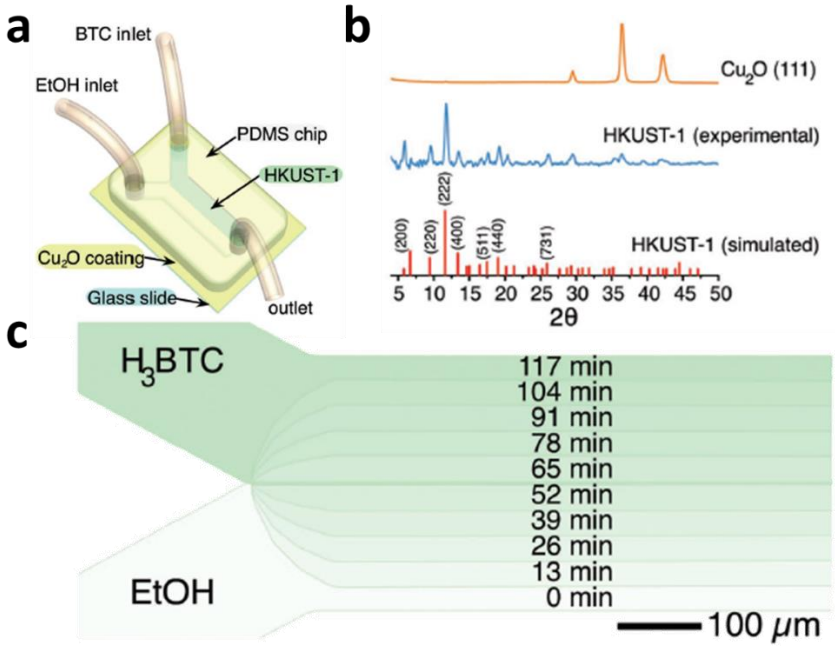

Figure 4.5 a) Schematic illustration of the Y-shaped microfluidic device used in their investigations. b) Grazing Incidence X-ray Diffraction (GIXRD) spectra of Cu_2O (111), HKUST-1 generated inside the microfluidic channel, and the simulated XRD pattern of HKUST-1. c) Schematic illustration of the generation of graded HKUST-1 surfaces inside the microfluidic channel. The time scale represents the total exposure time of the surface to the BTC stream. This controlled exposure can be accomplished by varying the flow rate of BTC (reactive) and ethanol (unreactive) flows. Adapted from reference 13.

4.2 Results and discussion

To check the influence of the control of the diffusion under dynamic systems on the synthesis of a MOF, **ZIF-8** has been selected.

Static system. In the first experiment, polydimethylsiloxane (PDMS) was used to control the diffusion of 2meimH solution (in methanol) above ZnO film (onto a glass slide). Methanol can diffuse through the PDMS structure polymer, such as in the agarose gel. The PDMS is the chosen polymer to construct the continuous-flow microfluidic devices and to compare the different experiments (note that the same polymer has been chosen for the static diffusion experiments). The thickness of the PDMS layer can be tuned very easily, and two very different sizes have been selected to check the influence of the PDMS thickness in the formation of the **ZIF-8 (**2 cm and 200 μm). **ZIF-8** crystals are expected to be formed in the interface between the PDMS block and the ZnO surface, thanks to the diffusion of the 2meimH and methanol through the polymer and subsequent reaction with ZnO.

Initially, we used a 2 cm PDMS block, putting the 2meimH solution above the PDMS with a spacer (Figure 4.6a). After 48 hours, it was possible to observe homogenous crystals of **ZIF-8** with a very defined morphology and high crystallinity, as shown in Figure 4.6b. Scanning electronic micrographs show the morphology of truncated rhombic dodecahedral **ZIF-8**, with 1.5 μm size. This result is in the agreement with the previous results from M. Hmadeh and B. A. Grzybowski.[4,5]

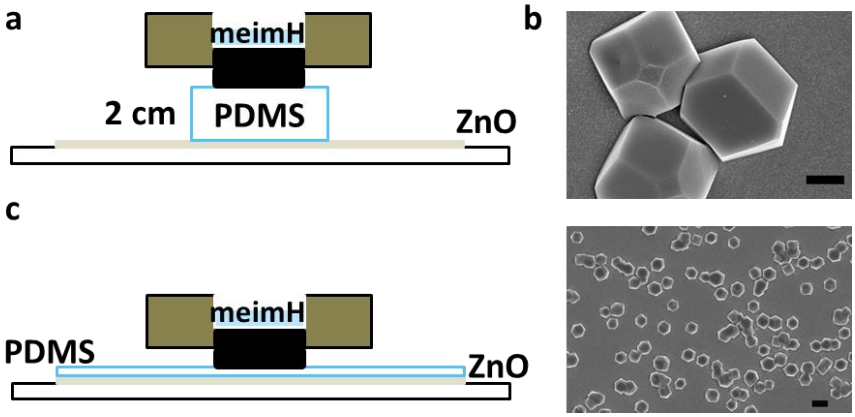

Figure 4.6 a) Scheme of the synthesis device for the static synthesis of **ZIF-8**. b) SEM images of the obtained **ZIF-8** by the static synthesis. Scale bars are 1µm (top) and 2µm (bottom). c) Scheme of the synthesis device for the static synthesis of **ZIF-8** with a thinner PDMS.

When the PDMS thickness is decreased to 200 µm (Figure 4.6c), different crystal growth is observed (Figure 4.7b). After 2 hours of reaction time, **ZIF-8** nanoparticles of around 100 nm were found, primarily located at the surface of the substrate. This observation is in agreement with the results found by M. Hmadeh[4] for short reaction times and previous studies about **ZIF-8** crystal growth,[12] with particle sizes around 100 nm. However, it should be noted the difference in "short" reaction times: 2 hours vs. 30 seconds. When the reaction time is left to proceed further, crystals of **ZIF-8** with high crystallinity were found. In particular, crystals with a particle size around 2-3 µm are found after 24 hours of reaction time (Figure 4.7a). Nevertheless, the most interesting observation found at this point deals with the morphology of the crystals. As clearly observed in the SEM images

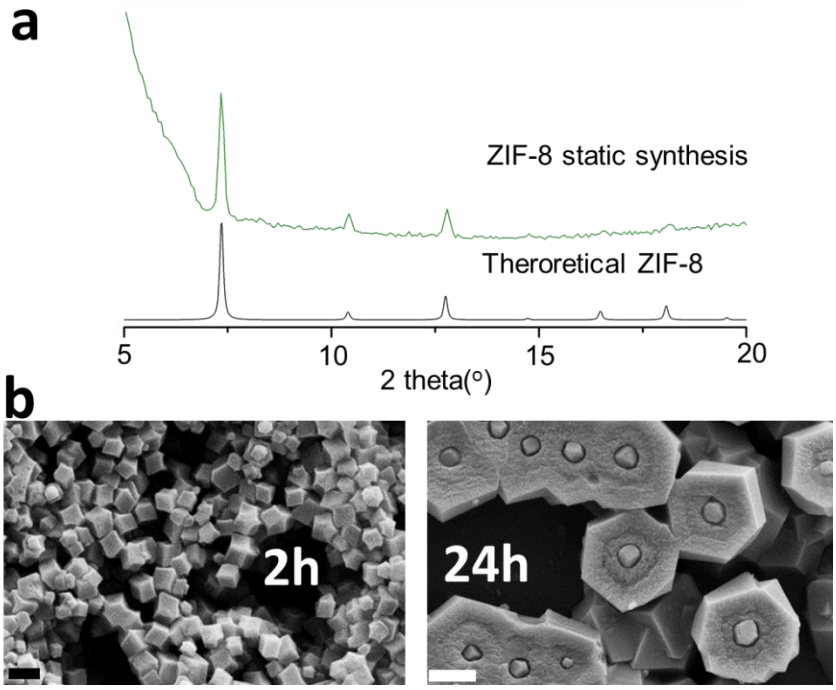

Figure 4.7 a) GIXRD diffractograms of a simulated single crystal of **ZIF-8** and experimental **ZIF-8** obtained by static controlled diffusion synthesis. b) **ZIF-8** crystals SEM images from static synthesis at different times. Scale bars are 200 nm and 1 μm, respectively.

(Figure 4.7b), the 24-hour crystals have grown around a seed of ca. 100 nm, i.e. a seed which is similar in size than those observed at 2-hour reaction time. In addition, close inspection of the images allows to differentiate two different shells of crystal growth around those seeds. The chemical composition of the central seed and the shells was checked by elemental analysis by the EDX technique at the SEM, confirming the same composition for the three regions (Figure 4.8).

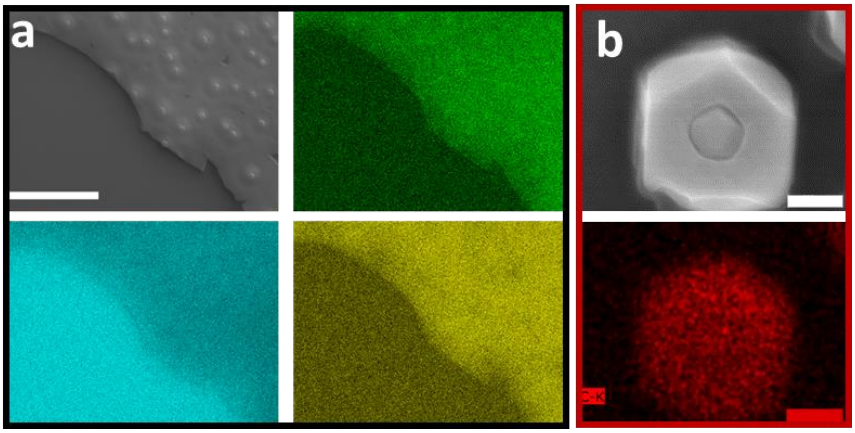

Figure 4.8 a) EDX analysis from the static synthesis of **ZIF-8**. Green, blue and yellow represents C, O and Zn, respectively. Scale bars are 2,5 μm. b) EDX analysis from one isolated crystal showing the same composition of the core and the shell. Red represents C content.

At intermediate times, it is possible to observe different crystal growth steps. The study with time shows different crystal sizes and statements before the 24 hours. At two hours, the formation of seed-like nanocrystals can be observed. In six hours of experiment, a combination of amorphous mass and seeds seem to form a pre-crystal status. At 24 hours crystals are formed with defined morphology, and for faraway zones, smaller crystal particles can be observed. For longer times no changes were appreciated (Figure 4.9). This suggests a crystal growth mechanism consisting of an initial formation of the seeds and a subsequent growth around a pre-formed seed of **ZIF-8**.

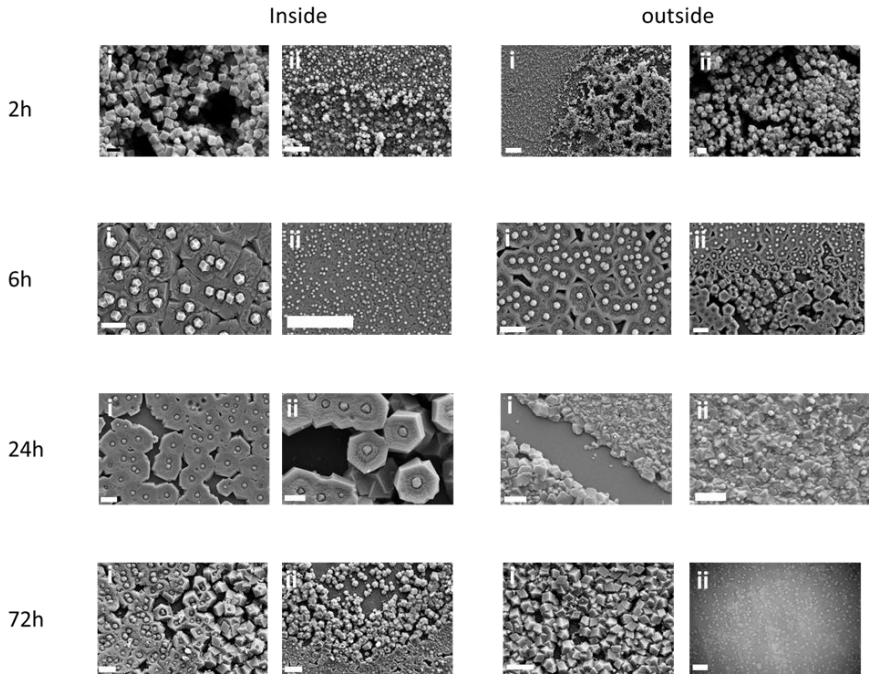

Figure 4.9 ZIF-8 crystals SEM images from static synthesis at different times. Scale bars are : 2h-I i) 200 nm ii) 1 μm, 2h-O i) 2 μm ii) 200 nm, 6h-I i) 1 μm ii) 10 μm, 6h-O i) 2 μm ii) 2 μm , 24h-I i) 2 μm ii) 1 μm, 24h-O i) 1 μm ii) 1 μm, 72h-I i) 1 μm ii) 2 μm, 72h-O i) 2 μm ii) 200 μm.

Continuous flow system. As already shown, the diffusion of 2meimH through the PDMS originates **ZIF-8** crystals on the surface of ZnO/glass substrates when a static configuration is used, i.e. a thermodynamic regime is used. On the contrary. continuous-flow can offer a kinetic regime and control over the diffusion thanks to the dynamic nature of the system. Therefore, the second step is the control of the flow rates of the reactants in a continuous system using laminar flow conditions. For that, the in-flow MOF lithography has been chosen,[13] using a PDMS chip with a single channel for the 2meimH solution in methanol, and ZnO films

covering glass substrates (similar to Figure 4.5a). Thus, the system used in this study is simpler, with only one inlet.

In this experiment, the continuous-flow substitutes the static system, thus permitting a permanent supply of fresh ligand solution for the formation of **ZIF-8**. Moreover, this device allows controlling the reaction time inside the channel through the flow rate. Under the 10 μL/min flow conditions and overnight, a continuous crystallization of **ZIF-8** is observed outside the channel, similar to a thick film. This means that the ligand is diffusing out of the channel and reacts with the surface. This is an important difference with the HKUST-1 in-flow MOF lithography, where the reaction occurs inside the channel. This is in contrast to the independent crystal formation in the previous experiment, and more similar to the results observed outside in the static reaction (24 hours reaction time) (Figure 4.10).

The crystallinity of the film was checked by grazing incidence X-ray diffraction (Figure 4.10a) and Raman spectroscopy (Figure 4.11a), confirming the nature of the film as being ZIF-8. In this case, the crystal formation of **ZIF-8** is completed and growth forming a film of crystals with a crystal size around 200 nm (Figure 4.10d), instead of discrete crystals like in the static synthesis. Inside the channel, a complete etching of the ZnO is observed (Figure 4.10b and Figure 4.11a). This means that the source of Zn for the formation of ZIF-8 proceeds from the inner part of the channel, whereas outside the channel crystal growth of the **ZIF-8** occurs upon diffusion of the reactants. In Figure 4.10c it can be appreciated the formation of periodic precipitations, owing to the continuous-flow and the

diffusion of 2meimH and methanol, formed by bigger crystals of around 1 μm (Figure 4.10f). This periodic precipitation can be followed by optical video across real-time (Figure 4.11b).

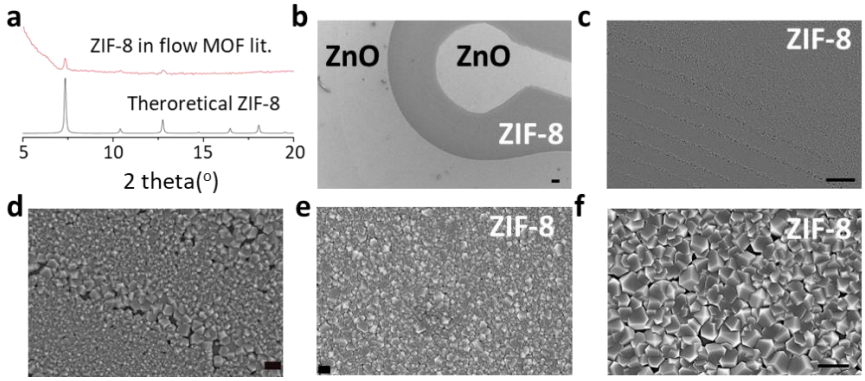

Figure 4.10 a) GIXRD diffractograms of a simulated single crystal of **ZIF-8** and experimental **ZIF-8** obtained by in-flow MOF lithography synthesis. b-f) SEM images from the substrates after the **ZIF-8** synthesis by in-flow MOF lithography. a shows the inlet part of the device and the difference between ZnO and **ZIF-8** contrast. c-d show the precipitation pattern formed by the synthesis of **ZIF-8** under this technique. Scale bars are 20 μm (c) and 2 μm (d). e-f show the particle size in the film, being smaller between lines (e, scale bar 200 nm) and bigger in the precipitation lines (f, scale bar 2 μm).

Compared with previous work based on in-flow MOF lithography, where the formation of the HKUST-1 was studied,[13] the results obtained here are completely different. In the case of HKUST-1 in-flow MOF lithography, Puigmartí and co-workers observed only MOF particles inside the channel. The mechanism of the reaction and crystal growth is different

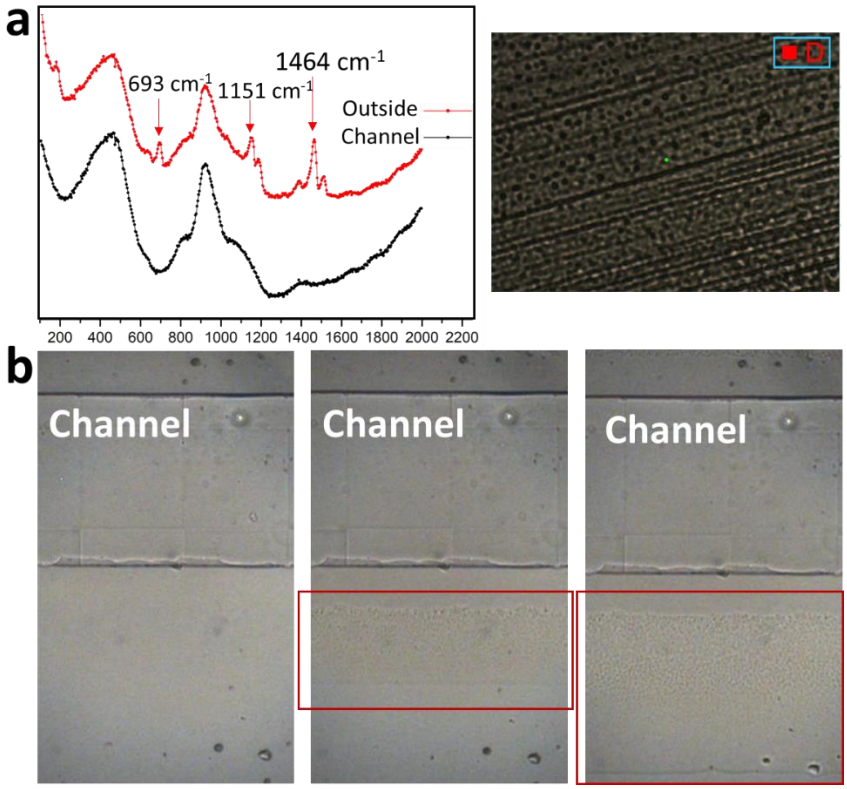

Figure 4.11 a) Raman spectra of the channel after the reaction and in the crystallization zone, showing the characteristic Raman peaks of the ZIF-8. b) Optical images from the channel at t = 0 (left), t = 6h (middle), t = 16h (right), showing the diffusion front and the crystallization of **ZIF-8**.

for the **ZIF-8**, with a clear diffusion of the 2meimH or pre-formed species such as $Zn(2meim)_x$ clusters through the PDMS. The detected PP is clear evidence of the influence of the diffusion across the PDMS chip. Further experiments are required to check the influence of flow rates, cross-section and the concentration of 2meimH, but these experiments are promising to understand and control the crystal growth of **ZIF-8** in a liquid-solid

interface, opening the door to constructing mixed ligand architectures to tune the properties of the composites onto a substrate.

Growing films. At this point, the formation of **ZIF-8** through diffusion and in continuous-flow has been proved to be possible. However, the observed absence of crystal formation inside the channel is interesting. In fact, the crystal growth outside the channel suggests the possibility to control the growth of **ZIF-8** films. Consequently, a third experiment was designed in order to combine the control of the diffusion through the PDMS and the control of flow rate in continuous conditions. This would merge the benefits of the first and second experiments to obtain a film of **ZIF-8**.

Two-dimensional architectures or films based in MOFs are promising candidates to build membranes for industrial applications in gas separation.[14,15] Recently, the group of V. Agrawal studied the formation of **ZIF-8**, ZIF-67 and ZIF-90 using a continuous synthesis to prevent Ostwald ripening and prevent the micrometer particle size of the ZIFs to form a sub-micrometric particle film.[16] The continuous-flow of **ZIF-8** precursor modifies the classical characteristics of solvothermal and turbulent synthesis and permit to achieve a different crystal growth.

In the particular case studied here, a similar set up to that of the second case has been used, i.e. a microfluidic chip based in PDMS and continuous-flow. However, in this experiment, the ZnO surface was covered by a film of 200 μm of PDMS. This work shows a continuous film which has been formed with this methodology (Figure 4.12 a-b). The size of the particles is around 200 nm and are randomly oriented. This film is crystalline and the higher intensity in the first peak of the diffractogram

matches with the bigger covered surface with the **ZIF-8** film compared with the previous experiment. The extension of this film can be around 1 mm.

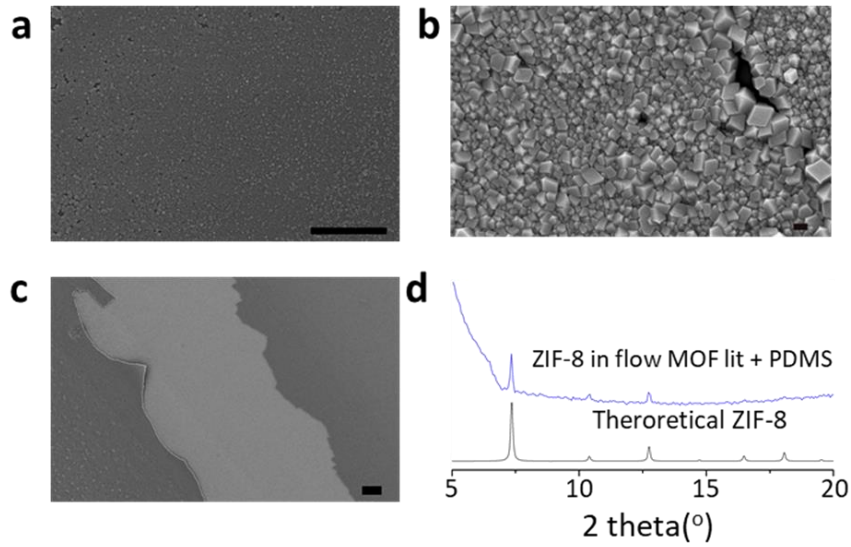

Figure 4.12 a-c) SEM images from the substrates after the **ZIF-8** synthesis by in-flow MOF lithography and thin-film PDMS for controlling the diffusion. a shows the large extension of the **ZIF-8** film. Scale bar is 30 µm. b shows the particle size in the film around 200 nm. The scale bar is 200 nm. c shows a break in the film due to the peeling off the PDMS film. d) GIXRD diffractograms of a simulated single crystal of **ZIF-8** and experimental **ZIF-8** obtained by in-flow MOF lithography synthesis and thin film of PDMS.

More experiments are in progress, but with this work it has been demonstrated that the use of microfluidics and RD systems is a promising strategy to control the crystal growth of MOFs. In particular, the possibility of films growth of **ZIF-8** with small particle size has been proved, thus

opening the door to the use of microfluidic systems to organize MOF in substrates through the control of crystal synthesis (Figure 4.13).

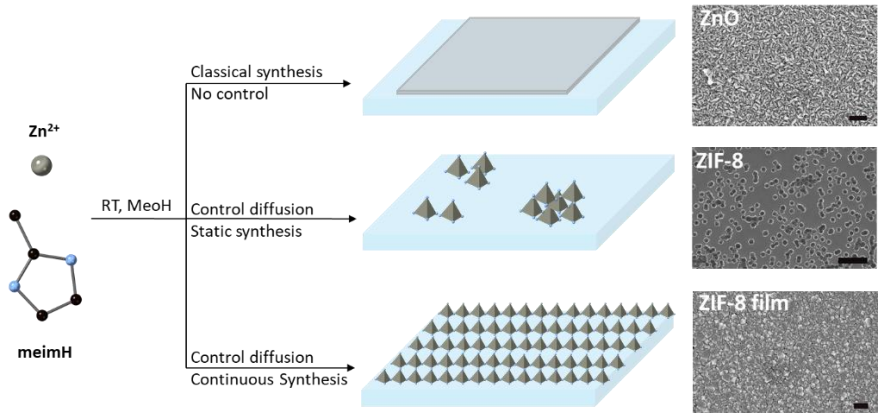

Figure 4.13 Schematic representation of different options of crystal growth of **ZIF-8** discussed in this work.

4.3 Conclusions

Reaction-diffusion (RD) systems are natural resources to control chemical reactions that permit to achieve functional morphologies or non-conventional compounds. The principles of RD can be applied to more sophisticated materials than ionic salt compounds, as commonly used, such as metal-organic frameworks. The study of RD in MOFs offer novel experiments to understand the assembly and the importance of mass transport during chemical reactions. Microfluidic systems as RD platforms offer a huge range of tunability of chemical variables to do more complete studies. The possibility to use metal oxides substrates and microfluidic chips in a solid-liquid phase reaction opens the door to study the growth of functional materials and control that growth to design and direct their assembly, in, for example, films (2D arrangements). We demonstrate the

applicability of microfluidic to the synthesis of MOFs, in particular ZIFs, obtaining at the last step a film of **ZIF-8** in a cheap and easy methodology with a potential application in the membranes industry.

4.4 Methods

Materials. PDMS base and curing agent were purchased as a Sylgard 184 Silicone elastomer kit from Dow Europe, Wiesbaden, Germany.2-methylimidazole (2meimH) was obtained from Sigma-Aldrich (St. Louis, USA). All reagents and solvents were commercially available and used without further purification.

ZnO Coated Glass Surfaces. ZnO films were deposited via Aerosol Assisted metal-organic chemical vapor deposition (MOCVD) using a homemade system. A 0.01 m trifluoroacetylacetonate (Strem Chemicals, Newburyport, Massachusetts, USA) solution in 0.5 L of absolute ethanol (Sigma-Aldrich, 99%, St. Louis, USA) was prepared. This precursor solution was atomized into fine droplets by a piezoelectric ceramic at 4.2 Hz and 6 W, forming a mist on top of the solution. The mist was then transported by a flow of nitrogen (2 L min^{-1}) into the deposition chamber (consuming the solution at a rate of 1.5 mL min^{-1}). The oxidizing gas flow was obtained by mixing 3 L min^{-1} flow of N_2 with a 5 L min^{-1} flow of air (12% of O_2). The oxidizing flow was divided into two separate lines: one that was bubbled through water at room temperature, to maintain humidity during the deposition process, and a second that was fed directly to the reactor. The humidity of the carrier gas could then be controlled by adjusting the relative flow rates. The deposition chamber was maintained

at close to atmospheric pressure, with deposition being performed at 335 °C onto planar glass substrates (Carl Roth, Karlsruhe, Germany).

Microfluidic Device Fabrication. The silicon master molds used in the fabrication of microfluidic devices were fabricated using standard photolithography techniques. Subsequently, a replica molding workflow was used to produce the microfluidic devices themselves. First, the silicon master mold was passivated with chlorotrimethylsilane under vacuum for 30 min. Then a mixture of PDMS base and curing agent (Sylgard 184 Silicone elastomer kit) mixed in a 10:1 ratio by weight was cast against the mold and cured at 70 °C overnight. The cured PDMS was peeled off the master mold and diced using a razor blade. The inlets and the outlet were formed using a 1.5 mm biopsy punch (1.5 mm, Miltex GmBH, Rietheim-Weilheim, Germany). All channels in the Y-shaped microfluidic device had a height of 50 μm, with the main channel having a width of 300 μm.

Static synthesis of ZIF-8 through PDMS on ZnO surfaces. Prior to experiments, all devices were clamped mechanically using a homemade stainless steel clamp over the ZnO coated glass slides. The 2meimH saturated solution was prepared by dissolving 0.7 g of 2meimH in 12 mL of methanol. Then, the 2meimH solution is deposited top on a PDMS piece (2 cm and 200 μm size) over the ZnO coated glass slide for a different time.

Microfluidic synthesis of ZIF-8 on ZnO surfaces. Prior to experiments, all microfluidics devices were clamped mechanically using a homemade stainless steel clamp over the ZnO coated glass slides. The 2meimH saturated solution was prepared by dissolving 0.7 g of 2meimH in 12 mL of methanol. Finally, the mixture was filtered using 0.45 μm Teflon syringe

filters (Merck KGaA, Darmstadt, Germany). A saturated solution of 2meimH was pumped at 10 μL min^{-1} through one inlet, ZnO was exposed to the solution overnight, a period of 16 h. Finally, the surface was rinsed with MeOH to eliminate excess 2meimH solution.

SEM. The SEM studies were performed on a Zeiss Ultra 55 microscope operating at an accelerating voltage of 5 kV. Samples were coated with a 4 nm thick film consisting of a mixture of Pt/Pd using a sputter Quorum Q150T-S.

X-ray diffraction. X-ray diffraction was measured with a Panalytical Empyrean diffractometer equipped with Cu Kα (λ = 1.54056 Å). Single scans were acquired in the 2θ = 5°–40° range in Bragg–Brentano geometry in air.

Raman. Raman spectra were acquired with a micro-Raman (model XploRA ONE from Horiba, Kyoto, Japan) with a grating of 2400 gr/mm, slit of 50 μm, and hole of 500 μm. The employed wavelength was 532 nm.

4.5 References

(1) Moghadam, P. Z.; Li, A.; Liu, X.-W.; Bueno-Perez, R.; Wang, S.-D.; Wiggin, S. B.; Wood, P. A.; Fairen-Jimenez, D. Targeted Classification of Metal–Organic Frameworks in the Cambridge Structural Database (CSD). *Chem. Sci.* **2020**, *11* (32), 8373–8387.

(2) Stock, N.; Biswas, S. Synthesis of Metal-Organic Frameworks (MOFs): Routes to Various MOF Topologies, Morphologies, and Composites. *Chem. Rev.* **2012**, *112* (2), 933–969.

(3) Grzybowski, B. A. *Chemistry in Motion*; John Wiley & Sons, Ltd: Chichester, UK, 2009.

(4) Saliba, D.; Ammar, M.; Rammal, M.; Al-Ghoul, M.; Hmadeh, M. Crystal Growth of ZIF-8, ZIF-67, and Their Mixed-Metal Derivatives. *J. Am. Chem. Soc.* **2018**, *140* (5), 1812–1823.

(5) Park, J. H.; Paczesny, J.; Kim, N.; Grzybowski, B. A. Shaping Microcrystals of Metal–Organic Frameworks by Reaction–Diffusion. *Angew. Chemie - Int. Ed.* **2020**, *59* (26), 10301–10305.

(6) Puigmartí-Luis, J. Microfluidic Platforms: A Mainstream Technology for the Preparation of Crystals. *Chem. Soc. Rev.* **2014**, *43* (7), 2253–2271.

(7) Gonidec, M.; Puigmartí-Luis, J. Continuous- versus Segmented-Flow Microfluidic Synthesis in Materials Science. *Crystals* **2018**, *9* (1), 12.

(8) Puigmartí-Luis, J.; Schaffhauser, D.; Burg, B. R.; Dittrich, P. S. A Microfluidic Approach for the Formation of Conductive Nanowires and Hollow Hybrid Structures. *Adv. Mater.* **2010**, *22* (20), 2255–2259.

(9) Rubio-Martinez, M.; Imaz, I.; Domingo, N.; Abrishamkar, A.; Mayor, T. S.; Rossi, R. M.; Carbonell, C.; deMello, A. J.; Amabilino, D. B.; Maspoch, D.; Puigmartí-Luis, J. Freezing the Nonclassical Crystal Growth of a Coordination Polymer Using Controlled Dynamic Gradients. *Adv. Mater.* **2016**, *28* (37), 8150–8155.

(10) Franco, C.; Rodríguez-San-Miguel, D.; Sorrenti, A.; Sevim, S.; Pons, R.; Platero-Prats, A. E.; Pavlovic, M.; Szilágyi, I.; Ruiz Gonzalez, M. L.; González-Calbet, J. M.; Bochicchio, D.; Pesce, L.; Pavan, G. M.; Imaz, I.; Cano-Sarabia, M.; Maspoch, D.; Pané, S.; De Mello, A. J.; Zamora, F.; Puigmartí-Luis, J. Biomimetic Synthesis of Sub-20 Nm Covalent Organic Frameworks in Water. *J. Am. Chem. Soc.* **2020**, *142* (7), 3540–3547.

(11) Sorrenti, A.; Jones, L.; Sevim, S.; Cao, X.; deMello, A. J.; Martí-Gastaldo, C.; Puigmartí-Luis, J. Growing and Shaping Metal–Organic Framework Single Crystals at the Millimeter Scale. *J. Am. Chem. Soc.* **2020**, *142* (20), 9372–9381.

(12) Cravillon, J.; Nayuk, R.; Springer, S.; Feldhoff, A.; Huber, K.; Wiebcke, M. Controlling

Zeolitic Imidazolate Framework Nano- and Microcrystal Formation: Insight into Crystal Growth by Time-Resolved in Situ Static Light Scattering. *Chem. Mater.* **2011**, *23* (8), 2130–2141.

(13) Sevim, S.; Franco, C.; Liu, H.; Roussel, H.; Rapenne, L.; Rubio-Zuazo, J.; Chen, X.; Pané, S.; Muñoz-Rojas, D.; DeMello, A. J.; Puigmartí-Luis, J. In-Flow MOF Lithography. *Adv. Mater. Technol.* **2019**, *4* (6), 1800666.

(14) Zhu, H.; Liu, D. The Synthetic Strategies of Metal–Organic Framework Membranes, Films and 2D MOFs and Their Applications in Devices. *J. Mater. Chem. A* **2019**, *7* (37), 21004–21035.

(15) Shekhah, O.; Chernikova, V.; Belmabkhout, Y.; Eddaoudi, M. Metal–Organic Framework Membranes: From Fabrication to Gas Separation. *Crystals* **2018**, *8* (11), 412.

(16) Hao, J.; Babu, D. J.; Liu, Q.; Chi, H. Y.; Lu, C.; Liu, Y.; Agrawal, K. V. Synthesis of High-Performance Polycrystalline Metal-Organic Framework Membranes at Room Temperature in a Few Minutes. *J. Mater. Chem. A* **2020**, *8* (16), 7633–7640.

Chapter 5

MUV-1-Cl: a 2D molecular material

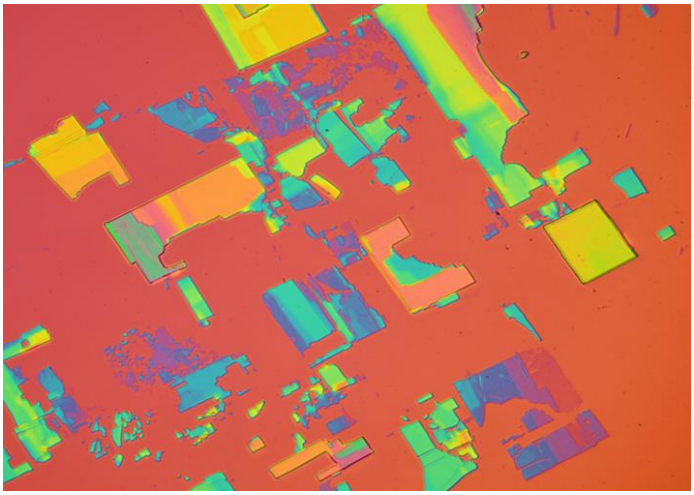

5.1 Introduction

Chapters 1.2, 2 and 3 have demonstrated that molecular chemistry is a powerful tool for the design coordination materials. For example, a huge family of coordination compounds analogues to zeolites can be obtained by chemical design using imidazole derivatives.[1,2] Different topologies can be achieved by the zeolitic imidazolate frameworks (ZIFS), tuning the crystal structure and functionalization by removing the functional groups in the organic part (Figure 5.1).[3] Despite their huge interest, ZIFs cannot compete with zeolites in applications where the thermal stability is essential, such as petroleum cracking and other industrial processing. However, their ample chemical versatility, resulting from their molecular nature,[4] results in attractive materials in other fields such as heterogeneous catalysis, membranes, heterostructures or bioapplications.[5–10] ZIFs can complement zeolites due to their easier functionalization (they are formed by organic ligands). The variety of metal centers accecible, control of topology through crystal engineering using different ligands, or higher biocompatibility due to their hybrid nature. An example of this versatility is the well-known and discussed ZIF-8. It can be synthesized with different metals, such as Zn, Co, Mn, Mg, Cd, and Fe, but it is also possible to functionalize the linker, obtaining isoreticular compounds, such as ZIF-7 (with benzimidazole), ZIF-90 (with 2-Imidazolecarboxaldehyde) and ZIF-65 (with 2-Nitroimidazole).

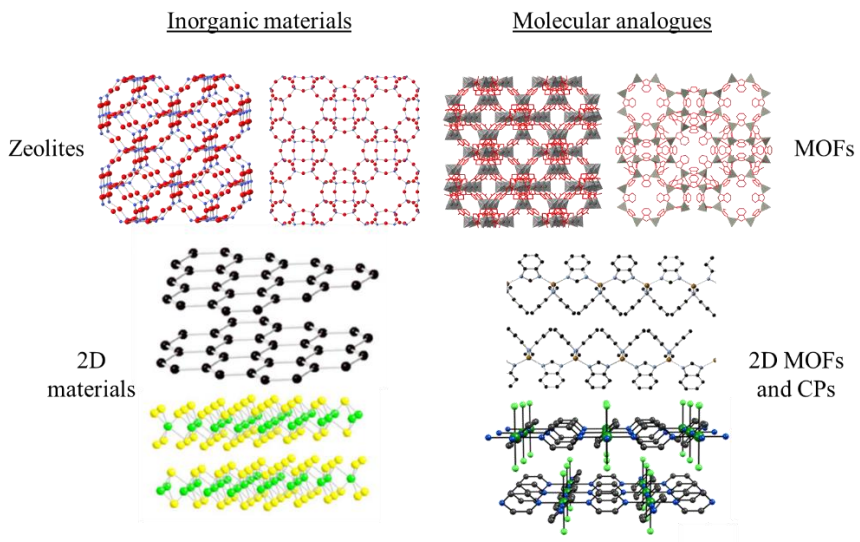

Figure 5.1 Analogy of classical inorganic materials and molecular analogues. The main difference is the composition which is based on atoms in inorganic materials or on molecules in the molecular based materials. The molecular nature of coordination compounds permits more precise chemistry design and higher tunability in their properties.

Besides porous materials, this chemical design approach can also be applied in other interesting fields such as two-dimensional materials (2D), which belong to the inorganic from point of view of compounds. Since the isolation of graphene in 2004,[11] this class of materials were popularized due to their unusual physical exotic properties related to the confinement in two-dimensions.[12] The physical phenomena were novel and interesting, still most of these materials were based on well-known inorganic layered structures reported in the 60s,[13] such as transition metal dichalcogenides, boron nitride or black phosphorous. Chemistry and, in particular, coordination chemistry, can contribute with novel materials in a similar

manner as ZIFs contribute to zeolites, bringing properties difficult or impossible to incorporate in inorganic 2D materials (Figure 5.1). For example, the incorporation of long-range ordered functionalities is difficult to achieve in inorganic 2D materials, but should be achievable in a 2D molecular material thanks to the hybrid nature of the molecules. The incorporation of magnetic order is another interesting property[14] which is difficult to study in inorganic 2D materials since they use to be air-unstable.[15,16] In this aspect 2D coordination polymers can be advantageous since they are generally air-stable and easily accommodate magnetic ion in the metallic nodes, while a vast library of ligands and SBUs permit to adjust the desired properties through chemical design.[17,18]

Nevertheless, coordination compounds present some disadvantages, like their fragility to the mechanical exfoliation.[19] For this reason, liquid assisted exfoliation has been primarily used for this purpose.[20,21] Although liquid exfoliation has advantages, such as the quantity of the exfoliated materials or better processability in solution, it often leads to lower quality flakes with smaller sizes than those obtained by dry mechanical exfoliation. This often limits the use of these flakes in 2D physics or electronics where the quality of the materials is a must.

In this chapter, we present a novel layered MOF composed of robust bonds between Fe(II) metallic nodes and 5-Chlorobenzimidazole as the ligand. The compound is prepared by a solvent-free approximation. Its extraordinary robustness, chemical stability and crystallinity permit its mechanical exfoliation and the investigation of its mechanical and magnetic properties, unprecedented in the coordination field.

5.2 Results and discussion

Synthesis of the layered MUV-1-Cl. The solvent-free reaction of 5-Chlorobenzimidazole (ClbimH) and ferrocene, adapting a previously described method for the preparation of iron azolates,[22,23] yields large, around 400 μm, laminar colorless crystals of formula [Fe(Clbim)$_2$] (abbreviated as **MUV-1-Cl**) (Figure 5.2).

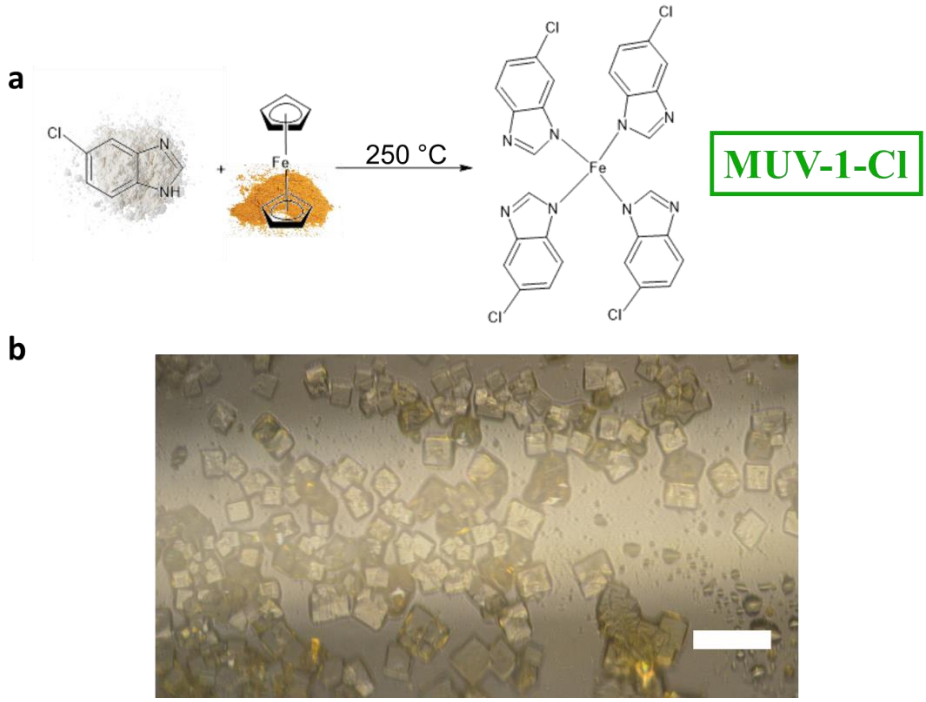

Figure 5.2 a) Schematic solvent-free synthesis of **MUV-1-Cl** based in benzimidazole derivate and ferrocene. b) Crystals of MUV-1-CL as synthesized inside the reaction tube. Scale bar is 400μm.

X-ray single crystal diffraction reveals that the structure of **MUV-1-Cl** is formed by distorted tetrahedral Fe(II) centers connected by 5-

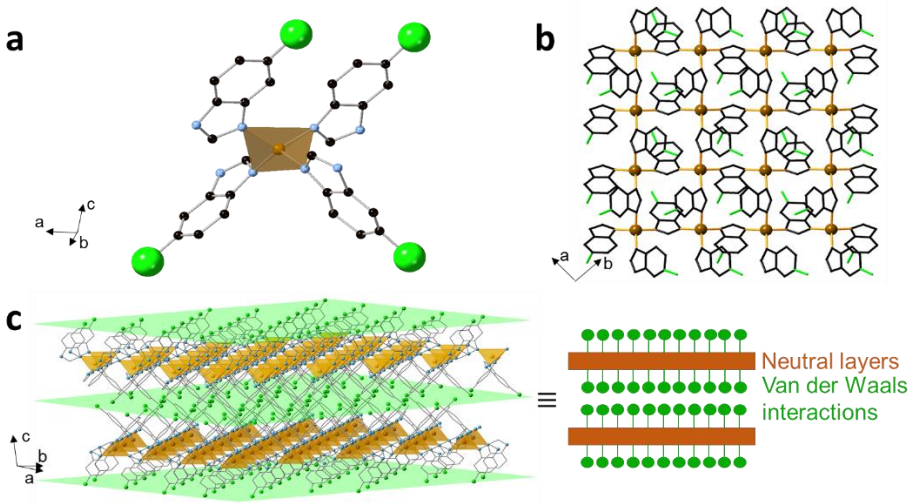

Figure 5.3 a) The tetrahedral environment of the Fe(II) centers. b) The square lattice extended in the *ab* plane. c) Layered structure of **MUV-1-Cl** showing the Cl atoms located at the surface of the layers, represented as green planes. Fe(II) centers are shown in orange (polyhedral representation), nitrogen atoms shown in blue, carbon atoms shown in black and chloride atoms shown in green. Hydrogen atoms have been omitted for clarity.

chlorobenzimidazolate bridges (Figure 5.3a) forming a neutral layered coordination polymer extended in the *ab* plane (Figure 5.3b). These layers weakly interact with each other through van der Waals interactions (Cl···Cl interactions). The compound is related to the diamagnetic Zn(II) analog [Zn(bimH)$_2$], which was obtained via the decomposition of a 3D MOF or by direct synthesis.[24] In these molecular layers, the Fe(II) atoms are located in the inner part of the layers whereas the Cl substituents are positioned at

the surface (Figure 5.3c), thus playing an active role in the chemical behavior of the molecular interface.

In the layer the Fe(II) centers form a square lattice with a distance between the metal centers of 5.9 Å (Figures 5.3b and 5.4a). The connection of the metal centers is through the benzimidazolate, by the nitrogen heteroatoms. These bonds define the short pathway Fe-N-C-N-Fe with a distance bond Fe-N of 2.0 Å. The ligands which connect these metallic nodes shape an angle of 47.7° between the *ab* plane formed by the square lattice and the tilt of the ligand (Figure 5.4b).

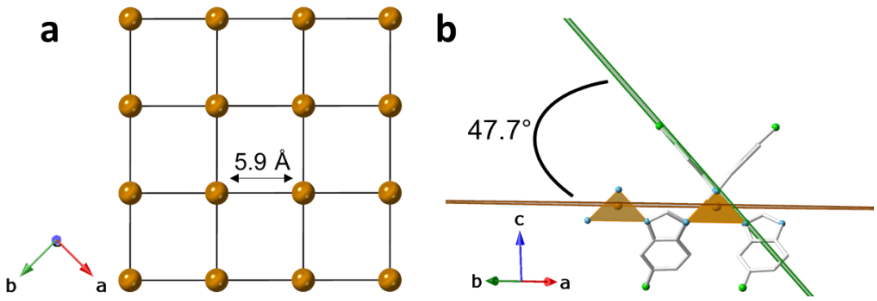

Figure 5.4 a) Square lattice formed by the Fe(II) with a 5.9 Å distance. b) Angle formed by the ligand and the *ab* plane composed by the metal centers.

The position of the chloride atom in the ligand is indistinguishable between the 5th and 6th position due to the deprotonation of the benzimidazole. These two positions provoke a disorder in the crystal structure, originating an infinite number of possibilities for the stacking of the layers (Figure 5.5).

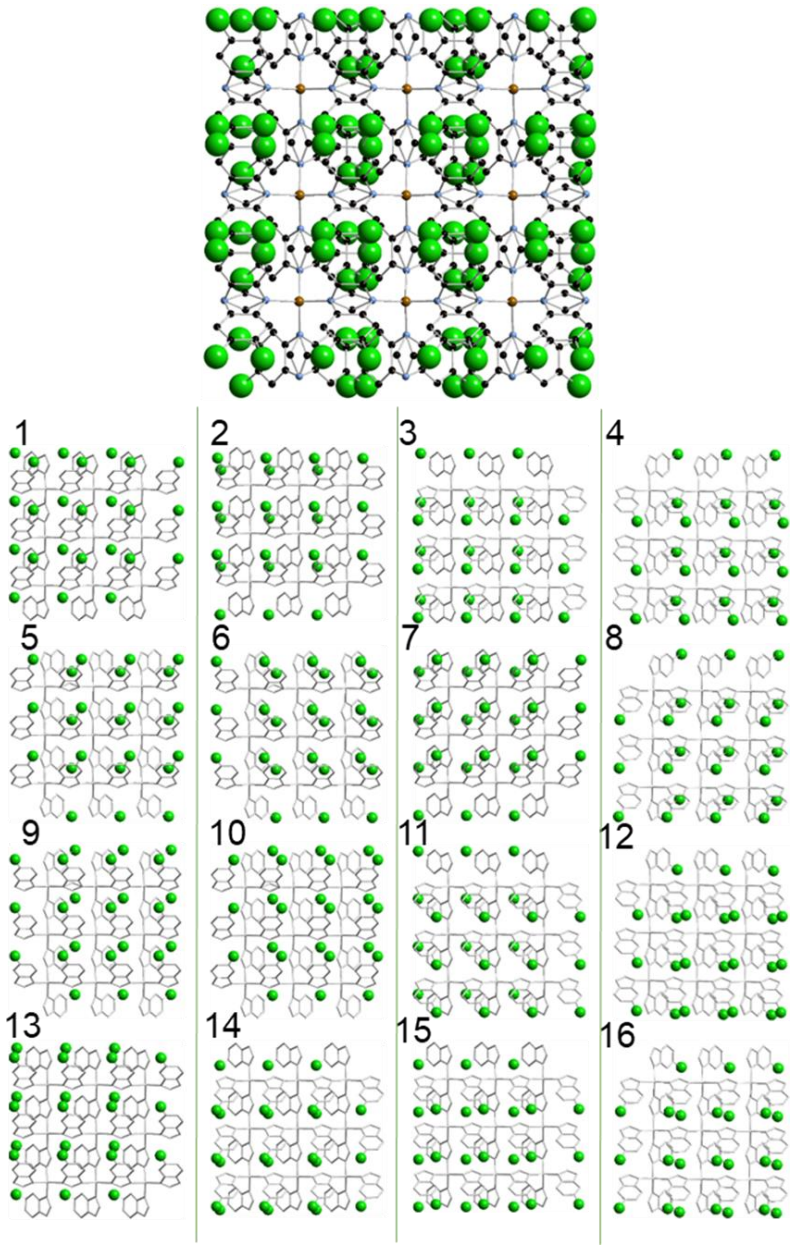

Figure 5.5 Structures for the different possible positions of chloride atoms for **MUV-1-Cl,** provoking different stackings of the layers for the bulk material.

The room temperature infrared and Raman spectra present coincident peaks, indicating a non-centrosymmetric structure (Figure 5.6). Furthermore, in collaboration with Prof. J. C. Waerenborgh and B. J. C. Vieira at Centro de Ciências e Tecnologias Nucleares, room temperature

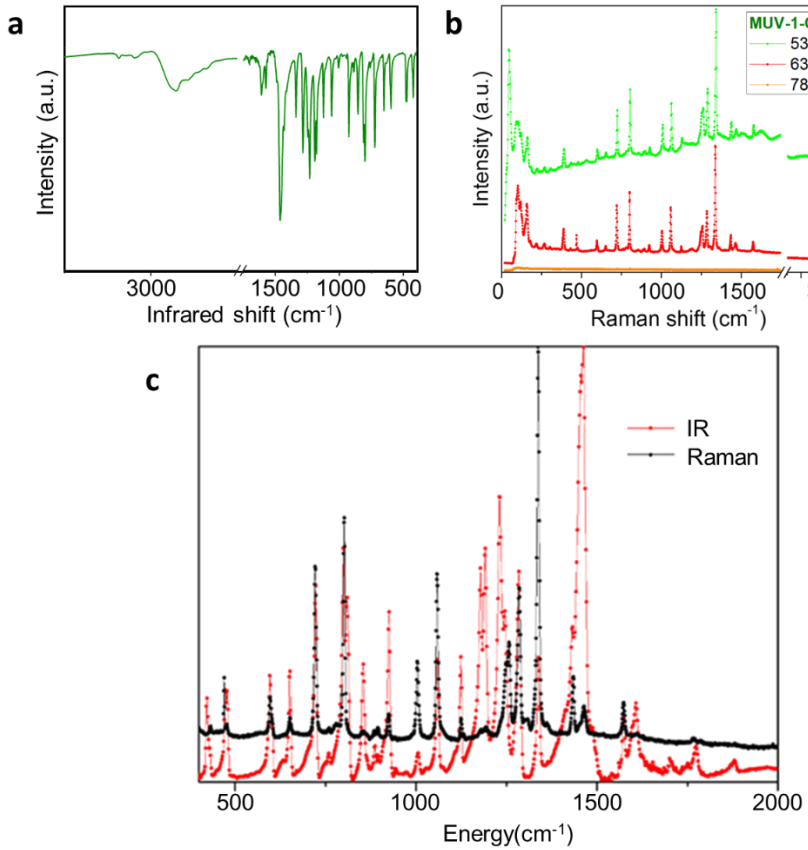

Figure 5.6 a) Infrared spectra of bulk crystals of **MUV-1-Cl.** b) Raman spectra of **MUV-1-Cl.** c) Comparison of Raman spectra and infrared spectra for **MUV-1-Cl.**

Mossbauer spectra were performed. These spectra consist of two doublets with the same relative area for Fe(II), indicating the presence of

two different Fe(II) sites with the same multiplicity. These features are consistent with the space group *C*2, although the presence of a racemic mixture causes a better refinement of the single-crystal X-ray data in the *C*2/*c* space group. This is related to the weak interlayer interactions, which prevent long-range order in the *c* direction, but which is advantageous for exfoliation, as will be described below.

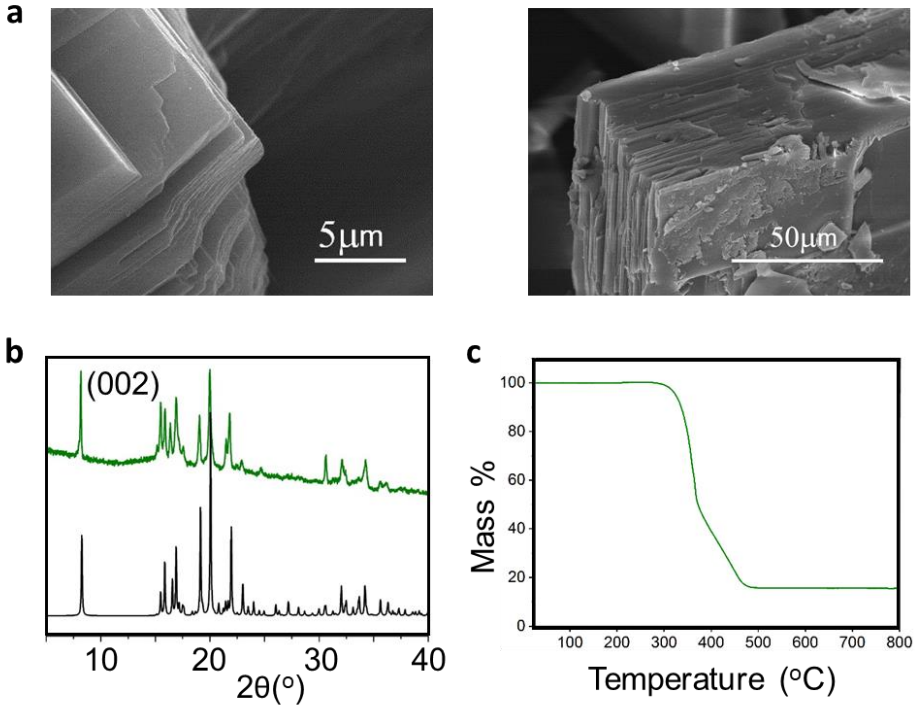

Figure 5.7 a) Scanning electron micrograph of bulk-type **MUV-1-Cl** b) X-ray powder patterns of **MUV-1-Cl**. The experimental pattern is shown in green and the calculated pattern from single-crystal data is shown in black. c) Thermal gravimetric analysis (TGA) of bulk crystals of **MUV-1-Cl.**

A close-up view with scanning electron microscopy (SEM) evidences the layered structure of **MUV-1-Cl** (Figure 5.7a), with a typical size of 400 µm approximately, whose purity is confirmed by powder X-ray diffraction (Figure 5.7b). The thermal stability, determined by thermal gravimetric analysis at a heating rate of 5 °C min^{-1}, indicates that it and decomposes at 350 °C (Figure 5.7c). In contrast to other coordination polymers, **MUV-1-Cl** exhibit high crystallinity, a layered structure and big size. Those features make this material a serious candidate to become a high quality 2D molecular material. Its thermal stability also permits to perform in the exfoliated layers an annealing to eliminate solvent from the ambient conditions or traces of glue from the micro-mechanical exfoliation.

The superexchange pathway between the Fe(II) centers, provided by the 5-Chlorobenzimidazolate bridges, facilitates the presence of magnetic exchange interactions in **MUV-1-Cl** (Figure 5.8a), as evidenced in the plot of the molar magnetic susceptibility (χ_m) as a function of the temperature (Figure 5.8b). The χ_m *vs.* T curve exhibits a broad maximum at 30.0 K and a sharp peak at *ca.* 20 K. In the plot of $\chi_m T$ *vs.* T, a $\chi_m T$ value of 2.94 emu·mol^{-1}·K is observed at room temperature, in agreement with that expected for a high-spin Fe(II), S = 2 (3.0 emu·mol^{-1}·K where g = 2.0), which decreases upon cooling down to 20 K (Figure 5.8c). The behavior in this region indicates the presence of dominant antiferromagnetic (AF) exchange coupling between the Fe(II) centers, confirmed by a negative Curie-Weiss temperature, θ = –80.6 K.

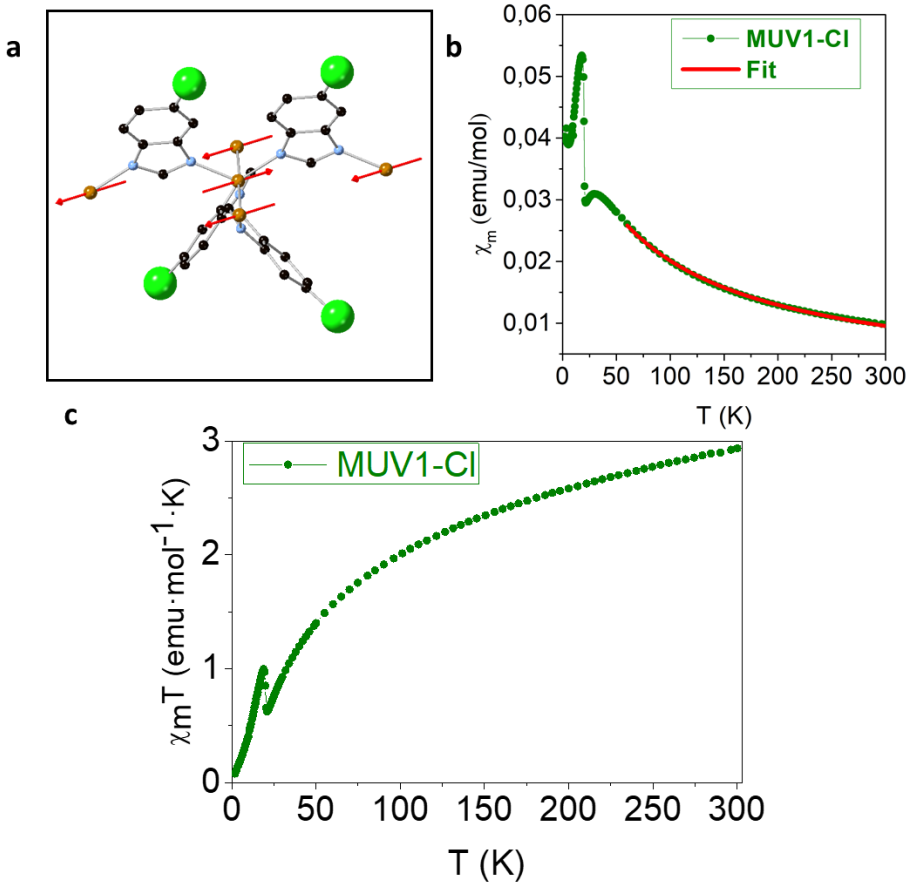

Figure 5.8 a) The magnetic pathway through the N-C-N bridges connecting Fe(II) centers b) Thermal dependence of the magnetic susceptibility (χ_m) in the temperature range 2-300 K. The data have been fitted following a Curie-Weiss law in the high-temperature range (60–300 K). c) Thermal dependence of the product of magnetic susceptibility and temperature ($\chi_m T$) in the temperature range 2-300 K showing an increase of the product around 20 K.

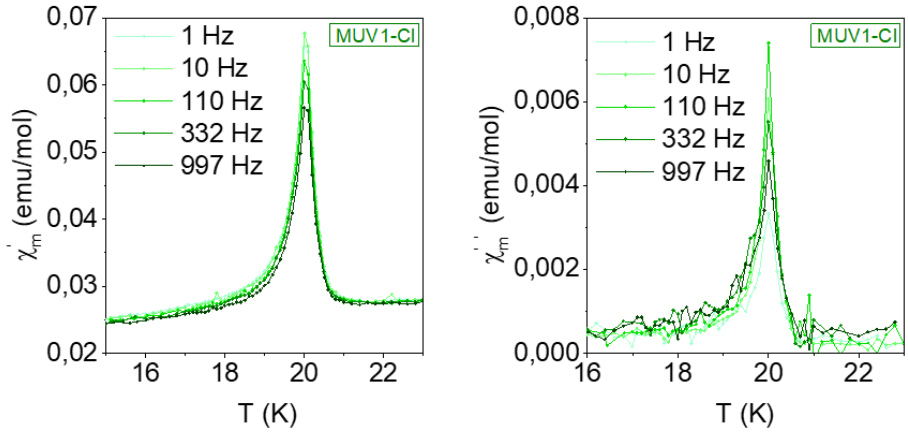

Figure 5.9 In-phase (left) and out-of-phase (right) dynamic susceptibility of **MUV-1-Cl** measured at different frequencies

The abrupt increase in both χ_m and $\chi_m T$ suggests the occurrence of a magnetic transition towards a canted spin structure below the Néel temperature, T_N, of 20 K. The presence of an out-of-phase susceptibility signal below 20 K in the *ac* measurements confirms this kind of magnetic order (Figure 5.9).

Powder neutron diffraction studies were performed in collaboration with Prof. Rodríguez-Velamazán at Institut Laue-Langevin. The data were collected at 1.8 K and 30 K, i.e. below and above the ordering temperature (Figure 5.10). They provide further support on the antiferromagnetic ordering in this material. Still, in the present case, these measurements are unable to detect the presence of the spin canting, which is below the limit of detection of these measurements, mainly due to the small value of the ferromagnetic component resulting from canting as shown by susceptibility measurements.

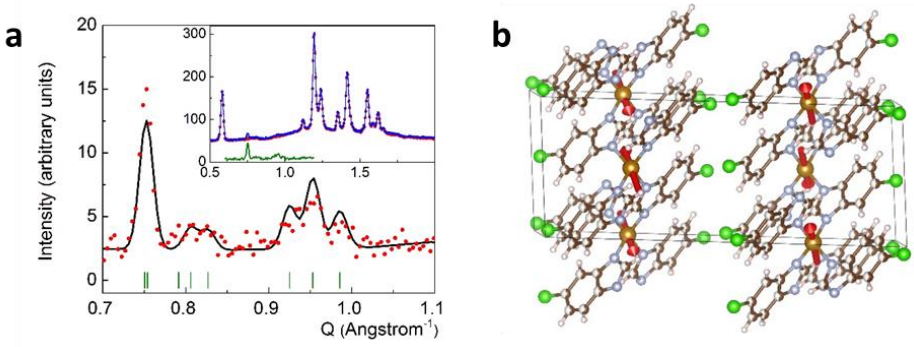

Figure 5.10 a) Difference neutron diffraction pattern (red symbols) between the measurements at 1.8 K and 30 K and Rietveld refinement of the magnetic model (black line) for **MUV-1-Cl**. The inset represents the experimental powder neutron diffraction patterns collected at 1.8 K (blue) and 30 K (red). The difference diffraction pattern (green, rescaled for clarity) stands for the contribution of the magnetic phase. b) View of the crystal and magnetic structures of **MUV-1-Cl** with the magnetic moments represented as red arrows.

Exploring the 2D limit. The layered nature of **MUV-1-Cl** and the absence of strong intermolecular interactions between adjacent layers prompted us to explore the possibility of mechanically exfoliating this material by the so-called *Scotch-tape* method, a conventional approach usually employed for graphene and other 2D materials, but rather scarce in coordination polymers due to the fragile nature of the crystals.[19] The advantage of this dry method over liquid exfoliation is the potential achieving of atomically thin-layers with high crystallinity, low amounts of defects and larger lateral sizes.

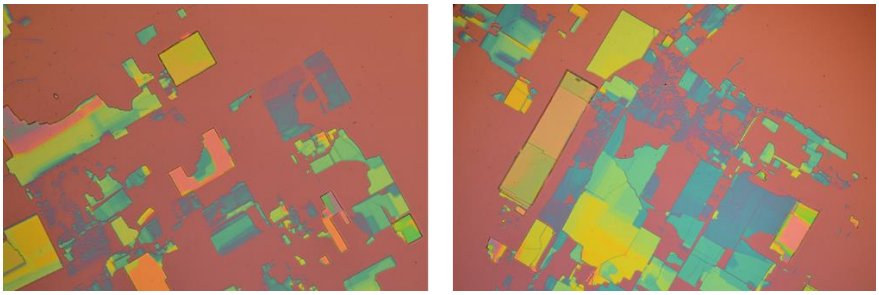

Figure 5.11 Typical *Scotch-tape* methodology for **MUV-1-Cl** exfoliation, showing a plethora of flakes on a silicon oxide substrate.

Bulk crystals of **MUV-1-Cl** were exfoliated using a plastic tape (Ultron Systems) and deposited onto a silicon substrate with 285 nm of thermally grown SiO_2. As a result, a plethora of flakes with remarkable well-defined rectangular shapes (lateral dimensions > 1 μm) and different thicknesses (ranging from a single layer up to hundreds of nanometers) were obtained, as can be clearly seen by optical (Figure 5.11) and atomic force (AFM) microscopies (Figure 5.12a). This contrasts with the lower quality nanosheets obtained in a Zn(II) analog compound by liquid exfoliation.[24] Remarkably, a monolayer of dimensions 4 x 1.5 μm^2 has been isolated (Figure 5.12a). The crystallinity, chemical composition and integrity of the exfoliated flakes were confirmed through Transmission Electron Microscopy (TEM) and Raman studies on specimens of different thicknesses (Figures 5.12b-c). To the best of our knowledge, this is the first time that selected-area electron diffraction (SAED) patterns have been obtained in a top-down micromechanically exfoliated LCP (Figure 5.12c). Previous reports indicated that these SAED patterns were only observed in

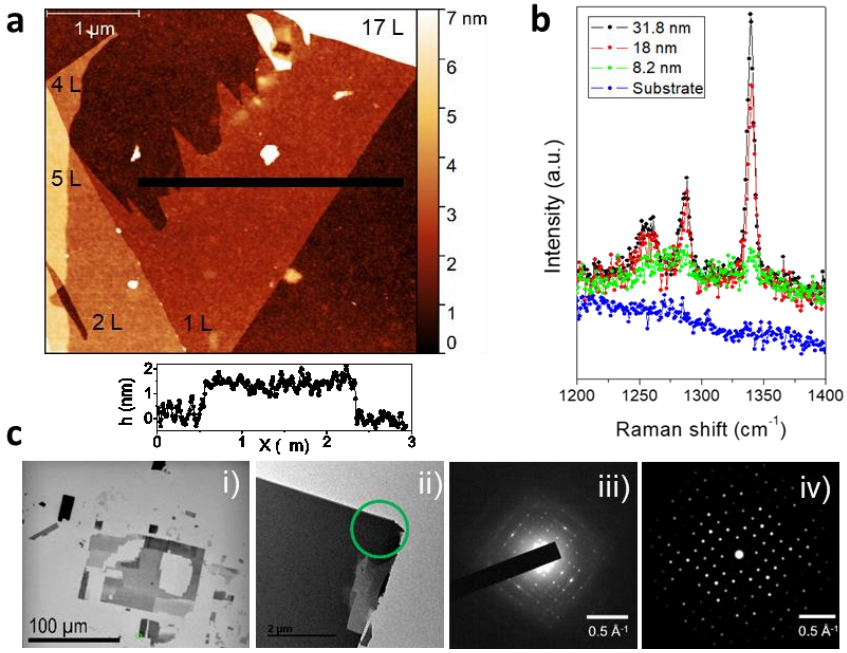

Figure 5.12 a) Atomic-force image with its profile of height for a flake of **MUV-1-Cl**. A different number of exfoliated layers are indicated in the image. b) Raman spectra for **MUV-1-Cl** flakes with different thicknesses. c) i: Low-magnification TEM image for **MUV-1-Cl** flakes, where darker gray areas are associated with thicker flakes. ii: A selected area (enclosed by a green circle on the TEM image) for which the experimental SAED pattern was obtained that corresponds to the [0 0 1] zone axis (iii), and which is in very good agreement with the simulated SAED pattern (iv).

inorganic materials, mainly members of transition metal dichalcogenides.[25,26]

The indexation of these patterns indicates that they correspond to the zone axis [0 0 1], confirming that the exfoliated flakes consist of one or

several layers stacking along the *c* axis. The close resemblance between the experimental and the simulated patterns (Figure 5.12c) provides further evidence of that. Moreover, the well-defined Bragg peaks observed in the SAED patterns point out that the exfoliation process does not damage the structure of the LCP, and the obtained flakes retain the crystallinity of the bulk material.

Note that some of the SAED patterns were obtained from layers as thin as 20 nm, which is a remarkable result due to the molecular nature of the material. No thickness-dependence of the unit cell or Raman peaks shift, compared to their bulk counterparts, were observed.

Mechanical properties. Apart from all the interesting properties to study in 2D materials, they can be integrated as nanodrums in devices, for example in mechanical resonators.[27–29] This part was performed collaboration with Prof. Steeneken and Prof. van der Zant at TU Delft. Their extraordinary micromechanical properties as Young's modulus elasticity and breaking strength make them perfect candidates to construct mass and pressure sensors.[30] The small mass of the 2D flakes in the devices is very sensitive to mass changes and this permit the detection of very small amounts of chemicals, for example, of gasses.[31] In this field, the incorporation of functional groups to the 2D materials it would also be interesting because apart from sensibility, selectivity can be important and interesting for particular gasses sensing.

The ability to tailor the functionality of **MUV-1-Cl**, combined with its mechanical resonant readout makes it attractive for sensing applications because the resonance frequency and Q-factor of these suspended

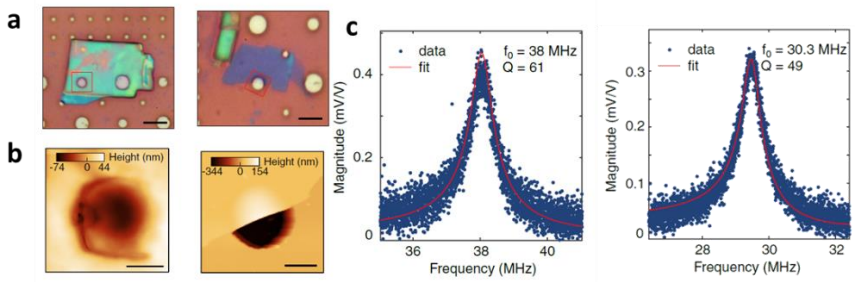

Figure 5.13 a)Optical images of two **MUV-1-Cl** flakes transferred on top of circular cavities on a Si/SiO_2 substrate (scale bars: 5 μm). left, the flake is 74 nm height; right, the flake is 20 nm height. The red boxes indicate the regions where AFM has been measured. b) AFM images of the two drums taken in the area enclosed by the red boxes in **a** (scale bars: 1 μm). left, the drum corresponds to the flake of 74 nm height shown in panel a, left; right, the drum corresponds to the flake of 20 nm height shown in the panel, a, right. c)Two frequency-domain measurements on two different nanomechanical resonators made of **MUV-1-Cl**, with thicknesses of 70 – 80 nm. These are similar to the ones shown in panels a,b. The extracted resonance frequencies and quality factors of the two resonators are shown in the top right corner.

membranes are expected to depend strongly on the mass and adhesion of captured molecules. To demonstrate this concept, we exfoliate and transfer thin flakes of **MUV-1-Cl** on top of a Si/SiO_2 substrate with prepatterned circular cavities. In Figure 5.13a we show optical images of two exemplary flakes transferred on top of cavities, forming suspended nanodrums. The AFM images of the drums (areas enclosed by the red boxes) are shown in Figure 5.13b. The device shown in the left panel of Figure 5.13b is 74 nm

thick, whereas the thickness of the one shown in the right panel is measured to be 20 nm. In Figure 5.13c we show the mechanical frequency response of two **MUV-1-Cl** nanodrums (with thicknesses of 70 – 80 nm). The measurements are performed in vacuum, using a laser interferometry setup, described in the Methods section. The resonance frequencies of the drums are 38 MHz and 30.3 MHz, with quality (Q) factors in the range of 45 – 65. This variation may result from a combination of different thicknesses and geometries of the drums.

The Q factors are comparable to those reported in nanomechanical resonators made of graphene and other two-dimensional materials.[28,29] The lower Q factors may be due to viscoelastic damping in this polymer material. Because of the large diameter-to-thickness ratio, the resonance frequencies of these nanodrums are mainly determined by the bending rigidity of the material. For the given resonance frequencies and geometry of the drums, we thus estimate the Young's modulus of **MUV-1-Cl** to be 3 – 7 GPa, which is almost three orders of magnitude lower than that of graphene and similar to that previously reported for a layered coordination polymer measured by AFM nanoindentation.[32] The results show that these polymer resonators, despite their low Young's modulus and despite potential viscous damping mechanisms, have surprisingly high Q factors and resonance frequencies, which are comparable to graphene membranes. In combination with their low weight and tunable functionalization these materials can be used to create future platforms for resonance based sensing.

5.3 Conclusions

In this work, we have presented a general strategy for the synthesis of a crystalline layered coordination polymer (LCP) exhibiting a magnetic order. Interestingly and in contrast with most of the reported MOFs, large crystals of this coordination polymer has been grown using a solvent-free synthesis. Such a possibility together with the layered nature of these materials and the very weak van der Waals forces between the layers have permitted isolation of micrometer size atomically-thin flakes down to the monolayer by mechanical and dry exfoliation methods. The high crystallinity, integrity and chemical composition of these mechanically exfoliated layers has been confirmed by TEM and Raman studies on LCP of different thicknesses.

On the other hand, and in contrast to what happens in the few examples of reported 2D ferromagnets based on solid state chemistry,[15] which have shown to be highly unstable in open air, this coordination chemistry approach has afforded the isolation of robust 2D magnetic materials. Such robustness has also enabled us to study the mechanical properties of these atomically-thin layers, a possibility that is unprecedented for coordination polymers. In fact, these 2D magnetic coordination polymers can lead towards the preparation of high-quality resonators, a fundamental aspect in order to open up novel perspectives in the application of these materials in nanodevices. Thus, these results open the door to the integration and application of 2D coordination polymers in different technological areas like microfluidics, nanoelectronics, coatings, molecular sensing or mechanical magnetic membranes, and, last but not

least, it brings new candidates for the study of magnetism and phase transitions in the two-dimensional limit. This can permit the combination of this magnetic 2D material with superconductors or graphene, thus prompting to new materials where unconventional physical phenomena might be present, such as Majorana fermions or photomagnon couplings. All these results have been published in Nature Chemistry.[33]

5.4 Methods

Synthesis of MUV-1-Cl. Ferrocene (30 mg, 0.16 mmol) and 5-Chlorobenzimidazole (0.34 mmol) were combined and sealed under vacuum in a layering tube (4 mm diameter). The mixture was heated at 250 °C for 3 days to obtain crystals suitable for X-ray single-crystal diffraction. The product was allowed to cool to room temperature, and the layering tube was then opened. The unreacted precursors were extracted with acetonitrile and benzene, and the product was isolated as colorless crystals (yield 80 %). Phase purity was established by X-ray powder diffraction. Energy dispersive X-ray analysis (EDAX) of **MUV-1-Cl** from SEM and TEM show in both cases a 70:30 ratio for Cl:Fe.

X-ray Structural Studies. X-ray data for compound **MUV-1-Cl** was collected at a temperature of 100 K using a synchrotron radiation at single crystal X-ray diffraction beamline I19 in Diamond Light Source, equipped with a Pilatus 2M detector and an Oxford Cryosystems nitrogen flow gas system. Data was measured using GDA suite of programs.

X-ray Powder Diffraction. A polycrystalline sample of **MUV-1-Cl** was lightly ground in an agate mortar and pestle and used to fill a 0.5 mm borosilicate capillariy that was mounted and aligned on an Empyrean

PANalytical powder diffractometer, using Cu Kα radiation (λ = 1.54056 Å). Two repeated measurements were collected at room temperature (2θ = 5−40 °) and merged in a single diffractogram.

Thermogravimetric analysis. Thermogravimetric analysis of **MUV-1-Cl** was carried out with a Mettler Toledo TGA/SDTA851e/SF/1100 apparatus in the 25–800 °C temperature range under a 5°C·min^{-1} scan rate and an air flow of 30 mL·min^{-1}.

SEM. Scanning Electronic Micrographs and atomic composition of bulk samples was estimated by electron probe microanalysis (EPMA) performed in a Philips SEM XL30 equipped with an EDAX microprobe and images were recorded in a Hitachi S-4800.

Raman spectroscopy. Raman spectra were acquired with a micro-Raman (model XploRA ONE from Horiba, Kyoto, Japan) with a grating of 2400 gr/mm, slit of 50 µm, and hole of 500 µm. The employed wavelengths were 532 nm, 638 nm, and 785 nm. The power density of the laser used for spectra measured at 532 nm was 5.25 mW/µm^2 (bulk crystals) and 170 µW/µm^2 (thin-layers), for spectra measured at 638 nm it was 7.58 mW/µm^2 (bulk crystals), and for those spectra measured at 785 nm it was 7.2 mW/µm^2 (bulk crystals).

AFM. Optical images were obtained with a NIKON Eclipse LV-100 Optical microscope and AFM images were performed with a Nanoscope IVa Multimode Scanning Probe Microscope (Bruker, Karlsruhe, Germany) in tapping mode.

TEM. Several mechanical exfoliated flakes were transferred onto a grid with a membrane of amorphous SiN (50 nm thick) using a dry and deterministic method (that involves the use of a micromanipulator and PDMS/PPC polymers, as reported in ref.[25]). TEM images and diffraction patterns were acquired with a JEOL JEM-2100F with a field emission gun operating at 200 kV. The simulated SAED patterns were generated with SingleCrystal software.

Magnetic Measurements. Variable-temperature (2−300 K) direct current (dc) magnetic susceptibility measurements were carried out in applied fields of 1.0 kOe and variable field magnetization measurements up to ± 5 T at 2.0 K. The susceptibility data were corrected from the diamagnetic contributions as deduced by using Pascal's constant tables. Variable-temperature (16−23 K) alternating current (ac) magnetic susceptibility measurements in a ±4.0 G oscillating field at frequencies in the range of 1 − 997 Hz were carried out in a zero dc field.

Nanomechanical resonators. Suspended membranes were fabricated by exfoliating **MUV-1-Cl** flakes directly on top of circular cavities lithographically defined on a Si/SiO2 substrate (SiO_2 thickness: 285 nm).

Laser interferometry measurements. The motion of the **MUV-1-Cl** mechanical resonators was measured in vacuum, using a laser interferometry setup, similar to the one reported in ref. [29]. A modulated blue laser is used to sequentially heat up the membrane, bringing it into motion. A different, red laser is focused onto the suspended membrane and is partly reflected by the membrane and partly by the silicon chip underneath. As the membrane moves, the effective cavity depth is modulated. This modulates

the intensity of the reflected laser beam by interference, which is captured by a photodiode. The measurements were done in a homodyne detection scheme, using a vector network analyser.

5.5 References

(1) Park, K. S.; Ni, Z.; Côté, A. P.; Choi, J. Y.; Huang, R.; Uribe-Romo, F. J.; Chae, H. K.; O'Keeffe, M.; Yaghi, O. M. Exceptional Chemical and Thermal Stability of Zeolitic Imidazolate Frameworks. *Proc. Natl. Acad. Sci. U. S. A.* **2006**, *103* (27), 10186–10191.

(2) Banerjee, R.; Phan, A.; Wang, B.; Knobler, C.; Furukawa, H.; O'Keeffe, M.; Yaghi, O. M. High-Throughput Synthesis of Zeolitic Imidazolate Frameworks and Application to CO_2 Capture. *Science* **2008**, *319* (5865), 939–943.

(3) Yaghi, O. M.; Furukawa, H.; Morris, W.; Doonan, C. J.; Banerjee, R. Crystals as Molecules: Postsynthesis Covalent Functionalization of Zeolitic Imidazolate Frameworks. *J. Am. Chem. Soc.* **2008**, *130* (38), 12626–12627.

(4) Noh, K.; Lee, J.; Kim, J. Compositions and Structures of Zeolitic Imidazolate Frameworks. *Isr. J. Chem.* **2018**, *58* (9), 1075–1088.

(5) Zhao, S.-N.; Song, X.-Z.; Song, S.-Y.; Zhang, H. Highly Efficient Heterogeneous Catalytic Materials Derived from Metal-Organic Framework Supports/Precursors. *Coord. Chem. Rev.* **2017**, *337*, 80–96.

(6) Bavykina, A.; Kolobov, N.; Khan, I. S.; Bau, J. A.; Ramirez, A.; Gascon, J. Metal–Organic Frameworks in Heterogeneous Catalysis: Recent Progress, New Trends, and Future Perspectives. *Chem. Rev.* **2020**, *120* (16), 8468–8535.

(7) Shekhah, O.; Chernikova, V.; Belmabkhout, Y.; Eddaoudi, M. Metal–Organic Framework Membranes: From Fabrication to Gas Separation. *Crystals* **2018**, *8* (11), 412.

(8) Wang, X.; Chen, X. Z.; Alcântara, C. C. J.; Sevim, S.; Hoop, M.; Terzopoulou, A.; de Marco, C.; Hu, C.; de Mello, A. J.; Falcaro, P.; Furukawa, S.; Nelson, B. J.; Puigmartí-Luis, J.; Pané, S. MOFBOTS: Metal–Organic-Framework-Based Biomedical Microrobots. *Adv. Mater.* **2019**, *31* (27), 2–8.

(9) Astria, E.; Thonhofer, M.; Ricco, R.; Liang, W.; Chemelli, A.; Tarzia, A.; Alt, K.; Hagemeyer, C. E.; Rattenberger, J.; Schroettner, H.; Wrodnigg, T.; Amenitsch, H.; Huang, D. M.; Doonan, C. J.; Falcaro, P. Carbohydrates@MOFs. *Mater. Horizons* **2019**, *6* (5), 969–977.

(10) Liang, K.; Ricco, R.; Doherty, C. M.; Styles, M. J.; Bell, S.; Kirby, N.; Mudie, S.; Haylock,

D.; Hill, A. J.; Doonan, C. J.; Falcaro, P. Biomimetic Mineralization of Metal-Organic Frameworks as Protective Coatings for Biomacromolecules. *Nat. Commun.* **2015**, *6*, 4–11.

(11) Novoselov, K. S. Electric Field Effect in Atomically Thin Carbon Films. *Science* **2004**, *306* (5696), 666–669.

(12) Ferrari, A. C.; Bonaccorso, F.; Fal'ko, V.; Novoselov, K. S.; Roche, S.; Bøggild, P.; Borini, S.; Koppens, F. H. L.; Palermo, V.; Pugno, N.; Garrido, J. A.; Sordan, R.; Bianco, A.; Ballerini, L.; Prato, M.; Lidorikis, E.; Kivioja, J.; Marinelli, C.; Ryhänen, T.; Morpurgo, A.; Coleman, J. N.; Nicolosi, V.; Colombo, L.; Fert, A.; Garcia-Hernandez, M.; Bachtold, A.; Schneider, G. F.; Guinea, F.; Dekker, C.; Barbone, M.; Sun, Z.; Galiotis, C.; Grigorenko, A. N.; Konstantatos, G.; Kis, A.; Katsnelson, M.; Vandersypen, L.; Loiseau, A.; Morandi, V.; Neumaier, D.; Treossi, E.; Pellegrini, V.; Polini, M.; Tredicucci, A.; Williams, G. M.; Hee Hong, B.; Ahn, J.-H.; Min Kim, J.; Zirath, H.; van Wees, B. J.; van der Zant, H.; Occhipinti, L.; Di Matteo, A.; Kinloch, I. A.; Seyller, T.; Quesnel, E.; Feng, X.; Teo, K.; Rupesinghe, N.; Hakonen, P.; Neil, S. R. T.; Tannock, Q.; Löfwander, T.; Kinaret, J. Science and Technology Roadmap for Graphene, Related Two-Dimensional Crystals, and Hybrid Systems. *Nanoscale* **2015**, *7* (11), 4598–4810.

(13) Wilson, J. A.; Yoffe, A. D. The Transition Metal Dichalcogenides Discussion and Interpretation of the Observed Optical, Electrical and Structural Properties. *Adv. Phys.* **1969**, *18* (73), 193–335.

(14) Burch, K. S.; Mandrus, D.; Park, J. G. Magnetism in Two-Dimensional van Der Waals Materials. *Nature* **2018**, *563* (7729), 47–52.

(15) Huang, B.; Clark, G.; Navarro-Moratalla, E.; Klein, D. R.; Cheng, R.; Seyler, K. L.; Zhong, Di.; Schmidgall, E.; McGuire, M. A.; Cobden, D. H.; Yao, W.; Xiao, D.; Jarillo-Herrero, P.; Xu, X. Layer-Dependent Ferromagnetism in a van Der Waals Crystal down to the Monolayer Limit. *Nature* **2017**, *546* (7657), 270–273.

(16) Gong, C.; Li, L.; Li, Z.; Ji, H.; Stern, A.; Xia, Y.; Cao, T.; Bao, W.; Wang, C.; Wang, Y.; Qiu, Z. Q.; Cava, R. J.; Louie, S. G.; Xia, J.; Zhang, X. Discovery of Intrinsic Ferromagnetism in Two-Dimensional van Der Waals Crystals. *Nature* **2017**, *546* (7657), 265–269.

(17) Mínguez Espallargas, G.; Coronado, E. Magnetic Functionalities in MOFs: From the Framework to the Pore. *Chem. Soc. Rev.* **2018**, 533–557.

(18) Coronado, E. Molecular Magnetism: From Chemical Design to Spin Control in Molecules, Materials and Devices. *Nat. Rev. Mater.* **2019**.

(19) Abhervé, A.; Mañas-Valero, S.; Clemente-León, M.; Coronado, E. Graphene Related Magnetic Materials: Micromechanical Exfoliation of 2D Layered Magnets Based on Bimetallic Anilate Complexes with Inserted $[Fe^{III}(Acac_2\text{-Trien})]+$ and $[Fe^{III}(Sal_2\text{-Trien})]^+$ Molecules. *Chem. Sci.* **2015**, *6* (8), 4665–4673.

(20) Zhao, M.; Huang, Y.; Peng, Y.; Huang, Z.; Ma, Q.; Zhang, H. Two-Dimensional Metal-Organic Framework Nanosheets: Synthesis and Applications. *Chem. Soc. Rev.* **2018**, *47* (16), 6267–6295.

(21) Ashworth, D. J.; Foster, J. A. Metal-Organic Framework Nanosheets (MONs): A New Dimension in Materials Chemistry. *J. Mater. Chem. A* **2018**, *6* (34), 16292–16307.

(22) Rettig, S. J.; Storr, A.; Summers, D. A.; Thompson, R. C.; Trotter, J. Transition Metal Azolates from Metallocenes . 2 . Synthesis , X-Ray Structure , and Magnetic Properties of a Three-Dimensional Polymetallic Iron (II) Imidazolate Complex , a Low-Temperature Weak Ferromagnet. *Society* **1997**, *7863* (Ii), 8675–8680.

(23) López-Cabrelles, J.; Giménez-Marqués, M.; Mínguez Espallargas, G.; Coronado, E. Solvent-Free Synthesis of a Pillared Three-Dimensional Coordination Polymer with Magnetic Ordering. *Inorg. Chem.* **2015**, *54* (21), 10490–10496.

(24) Peng, Y.; Li, Y.; Ban, Y.; Jin, H.; Jiao, W.; Liu, X.; Yang, W. Metal-Organic Framework Nanosheets as Building Blocks for Molecular Sieving Membranes. *Science* **2014**, *346* (6215), 1356–1359.

(25) Nguyen, L.; Komsa, H. P.; Khestanova, E.; Kashtiban, R. J.; Peters, J. J. P.; Lawlor, S.; Sanchez, A. M.; Sloan, J.; Gorbachev, R. V.; Grigorieva, I. V.; Krasheninnikov, A. V.; Haigh, S. J. Atomic Defects and Doping of Monolayer $NbSe_2$. *ACS Nano* **2017**, *11* (3), 2894–2904.

(26) Rooney, A. P.; Kozikov, A.; Rudenko, A. N.; Prestat, E.; Hamer, M. J.; Withers, F.; Cao, Y.; Novoselov, K. S.; Katsnelson, M. I.; Gorbachev, R.; Haigh, S. J. Observing Imperfection in Atomic Interfaces for van Der Waals Heterostructures. *Nano Lett.* **2017**, *17* (9), 5222–5228.

(27) Chen, C.; Rosenblatt, S.; Bolotin, K. I.; Kalb, W.; Kim, P.; Kymissis, I.; Stormer, H. L.;

Heinz, T. F.; Hone, J. Performance of Monolayer Graphene Nanomechanical Resonators with Electrical Readout. *Nat. Nanotechnol.* **2009**, *4* (12), 861–867.

(28) Castellanos-Gomez, A.; Van Leeuwen, R.; Buscema, M.; Van Der Zant, H. S. J.; Steele, G. A.; Venstra, W. J. Single-Layer MoS_2 Mechanical Resonators. *Adv. Mater.* **2013**, *25* (46), 6719–6723.

(29) Bunch, J. S.; van der Zande, A. M.; Verbridge, S. S.; Frank, I. W.; Tanenbaum, D. M.; Parpia, J. M.; Craighead, H. G.; McEuen, P. L. Electromechanical Resonators from Graphene Sheets. *Science* **2007**, *315* (5811), 490–493.

(30) Koenig, S. P.; Wang, L.; Pellegrino, J.; Bunch, J. S. Selective Molecular Sieving through Porous Graphene. *Nat. Nanotechnol.* **2012**, *7* (11), 728–732.

(31) Davidovikj, D.; Bouwmeester, D.; Van Der Zant, H. S. J.; Steeneken, P. G. Graphene Gas Pumps. *2D Mater.* **2018**, *5* (3).

(32) Hermosa, C.; Horrocks, B. R.; Martínez, J. I.; Liscio, F.; Gómez-Herrero, J.; Zamora, F. Mechanical and Optical Properties of Ultralarge Flakes of a Metal–Organic Framework with Molecular Thickness. *Chem. Sci.* **2015**, *6* (4), 2553–2558.

(33) López-Cabrelles, J.; Mañas-Valero, S.; Vitórica-Yrezábal, I. J.; Bereciartua, P. J.; Rodríguez-Velamazán, J. A.; Waerenborgh, J. C.; Vieira, B. J. C.; Davidovikj, D.; Steeneken, P. G.; van der Zant, H. S. J.; Mínguez Espallargas, G.; Coronado, E. Isoreticular Two-Dimensional Magnetic Coordination Polymers Prepared through Pre-Synthetic Ligand Functionalization. *Nat. Chem.* **2018**, *10* (10), 1001–1007.

Chapter 6

Surface modification of 2D molecular materials

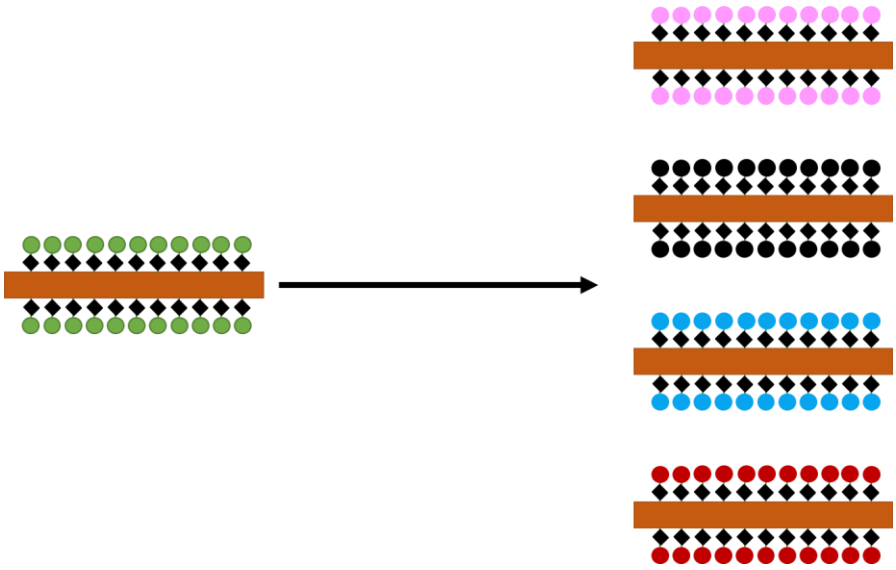

6.1 Introduction

In 2D materials, such as graphene or transition metal dichalcogenides (MX_2, M: transition metal, X: S, Se, Te), functionalization in solution is the most common way to tune the physical properties with the aim of improving their performance for a given application.[1,2] However, as typical 2D materials are very inert compounds from a chemical point of view, the covalent functionalization process requires a lot of energy, i.e. high temperatures, and therefore it is an uncontrolled step, thus provoking defects, low degree of functionalization and attachment of the molecules in random positions. Non-covalent functionalization is also an alternative approach, but it typically lacks long-range order, thus resulting in a material more near to a composite. Examples of high covalent functionalization in graphene have been reported in the recent years, revealing the need of very particular conditions for a successful incorporation of different molecular moieties.[3] In other 2D materials such as transition metal dichalcogenides, there is an ongoing discussion between covalent functionalization and physisorption of the molecules. In fact, the mechanism and reaction between MS_2 and molecules with a functional group of S is not clear, and the reports based on the covalent functionalization of S vacancies are causing an intense debate.[4] There is also an improvement of the covalent functionalization, with a smart strategy taking advantage of the soft nucleophilic character of the S, a completely different approach to the vacancies or physisorption. Nevertheless, this approach also lead to a low degree of functionalization of around 20%.[5] Thus, a controlled and high degree functionalization is still a challenge in transition metal dichalcogenides. That point, besides of the need of requiring a wet

methodology (exfoliation and/or functionalization), makes it attractive the search of a different approximation for a controlled, long-range functionalization in the absence of solvents.

Coordination chemistry, and reticular design in particular, can give rise to better functionalizations than those achieved in inorganic materials thanks to its greater chemical versatility and tunability.[6] The rise of 2D materials has increased the interest in finding molecular analogues.[7] The molecular nature of a layered coordination polymers (LCPs) permits, a priori, the incorporation of different functionalization onto the 2D molecular material. This is a common approximation in the field of Metal-Organic Frameworks (MOFs) and cooordination polymers (CPs), which are crystalline materials that can be functionalized in a post-synthetic manner in solution (Figure 6.1a).[8–10]

However, the hybrid composition of MOFs and CPs allows also to modify the organic linker before the synthesis of the material, feature that is impossible to achieve in inorganic materials. In particular, this has been exemplified with the synthesis of isostructural compounds with different functional groups,[12] as is the case of IRMOF-74. or MOF-74, which can be prepared with different functional groups such as CH_3 or NH_2 just using a pre-functionalized organic linker (Figure 6.1b).

This strategy preserves the crystal structure but modifies the physical properties, as for example the CO_2 affinity of the pores.[11]

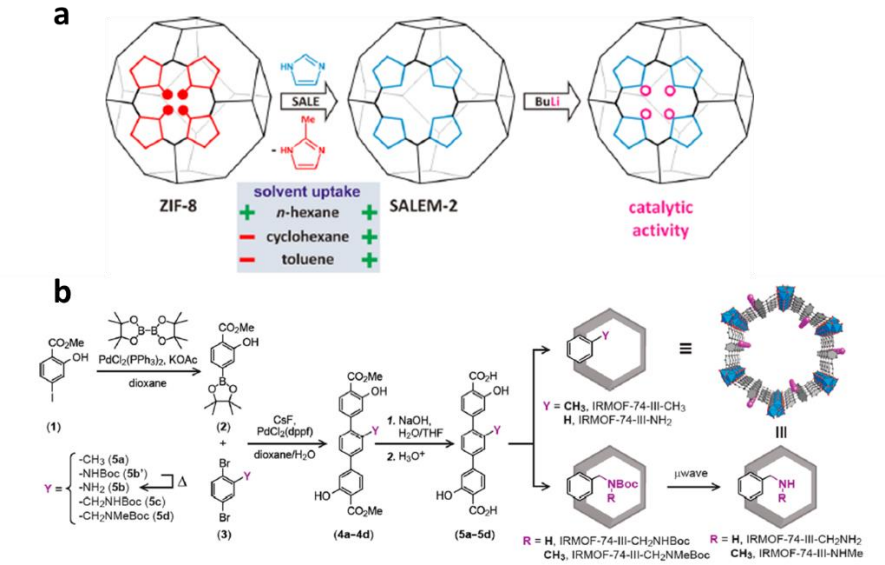

Figure 6.1 a) Solvent-assisted linker exchange (SALE) in ZIF-8 to introduce unsubstituted imidazole linker. b) Synthetic pathway for the functionalized organic linkers used in the synthesis of IRMOF-74-III. Adapted from references 9,11.

The pre-functionalization of organic linkers in molecular materials can be a great option to circumvent the problem of functionalization of 2D materials. In addition, in combination with a dry exfoliation after the synthesis of a pre-functionalized bulk, makes layered MOFs and LCP good candidates to obtain 2D materials with long-range functionalization order.

In this Chapter, we present a novel family of isoreticular layered MOFs composed of robust bonds between Fe(II) metallic nodes and benzimidazole derivate as ligands. The aim of our work has been to prepare robust magnetic coordination polymers with a controlled functionalization thanks to the presence of the organic ligand. Their extraordinary robustness,

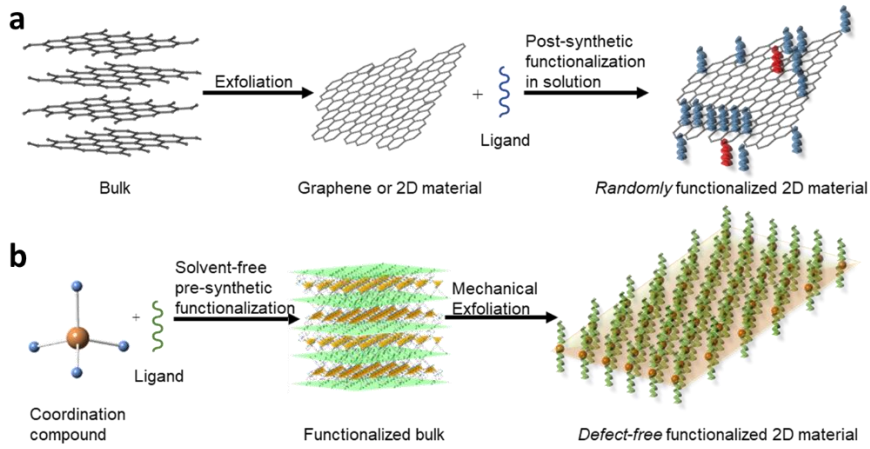

Figure 6.2 Schematic representation of the post-synthetic covalent functionalization vs. the pre-synthetic functionalization used here. The top part (a) exemplifies the commonly used strategy to functionalize two-dimensional (inorganic) materials consisting on two steps: i) mechanical or liquid exfoliation of the bulk material; ii) functionalization in a solution of the exfoliated material, yielding a random distribution of the functional groups, represented in blue. This route can also produce ligand modifications, represented with a color change from blue to red. The bottom part (b) indicates a pre-synthetic functionalization in which the functionalized bulk is first obtained before be mechanically exfoliated, thus yielding a quasi-perfect array of unaltered functional groups attached to the surface.

chemical stability, and crystallinity permit their mechanical exfoliation with great results, similar to the explored in the previous chapter with the layered coordination polymer, **MUV-1-Cl**. In a pre-synthetic methodology, functionalization of these compounds before the exfoliation process (in

bulk) permits to obtain flakes of a 2D molecular material with a long-range functionalization order (Figure 6.2).

6.2 Results and discussion

Pre-synthetic functionalization. Surface engineering is a demanding challenge in 2D materials since it permits to tune the surface chemistry at will, modifying, for example, the hydrophobicity/hydrophilicity of a material. As a proof of concept, we have changed, by chemical design, the substituent in the fifth position (Cl in **MUV-1-Cl**) by different groups such as CH_3 (**MUV-1-CH_3**), H (**MUV-1-H**), Br (**MUV-1-Br**) and NH_2 (**MUV-1-NH_2**) (Figure 6.3a), obtaining an isostructural family of crystalline material, only changing the interlayer distance between layers (Figure 6.3b).

Similarly to the synthesis of **MUV-1-Cl**, the solvent-free reaction of 5-Xbenzimidazole (X = H, CH_3, NH_2 and Br) and ferrocene, [13–15] yields large (≈ 200 μm) laminar colorless crystals of formula [Fe(Xbim)$_2$] (abbreviated as **MUV-1-X**), which allows structure determination through single crystal X-ray diffraction. The structures of all compounds consist of distorted tetrahedral Fe(II) centers connected by 5-Xbenzimidazolate bridges (Figure 6.4) forming a neutral layered coordination polymer extended in the *ab* plane. These layers weakly interact with each other through van der Waals interactions (X···X interactions). The functional groups are located at the surface (Figure 6.4), thus playing an active role in the chemical behavior of the molecular interface.

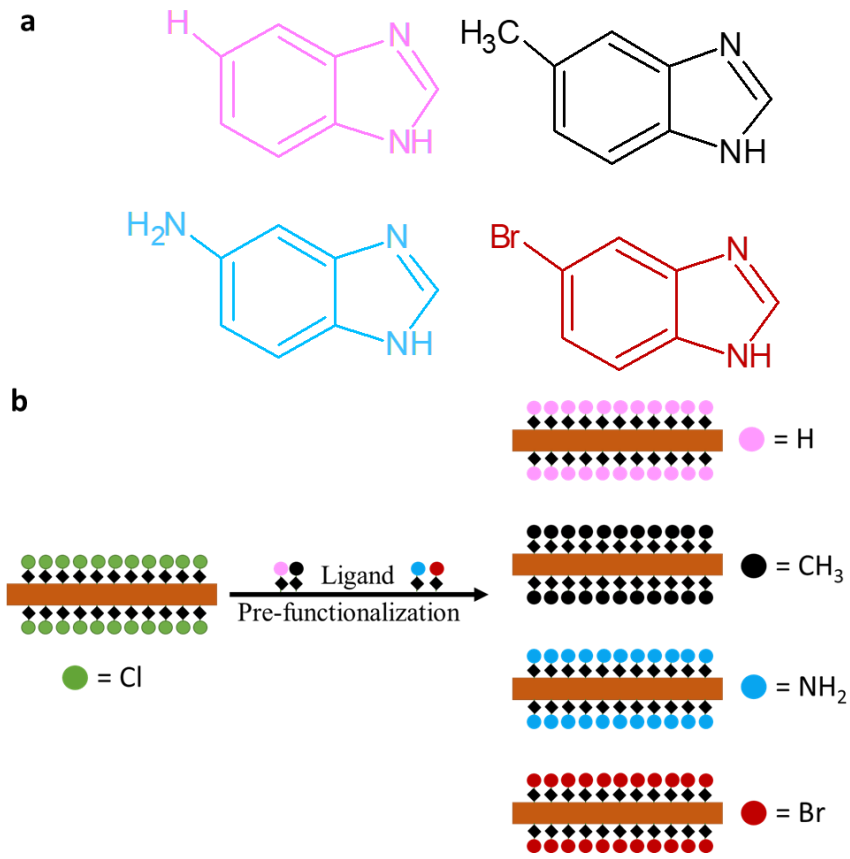

Figure 6.3 a) The organic ligands used for the synthesis of **MUV-1-X**. **b)** Conceptual representation of the ligand pre-synthetic functionalization to modify the surface of the **MUV-1-X.**

The different functional groups give rise to differences in the distance between layers, corresponding to the *c* axis. Thus, a different position of the first peak in the X-ray powder diffraction data (2Θ values of 9.3, 8.0, 8.3 and 7.8º for **MUV-1-H**, **MUV-1-CH$_3$**, **MUV-1-NH$_2$** and **MUV-1-Br,** respectively, is observed (Figure 6.5). As expected, the smallest distance

between layers belongs to **MUV-1-H**, with a cell parameter of 18.7 Å for *c* axis.

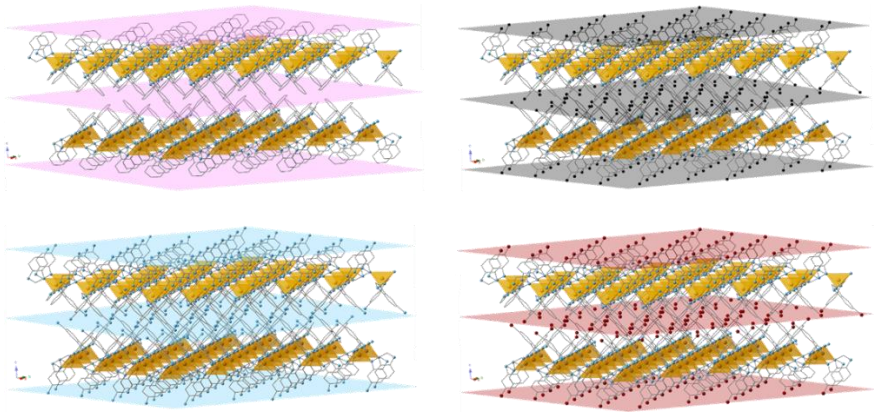

Figure 6.4 Crystal structure of the isoreticular **MUV-1-X** family. H, CH_3, NH_2 and Br are represented in pink, black, cyan and garnet, respectively**.**

All these compounds present a layered morphology regardless of the functional groups, which do not influence the layered crystal growth. This is clearly observed in the SEM images (Figure 6.6). However, close inspection of the bulk allows to appreciate small differences between the compounds: whereas **MUV-1-H** and **MUV-1-Cl** are more detailed square-like crystals, **MUV-1-CH_3** and **MUV-1-Br** are thinner and prismatic crystals.

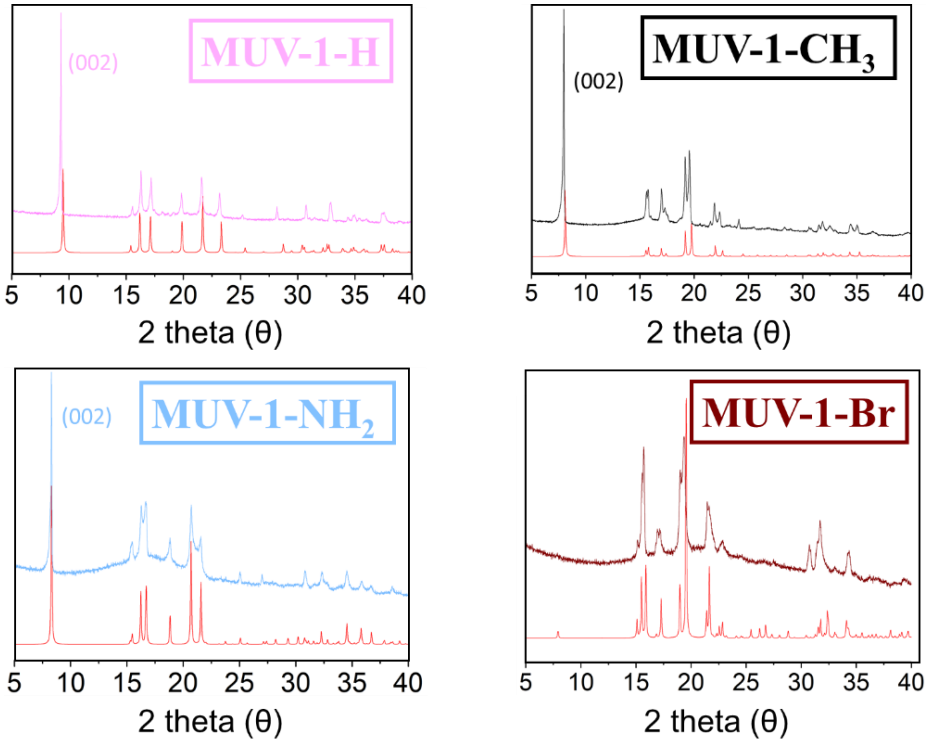

Figure 6.5 X-ray powder diffraction patterns for the whole family of **MUV-1-X**. The first peak corresponds to the (002) *hkl* plane. In the case of the **MUV-1-Br**, the intensity is lower and cannot be appreciated in the experimental pattern.

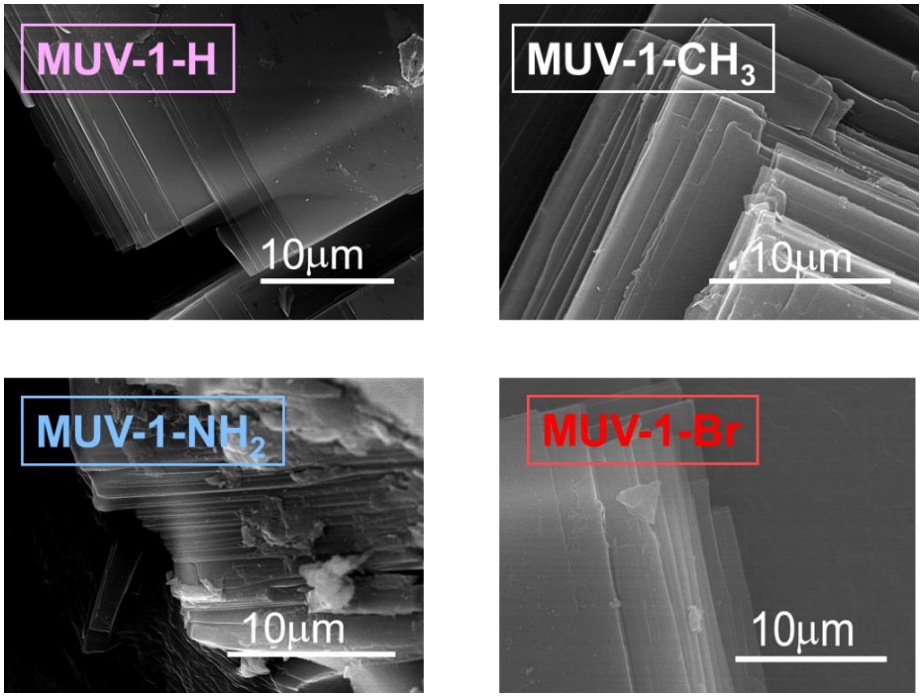

Figure 6.6 Scanning electronic micrographs of the **MUV-1-X** family showing the layered crystal structure.

The functional groups are relatively far from the metal centers and the metal-ligand bridge. For this reason, the electronic properties are not expected to be affected by the different functional groups. The inner part, the core, composed by Fe(II) centres, is in a "sandwich" of benzimidazoles, which serve as an organic protection. The use of halogen groups or alkyl/aromatic groups enhance the stability of the materials, due to their high hydrophobicity,[16] preventing hydrolysis of sensible materials, such as Fe(II) compounds. The structure and connection between the metallic nodes is common for all the compounds (Figure 6.7), being the Fe-imidazole motif the responsible of the crystal structure and the electronic properties. The replacement of the functional group in the ligand does not

cause any modification of the inner part, and therefore this change only affects the properties of the surface of the compound, whereas the electronic properties are expected to be unaltered.

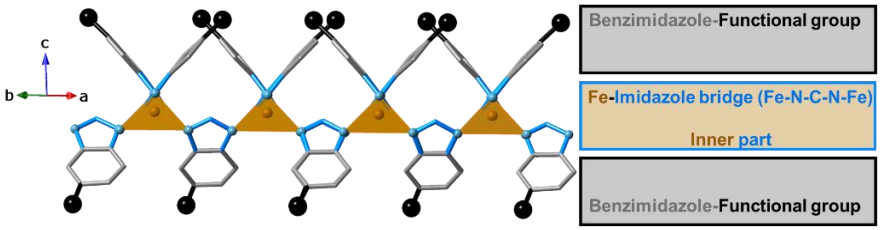

Figure 6.7. The "sandwich" structure for the **MUV-1-X** layers, formed by a core composed by the Fe(II) centers and imidazole bridges, locating the functionalities in the surface.

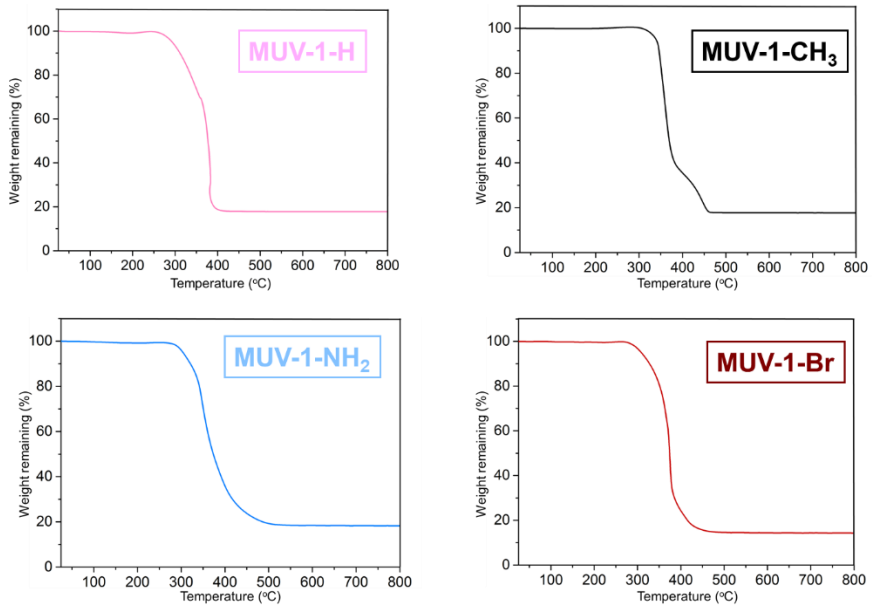

Figure 6.8. Thermogravimetric analysis of the **MUV-1-X** family at a heating rate of 5 °C min^{-1}.

All the family shows a high thermal stability due to the similar crystal structure decomposition at around 350 °C (Figure 6.8). Importantly, the different functional groups of this family form part of the organic ligand and, as thermogravimetric analysis measurements shows, there is no mass loss due to the detachment of the functional group. As observed in 2D materials, the covalent functionalization can be observed in thermogravimetric analyses, due to the mass loss of the functional groups.[5,17] In this case, the covalent attachment of the functional groups to the ligand is stronger than the Fe-N coordination bond, responsible of the structure.

The magnetic properties to all compounds were investigated in order to examine the influence of the different functional groups in the magnetic ordering. Figure 6.9 shows a similar behavior for all compounds, exhibiting a broad maximum at 30 K due to the antiferromagnetic ordering, and a sharp peak at 20 K, indicating the phase transition to a canted antiferromagnetic ordering. This is not unexpected, as the magnetic properties are dominated by the metal center, their connectivity and the coordination environment. As discussed before, the Fe(II) environment is very similar in all the compounds of the **MUV-1-X** family. Despite the possible influence of the different functional groups in the electronic environment, around the Fe(II) metal their faraway position does not affect the magnetic properties.

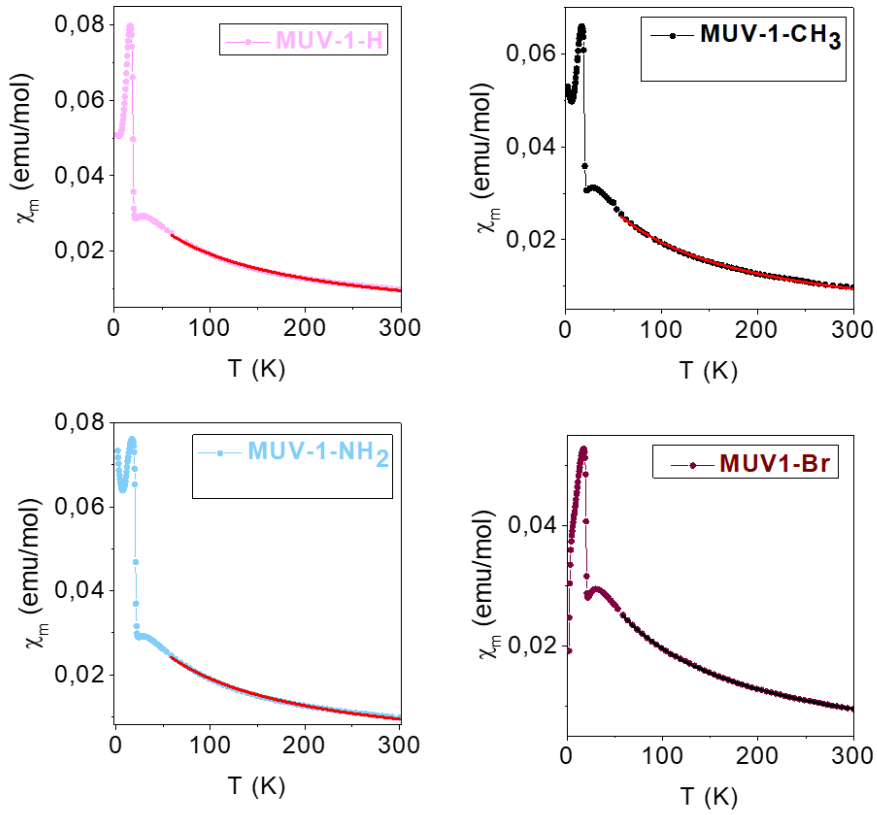

Figure 6.9 Thermal dependence of χ_m in the temperature range 2-300 K. The data have been fitted following a Curie-Weiss law in the high temperature range (60–300 K).

The temperature dependence of the ac magnetic susceptibilities (in-phase signal, χ_m') at different frequencies were measured from 16 to 23 K, as shown in Figure 6.10. Sharp peak at T_N, obtained at the value when χ_m'' differs to 0 is observed, that indicates the onset of a long-range magnetic order (Table 6.1).

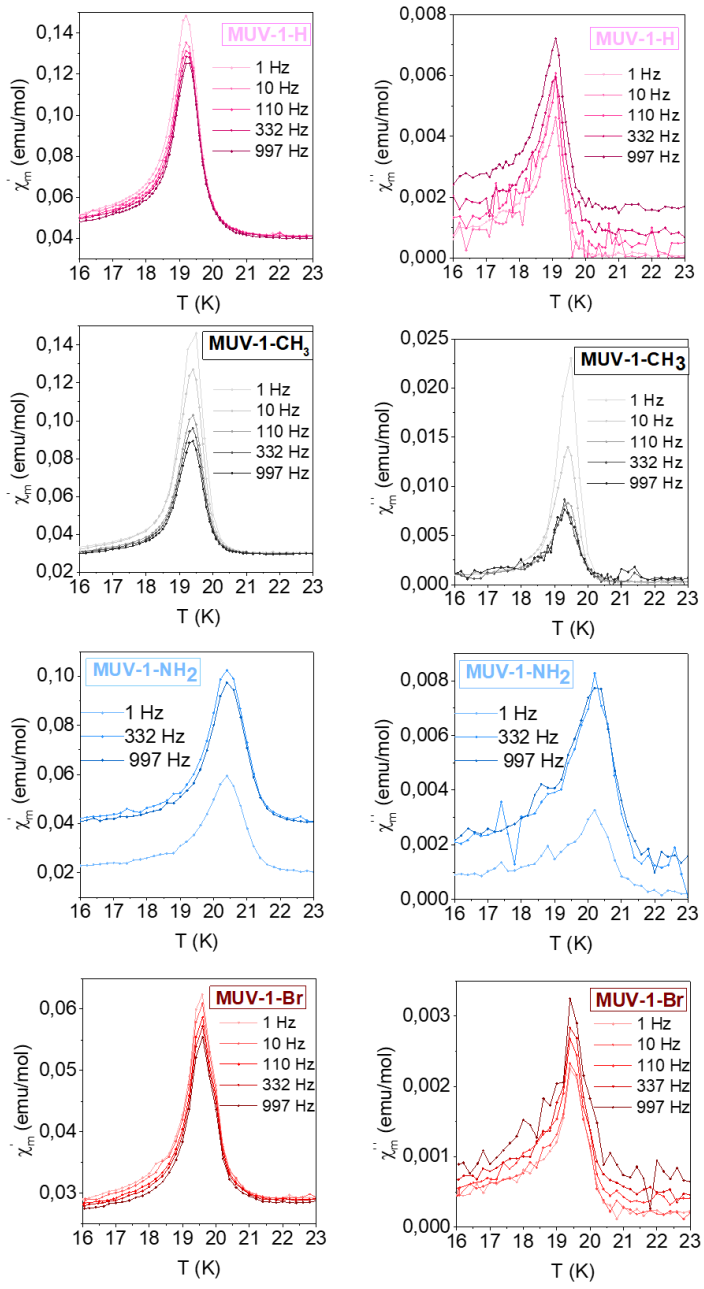

Figure 6.10 In-phase (left) and out-phase (right) dynamic susceptibility of **MUV-1-X** measured at different frequencies.

Table 6.1 Magnetic ordering temperatures for the MUV-1-X family.

	MUV-1-H	MUV-1-CH_3	MUV-1-NH_2	MUV-1-Br
T_N	20.0 K	20.1 K	21.2 K	20.0 K

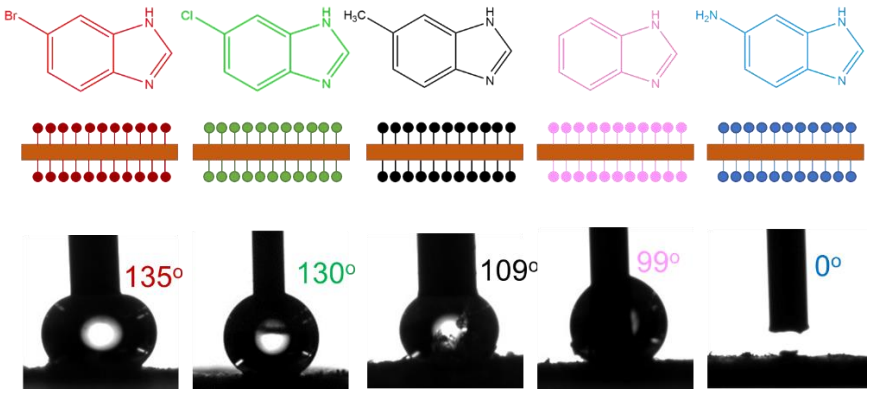

Figure 6.11 Surface modification in **MUV-1-X.** The atoms at the surface of **MUV-1-X** can be changed by chemical design (X = Br, Cl, CH_3, H, NH_2) in a pre-synthetic manner to obtain different surface behaviors which change the water contact angle. No changes in the magnetic properties are observed upon the chemical modification.

Surface modification. The different "decoration" of the **MUV-1** family has been achieved incorporating different functional groups. These changes tune the behavior in front of water of the surface. This behavior was measured by continuous contact angle (Figure 6.11). Alkane groups (H, CH_3) present values of contact angles of 99º and 109º respectively (i.e. moderate hydrophobic behavior); the inclusion of halides substituents causes an increase in the contact angle values (130º and 135º for Cl and Br,

respectively), thus showing an increase in the hydrophobic character. On the contrary, the inclusion of the amino group (NH_2) causes a decrease of the contact angle value to 0º, indicating superhydrophilic properties.

The five different ligands successfully employed already demonstrate large tunability, although we can anticipate that one of the possible limitations of this approach relies on the use of larger substituents that can interfere with the formation of the crystalline layered structure. However, preliminary results indicate that bulkier groups of up to 3 non-H atoms can also be incorporated with this approach, although further studies are still on-going.

2D molecular materials family. As already described, the entire family of isoreticular **MUV-1-X** compounds retains, in bulk, the properties and crystallinity as described for **MUV-1-Cl**. However, the location of different functional groups at the interfaces between the different layers can exert some influence on the delamination process. We investigated the exfoliation of the complete family of **MUV-1-X** using the same top-down procedure described for **MUV-1-Cl**.

Using the *Scotch tape* methodology, all the members of the family **MUV-1-X** were successfully exfoliated by mechanical methods. The obtained flakes were deposited onto silicon substrates with 285 nm of thermally grown SiO_2 and inspected by different microscopies such as atomic force microscopy and transmission electron microscopy.

Figure 6.12 shows characteristic examples of flakes from each of the members of the **MUV-1-X** family, presenting a thickness for a few layers

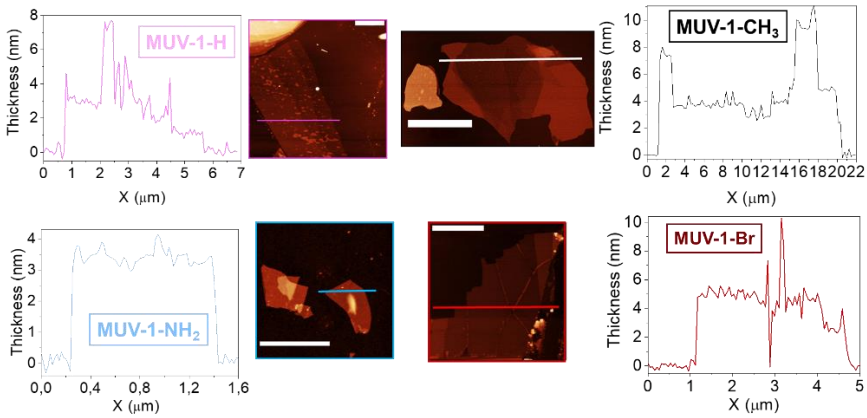

Figure 6.12 Atomic force microscopy for the **MUV-1-X** family, showing the possibility to achieve 2D molecular materials with high-quality flakes (lateral size and morphology).

of flakes (3-4 layers). It should be stressed that many flakes can be obtained for each material, but just a representative example of each of them is shown here. As can be seen, the different functional groups do not affect the top-down technique, and all compounds are easy to exfoliate and deposit onto the Si/SiO_2 substrate, in the same manner as for **MUV-1-Cl**. The chemical composition and crystallinity needs to be characterized, but the possibility to achieve large 2D materials with a long-range order in the functionalities without defects is a difficult challenge in 2D inorganic materials. To the best of our knowledge, this is the first time that high quality flakes with a high percentage of coverage of the functionalities is reported. This is due to the functional group being covalently attached to the ligand. Thus, as observed in the thermogravimetric analysis, the compound decomposes before the detachment of the functional group. In other words, the compound retains the crystallinity and the chemical

composition before it decomposes, meaning that there is a long-order distribution of the functionalities in the 2D molecular material due to the compulsory presence of the linker in the crystal structure.

To check the chemical composition and crystallinity two techniques were used, namely Raman spectroscopy and transmission electron microscopy (TEM). Raman measurements demonstrate the chemical nature compared with the bulk measurements (Figure 6.13). In the case of the graphene, Raman spectra allows to follow the defects, functionalization, and the number of the layers thanks to a clear spectrum with a small number of peaks (a consequence of being formed by a single type of atom).[1] The principal vibration corresponds to the C-C sp^2 (G and G' band), which is sensitive to the presence of defects, covalent attachments or π-stacking (for a few-layer graphene) appearing more bands (such as D and D' bands). In the case of **MUV-1-X**, which is chemically more complex, there is a higher number of vibrations. This factor prevents the high accuracy for detecting changes in the structure. However, we can unambiguously identify the presence of the ligand for all compounds, and the decrease of the intensity with the thickness, revealing that the exfoliated flakes correspond to the material. Flakes of different thickness were measured for all the members of the family of **MUV-1-X**, revealing characteristic peaks with a limit near to 20 nm thickness. These peaks can be attributed to the organic part, and in principle this only demonstrates the presence of the organic linker. As shown in Figure 6.13, all the Raman spectra in **MUV-1-X** family are comparable.

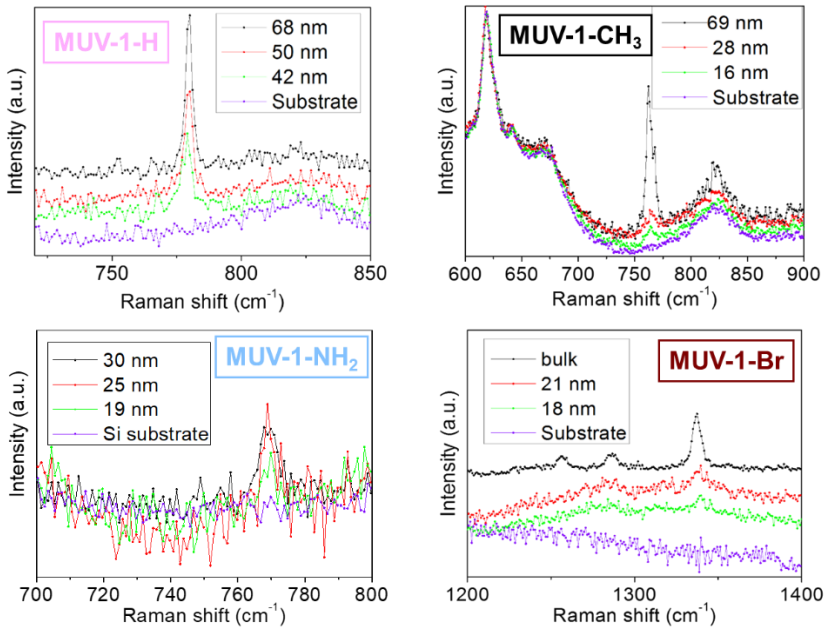

Figure 6.13 Raman study of thickness of **MUV-1-X** flakes.

For these reasons, Raman spectra are used to check the presence of vibrations due to the ligand, and the effect of the thickness in the intensity as a good indicative of the chemical stability and presence of the **MUV-1-X**.

To ensure the crystal structure and the functionality onto the 2D molecular material, Transmission Electron Microscopy (TEM) has been used, in collaboration with P. Bereciartua from the ITQ. TEM images with their corresponding selected area electron diffraction patterns show the retained crystallinity for all the compounds (Figure 6.14). It must be highlighted the high resemblance between the theoretical (Figure 6.15) and the experimental patterns (Figure 6.14). Importantly, the thickness of the measured areas by TEM was assessed by measuring the same flake with

AFM (around 20 nm). This has been possible thanks to the robustness of **MUV-1-X**, which has allowed a mechanical exfoliation and transfer into silicon nitride membranes for TEM study. Afterwards, it has been possible the study by AFM of the same flakes.

The physical properties, and thanks to the unaltered core, making possible the exfoliation and achieving high quality 2D molecular materials. The high crystallinity of the 2D systems ensures the long-range order in the functionalities, being one of the best examples on high percentage covering in functionalized 2D materials.

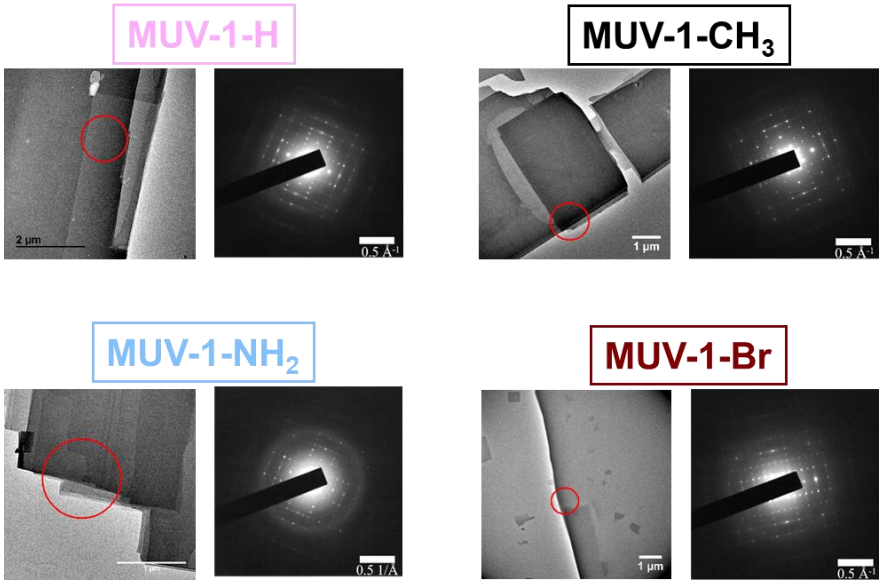

Figure 6.14 TEM image of the diffracted area with its corresponding selected area electron diffraction pattern.

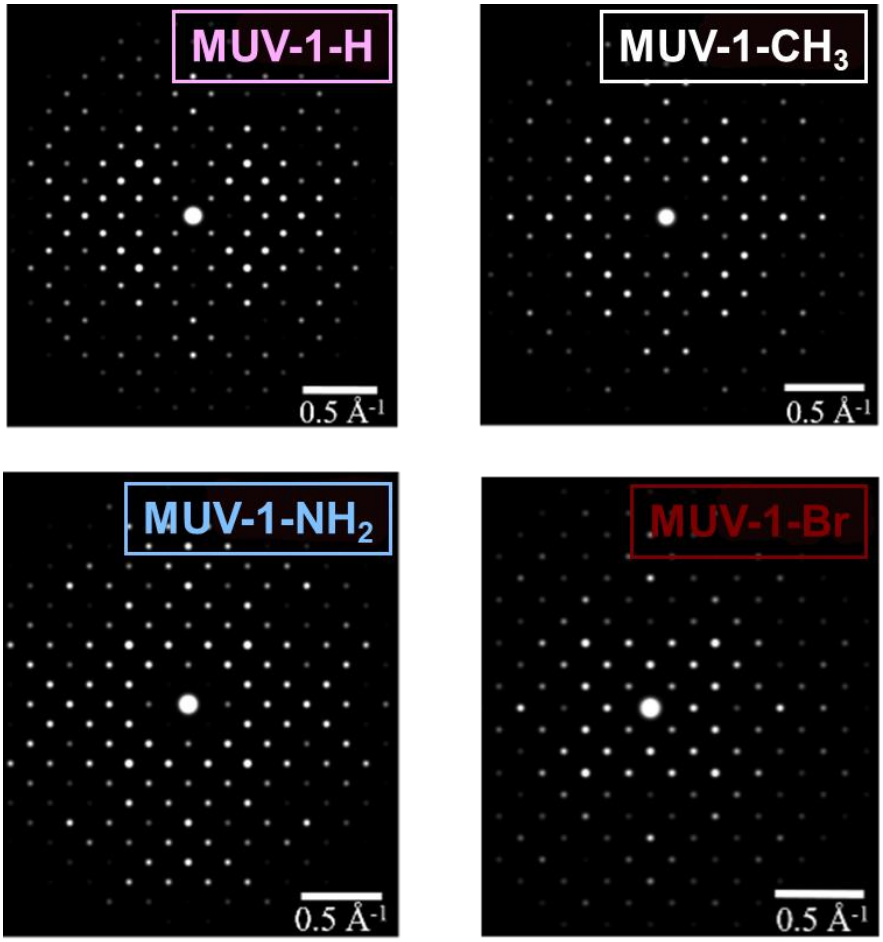

Figure 6.15 Theoretical diffraction patterns along with the [0 0 1] direction for **MUV-1-X.**

6.3 Conclusions

In this chapter, we have presented a general strategy for the synthesis of crystalline layered coordination polymers (LCP) exhibiting a magnetic order and providing an unconventional route to tune at will the surface chemistry of the individual layers. In particular, by the election of different

ligands, we have obtained a new family of LCP denoted as **MUV-1-X** (where X = Br, H, CH_3, or NH_2, in addition to Cl which was presented in Chapter 5), with surface properties ranging from hydrophobic to hydrophilic, that retain their magnetic properties under the different surface modifications. The changes in the functional groups at surface do not affect to the crystallinity, maintaining all the compounds of the family the isoreticular structure This work opens the door to design novel 2D materials based on molecular and coordination chemistry to taking advantage of the huge possibilities in functionalization and tunability provided by this approach in terms of surface properties and electronic properties.

6.4 Methods

Synthesis of MUV-1-X. Ferrocene (30 mg, 0.16 mmol) and benzimidazole (or derivates) (0.34 mmol) were combined and sealed under vacuum in a layering tube (4 mm diameter). The mixture was heated at 250 °C for 3 days to obtain crystals suitable for X-ray single-crystal diffraction. The product was allowed to cool to room temperature, and the layering tube was then opened. The unreacted precursors were extracted with acetonitrile and benzene, and the product was isolated as colorless crystals (yield 80 %). Phase purity was established by X-ray powder diffraction.

X-ray Structural Studies. X-ray data for compounds **MUV-1-H** was collected at a temperature of 100 K using a synchrotron radiation at single crystal X-ray diffraction beamline I19 in Diamond Light Source, equipped with a Pilatus 2M detector and an Oxford Cryosystems nitrogen flow gas system. Data was measured using GDA suite of programs. X-ray data for compounds **MUV-1-Br**, **MUV-1-CH_3** and **MUV-1-NH_2** were collected at

the University of Manchester (UK) at a temperature of 100/150 K using a Rigaku FR-X rotating anode diffractometer, equipped with Hybrid Photon detector HyPix-6000HE and an Oxford Cryosystems nitrogen flow gas system.

X-ray Powder Diffraction. Polycrystalline samples of **MUV-1-X** were each lightly ground in an agate mortar and pestle and used to fill 0.5 mm borosilicate capillaries that were mounted and aligned on an Empyrean PANalytical powder diffractometer, using Cu Kα radiation (λ = 1.54056 Å). For each compound, two repeated measurements were collected at room temperature (2θ = 5−40 °) and merged in a single diffractogram.

Thermogravimetric analysis. Thermogravimetric analysis of **MUV-1-X** was carried out with a Mettler Toledo TGA/SDTA851e/SF/1100 apparatus in the 25–800 °C temperature range under a 5°C·min^{-1} scan rate and an air flow of 30 mL·min^{-1}.

SEM. Scanning Electronic Micrographs and atomic composition of bulk samples was estimated by electron probe microanalysis (EPMA) performed in a Philips SEM XL30 equipped with an EDAX microprobe and images were recorded in a Hitachi S-4800.

Raman spectroscopy. Raman spectra were acquired with a micro-Raman (model XploRA ONE from Horiba, Kyoto, Japan) with a grating of 2400 gr/mm, slit of 50 µm, and hole of 500 µm. The employed wavelengths were 532 nm, 638 nm, and 785 nm. The power density of the laser used for spectra measured at 532 nm was 5.25 mW/µm^2 (bulk crystals) and 170 µW/µm^2 (thin-layers), for spectra measured at 638 nm it was 7.58 mW/µm^2

(bulk crystals), and for those spectra measured at 785 nm it was 7.2 mW/μm^2 (bulk crystals).

AFM. Optical images were obtained with a NIKON Eclipse LV-100 Optical microscope and AFM images were performed with a Nanoscope IVa Multimode Scanning Probe Microscope (Bruker, Karlsruhe, Germany) in tapping mode.

TEM. Several mechanical exfoliated flakes were transferred onto a grid with a membrane of amorphous SiN (50 nm thick) using a dry and deterministic method (that involves the use of a micromanipulator and PDMS/PPC polymers, as reported in ref.[18]). TEM images and diffraction patterns were acquired with a JEOL JEM-2100F with a field emission gun operating at 200 kV. The simulated SAED patterns were generated with SingleCrystal software.

Contact Angle (CA) Measurements. Continuous water contact angle measurements of the samples were performed in air using a Rame-hart 200 standard goniometer equipped with an automated dispensing system. The initial drop volume was 0.17 μL, increased by additions of 0.08 μL.

Magnetic Measurements. Variable-temperature (2−300 K) direct current (dc) magnetic susceptibility measurements were carried out in applied fields of 1.0 kOe and variable field magnetization measurements up to ± 5 T at 2.0 K. The susceptibility data were corrected from the diamagnetic contributions as deduced by using Pascal's constant tables. Variable-temperature (16−23 K) alternating current (ac) magnetic susceptibility

measurements in a ±4.0 G oscillating field at frequencies in the range of 1 − 997 Hz were carried out in a zero dc field.

6.5 References

(1) Bottari, G.; Ángeles Herranz, M.; Wibmer, L.; Volland, M.; Rodríguez-Pérez, L.; Guldi, D. M.; Hirsch, A.; Martín, N.; D'Souza, F.; Torres, T. Chemical Functionalization and Characterization of Graphene-Based Materials. *Chem. Soc. Rev.* **2017**, *46* (15), 4464–4500.

(2) Chu, X. S.; Yousaf, A.; Li, D. O.; Tang, A. A.; Debnath, A.; Ma, D.; Green, A. A.; Santos, E. J. G.; Wang, Q. H. Direct Covalent Chemical Functionalization of Unmodified Two-Dimensional Molybdenum Disulfide. *Chem. Mater.* **2018**, *30* (6), 2112–2128.

(3) Navarro, J. J.; Calleja, F.; Miranda, R.; Pérez, E. M.; Vázquez De Parga, A. L. High Yielding and Extremely Site-Selective Covalent Functionalization of Graphene. *Chem. Commun.* **2017**, *53* (75), 10418–10421.

(4) Chen, X.; Berner, N. C.; Backes, C.; Duesberg, G. S.; McDonald, A. R. Functionalization of Two-Dimensional MoS2: On the Reaction between MoS2 and Organic Thiols. *Angew. Chemie - Int. Ed.* **2016**, *55* (19), 5803–5808.

(5) Vera-Hidalgo, M.; Giovanelli, E.; Navío, C.; Pérez, E. M. Mild Covalent Functionalization of Transition Metal Dichalcogenides with Maleimides: A "Click" Reaction for 2H-MoS_2 and WS_2. *J. Am. Chem. Soc.* **2019**, *141* (9), 3767–3771.

(6) Yaghi, O. M.; M, O. K.; Ockwig, N. W.; Chae, H. K.; Eddaoudi, M.; Kim, J. Reticular Synthesis and the Design of New Materials. *Nature* **2003**, *423* (6941), 705–714.

(7) Liu, W.; Yin, R.; Xu, X.; Zhang, L.; Shi, W.; Cao, X. Structural Engineering of Low-Dimensional Metal–Organic Frameworks: Synthesis, Properties, and Applications. *Advanced Science*. John Wiley and Sons Inc. June 2019.

(8) Yaghi, O. M.; Furukawa, H.; Morris, W.; Doonan, C. J.; Banerjee, R. Crystals as Molecules: Postsynthesis Covalent Functionalization of Zeolitic Imidazolate Frameworks. *J. Am. Chem. Soc.* **2008**, *130* (38), 12626–12627.

(9) Karagiaridi, O.; Lalonde, M. B.; Bury, W.; Sarjeant, A. a.; Farha, O. K.; Hupp, J. T. Opening ZIF-8: A Catalytically Active Zeolitic Imidazolate Framework of Sodalite Topology with Unsubstituted Linkers. *J. Am. Chem. Soc.* **2012**, *134* (45), 18790–18796.

(10) Giménez-Marqués, M.; Bellido, E.; Berthelot, T.; Simón-Yarza, T.; Hidalgo, T.; Simón-

Vázquez, R.; González-Fernández, Á.; Avila, J.; Asensio, M. C.; Gref, R.; Couvreur, P.; Serre, C.; Horcajada, P. Metal-Organic Framework Surface Functionalization: GraftFast Surface Engineering to Improve MOF Nanoparticles Furtiveness. *Small* **2018**, *14* (40), 1870182.

(11) Fracaroli, A. M.; Furukawa, H.; Suzuki, M.; Dodd, M.; Okajima, S.; Gándara, F.; Reimer, J. A.; Yaghi, O. M. Metal-Organic Frameworks with Precisely Designed Interior for Carbon Dioxide Capture in the Presence of Water. *J. Am. Chem. Soc.* **2014**, *136* (25), 8863–8866.

(12) Ahnfeldt, T.; Gunzelmann, D.; Loiseau, T.; Hirsemann, D.; Senker, J.; Férey, G.; Stock, N. Synthesis and Modification of a Functionalized 3D Open-Framework Structure with MIL-53 Topology. *Inorg. Chem.* **2009**, *48* (7), 3057–3064.

(13) Rettig, S. J.; Storr, A.; Summers, D. A.; Thompson, R. C.; Trotter, J. Transition Metal Azolates from Metallocenes . 2 . Synthesis , X-Ray Structure , and Magnetic Properties of a Three-Dimensional Polymetallic Iron (II) Imidazolate Complex , a Low-Temperature Weak Ferromagnet. *Society* **1997**, *7863* (Ii), 8675–8680.

(14) López-Cabrelles, J.; Giménez-Marqués, M.; Mínguez Espallargas, G.; Coronado, E. Solvent-Free Synthesis of a Pillared Three-Dimensional Coordination Polymer with Magnetic Ordering. *Inorg. Chem.* **2015**, *54* (21), 10490–10496.

(15) López-Cabrelles, J.; Mañas-Valero, S.; Vitórica-Yrezábal, I. J.; Bereciartua, P. J.; Rodríguez-Velamazán, J. A.; Waerenborgh, J. C.; Vieira, B. J. C.; Davidovikj, D.; Steeneken, P. G.; van der Zant, H. S. J.; Mínguez Espallargas, G.; Coronado, E. Isoreticular Two-Dimensional Magnetic Coordination Polymers Prepared through Pre-Synthetic Ligand Functionalization. *Nat. Chem.* **2018**, *10* (10), 1001–1007.

(16) Jayaramulu, K.; Geyer, F.; Schneemann, A.; Kment, Š.; Otyepka, M.; Zboril, R.; Vollmer, D.; Fischer, R. A. Hydrophobic Metal–Organic Frameworks. *Adv. Mater.* **2019**, *31* (32), 1–31.

(17) Hof, F.; Schäfer, R. A.; Weiss, C.; Hauke, F.; Hirsch, A. Novel Λ3-Iodane-Based Functionalization of Synthetic Carbon Allotropes (SCAs) - Common Concepts and Quantification of the Degree of Addition. *Chem. - A Eur. J.* **2014**, *20* (50), 16644–16651.

(18) Nguyen, L.; Komsa, H. P.; Khestanova, E.; Kashtiban, R. J.; Peters, J. J. P.; Lawlor, S.;

Sanchez, A. M.; Sloan, J.; Gorbachev, R. V.; Grigorieva, I. V.; Krasheninnikov, A. V.; Haigh, S. J. Atomic Defects and Doping of Monolayer $NbSe_2$. *ACS Nano* **2017**, *11* (3), 2894–2904.

Chapter 7

Tunability in 2D molecular materials

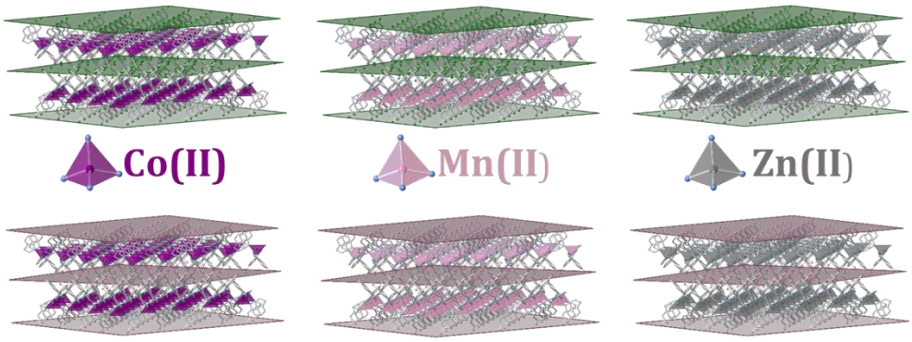

7.1 Introduction

The rise of 2D molecular materials offers a complementary alternative to the classical 2D inorganic materials.[1,2] One of these benefits is the huge range of tunability due to the hybrid nature of coordination materials. As shown in previous Chapters, the pre-functionalization of a 2D material is possible with coordination chemistry, which has been exemplified with changes in the organic linker. However, this tunabilitiy is not limited to the ligands, as modifications of the metallic nodes (inorganic part) are also possible. This change will exert further changes in the physical properties of the materials, including in some cases a change in the coordination environment that may affect the topology and crystal structure. For example, in systems based in 2,3,6,7,10,11-hexahydroxytriphenylene (H_6HHTP), the influence of the metal is enormous. In the case of Ni(II) and Co(II) layered compounds are formed stabilized by clusters between layers. The metal centers are in an octahedral environment, coordinated by 4 oxygen atoms from the ligand, completing the coordination sphere with water molecules (Figure 7.1a).[3] On the contrary, when using Cu(II) instead of Ni(II) or Co(II), the formation of the cluster is not observed, and the extended solid is only composed by the extended layers formed by Cu(II) and the organic linker (Figure 7.1b).[4] These materials are all formed by transition metals of the first series, with similar in electronic structures coming from *d* electrons, but despite the enormous similarities between them, small differences are observed in the crystal structure between Ni-Co and Cu. If other metals are included in this discussion, such as lanthanides, the difference in electronic structure is more pronounced, as the electrons are in *f* orbitals, and also the metal charge

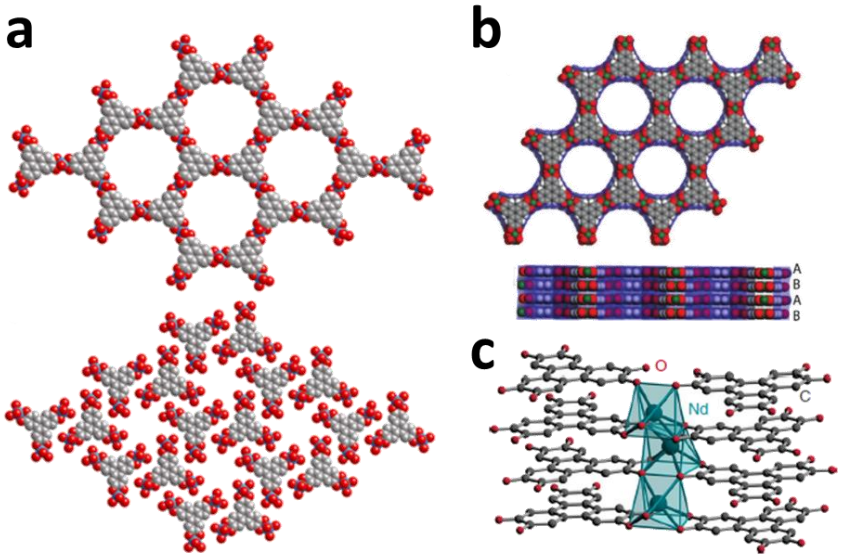

Figure 7.1 a) (Top) Layered structure for $(M_3(HHTP)_2(H_2O)_6$, (M = Co, Ni) the extended system. (Below)The discrete system $M_3(HHTP)(H_2O)_{12}$, (M = Co, Ni) formed between layers. b) The crystal structure of $Cu_3(HHTP)_2(H_2O)_6$ and their stacking without discrete species between them. c) $Ln_{1+x}HHTP(H_2O)_n$ crystal structure, where the Ln atom connects two layers of the organic ligand. Adapted from references 3-5.

and coordination environment, (i.e. Ln(III) vs M(II)). This affects the coordination nature for the bonding, being more ionic in the case of lanthanoids, and also the coordination numbers, which are higher in lanthanoids. All these features lead to different crystal structures.[5] For example, in the reaction of lanthanides and H_6HHTP the result is a 3D network, formed by the layered arrangement of the linkers, where the Ln^{3+} are connected by six oxygen atoms from two different layers, and a water

molecule complete their coordination sphere in a prismatic environment (Figure 7.1c).

In inorganic 2D materials, formed by single atoms, graphene, black phosphorous, antimonene, this approximation is precluded.[6,7] However, in another well-known family of 2D materials, transition metal dichalcogenides (TMDCs), it is possible to use different metals that can affect the electronic properties, as electronic conductivity, superconductivity, or the apparition of charge density waves phases (CDW) (Figure 7.2a). The most common crystal structures found in TMDCs are the 1T phase and the 2H phase, common for the available metals (Nb, Ta, Mo, W, among others).[8] The thermodynamic phase depends on the particular combination of transition metal and chalcogen element (S, Se or Te). The 1T phase, themodynamically favoured for example in $TiSe_2$, is a trigonal crystal system, where the metal is in an octahedral environment. The 2H phase, themodynamically favoured for example in Group VI (MoS_2, $MoSe_2$, WS_2, WSe_2), is a trigonal prismatic environment which determines the hexagonal crystal system and the metal is in a trigonal prism environment. The 1T and 2H phases form hexagonal lattices, in which the metal layer is sandwiched between two dichalcogenide layers (placed at the surface) (Figure 7.2b). In other words, in this family it is possible to maintain the crystal structure changing the metal to alter the electronic properties.

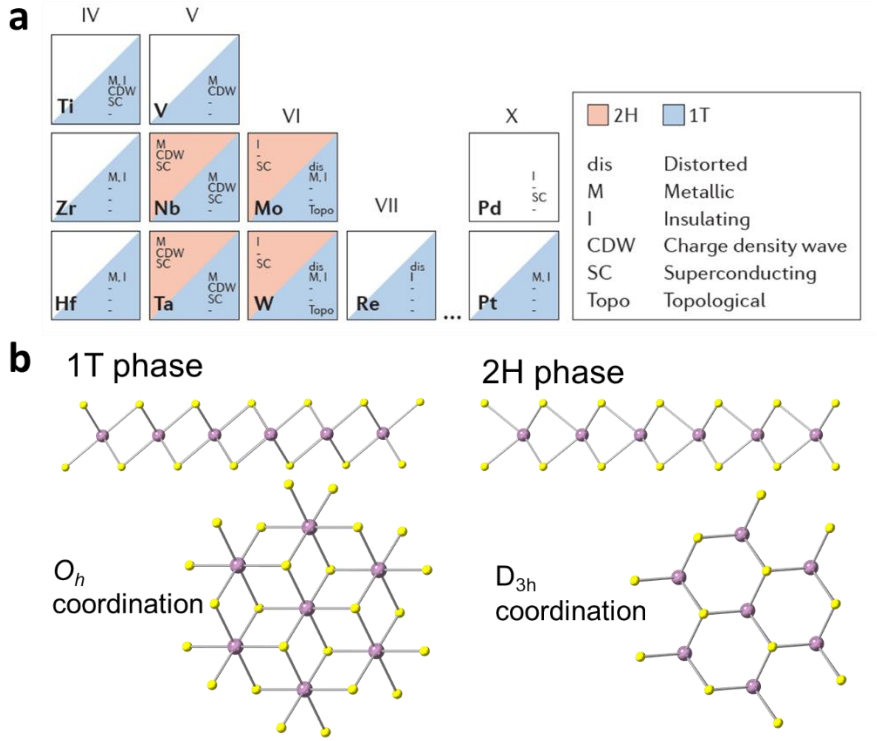

Figure 7.2 a) The different electronic properties of TMDCs depending on the metals and the chalcogenide. Adapted from reference 8. b) Two of the most common phases in TMDCs, their layered structure, and their coordination environments. The top part of this image shows the lateral view of a single layer, whereas the bottom part shows a view perpendicular to the layers.

The changes in the crystal structure for MOFs systems can be minimized by using similar metals, such as 3*d* metals of the first transition series. In the particular example of ZIFs, many crystal structures are available with different metallic cations of the first transition metal series (and Cd)[9–13] which have an influence on, for example, the flexibility of the

framework.[14,15] Another example in layered coordination polymers which has been vastly investigated is the use of different metal cations to change the magnetic properties.[16] An example of this versatility is the classical oxalate-based compounds.[17] These materials are composed by a subunit of $[M(III)(oxalate)_3]^{3-}$ (with M(III) = Cr, Fe, Ru), and in a combination of different transition metal cations, M^{2+}, such as Mn^{2+}, Fe^{2+}, Co^{2+}, Ni^{2+}, Cu^{2+} and a countercation, form extended layered materials. They present ferromagnetic ordering with different T*c*, which depends on the metal (maintaining the countercations, which can also be changed).

Following the reported examples in ZIFs, similar in chemical bonding and structure to **MUV-1-X** family, and oxalates changing the Tc using similar metallic cations of the first transition series, has been chosen three metals from the first transition series, and due to the different electronic environment of the cations has been expected to show different magnetic behaviors or T_c.

Herein, we design an approximation to extend the metallic cations from Fe^{2+} to Co^{2+}, Mn^{2+} and Zn^{2+} obtaining different metallic nodes in 2D molecular in the **MUV-1-X** family using the solvent-free synthesis described in the previous chapters to tune the magnetic properties (Figure 7.3).

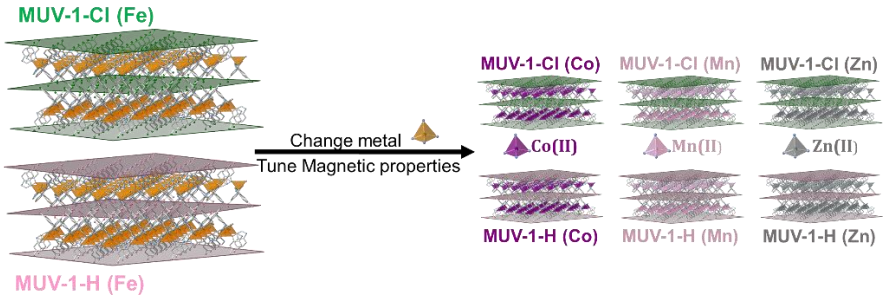

Figure 7.3. Broad versatility of the **MUV-1-Cl** and **MUV-1-H** system: it is possible to modify the magnetic properties while keeping the layered morphology needed for a two-dimensional material by changing the metallic cation.

7.2 Results and discussion

Changing metallic nodes. The existence of different metal sources compatible with chemical vapor deposition and solvent-free methods,[13] explored in Chapters 2 and 3, permits the modification of the reaction previously described in Chapters 5 and 6,[1] where benzimidazole derivates (XbimH, X = Cl, Br, CH_3, H, NH_2) and ferrocene were employed. Obtaining isostructural materials changing the metal node is a challenge that can lead to the modification of the physical properties of the materials, such as the magnetic properties (Figure 7.3). An important feature is the compatibility of the reactants and the solvent-free synthesis, to be suitable with for example, chemical vapor deposition (CVD). For this reason, the following metal precursors were selected: biscyclopentadienyl cobalt (II), tetramethylcyclopentadienyl manganese (II), bis(2,2,6,6-tetramethyl-3,5-heptanedionato) zinc (II) and ZnO. These metal precursors have been used in a solvent-free method to synthesize isostructural compounds of **MUV-**

1-Cl and **MUV-1-H**. The crystals obtained in the synthesis were characterized by single-crystal diffraction and powder X-ray diffraction (Figure 7.4), obtaining three isostructural compounds of **MUV-1-Cl** (Co, Mn, and Zn) and three of **MUV-1-H** (Co, Mn, and Zn). In these structures the metal cation is located in the inner part of the layers in a distorted tetrahedral environment, connected by benzimidazole bridges, allowing the magnetic exchange between the metal centers.

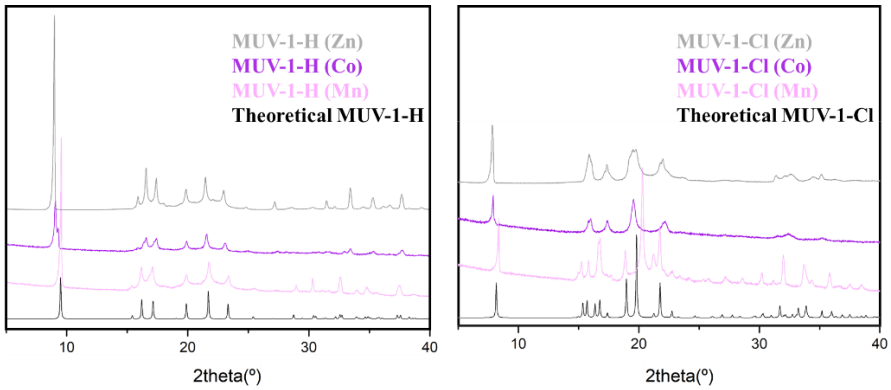

Figure 7.4 X-ray powder patterns of **MUV-1-H (M^{II})** and **MUV-1-Cl (M^{II})**. The experimental patterns are shown in pink (Mn(II)), purple (Co(II)) and grey (Zn(II)) for the respective compounds, and the calculated pattern from single-crystal data is shown in black for all compounds.

The size of the crystals depends on the metal used. The cobalt and compounds are sensitive smaller (around 40 µm) than the previously reported Fe(II) compound, whereas the Mn and Zn compounds are only obtained as crystalline powders (around 20 µm). Still, all these materials keep the layered morphology, as shown in Figure 7.5, which depicts characteristic SEM images of the different samples. Interestingly, **MUV-1-**

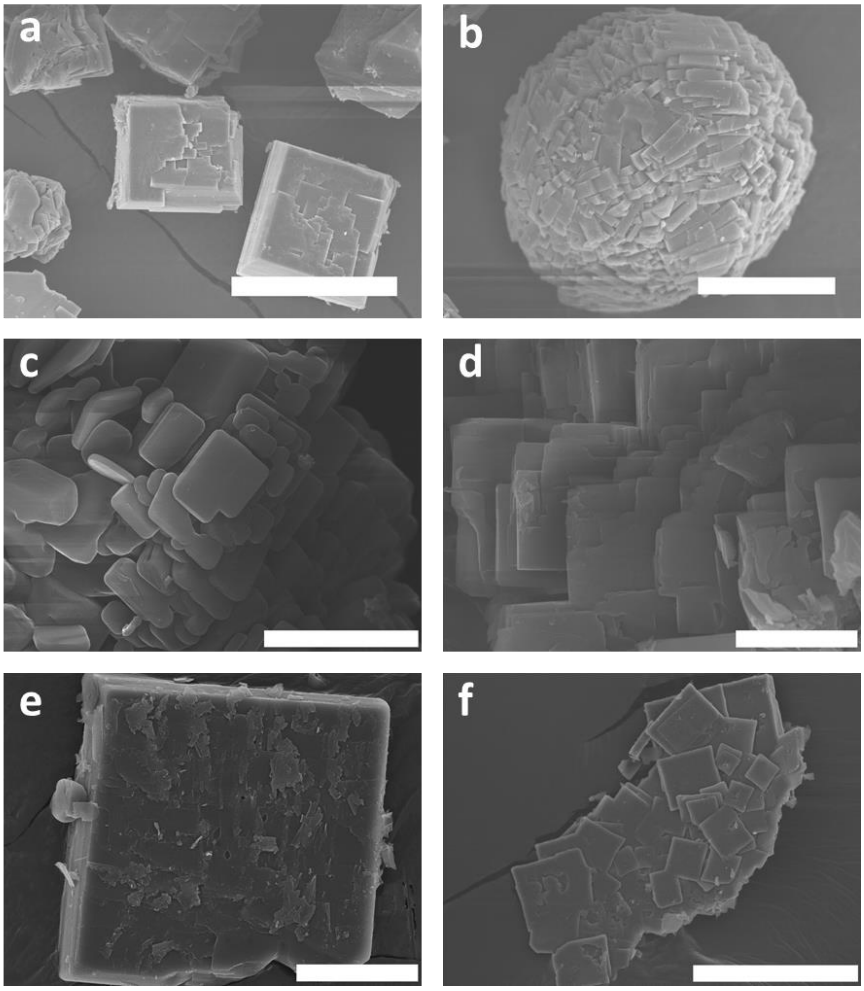

Figure 7.5 Scanning electron micrograph of bulk-type **MUV-1-H (Co)** (a), **MUV-1-Cl (Co)** (b), **MUV-1-H (Mn)** (c), **MUV-1-Cl (Mn)** (d), **MUV-1-H (Zn)** (e), **MUV-1-Cl (Zn)** (f). Scale bar is a) 40 µm, b) 20 µm, c) 5 µm, d) 10 µm, e) 10 µm, f) 40 µm.

Cl (Co) present spontaneous crystal aggregation with spherical uncommon morphologies (Figure 7.5b), suggesting more flexibility than the Fe(II) compound.

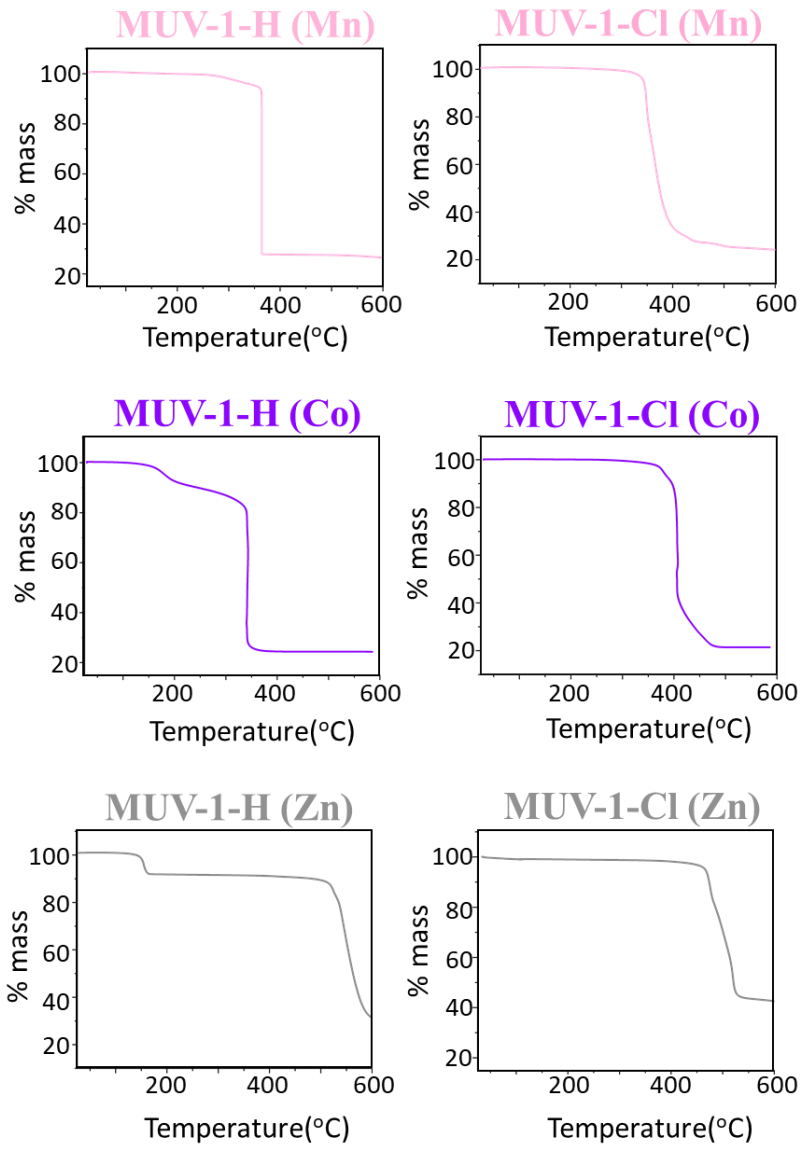

Figure 7.6 Thermal gravimetric analysis (TGA) of bulk crystals of **MUV-1-H (Co), MUV-1-Cl (Co)**, **MUV-1-H (Mn), MUV-1-Cl (Mn), MUV-1-H (Zn)** and **MUV-1-Cl (Zn)** at a heating rate of 20 ^{o}C min^{-1}.

The thermal stability of the Co(II) and Mn(II) analogues are similar to the Fe(II) compound, around 350°C for **MUV-1-H** and 400°C for **MUV-1-Cl** compound (Figure 7.6). However, the Zn(II) analogues of the two families present higher thermal stability, above 500°C.

Magnetic properties. The magnetic interactions between the metallic centers of the **MUV-1-X (M^{II})** were investigated by conventional susceptibility in the case of the bulk sample. Due to the diamagnetic nature of the Zn centers, (d^{10} electronic configuration) **MUV-1-X (Zn)** is non-magnetic. For **MUV-1-X (Co)** and **MUV-1-X (Mn)** the susceptibility, χ_m, shows antiferromagnetic interactions (Figure 7.7a). Moreover, as in the case of **MUV-1 (Fe),** a sharp increase of the molar susceptibility and the product, χ_m T is observed in **MUV-1 (Co)**, thus suggesting a spin-canted structure below the Néel temperature (11 K and 12 K, Figure 7.7a), an expected behavior compared with other Co azolates.[18,19] As has been observed by Thompson and co-workers in imidazole-based analogous compounds of Fe(II) and Co(II), which present antiferromagnetic ordering with spin-canting, Co(II) materials show lower T_C than the Fe(II) materials. In this compound, tetrahedral Co(II) is in the high spin state (S = 3/2) (electronic term $^4A_2$)

This kind of ordering is corroborated by the presence of magnetic hysteresis loops (Figure 7.7b) and the existence of an out-of-phase component in the ac magnetic susceptibility (Figure 7.8). On the contrary, **MUV-1-X (Mn)** does not show any uncompensated moment at low temperatures, and χ_m measurements show a maximum at 20 K, in agreement with the presence of antiferromagnetic order around 20 K. This

result agrees with the isotropic nature of the spin in Mn(II) (S = 5/2 with an orbitally non-degenerate electronic term $^6A_1$). It is consistent with unpublished works developed in our group comparing the magnetic behavior between a Fe(II) pillar layered material[20] and an isostructural Mn(II) compound.

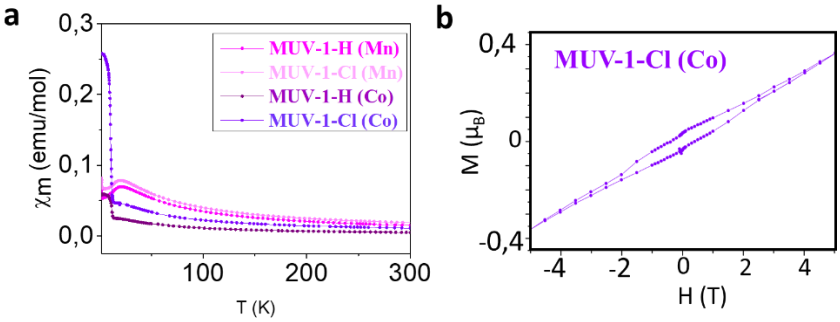

Figure 7.7 a) Thermal dependence of χ_m in the temperature range 2-300 K for the different compounds of the **MUV-1-X (M^{II}).** b) Magnetic hysteresis loops at 2 K for the **MUV-1-Cl (Co)** compound.

Table 7.1 T_N for the **MUV-1-X (M^{II})**

	MUV-1-Cl(Co)	**MUV-1-H(Co)**	**MUV-1-Cl(Mn)**	**MUV-1-H(Mn)**
T_N	11 K	12 K	20 K	20 K

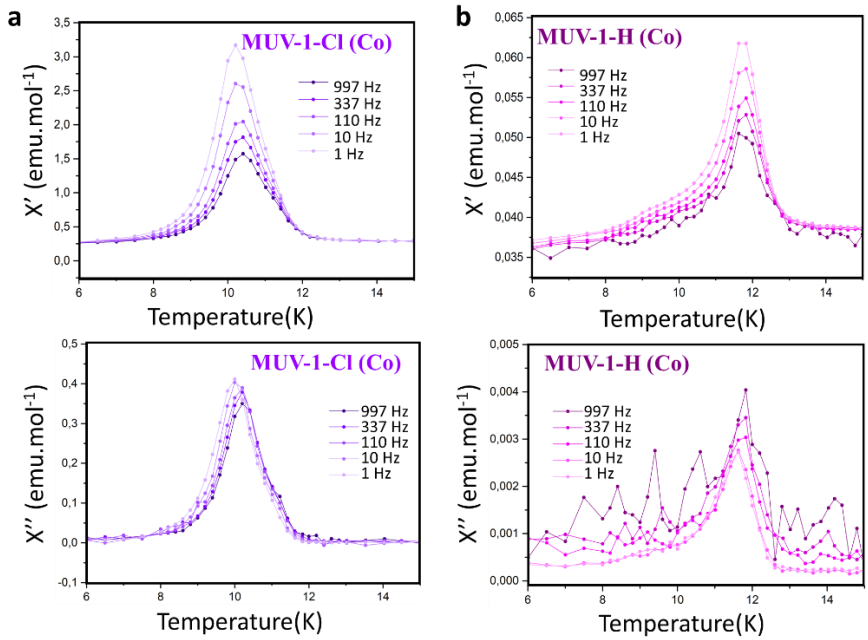

Figure 7.8. a) In-phase (top) and out of phase (below) dynamic susceptibility χ measured at different frequencies for the different compounds of the **MUV-1-Cl (Co)** b) In-phase (top) and out of phase (below) dynamic susceptibility χ measured at different frequencies for the different compounds of the **MUV-1-H (Co).**

Micromechanical exfoliation. The layered morphology of the crystals of **MUV-1-X (**M^{II}**)** (Figure 7.9) allows its delamination and the possibility to explore the 2D limit in these compounds. Due to the pure antiferromagnet ordering of **MUV-1-X** (Mn) and diamagnetic behavior of **MUV-1-X** (Zn), we have focused on the cobalt system in the **MUV-1-X** family. Bulk crystals of **MUV-1-X (Co)** were thinned-down by mechanical exfoliation as previously performed in **MUV-1-Cl**, yielding flakes with well-defined shapes (lateral dimensions of > 1 μ m) and different

thicknesses (from hundreds of nanometers down to few layers). The obtained flakes were characterized by optical and atomic force (AFM) microscopies (Figure 7.9) and, with Raman spectroscopy, then confirming its integrity and chemical composition. The Raman spectra are very similar to the **MUV-1-X** Fe(II), the expected for the Raman spectroscopy, due to the use of the same organic ligands.

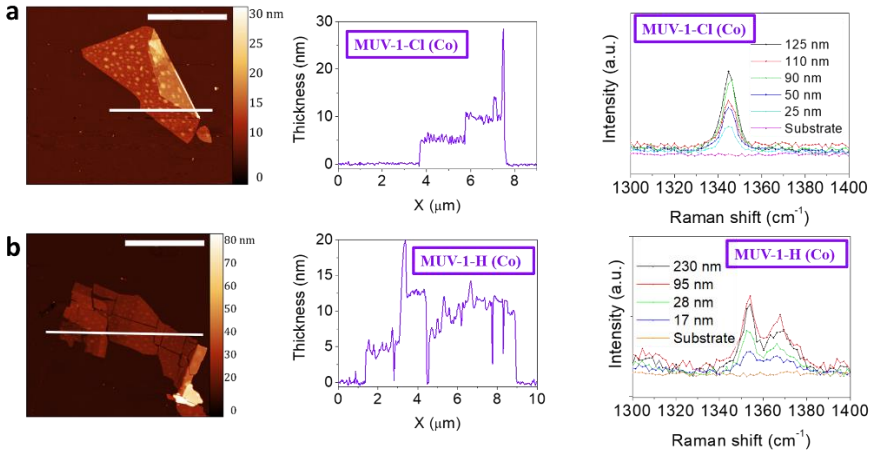

Figure 7.9 a) AFM image (left) and profile (middle) of a typical exfoliated flakes, scale bars are 5 μm, and the selected region of the Raman spectra for different thicknesses flakes of **MUV-1-Cl (Co)** (a) and **MUV-1-H (Co)** (b).

Magnetism detection in the 2D limit. The magnetic order of the mechanically exfoliated thin-layers could not be investigated by conventional magnetometers due to the small amount of material to be sensed. In fact, magnetic ordering in 2D materials has been only studied recently by the Magneto-Optical Kerr effect or NV (nitrogen vacancies) centers.[21,22] However, the previous techniques are not suitable for sensing

antiferromagnets or spin canted antiferromagnets interactions since the total magnetization is zero or very weak. Therefore, we have employed nano-resonators, a technique that has recently been shown to successfully probe magnetic phase transitions.[23]

In collaboration with the Steneeken group at TU Delft (Netherlands), we exfoliated flakes of well-known **MUV-1-Cl (Fe) (**to compare the magnetic ordering temperature) and **MUV-1-H (Co)** and transferred these on top of circular cavities (diameter d = 5 – 6 μm) etched in a SiO_2/Si substrate using deterministic dry viscoelastic stamping to form freestanding nanodrums (Figure 7.10a). Due to large flexibility, low estimated Young's modulus and thus low bending rigidity of these MOF sheets, suspended flakes behave as membranes even at relatively large thicknesses for a given range of cavity diameters. Samples are placed on a dry cryostat and cooled down to the temperatures of 4 K at the pressure below 10^{-6} mbar. Temperature-dependent mechanical properties of the nanodrums are then investigated using laser interferometry technique from 4 to 50 K in the absence of magnetic field. Figure 7.10b shows resonances of a fundamental membrane mode at 40 K for **MUV-1-Cl (Fe)** and **MUV-1-H (Co)**, respectively (black solid dots).

We fit the measured resonance peaks to a standard harmonic oscillator (colored solid lines) to extract the fundamental mode resonance frequency f_0 and mechanical quality factor Q. Substantially large Q factors ranging from 1000 to 3500 and high resonance frequencies of 32.1 – 40.67 MHz at 40 K indicate a high tension in the membranes due to a build-up of the thermal strain. For comparative purposes, graphene at 50 K has Q factor

of 1800. The thermal strain in the membranes is related to the thermal expansion coefficient and thus to the specific heat of the material, c_v. This interrelation allows to observe phase transition-related anomalies in $c_v(T)$ reflected in $f_0(T)$, since $c_v(T) \propto -- d(f^2_0(T))/dT$.

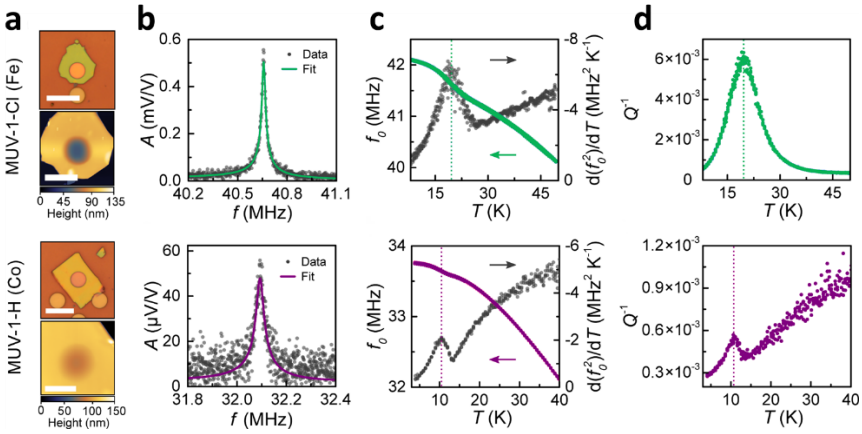

Figure 7.10 Mechanical resonances of thin metal-organic framework **MUV-1-Cl (Fe)** and **MUV-1-H (Co)** membranes. a) Peak-force atomic force microscopy (AFM) images. b) Resonance peaks of a fundamental membrane mode at 40 K. c) Coloured dots - resonance frequency f_0 as a function of temperature, black dots - temperature derivative of f^2_0 (T) as a function of temperature. d) Mechanical dissipation Q^{-1} as a function of temperature.

In Figure 7.10c we plot measured f_0 (colored filled dots) and corresponding temperature derivative of f^2_0 (black filled dots) for the two compounds. The phase transition-related anomaly is well visible as a kink in $f_0(T)$ and is even more pronounced in $d(f^2_0(T))/dT$, with peaks at 19.5 ± 1.0 K for **MUV-1-Cl(Fe)**, and 10.5 ± 0.5 K for **MUV-1-H(Co)**. This originates from the discontinuity in specific heat of the compounds at T_N

according to the Landau theory of phase transitions.[23] Mechanical dissipation $Q^{-1}(T)$ also exhibits a local maximum near T_N, as displayed in Figure 7.12d, that can be related to thermoelastic or other more intricate magnetomotive damping mechanism. Thus, we unequivocally show that thin flakes retain the magnetic properties of the bulk.

Table 7.2 T_N of **MUV-1-Cl(Fe)** and **MUV-1-H(Co)** compared by the two used techniques, SQUID measurements for bulk material, and mechanical nanoresonators for the exfoliated material.

	MUV-1-Cl(Fe)	**MUV-1-H(Co)**
Mechanical Resonators	19.5 K	10.5 K
SQUID (Bulk)	20.0 K	12.0 K

7.3 Conclusions

We have demonstrated here how the coordination chemistry and chemical design are useful tools to synthesize and tune the properties of layered compounds and 2D molecular materials. Using a solvent-free synthetic route we prepared a family of 2D molecular materials, in which various transition metals have been incorporated in the nodes (Mn(II), Co(II), Zn(II)). This has provided the possibility to study the magnetic properties at the 2D limit using for the first time mechanical resonators to investigate the magnetic order in antiferromagnetic MOFs. This has been possible thanks to the robustness and quality of the 2D molecular flakes which have permitted to construct mechanical membranes.

7.4 Methods

Synthesis of MUV-1-X (M^{II}). Metallic source (biscyclopentadienyl cobalt (II), tetramethylcyclopentadienyl manganese (II), bis(2,2,6,6-tetramethyl-3,5-heptanedionato) zinc (II) and ZnO) (0.16 mmol) and benzimidazole derivate (0.34 mmol) were combined and sealed under vacuum in a layering tube (4 mm diameter). The mixture was heated at 150 °C for Co(II) compounds and 250 °C for Mn(II) and Zn(II) compounds, for 4 days to obtain crystals suitable for X-ray single-crystal diffraction (In case of **MUV-1-H(Co)** and **MUV-1-Cl(Mn)**). The product was allowed to cool to room temperature, and the layering tube was then opened. The unreacted precursors were extracted with acetonitrile and benzene, and the main compound was isolated as crystals (yield 40 %). Phase purity was established by X-ray powder diffraction.

Single crystal. X-ray data for compounds **MUV-1-H (Co)** and **MUV-1-Cl (Mn)** were collected at a temperature of 100 K using synchrotron radiation at single crystal X-ray diffraction beamline I19 in Diamond light Source[24], equipped with an Pilatus 2M detector and an Oxford Cryosystem nitrogen flow gas system. Data was measured using GDA suite of programs. X-ray data was processed and reduced using CrysAlisPro suite of programs. Absorption correction was performed using empirical methods (SCALE3 ABSPACK) based upon symmetry-equivalent reflections combined with measurements at different azimuthal angles.[25–27] The crystal structures were solved and refined against all F^2 values using the SHELXL and Olex 2 suite of programs.[28,29] Despite that the coordination polymers are intrinsically chiral, the centrosymmetric space group *C*2/*c* was found as

result of the racemic distribution of the disordered layers of the **MUV-1-H (Co)**.

X-ray powder diffraction. Polycrystalline samples of **MUV-1-H (Co), MUV-1-Cl (Co)**, **MUV-1-H (Mn)**, **MUV-1-Cl (Mn)**, **MUV-1-H (Zn)**, **MUV-1-Cl (Zn)** were lightly ground in an agate mortar and pestle and used to fill 0.5 mm borosilicate capillaries that was mounted and aligned on an Empyrean PANalytical powder diffractometer, using Cu Kα radiation (λ = 1.54056 Å). Two repeated measurements were collected at room temperature for each compound (2θ = 5−40 °) and merged in a single diffractogram.

Thermogravimetric analisys. Thermogravimetric analyzes of **MUV-1-X (M^{II})** were carried out with a Mettler Toledo TGA/SDTA851e/SF/1100 apparatus in the 25–600 °C temperature range under a 5°C·min^{-1} scan rate and an air flow of 30 mL·min^{-1}.

Scanning Electronic Microscopy. Scanning Electronic Micrograph were estimated by electron probe microanalysis (EPMA) performed in a Philips SEM XL30 equipped with an EDAX microprobe and images were recorded in a Hitachi S-4800.

Raman spectra. Raman spectra were acquired with a micro-Raman (model XploRA ONE from Horiba, Kyoto, Japan) with a grating of 2400 gr/mm, slit of 50 µm, and hole of 500 µm. The employed wavelengths were 532 nm, 638 nm, and 785 nm. The power density of the laser used for spectra measured at 532 nm was 5.25 mW/μm^2 (bulk crystals) and 170 µW/μm^2 (thin-layers), for spectra measured at 638 nm it was 7.58 mW/μm^2 (bulk

crystals), and for those spectra measured at 785 nm it was 7.2 mW/μm^2 (bulk crystals).

Magnetic properties. Variable-temperature (2−300 K) direct current (dc) magnetic susceptibility measurements were carried out in an applied field of 1.0 kOe and variable field magnetization measurements up to ±5 T at 2.0 K. The susceptibility data were corrected from the diamagnetic contributions as deduced by using Pascal's constant tables. Variable-temperature (16−23 K) alternating current (ac) magnetic susceptibility measurements in a ±4.0 G oscillating field at frequencies in the range of 1−997 Hz were carried out in a zero dc field. All the measurements were performed with a SQUID magnetometer (Quantum Design MPMS-XL-5 & MPMS-XL-7).

Laser interferometry. The motion of the nanodrums was measured using a laser interferometry set-up, similar to the one reported in ref. 2. The sample is mounted on a xyz piezomotive nanopositioning stage. A blue diode laser (λ = 405 nm), that is power-modulated by a Vector Network Analyser (VNA), is focused at the centre of the membrane and used to optothermally excite the membrane to motion at a given frequency. A red He-Ne laser (λ = 632 nm) is used to read out vibrations of the nanodrum, motion of which is analyzed using homodyne detection scheme and processed by VNA. Laser spot diameter is in the order of 1 μm. It is checked that the resonance frequency changes due to laser heating are insignificant for all membranes.

Peak-force AFM. All peak-force AFM data is acquired at a constant 50 nN of applied peak force using a cantilever with a spring constant k = 22:8

Nm^{-1} on Bruker Dimension FastScan AFM. The thickness of the sample is estimated taking the average of 3 to 5 profile scans.

7.5 References

(1) López-Cabrelles, J.; Mañas-Valero, S.; Vitórica-Yrezábal, I. J.; Bereciartua, P. J.; Rodríguez-Velamazán, J. A.; Waerenborgh, J. C.; Vieira, B. J. C.; Davidovikj, D.; Steeneken, P. G.; van der Zant, H. S. J.; Mínguez Espallargas, G.; Coronado, E. Isoreticular Two-Dimensional Magnetic Coordination Polymers Prepared through Pre-Synthetic Ligand Functionalization. *Nat. Chem.* **2018**, *10* (10), 1001–1007.

(2) Pedersen, K. S.; Perlepe, P.; Aubrey, M. L.; Woodruff, D. N.; Reyes-Lillo, S. E.; Reinholdt, A.; Voigt, L.; Li, Z.; Borup, K.; Rouzières, M.; Samohvalov, D.; Wilhelm, F.; Rogalev, A.; Neaton, J. B.; Long, J. R.; Clérac, R. Formation of the Layered Conductive Magnet CrCl2(Pyrazine)2 through Redox-Active Coordination Chemistry. *Nat. Chem.* **2018**, *10* (10), 1056–1061.

(3) Hmadeh, M.; Lu, Z.; Liu, Z.; Gándara, F.; Furukawa, H.; Wan, S.; Augustyn, V.; Chang, R.; Liao, L.; Zhou, F.; Perre, E.; Ozolins, V.; Suenaga, K.; Duan, X.; Dunn, B.; Yamamto, Y.; Terasaki, O.; Yaghi, O. M. New Porous Crystals of Extended Metal-Catecholates. *Chem. Mater.* **2012**, *24* (18), 3511–3513.

(4) Rubio-Giménez, V.; Galbiati, M.; Castells-Gil, J.; Almora-Barrios, N.; Navarro-Sánchez, J.; Escorcia-Ariza, G.; Mattera, M.; Arnold, T.; Rawle, J.; Tatay, S.; Coronado, E.; Martí-Gastaldo, C. Bottom-Up Fabrication of Semiconductive Metal–Organic Framework Ultrathin Films. *Adv. Mater.* **2018**, *30* (10), 1–8.

(5) Skorupskii, G.; Trump, B. A.; Kasel, T. W.; Brown, C. M.; Hendon, C. H.; Dincă, M. Efficient and Tunable One-Dimensional Charge Transport in Layered Lanthanide Metal–Organic Frameworks. *Nat. Chem.* **2020**, *12* (2), 131–136.

(6) Castellanos-Gomez, A. Black Phosphorus: Narrow Gap, Wide Applications. *J. Phys. Chem. Lett.* **2015**, *6* (21), 4280–4291.

(7) Ares, P.; Aguilar-Galindo, F.; Rodríguez-San-Miguel, D.; Aldave, D. A.; Díaz-Tendero, S.; Alcamí, M.; Martín, F.; Gómez-Herrero, J.; Zamora, F. Mechanical Isolation of Highly Stable Antimonene under Ambient Conditions. *Adv. Mater.* **2016**, *28* (30), 6332–6336.

(8) Manzeli, S.; Ovchinnikov, D.; Pasquier, D.; Yazyev, O. V.; Kis, A. 2D Transition Metal Dichalcogenides. *Nature Reviews Materials*. 2017.

(9) Banerjee, R.; Phan, A.; Wang, B.; Knobler, C.; Furukawa, H.; O'Keeffe, M.; Yaghi, O.

M. High-Throughput Synthesis of Zeolitic Imidazolate Frameworks and Application to CO2 Capture. *Science* **2008**, *319* (5865), 939–943.

(10) Tian, Y.-Q.; Yao, S.-Y.; Gu, D.; Cui, K.-H.; Guo, D.-W.; Zhang, G.; Chen, Z.-X.; Zhao, D.-Y. Cadmium Imidazolate Frameworks with Polymorphism, High Thermal Stability, and a Large Surface Area. *Chem. - A Eur. J.* **2010**, *16* (4), 1137–1141.

(11) Kadota, K.; Sivaniah, E.; Bureekaew, S.; Kitagawa, S.; Horike, S. Synthesis of Manganese ZIF-8 from $[Mn(BH_4)_2 \cdot 3THF] \cdot NaBH_4$. *Inorg. Chem.* **2017**, *52334* (4), 8744–8747.

(12) Kadota, K.; Sivaniah, E.; Bureekaew, S.; Kitagawa, S.; Horike, S. Synthesis of Manganese ZIF-8 from $[Mn(BH_4)_2$ 3THF] $NaBH_4$. **2017**, *52334* (4), 8–11.

(13) López-Cabrelles, J.; Romero, J.; Abellán, G.; Giménez-Marqués, M.; Palomino, M.; Valencia, S.; Rey, F.; Mínguez Espallargas, G. Solvent-Free Synthesis of ZIFs: A Route toward the Elusive Fe(II) Analogue of ZIF-8. *J. Am. Chem. Soc.* **2019**, *141* (17), 7173–7180.

(14) McGuirk, C. M.; Runčevski, T.; Oktawiec, J.; Turkiewicz, A.; Taylor, M. K.; Long, J. R. Influence of Metal Substitution on the Pressure-Induced Phase Change in Flexible Zeolitic Imidazolate Frameworks. *J. Am. Chem. Soc.* **2018**, *140* (46), 15924–15933.

(15) Andres-Garcia, E.; López-Cabrelles, J.; Oar-Arteta, L.; Roldan-Martinez, B.; Cano-Padilla, M.; Gascon, J.; Mínguez Espallargas, G.; Kapteijn, F. Cation Influence in Adsorptive Propane/Propylene Separation in ZIF-8 (SOD) Topology. *Chem. Eng. J.* **2019**, *371* (March), 848–856.

(16) Thorarinsdottir, A. E.; Harris, T. D. Metal-Organic Framework Magnets. *Chem. Rev.* **2020**, acs.chemrev.9b00666.

(17) Tamaki, H.; Zhong, Z. J.; Matsumoto, N.; Kida, S.; Koikawa, M.; Achiwa, N.; Hashimoto, Y.; Okawa, H. Design of Metal-Complex Magnets. Syntheses and Magnetic Properties of Mixed-Metal Assemblies $\{NBu_4[MCr(Ox)_3]\}x$ (NBu_4^+ = Tetra(n-Butyl)Ammonium Ion; Ox2- = Oxalate Ion; M = Mn^{2+}, Fe^{2+}, Co^{2+}, Ni^{2+}, Cu^{2+}, Zn^{2+}). *J. Am. Chem. Soc.* **1992**, *114* (18), 6974–6979.

(18) Tian, Y. Q.; Cai, C. X.; Ren, X. M.; Duan, C. Y.; Xu, Y.; Gao, S.; You, X. Z. The Silica-Like Extended Polymorphism of Cobalt(II) Imidazolate Three-Dimensional Frameworks:

X-Ray Single-Crystal Structures and Magnetic Properties. *Chem. - A Eur. J.* **2003**, *9* (22), 5673–5685.

(19) Tian, Y. Q.; Chen, Z. X.; Weng, L. H.; Guo, H. Bin; Gao, S.; Zhao, D. Y. Two Polymorphs of Cobalt(II) Imidazolate Polymers Synthesized Solvothermally by Using One Organic Template N,N-Dimethylacetamide. *Inorg. Chem.* **2004**, *43* (15), 4631–4635.

(20) López-Cabrelles, J.; Giménez-Marqués, M.; Mínguez Espallargas, G.; Coronado, E. Solvent-Free Synthesis of a Pillared Three-Dimensional Coordination Polymer with Magnetic Ordering. *Inorg. Chem.* **2015**, *54* (21), 10490–10496.

(21) Huang, B.; Clark, G.; Navarro-Moratalla, E.; Klein, D. R.; Cheng, R.; Seyler, K. L.; Zhong, Di.; Schmidgall, E.; McGuire, M. A.; Cobden, D. H.; Yao, W.; Xiao, D.; Jarillo-Herrero, P.; Xu, X. Layer-Dependent Ferromagnetism in a van Der Waals Crystal down to the Monolayer Limit. *Nature* **2017**, *546* (7657), 270–273.

(22) Thiel, L.; Wang, Z.; Tschudin, M. A.; Rohner, D.; Gutiérrez-Lezama, I.; Ubrig, N.; Gibertini, M.; Giannini, E.; Morpurgo, A. F.; Maletinsky, P. Probing Magnetism in 2D Materials at the Nanoscale with Single-Spin Microscopy. *Science* **2019**, *364* (6444), 973–976.

(23) Šiškins, M.; Lee, M.; Mañas-Valero, S.; Coronado, E.; Blanter, Y. M.; van der Zant, H. S. J.; Steeneken, P. G. Magnetic and Electronic Phase Transitions Probed by Nanomechanical Resonators. *Nat. Commun.* **2020**, *11* (1), 2698.

(24) Nowell, H.; Barnett, S. A.; Christensen, K. E.; Teat, S. J.; Allan, D. R. I19, the Small-Molecule Single-Crystal Diffraction Beamline at Diamond Light Source. *J. Synchrotron Radiat.* **2012**, *19* (3), 435–441.

(25) Krause, L.; Herbst-Irmer, R.; Sheldrick, G. M.; Stalke, D. Comparison of Silver and Molybdenum Microfocus X-Ray Sources for Single-Crystal Structure Determination. *J. Appl. Crystallogr.* **2015**, *48* (1), 3–10.

(26) Blessing, R. H. An Empirical Correction for Absorption Anisotropy. *Acta Crystallogr. Sect. A Found. Crystallogr.* **1995**, *51* (1), 33–38.

(27) Sheldrick, G. M. SADABS, Empirical Absorption Correction Program Based upon the Method of Blessing. 1994, p University of Göttingen, Göttingen.

(28) Sheldrick, G. M. Crystal Structure Refinement with SHELXL. *Acta Crystallogr. Sect. C Struct. Chem.* **2015**, *71* (1), 3–8.

(29) Dolomanov, O. V.; Bourhis, L. J.; Gildea, R. J.; Howard, J. A. K.; Puschmann, H. OLEX2 : A Complete Structure Solution, Refinement and Analysis Program. *J. Appl. Crystallogr.* **2009**, *42* (2), 339–341.

Chapter 8

Beyond MUV-1: novel strategies for 2D molecular materials

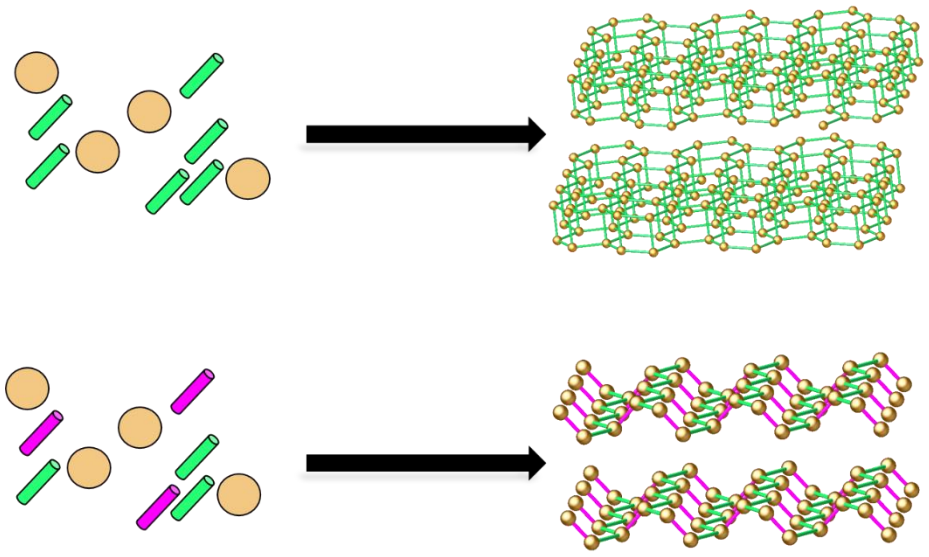

8.1 Introduction

During the last Chapters (5-7), **MUV-1-X** has shown to be a 2D material facile to be tuned and modified through a proper chemical design while preserving its crystal structure. However, the versatility of coordination chemistry in the field of 2D materials allows to go beyond with the aim of obtaining different properties. In this context, two different strategies can be foreseen to successfully prepare new 2D molecular materials. The first, and more intuitive, is the addition of a second functional group to the benzimidazoles, which causes a steric hindrance and may result in a change in the topology. This has been explored in other ZIFs: when a larger substituent is introduced in the imidazole ligand, different topologies are obtained for each substituent. For example, the SOD topology can be found when using 2-methylimidazole and Zn^{2+}, as in ZIF-8 among others, but when using 2-ethylimidazole a material with RHO topology is obtained (see Figure 8.1).[1]

In the case of **MUV-1**, where the organic ligand is 5-X-benzimidazole, additional substituents could be introduced in either position 2 or position 6 (see Figure 8.2). Upon close inspection of the crystal structure of **MUV-1**, it can be observed that the square disposition of the Fe(II) atoms in the layers is not compatible with the incorporation of another substituent in position 6. Thus, its inclusion should result in a different arrangement, in a similar way that the incorporation of an ethyl group in the imidazole ligand causes a change in the ZIF-8 structure (Figure 8.1).

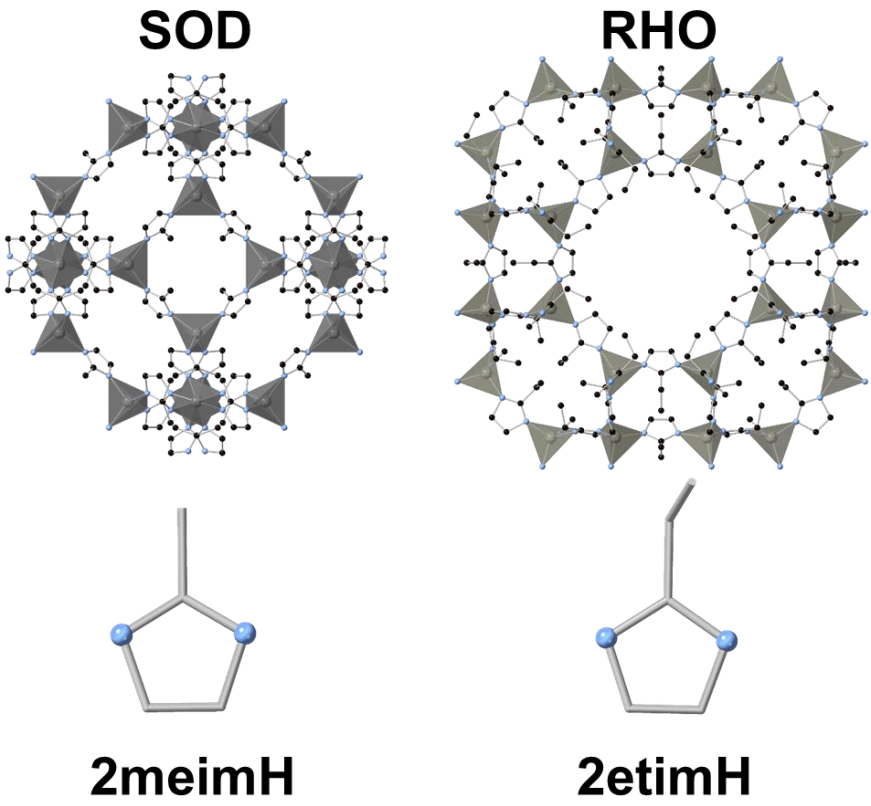

Figure 8.1 Two different achievable crystal structures changing the functional group in the imidazole ligand.

The second strategy that can be followed to obtain a different 2D material based on coordination chemistry consists of identifying a 3D pillared structure and chemically modify the pillar to prevent the bonding between the layers, i.e. replacing the pillar by a terminal ligand.[2,3] Although it looks simple, this is a challenging approach, and only few examples have been reported using this strategy. For instance, Grey and co-workers recently showed the preferential crystal growth in the *ab* plane of UiO-67,

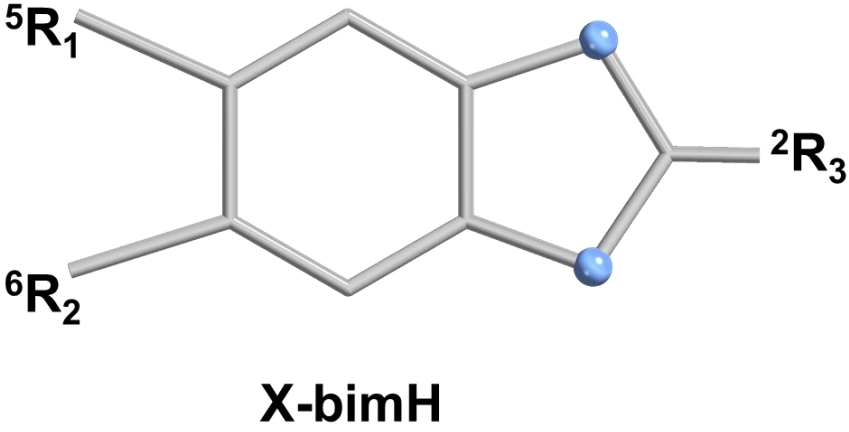

Figure 8.2 Possible position for functional groups in the benzimidazoles linker.

a combination of Hf clusters and terephthalic acid, resulting in a different phase. They achieved this crystal structure through a controlled introduction of defects that weaken the *c* direction. This permits to exfoliate the MOF in nanosheets by applying soft forces such as sonication or mechanical grinding (Figure 8.3a).[4] Another example was developed by Zhou's group, introducing a pillar in a pre-formed layered MOF. This pillar ligand incorporates a S-S bond, easy to break by oxidation. The intercalation of this pillar separates the layers from the MOF, and subsequent oxidation breaks the pillars thus facilitating the exfoliation process (Figure 8.3b).[5]

Using these two strategies, we design here two different approximations to obtain different 2D molecular materials through the **MUV-1-X** solvent-free synthesis: **a)** a second substituent is inserted in the benzimidazole ligand to force a structural change, while retaining the

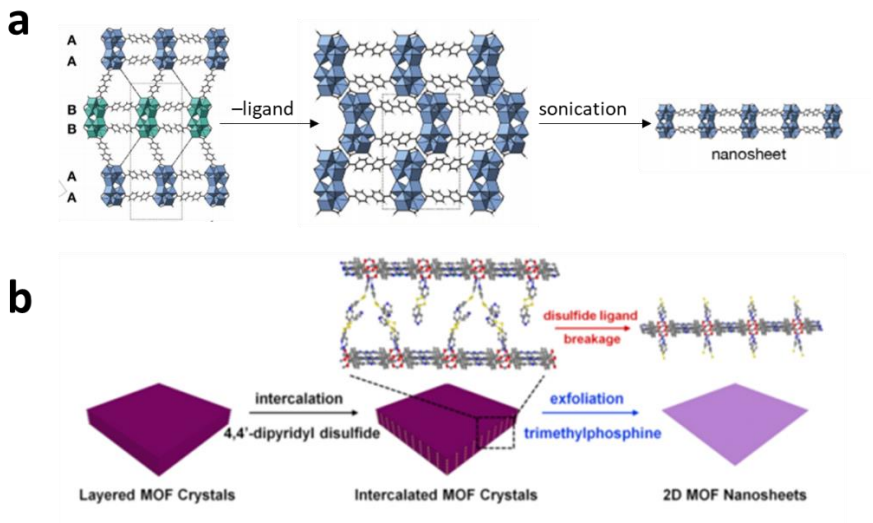

Figure 8.3 a) The facilitate exfoliation process through the introduction of defects in a UiO-67 novel phase. b) Intercalation of redox-active pillar ligand to favor the exfoliation mechanism to obtain MOF nanosheets. Adapted from references 5 and 6.

layered morphology and magnetic properties. **b)** A strategy using a mixed-based ligand synthesis to facilitate the exfoliation process in a pillar layered material (Figure 8.4).

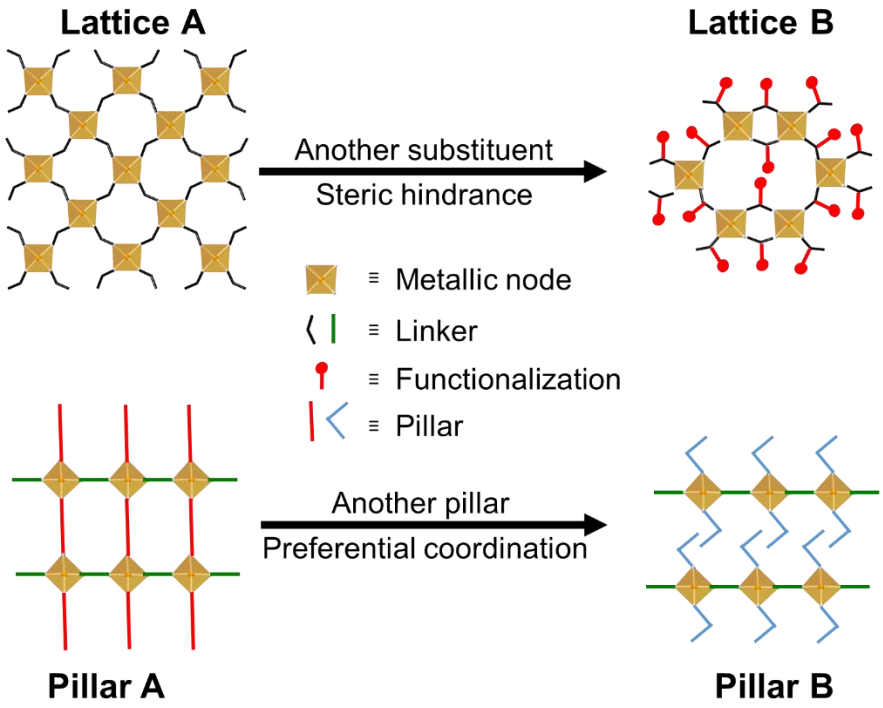

Figure 8.4 The two different approaches followed in this Chapter to synthesize novel layered coordination polymers and layered MOFs.

8.2 Results and discussion

Steric hindrance strategy. The molecular nature of the coordination polymers not only permits changes in the metal nodes but also in the ligand part, *i.e.* on the functional groups. Specifically, the organic ligand used for the preparation of **MUV-1-X**, 5-X-benizimidazole (see Figure 8.5), is modified with the addition of a second substituent adjacent to the 5th position. Thus, two different ligands have been used, namely 5,6-dichlorobenzimidazole (Cl_2bimH) and 5,6-dimethylbenzimidazole ($(CH_3)_2$bimH).

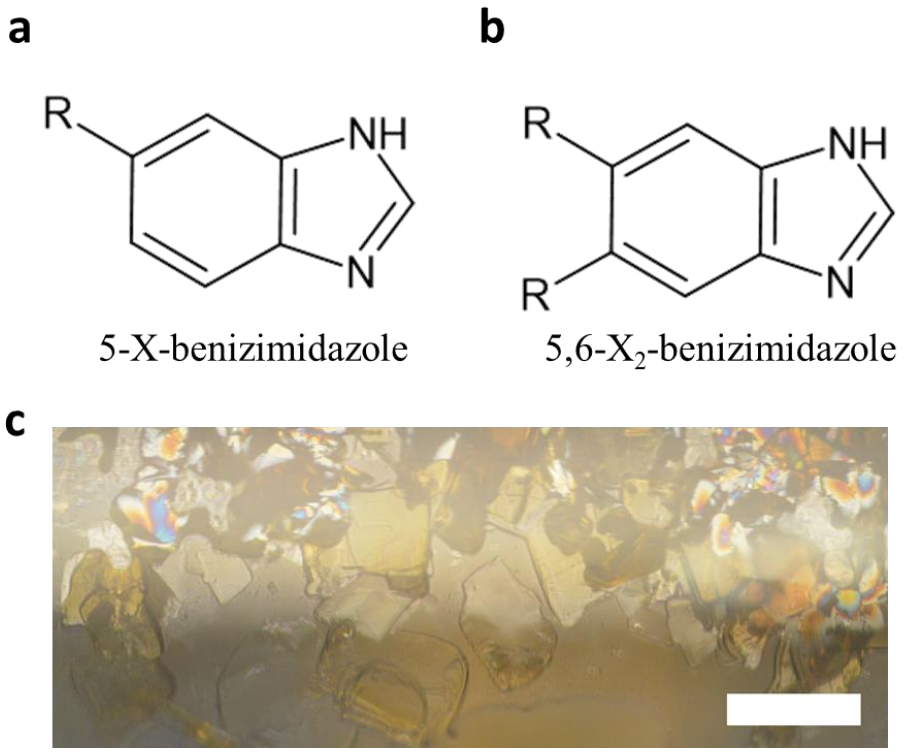

Figure 8.5 a) The monosubstituted ligand used to construct the **MUV-1-X** family. b) The disubstituted ligand used to synthesize the **MUV-8-X_2** family. c) Crystals of **MUV-8-Cl2** as syhthesized inside the reaction tube. Scale bar is 400 μm.

Importantly, upon solvent-free reaction of these ligands with ferrocene two new coordination polymers are obtained, the so-called **MUV-8-Cl_2** and **MUV-8-$(CH_3)_2$**. The obtained crystals of **MUV-8-Cl_2** were big enough (around 500 μm) to solve its crystal structure by single-crystal diffraction. However, the small size of the **MUV-8-$(CH_3)_2$** crystals (under 10 μm) precludes to solve its crystal structure. Still, its X-ray powder diffraction pattern is in good agreement with the calculated from the single

crystal data of **MUV-8-Cl$_2$** (Figure 8.6), confirming the isoreticularity of both compounds, **MUV-8-Cl$_2$** and **MUV-8-(CH$_3$)$_2$**.

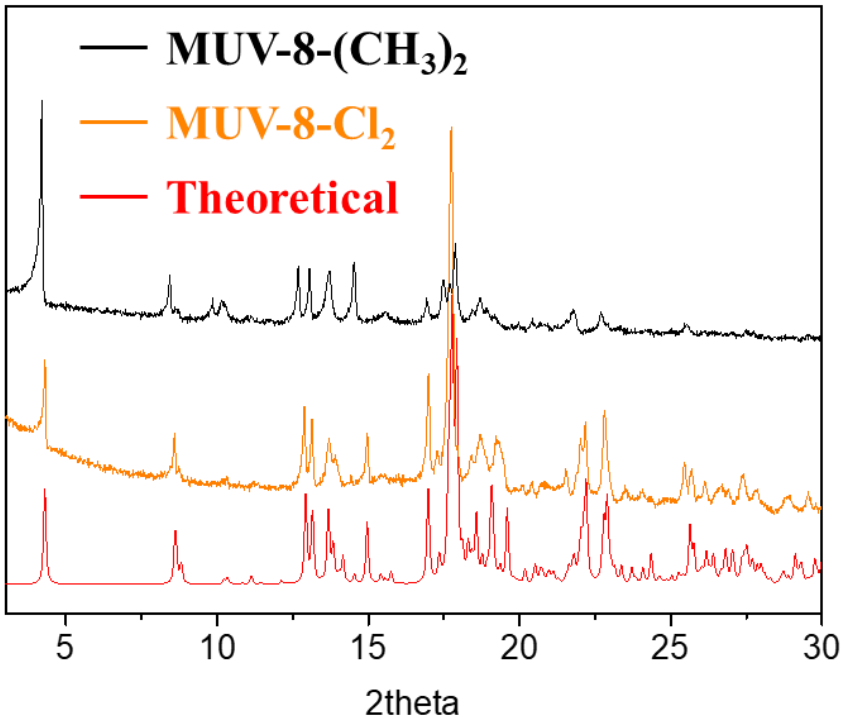

Figure 8.6 X-ray powder patterns of **MUV-8-Cl$_2$** and **MUV-8-(CH$_3$)$_2$.** The experimental patterns are shown in orange and black for the respective compounds, and the calculated pattern from single-crystal data (from **MUV-8-Cl$_2$**) is shown in red.

The crystal structure shows that **MUV-8-Cl$_2$** is a layered material. The individual sheets of these materials are composed of double layers of iron centers connected by benzimidazolate bridges, with three ligands in the *ab* plane (top or bottom layers), and a fourth ligand connecting two iron centers each in its respective layer (*c* axis) (Figure 8.7). The iron centers

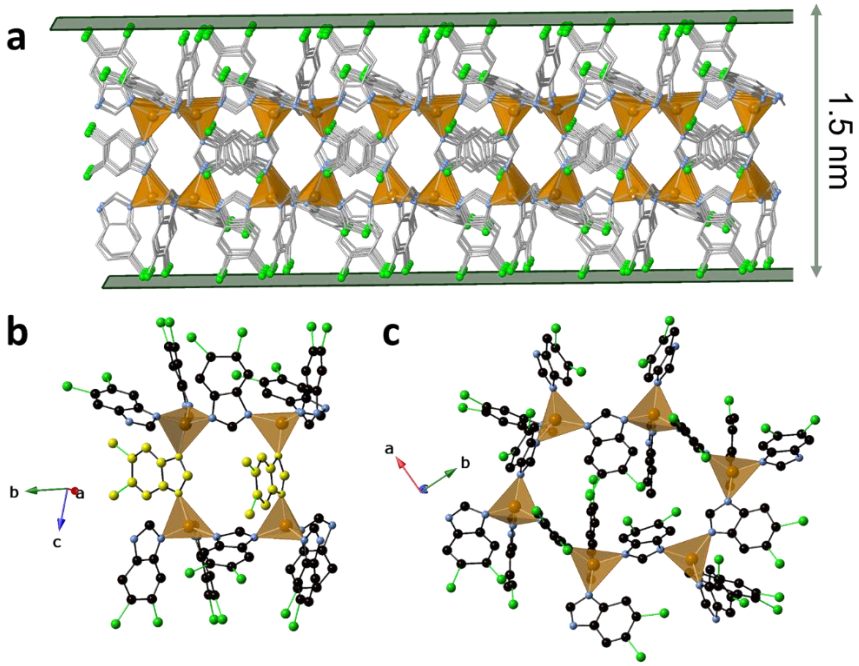

Figure 8.7 a) Crystal structure of the **MUV-8-Cl$_2$**, composed by Fe(II) centers in a tetrahedral environment, forming extended layers in the *ab* plane. b) The connectivity in one sheet, three ligands connecting in *ab* plane, and the fourth ligand (in yellow) connecting the two layers of iron centers (the Fe bilayer). c) The distorted hexagonal lattice in the perpendicular *ab* plane view.

are located in very distorted tetrahedral sites, with Fe–N bond lengths between 1.8-2.1 Å. In the perpendicular view of the *ab* plane, the sheet has a distorted hexagonal arrangements, different from the square lattice arragment of **MUV-1**.

There are seven crystallographic different iron centers in one double layer sheet. In this case, the connection between the two Fe layers inside

one sheet, i.e. a Fe "double-layer", is a coordination bond, unlike the weak van der Waals interactions through the stacked layers of the material. These neutral layers are superposed in a similar arrangement to an AB stacking, with a small shift between iron centers (Figure 8.8a).

The chloride atoms are located at the surfaces at 3.45 Å distance between sheets, weakly interacting through van der Waals forces like in the **MUV-1-Cl** case. Thus, if compared with the parent **MUV-1**, an individual layer of **MUV-8** has a thickness of 1.5 nm formed by the sequence "ligand layer/Fe double-layer/ligand layer" whereas, in **MUV-1**, it is only 1 nm since it is formed just by one layer of Fe centers (sequence of "ligand layer/single Fe layer/ligand layer") (see Figure 8.9).

Moreover, between the **MUV-8-X_2** sheets, some ferrocene molecules are located, interacting weakly with the layers of the compound (Figure 8.8b). Interestingly, these ferrocene molecules between sheets of **MUV-8-Cl_2** cannot be removed by heating the samples as can be seen in the thermogravimetric analysis (Figure 8.10). The presence of a metallic complex to stabilize the crystal structure is also common in other molecular layered materials such as hexahydroxytriphenylene family.[6] Besides, in another Fe(II) 3D network composed by 2-methylimidazolate the ferrocene complex is also present in the cavities, and but cannot be removed without structural degradation.[7]

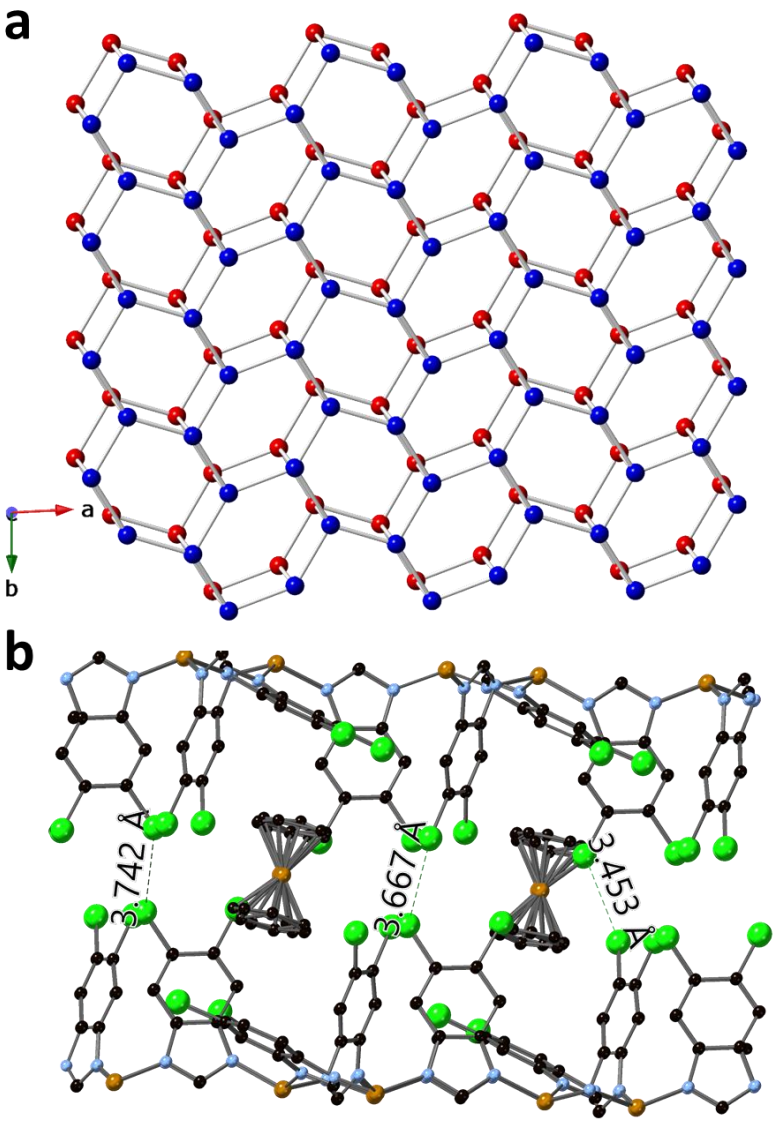

Figure 8.8 a) *ab* plane formed by the two Fe(II) centers in a monolayer of **MUV-8-X$_2$**. b) Layered structure with the ferrocene molecules located between the **MUV-8-Cl$_2$** layers, showing the interaction between Cl atoms and the location of ferrocene molecules.

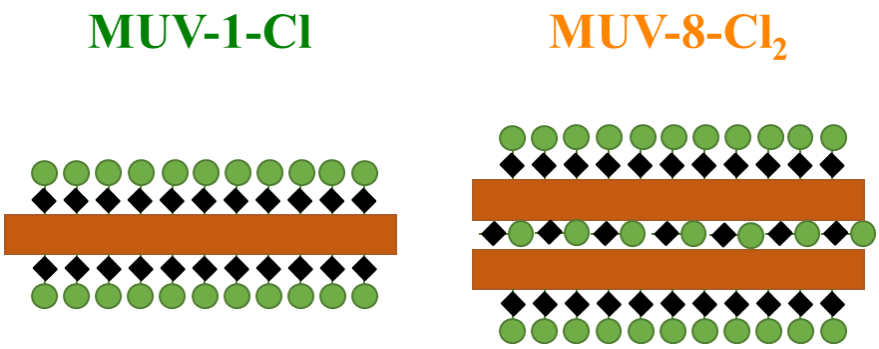

Figure 8.9 The compared layered structures of **MUV-1-Cl** and **MUV-8-Cl_2**.

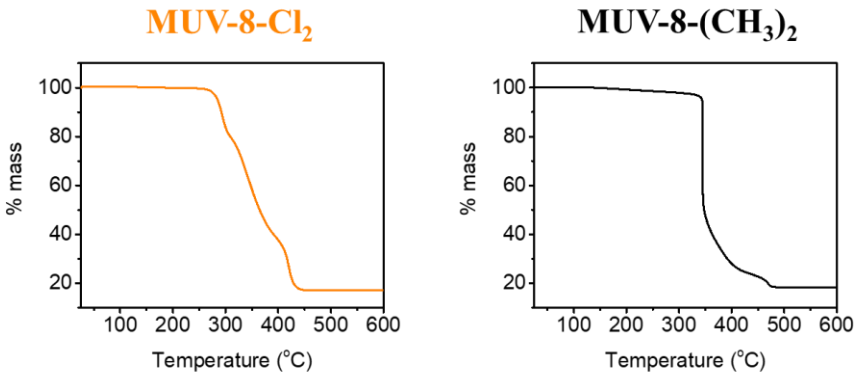

Figure 8.10 Thermogravimetric analysis of **MUV-8-Cl_2** and **MUV-8-$(CH_3)_2$**.

The addition of a second functional group induces an important structural change, originating an unprecedented metallic double-layer in an individual sheet. In this structure the iron centers are arranged in distorted

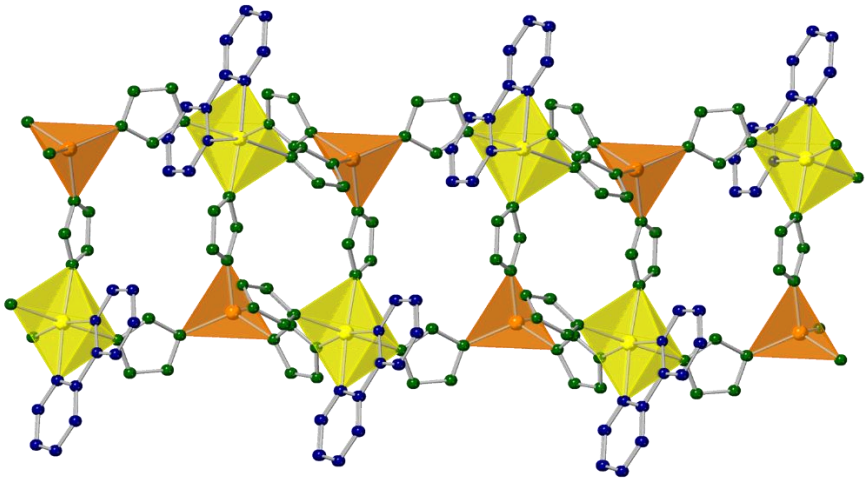

Figure 8.11 The crystal structure of $Fe_2(im)_4(2,2\text{-bipy})$. The Fe(II) centers are in octahedral and tetrahedral environments, connected by imidazolate bridges inside the double layer sheets. Bipyridine ligands complete the coordination sphere and prevent the 3D extension of the layers. In green, the imidazolate units, in blue, the bipyridine ligands, and in orange/ yellow the Fe(II) centers for tetrahedral/octahedral environments.

hexagons. Hence, the strategy to force the growth in a different layered structure through the incorporation of a second substituent was successful.

Notice that the **MUV-8-X$_2$** structural arrangement is very unusual for a layered material. In inorganic 2D materials, such as graphene or *h*-boron nitride, their monolayers present a monoatomic thickness, i.e. 0.3 Å, or a zig-zag structure as in the case of black phosphorus, resulting in a larger value of thickness (0.5 Å). Other important inorganic 2D materials present thicker monolayers, as is the case of transition metal dichalcogenides, metal trihalides, or GaSe. The structures of transition metal dichalcogenides and metal trihalides are formed by a single layer of metal atoms which are

"sandwiched" by the chalcogenides/halides atoms, thus resulting in monolayers of 0.6 Å thicknesses. GaSe is different, as it presents a double layer of metallic atoms inside a monolayer, with bonds between the Ga atoms, resulting in 0.8 Å.[8]

In coordination polymers, compounds exhibiting similar double-layers have been reported, although they have not been exfoliated. For instance, there is a molecular material based on a mixed-ligand composition using 2,2-bipyridine and imidazole, of formula $Fe_2(im)_4(2,2\text{-bipy})$.[9] This compound also presents a double-layer sheet building, although contrary to what is observed in **MUV-8-X_2**, where all the metal centers are in a tetrahedral environment, an alternating assembly of tetrahedral-octahedral arrangement of metallic centers is found (Figure 8.11). This configuration and the combination of octahedral/tetrahedral environments confer unusual magnetic properties to the material, combining spin-crossover and spin canting, and three crystallographic phase transitions.

The magnetic interactions between the metallic centers of **MUV-8** were investigated by conventional SQUID measurements. The magnetic susceptibility, χ_m, shows antiferromagnetic interactions for both **MUV-8** systems(Figure 8.12). Nonetheless, as also observed in all the derivatives of **MUV-1,** a sharp increase of the molar susceptibility at low temperatures is observed in **MUV-8**, suggesting a spin-canted structure below the Néel temperature (24 K and 23 K), for **MUV-8-Cl_2** and **MUV-8-$(CH_3)_2$**, respectively, Figure 8.12). This kind of ordering is corroborated by AC magnetic susceptibility measurements (Figure 8.12b and Figure 8.12c).

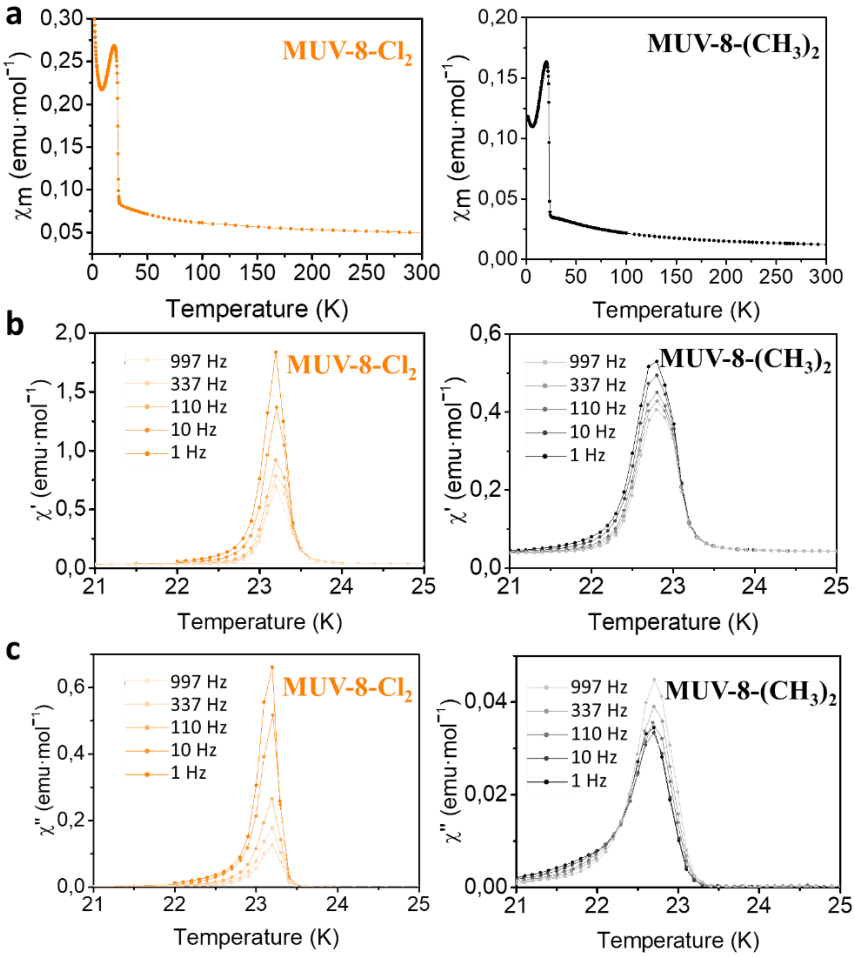

Figure 8.12 a) Thermal dependence of χ_m in the temperature range 2-300 K for **MUV-8-Cl$_2$** and **MUV-8-(CH$_3$)$_2$**. b) In-phase dynamic susceptibility χ' measured at different frequencies for **MUV-8-Cl$_2$** and **MUV-8-(CH$_3$)$_2$**. c) Out-phase dynamic susceptibility χ'' measured at different frequencies for **MUV-8-Cl$_2$** and **MUV-8-(CH$_3$)$_2$.**

The layered morphology of the crystals of **MUV-8-X_2** (Figure 8.13) is similar to that found in **MUV-1** family. This suggests the possibility of delaminating and exploring the 2D limit in these compounds. Importantly, the square-like morphology observed in crystals of **MUV-1**, which is related to the square lattice structure, is not found in **MUV-8**. In this case, triangular crystals (**MUV-8-Cl_2**) and rectangular (**MUV-8-$(CH_3)_2$)** plates are found, which can be related to the hexagonal lattice of the crystal structure.

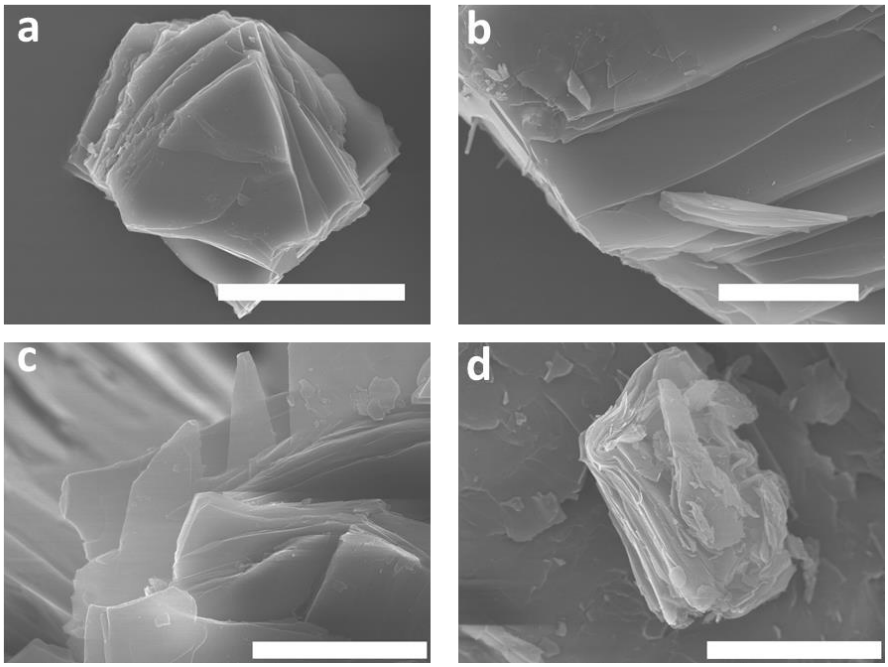

Figure 8.13 Scanning electron micrograph of bulk-type **MUV-8-Cl_2** (a,b) and **MUV-8-$(CH_3)_2$** (c,d). Scale bar is a) 30 μm b-d) 10 μm.

MUV-8-X_2 were thinned-down by mechanical exfoliation as previously realized in **MUV-1**, yielding flakes with well-defined shapes,

large lateral dimensions (> 1 μm) and different thicknesses (from hundreds of nanometers down to few layers). The obtained flakes were characterized by optical and atomic force (AFM) microscopies (Figure 8.14) and, as well, by Raman spectroscopy, then confirming its integrity and chemical composition. The higher mass of the monolayer, thanks to the incorporation of the double number of Fe(II) centers, permits a smaller detection limit, near to the three-layer compound (around 6 nm).

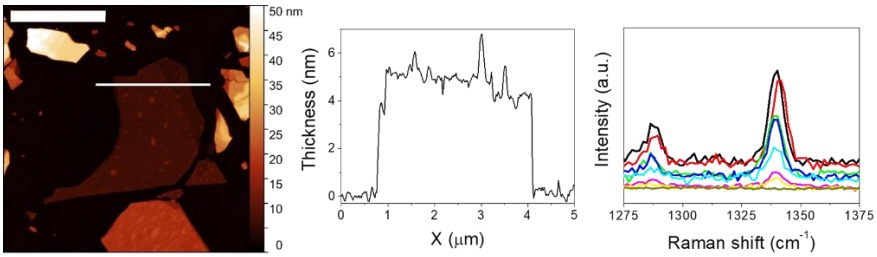

Figure 8.14 AFM image (left) and profile (middle) of a typical exfoliated flake, scale bars are 5 μm, and a selected region of the Raman spectra for different thicknesses flakes of **MUV-8-Cl$_2$**.

Asymmetric ligand strategy. Pillared-layer coordination polymers formed by neutral polymeric layers which are linked in the third direction by additional neutral ligands present an attractive approach for the rapid modulation of the materials through simple modification of the pillar ligand and/or the layer bridge while keeping the overall structure.[10–12] These pillar-layered materials can offer a platform as model systems or as materials that can be exfoliated due to the different strength of the bonds across two axes plane or the other axis across the pillar ligand.[2] As a starting pillar-layered material, we have used **MUV-0**, which was the first result obtained in the group with the solvent-free approach.[13] This material is composed of Fe(II)

centers connected by four imidazolate bridges in the *ab* plane, forming a 2D layer. In the third direction, in the *c* axis, these planes are connected by 4,4-bipyridines, completing the octahedral environment of the Fe(II) (Figure 8.15).

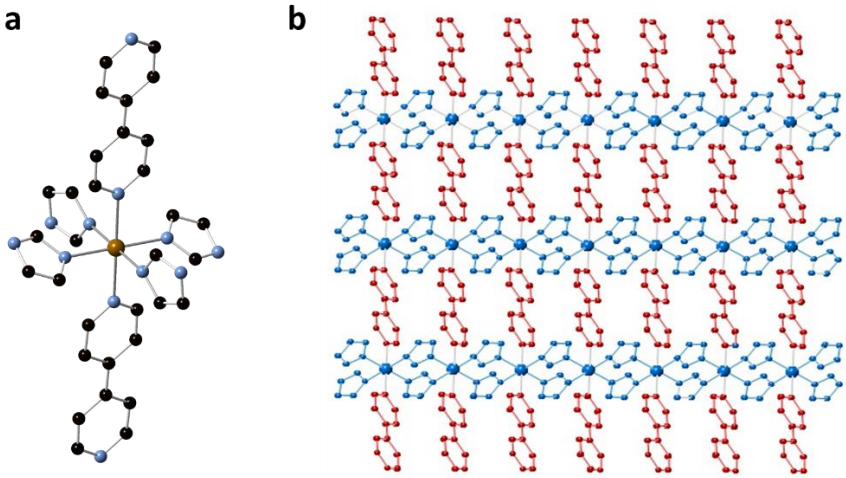

Figure 8.15 a) Coordination environment of the Fe(II) in the pilar-layered material, **MUV-0**. b) Crystal structure of the **MUV-0**, composed by bipyridines as pillars, and 2D sheets composed by imidazolate and Fe(II) centers.

As expected, the bipyridine-iron bond is too strong to allow the exfoliation process. However, this ligand can be modified in order to change the pillars of the structure. Specifically, the use of an asymmetric ligand was chosen to induce differences in the bonding unit of the pillar. In particular a pyrazole-pyridine ligand was chosen due to the different strength bonds of the two functional groups, i.e a stronger bond formed by

the pyrazole motif due to the possibility of coordinating in a bidentate manner and due to their stronger basicity (negative charge).

The reaction of 4-(1H-pyrazol-4-yl)pyridine (abbreviated as pypyzH) (Figure 8.16a), imidazole and ferrocene at 250 ºC for 72 h in a sealed ampoule, in the absence of solvents, produces crystals of formula $Fe_3(im)_4(pypyz)_2$, big enough to determine its structure by single-crystal X-ray diffraction. This reveals a pillar-layered structure, as shown in Figure 8.16b.

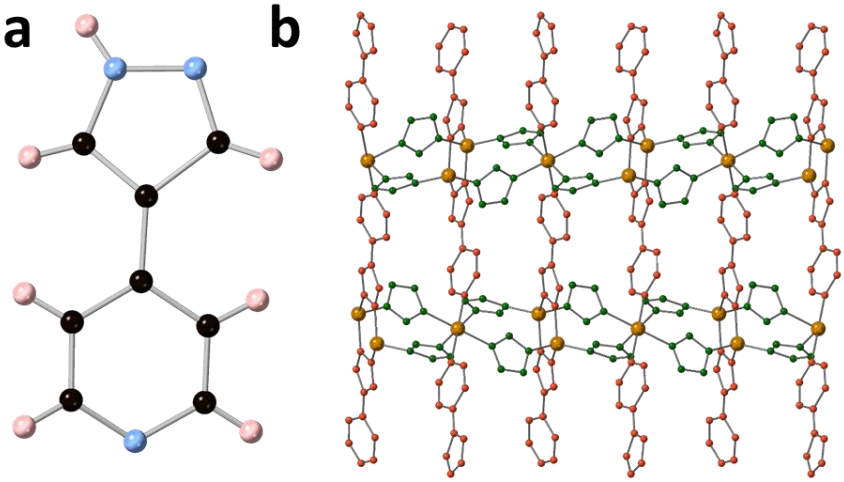

Figure 8.16 a) The ligand 4-(1H-pyrazol-4-yl)pyridine. b) The 3D crystal structure of the compound obtained by mixed-ligand strategy. In red, the $pypyz^-$ ligand, in green the imidazolate and dark yellow the Fe(II) centers.

Structural analysis reveals that two crystallographically independent Fe(II) centers are present in the structure, shown in different colors in Figure 8.17. The first Fe(II) (in orange in Figure 8.17) is a four-coordinated metal center, in a tetrahedral environment. Its coordination sphere is

composed by two N atoms from two different imidazoles, and two N from two pyrazolate units (Figure 8.17b). The other Fe(II) center (in yellow in Figure 8.17) is a six-coordinated node, with an octahedral geometry. Four imidazolate ligands bond the metal center in the equatorial plane, with the coordination sphere completed in the axial positions by two N atoms from two pyridine moieties. The imidazolate bridges connect the different crystallographic Fe(II) centers forming a layer, and the asymmetric ligand links the layers, also between octahedral-tetrahedral metal centers (Figure 8.17).

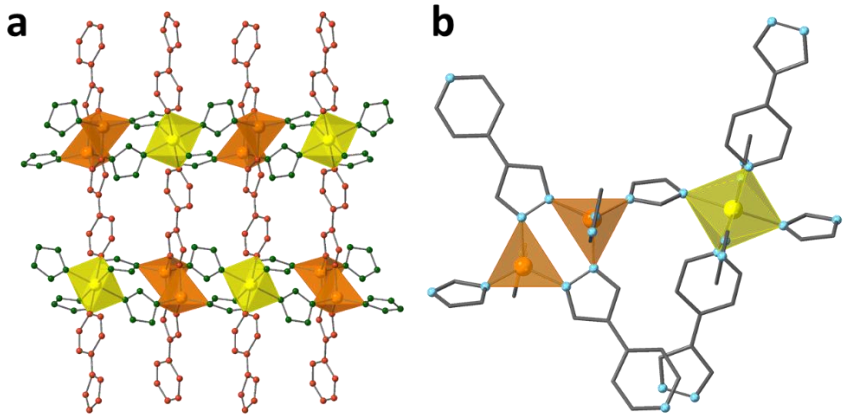

Figure 8.17 a) The disposition of the two different Fe(II) nodes. In orange, the tetrahedral Fe(II) centers and yellow the octahedral Fe(II) centers. b) The connectivity between the octahedral-tetrahedral metallic centers. Pyrazolate connects tetrahedral centers and pyridine/imidazolate bridges link octahedral-tetrahedral nodes.

This 3D crystal structure is a dense material. The approximation to obtain layered structures or easily pillared-layered compounds does not work in this case. However, close inspection of the crystal structure reveals

a possible solution to force to the growth in a different crystal structure. The incorporation of a functional group in the 2nd position of the imidazole ligand is not compatible with this structure. Similar to what was observed in the case of **MUV-8-X$_2$**, the addition of a functional group in the ligand can force the crystallization of different material.

Therefore, the analogous reaction using 2-methylimidazole (2meimH) instead of imidazole, i.e. pypyzH, 2meimH and ferrocene at 250 °C for 72 h in the absence of solvent, originates a novel plate-like compound, called **MUV-9**. Big and high-quality crystals permit to solve its crystal structure by single-crystal diffraction. Different to the previous compound, **MUV-9** is composed by only tetrahedral Fe(II) centers. The metallic nodes form a pair of Fe(II) cores, bonded through the pyrazolate motifs, with a Fe–N distance of 2.04 Å (Figure 8.18a). The other two coordination positions are occupied by 2meim ligands, linking the Fe-pyrazole units, with Fe–N distances of 2.02 Å and 2.03 Å (Figure 8.18b). The pypyz$^-$ ligands are orthogonal to the sheets, being the pyridine functionalities at the outer part of the surface of the layers. The plane formed by Fe(II) centers and the plane drawn by pypyz$^-$ linkers forms a 60° angle (Figure 8.18c). The functional group of the pyridine is not coordinating any atom, i.e. it is a free functionality.

The 2meim$^-$ ligand connects the Fe(II) along a chain. In the two-dimension plane, 2meim$^-$ is bridging the Fe(II) pairs forming a chain inside the extended sheet (Figure 8.19ab). Pyrazolate motifs connect these chains to construct the 2D polymer (Figure 8.19cd). The Fe···Fe distances in the

chain across the 2meim is around 6.0 Å and 3.5 Å for the Fe-Fe distance through the pyrazolate.

The layered structure is determined by the free pyridine group at the surface of the sheets, interacting between them weakly (Figure 8.20).

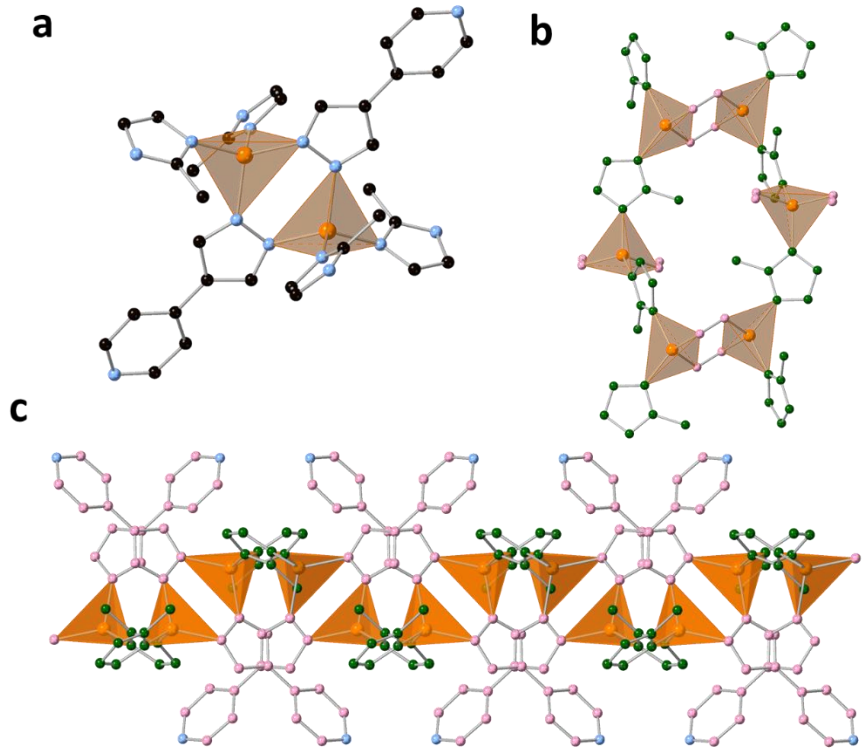

Figure 8.18 a) The coordination environment of the Fe(II) centers. b) The connectivity across the 2meim ligand. c) The crystal structure of **MUV-9** in different colors to clarify the different parts of the structure. In orange, the tetrahedral Fe(II) centers, in pink, the pypyz ligand oriented to the surface of the sheet (in blue the N atom of the pyridine functional group) and in dark green, the 2meim linker.

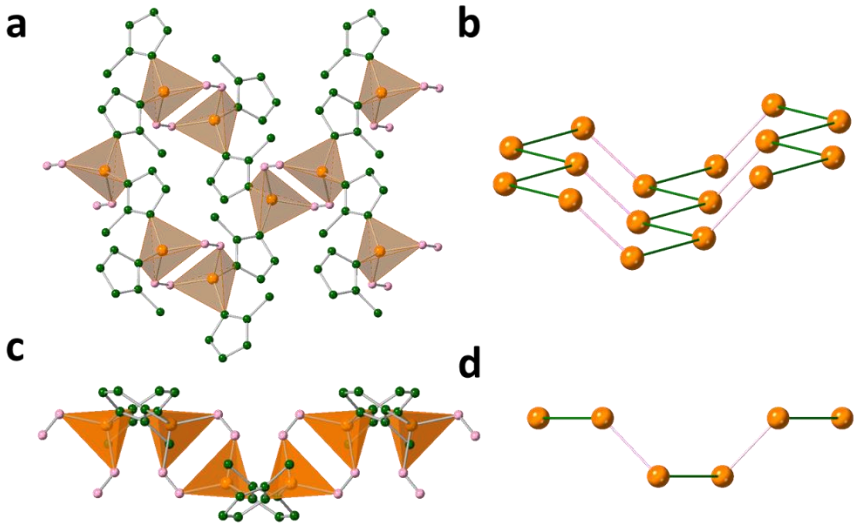

Figure 8.19 a) The connection of the Fe(II) pairs across the 2meim, forming 1D chains. b) Simplified structure with only the metallic nodes, to appreciate the chains connected by pyrazolate motifs. The pink line represents the connectivity through the pyrazolate and the dark green line the bridges of 2meim. c) The front view of one **MUV-9** sheet. d) The chains are parallel to the layers and the pypyz ligand is tilted 60° to the plane formed by the layer.

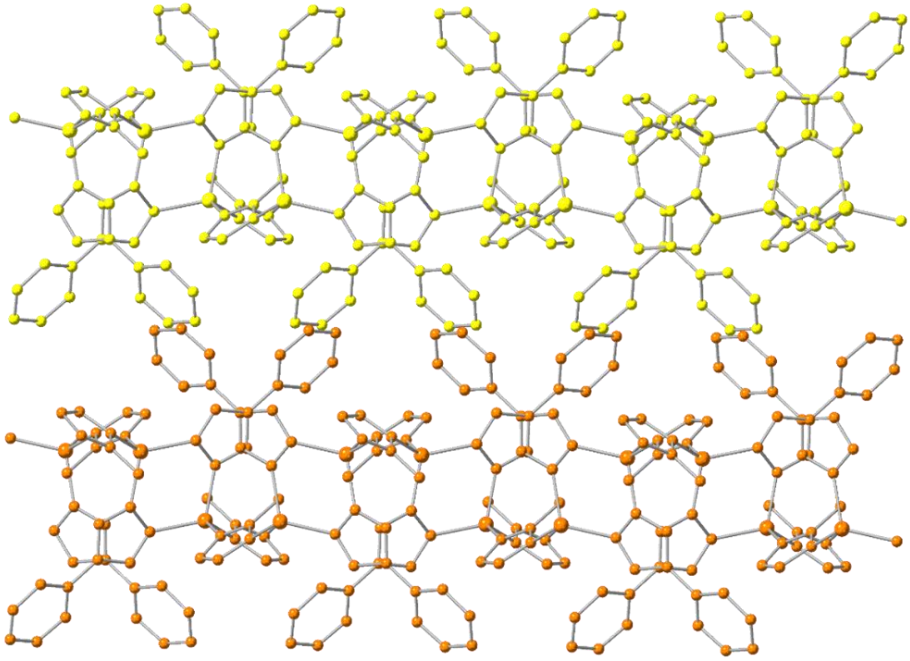

Figure 8.20 Two different layers of **MUV-9** in different colors to distinguish between the laminar separation.

The phase purity was determined by X-ray powder diffraction, and reveals the presence of an impurity depending on the synthetic conditions. This impurity was fully characterized through X-ray single crystal diffraction, showing a 1D polymer formed by only pypyz ligand and Fe(II) centers. Careful adjustment of the temperature and the ratio of the ligands allows to control the absence of this impurity, thus obtaining pure **MUV-9**. Figure 8.21 shows the diffractograms for all the crystalline phases. It should be noted that the peak at 13.7° corresponds to the **MUV-9** structure, although in the theoretical patterns the intensity of this peak is very small ([1 0 1] plane). This change in intensity is probably due to temperature effect in the packing between layers, owing to the temperature diference

between the measurements (single-crystal diffraction at 120 K and X-ray powder diffraction at room temperature).

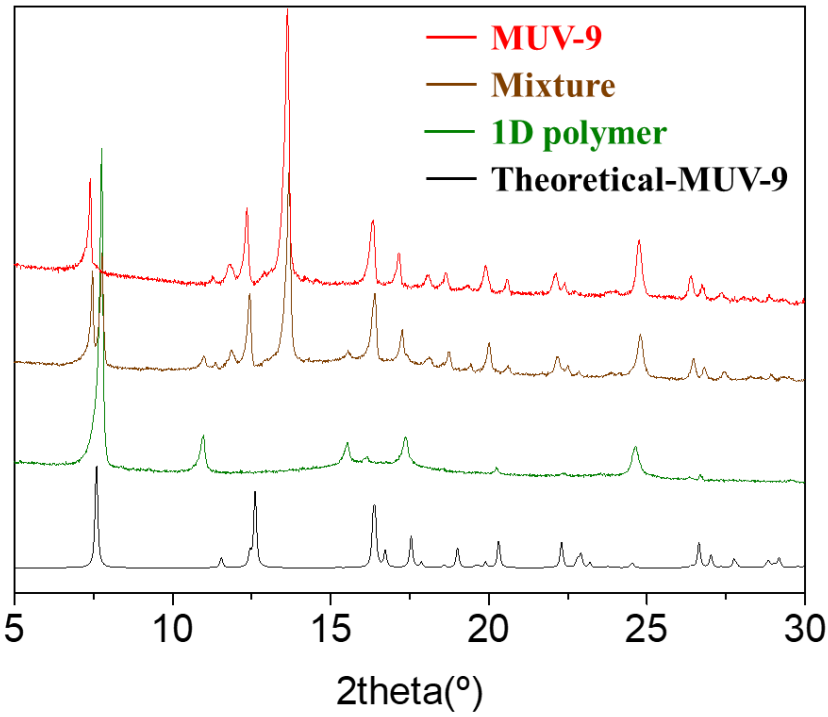

Figure 8.21 X-ray powder diffractograms of **MUV-9** (black and red). In a non-optimized synthesis, a 1D coordination polymer is present as an impurity (in brown the mixture, in green the isolated impurity).

The layered structuration of **MUV-9** is reflected in its morphology. Inspecting by SEM that fact, it is possible to appreciate the laminar morphology of the crystals and a rectangular shape (Figure 8.22). Such as the **MUV-1** and **MUV-8** families, its macroscale morphology is related to

its crystal structure, showing a sheet composition as that of the crystal structure.

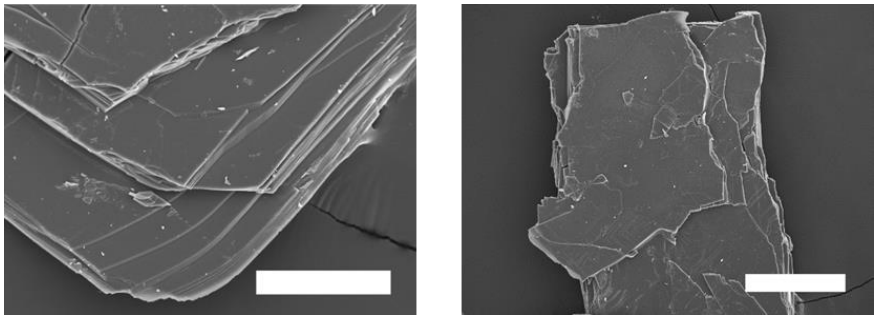

Figure 8.22 Scanning electron micrographs of **MUV-9** showing its laminar morphology. Scale bars are 50 and 100 μm.

The appropriate bridges between the Fe(II) centers permit the magnetic exchange. To investigate the magnetic properties of this novel material, the susceptibility χ_m was measured. The plot of χ_m versus T shows three key points (Figure 8.23a). Around 40 K there is a decrease of the magnetic susceptibility, and then, around 10 K, a sharp increase is observed, followed by an additional change of slope below 6 K. This complex behavior suggests different phase changes when the **MUV-9** sample is cooled down. In order to clarify this, AC measurements were carried out. Figures 8.23cd show the appearance of peaks at 12 K. However, no AC signal is observed at around 40 K. This can be explained by an antiferromagnetic order between some Fe(II) centers, similar to the very known Fe(II)-imidazole bridges discussed in this thesis. For the other uncompensated magnetic moments, the connectivity of the metallic nodes in **MUV-9** is a little bit more complex in comparison to the **MUV-1** and **MUV-8** families. The existence of the pyrazolate bridge between the Fe(II)

centers and this chain-like structure of pairs of Fe(II) centers requires more studies and measurements to elucidate and to understand this complex magnetic behavior.

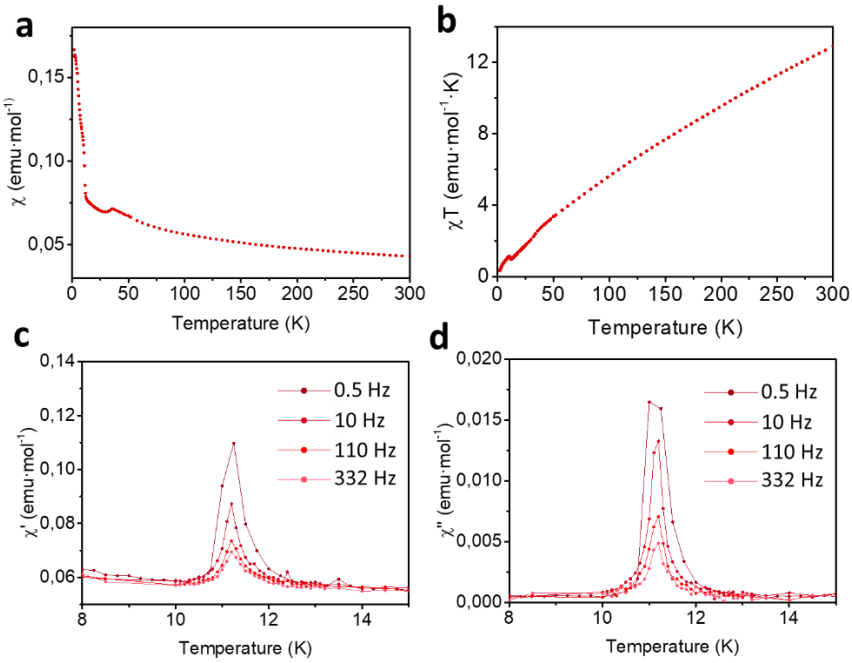

Figure 8.23 a) Thermal dependence of χ_m in the temperature range 2-300 K for **MUV-9**. b) Zoom of the χ_m versus T plot in the range 2-50 K. c) In-phase dynamic susceptibility χ' measured at different frequencies for **MUV-9**. d) Out-phase dynamic susceptibility χ'' measured at different frequencies for **MUV-9.**

The interlayer space and functional group at the surface of the sheets of **MUV-9** are quite different from **MUV-1** and **MUV-8**. However, the layered morphology and the crystal growth as rectangular plates suggest the possibility to explore the delamination process. Using the Scotch tape

methodology as with previous materials discussed during this thesis, the micromechanical exfoliation was explored and its subsequent deposition onto SiO_2 substrates (Figure 8.24).

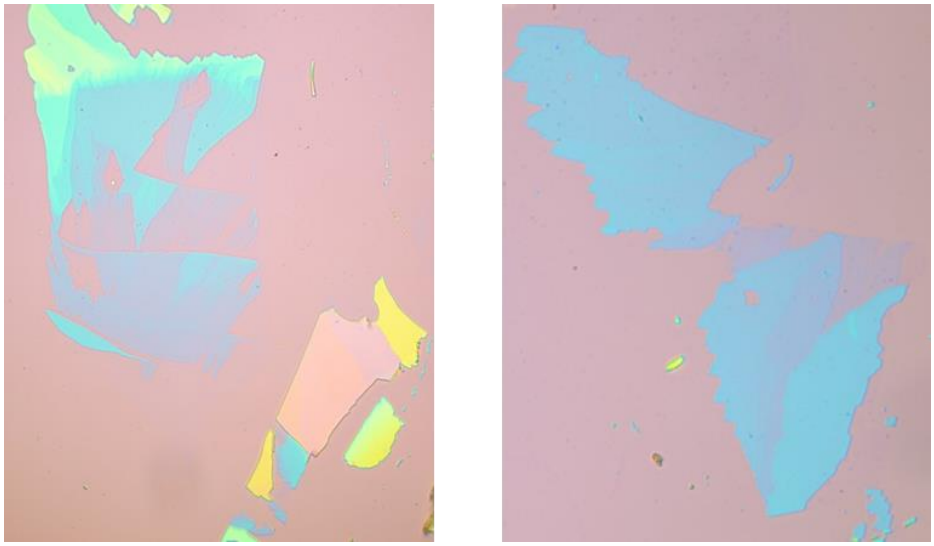

Figure 8.24 Optical photos from exfoliated flakes of **MUV-9** by micromechanical exfoliation.

Interestingly, the micromechanical processing is also successful in this case, obtaining very thin flakes of **MUV-9**, with large lateral dimensions (bigger than 10 μm), and thicknesses of 2 nm (around 2 layers) (Figure 8.25).

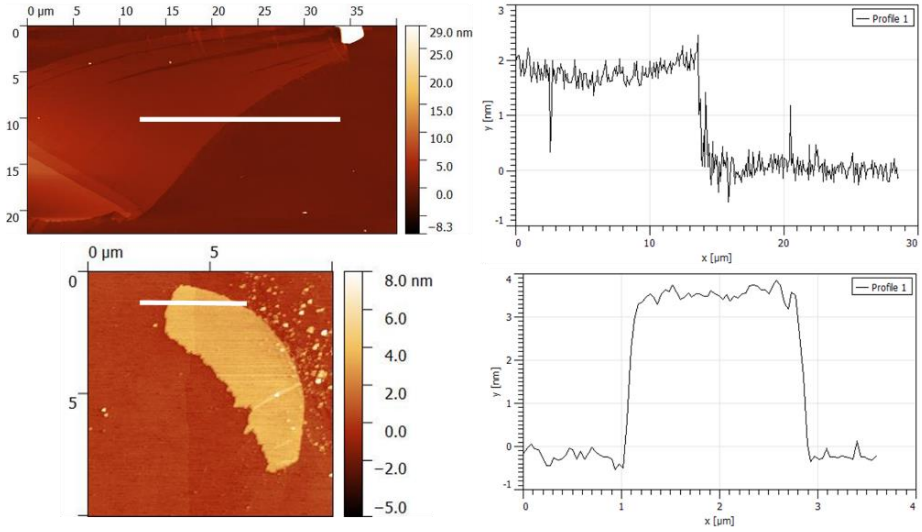

Figure 8.25 Two examples of exfoliated flakes measured by AFM, with around two-layers and three-layers thickness. The horizontal white lines correspond to the profile shown on the right

8.3 Conclusions

In this chapter, two different approaches to expand the strategies to synthesize layered MOFs have been discussed. Taking the family model of **MUV-1**, is possible to introduce small changes in the ligand to favor structural differences to obtain novel layered materials. The steric hindrance of a second substituent in the benzimidazoles ligand gives rise to a novel material with different topology and exotic double-layer sheets of Fe(II) centers. The second approach has-taken as reference a 3D pillar-layered material. Through a ligand-mixed strategy and the inclusion of substituents to provoke a steric hindrance a novel layered materials has been designed. The new material combines the presence of pairs of Fe(II)

centers with free pyridine N atoms at the surface of **MUV-9** sheets. Interestingly, the functionalized surface with the coordinative free pyridine may allow to attach these ñayers on metallic substrates or nanostructures, thus forming hybrid molecular/metallic heterostructures.

8.4 Methods

Synthesis of MUV-8-X_2. Ferrocene (30 mg, 0.16 mmol) and 5,6-dichlorobenzimidazole (0.34 mmol) or 5,6-methylbenzimidazole (0.34 mmol) were combined and sealed under vacuum in a layering tube (4 mm diameter). The mixture was heated at 250 °C for 3 days to obtain colorless crystals suitable for X-ray single-crystal diffraction. The product was allowed to cool to room temperature, and the layering tube was then opened. The unreacted precursors were extracted with acetonitrile and benzene, and the main compound was isolated as colorless crystals (yield 60 %). Phase purity was established by X-ray powder diffraction.

Synthesis of MUV-9. Ferrocene (30 mg, 0.16 mmol) and 2-methylimidazole (0.34 mmol) and 4-(1H-Pyrazol-4-yl)pyridine (0.16 mmol) were combined and sealed under vacuum in a layering tube (4 mm diameter). The mixture was heated at 250 °C for 3 days to obtain colorless crystals suitable for X-ray single-crystal diffraction. The product was allowed to cool to room temperature, and the layering tube was then opened. The unreacted precursors were extracted with acetonitrile and benzene, and the main compound was isolated as colorless crystals (yield 30 %). Phase purity was established by X-ray powder diffraction.

Single crystal. X-ray data for compounds **MUV-8-X$_2$**, **MUV-9** and $Fe_3(im)_4(pypyz)_2$ were mounted on cryoloops using a viscous hydrocarbon oil to coat the crystals. X-ray data were collected at 120 K on a Supernova diffractometer equipped with a graphite-monochromated Enhance (Mo) X-ray Source (λ = 0.71073 Å). The program CrysAlisPro, Oxford Diffraction Ltd., was used for unit cell determinations and data reduction. Empirical absorption correction was performed using spherical harmonics, implemented in the SCALE3 ABSPACK scaling algorithm. Crystal structures were solved and refined against all F^2 values by using the SHELXTL and Olex2 suite of programs.[15,16] Non-hydrogen atoms were refined anisotropically and hydrogen atoms were placed at calculated positions (riding model).

X-ray powder diffraction. Polycrystalline samples of **MUV-8-X$_2$** and **MUV-9** were lightly ground in an agate mortar and pestle and used to fill a 0.5 mm borosilicate capillariy that was mounted and aligned on an Empyrean PANalytical powder diffractometer, using Cu Kα radiation (λ = 1.54056 Å). Two repeated measurements were collected at room temperature (2θ = 5−40 °) and merged in a single diffractogram.

Thermogravimetric analysis. Thermogravimetric analysis of **MUV-8-X$_2$** were carried out with a Mettler Toledo TGA/SDTA851e/SF/1100 apparatus in the 25–600 °C temperature range under a 5°C·min^{-1} scan rate and an air flow of 30 mL·min^{-1}.

Scanning Electronic Microscopy. Scanning Electronic Micrograph of bulk samples were recorded in a Hitachi S-4800.

Raman spectra. Raman spectra were acquired with a micro-Raman (model XploRA ONE from Horiba, Kyoto, Japan) with a grating of 2400 gr/mm, slit of 50 μm, and hole of 500 μm. The employed wavelengths were 532 nm, 638 nm, and 785 nm. The power density of the laser used for spectra measured at 532 nm was 5.25 mW/μm^2 (bulk crystals) and 170 μW/μm^2 (thin-layers), for spectra measured at 638 nm it was 7.58 mW/μm^2 (bulk crystals), and for those spectra measured at 785 nm it was 7.2 mW/μm^2 (bulk crystals).

Magnetic properties. Variable-temperature (2−300 K) direct current (dc) magnetic susceptibility measurements were carried out in an applied field of 1.0 kOe. The susceptibility data were corrected from the diamagnetic contributions as deduced by using Pascal's constant tables. Variable-temperature (16−23 K) alternating current (ac) magnetic susceptibility measurements in a ±4.0 G oscillating field at frequencies in the range of 1−997 Hz were carried out in a zero dc field. All the measurements were performed with a SQUID magnetometer (Quantum Design MPMS-XL-5 & MPMS-XL-7).

8.5 References

(1) Huang, X.-C.; Lin, Y.-Y.; Zhang, J.-P.; Chen, X.-M. Ligand-Directed Strategy for Zeolite-Type Metal–Organic Frameworks: Zinc(II) Imidazolates with Unusual Zeolitic Topologies. *Angew. Chemie Int. Ed.* **2006**, *45* (10), 1557–1559.

(2) Huang, J.; Li, Y.; Huang, R. K.; He, C. T.; Gong, L.; Hu, Q.; Wang, L.; Xu, Y. T.; Tian, X. Y.; Liu, S. Y.; Ye, Z. M.; Wang, F.; Zhou, D. D.; Zhang, W. X.; Zhang, J. P. Electrochemical Exfoliation of Pillared-Layer Metal–Organic Framework to Boost the Oxygen Evolution Reaction. *Angew. Chemie - Int. Ed.* **2018**, *57* (17), 4632–4636.

(3) Wen, Y.; Liu, Q.; Su, S.; Yang, Y.; Li, X.; Zhu, Q. L.; Wu, X. Coordination Tailoring of Water-Labile 3D MOFs to Fabricate Ultrathin 2D MOF Nanosheets. *Nanoscale* **2020**, *12* (24), 12767–12772.

(4) Cliffe, M. J.; Castillo-Martínez, E.; Wu, Y.; Lee, J.; Forse, A. C.; Firth, F. C. N.; Moghadam, P. Z.; Fairen-Jimenez, D.; Gaultois, M. W.; Hill, J. A.; Magdysyuk, O. V.; Slater, B.; Goodwin, A. L.; Grey, C. P. Metal–Organic Nanosheets Formed via Defect-Mediated Transformation of a Hafnium Metal–Organic Framework. *J. Am. Chem. Soc.* **2017**, *139* (15), 5397–5404.

(5) Ding, Y.; Chen, Y. P.; Zhang, X.; Chen, L.; Dong, Z.; Jiang, H. L.; Xu, H.; Zhou, H. C. Controlled Intercalation and Chemical Exfoliation of Layered Metal-Organic Frameworks Using a Chemically Labile Intercalating Agent. *J. Am. Chem. Soc.* **2017**, *139* (27), 9136–9139.

(6) Hmadeh, M.; Lu, Z.; Liu, Z.; Gándara, F.; Furukawa, H.; Wan, S.; Augustyn, V.; Chang, R.; Liao, L.; Zhou, F.; Perre, E.; Ozolins, V.; Suenaga, K.; Duan, X.; Dunn, B.; Yamamto, Y.; Terasaki, O.; Yaghi, O. M. New Porous Crystals of Extended Metal-Catecholates. *Chem. Mater.* **2012**, *24* (18), 3511–3513.

(7) Rettig, S. J.; Storr, A.; Summers, D. A.; Thompson, R. C.; Trotter, J. Iron(II) 2-Methylimidazolate and Copper(II) 1,2,4-Triazolate Complexes: Systems Exhibiting Long-Range Ferromagnetic Ordering at Low Temperatures. *Can. J. Chem.* **1999**, *77* (4), 425–433.

(8) Tan, C.; Cao, X.; Wu, X.-J.; He, Q.; Yang, J.; Zhang, X.; Chen, J.; Zhao, W.; Han, S.; Nam, G.-H.; Sindoro, M.; Zhang, H. Recent Advances in Ultrathin Two-Dimensional

Nanomaterials. *Chem. Rev.* **2017**, *117* (9), 6225–6331.

(9) Patrick, B. O.; Reiff, W. M.; Sánchez, V.; Storr, A.; Thompson, R. C. Poly[(2,2′-Bipyridine)Tetrakis(Imidazolato)Diiron(II)]: Structural and Spin-State Phase Transitions and Low-Temperature Magnetic Ordering in a Unique 2-Dimensional Material. *Inorg. Chem.* **2004**, *43* (7), 2330–2339.

(10) Noro, S.; Kitagawa, S.; Kondo, M.; Seki, K. A New, Methane Adsorbent, Porous Coordination Polymer [{$CuSiF_6$(4,4′-Bipyridine)$_2$}n]. *Angew. Chemie Int. Ed.* **2000**, *39* (12), 2081–2084.

(11) Kondo, M.; Takashima, Y.; Seo, J.; Kitagawa, S.; Furukawa, S. Control over the Nucleation Process Determines the Framework Topology of Porous Coordination Polymers. *CrystEngComm* **2010**, *12* (8), 2350.

(12) Nugent, P.; Belmabkhout, Y.; Burd, S. D.; Cairns, A. J.; Luebke, R.; Forrest, K.; Pham, T.; Ma, S.; Space, B.; Wojtas, L.; Eddaoudi, M.; Zaworotko, M. J. Porous Materials with Optimal Adsorption Thermodynamics and Kinetics for CO_2 Separation. *Nature* **2013**, *495* (7439), 80–84.

(13) López-Cabrelles, J.; Giménez-Marqués, M.; Mínguez Espallargas, G.; Coronado, E. Solvent-Free Synthesis of a Pillared Three-Dimensional Coordination Polymer with Magnetic Ordering. *Inorg. Chem.* **2015**, *54* (21), 10490–10496.

(14) Zhai, Y. Q.; Deng, Y. F.; Fu, Z.; Feng, E.; Su, Y.; Shiga, T.; Oshio, H.; Zheng, Y. Z. Reentrant Spin Glass and Large Coercive Field Observed in a Spin Integer Dimerized Honeycomb Lattice. *Adv. Funct. Mater.* **2020**, *2004744*, 1–10.

(15) Dolomanov, O. V.; Bourhis, L. J.; Gildea, R. J.; Howard, J. A. K.; Puschmann, H. OLEX2 : A Complete Structure Solution, Refinement and Analysis Program. *J. Appl. Crystallogr.* **2009**, *42* (2), 339–341.

(16) Sheldrick, G. M. Crystal Structure Refinement with SHELXL. *Acta Crystallogr. Sect. C Struct. Chem.* **2015**, *71* (1), 3–8.

Resumen de la

tesis doctoral

Objetivos

Esta tesis fue planteada para el desarrollo de nuevos polímeros de coordinación y materiales híbridos metalorgánicos (MOFs) basados en rutas sintéticas novedosas en ausencia de disolvente. Esta novedosa metodología de síntesis permite acceder a nuevos materiales inalcanzables por rutas más clásicas como las solvotermales. La tesis se centra en la obtención de materiales basados en Fe(II), el cual es sensible a ser oxidado durante las reacciones de formación de MOFs a Fe(III). Por ello se utilizó una síntesis en ausencia de disolvente en atmosfera inerte compatible con Fe(II). Para ello se utiliza una familia de ligandos sublimables tipo imidazol y metalocenos, como el ferroceno como fuente metálica. Este tipo de materiales basados en derivados de imidazol suelen denominarse "Zeolitic Imidazolate Frameworks" (ZIFs) ya que poseen una topología similar a las zeolitas.

Metodología

Síntesis. La ruta sintética principal utilizada durante esta tesis se basa en una metodología en ausencia de disolvente. Eso significa que se mezclan en fase sólida todos los componentes en un tubo de vidrio de tamaño variable y después de tres ciclos de vacío y purga con Ar, se sellan para mantener la atmosfera inerte durante la reacción. Los componentes suelen ser metalocenos, que son compuestos que tienen un punto de sublimación entre 100 °C y 200 °C, junto con ligandos orgánicos con puntos de fusión también entre 100 °C y 200 °C. Estos tubos con todos los componentes se meten en un horno de reacción durante 72-96 horas a 150-250 °C. El resultado de esta reacción se abre con una punta de diamante y se lava con

acetonitrilo para disolver el ligando no reaccionado y con benceno para disolver el metaloceno no reaccionado. Los cristales aislados se secan.

Técnicas de caracterización. Para caracterizar los cristales obtenidos durante la síntesis anteriormente descrita se utilizan varias técnicas de caracterización.

La difracción de rayos-X de monocristal se utiliza para conocer la estructura ordenada de los compuestos a partir de un cristal monodominio, es decir, para conocer la posición de los átomos y moléculas del material ordenados en el espacio. Esta técnica es muy útil ya que conocer en profundidad la estructura cristalina de los materiales ayuda a entender sus propiedades. Una de sus desventajas es que esta técnica se basa solo en un cristal de los cientos o miles obtenidos, por ello debe ser complementada con otra técnica, la difracción de rayos-X de polvo, para discernir que todos los cristales pertenezcan a la misma fase cristalina. Es posible, a partir de la estructura cristalina resuelta, obtener el difractograma de polvo teórico para poder compararlo con el experimental.

La difracción de rayos-X de polvo consiste en analizar una pequeña cantidad de material utilizando un capilar de 0.5-0.7 mm de diámetro compuesto de borosilicato (material amorfo, invisible para los rayos-X). Este análisis da un promedio de todos los cristales introducidos en el capilar facilitando la detección de más de una fase cristalina o la presencia de impurezas. A diferencia de la difracción de monocristal, aquí no se obtiene una estructura tridimensional con las posiciones de los átomos si no que se obtiene un difractograma bidimensional donde los picos observados pertenecen a planos cristalográficos de la estructura tridimensional. Por

ello, dilucidar la estructura cristalina a partir de datos de difracción de polvo es mucho más complicado. Lo ideal es combinar las dos técnicas para conocer lo mejor posible la estructura del material y las posibles impurezas.

Los análisis termigravimétricos consisten en calentar cierta cantidad de un material en atmosfera de N_2 o aire para ir observando las pérdidas de masa a consecuencia de la descomposición o transformación del compuesto. Durante la tesis se utiliza esta técnica para hallar la temperatura de estabilidad térmica o para observar las temperaturas de activación de los materiales (cuando pierden disolventes que no pertenecen a la estructura cristalina si no que ocupan los poros).

Las medidas magnéticas se basan en análisis con temperatura de los compuestos sintetizados en los equipos SQUID (dispositivo superconductor de interferencia cuántica). En este compendio de trabajos, el rango de temperatura fue 2–300 K con un campo aplicado de 0.1 T para las medidas de susceptibilidad magnética (DC) y un rango de 10–26 K para las medidas de corriente alterna (AC) para diferentes frecuencias 1–997 Hz. Las medidas de DC permiten conocer si hay ordenamiento magnético como es discutido en esta tesis doctoral. La mayoría de los materiales sintetizados durante este trabajo presentan un ordenamiento antiferromagnético o antiferromagnético con “canting”.

Las técnicas de microscopia, como la microscopia electrónica de barrido (SEM) y la microscopia electrónica de transmisión (TEM), se utilizan para obtener imágenes y mapas de la composición de los materiales (con técnicas complementarias, EDX). En estos casos, se utilizan haces de electrones en alto vacío para obtener altas resoluciones y poder ver con gran

calidad detalles de los materiales. Los materiales utilizados durante la tesis no son conductores, uno de los requisitos para usar SEM, por ello se recubren con Ag.

Las espectroscopias, como la Raman e infrarroja (IR) se utilizan para detectar la presencia de grupos funcionales característicos de los compuestos a través de la interacción de sus modos vibracionales con las radiaciones electromagnéticas (luz monocromática para Raman e infrarroja para el IR).

La microscopia de fuerza atómica (AFM) se utiliza para conocer la topografía, el espesor y el tamaño de las capas exfoliadas de los materiales laminares sintetizados y procesados durante la tesis.

La adsorción de gases, como N_2 y CO_2, permiten la caracterización de la porosidad de los compuestos. Los espacios vacíos que se encuentran en los materiales diseñados, las redes metal-orgánicas, se pueden rellenar de cantidades conocidas de determinados gases para cuantificar el "vacío" existente en el compuesto y así saber cuál es el área disponible.

Resumen y conclusiones

En el Capítulo 1 se hace un repaso de cómo nacen los compuestos metal–orgánicos porosos desde las primeras estructuras halladas por B. Hoskins y R. Robson en 1989 hasta las últimas tendencias en MOFs. Los primeros años fueron marcados por la búsqueda de nuevas estructuras con porosidad accesible y que pudiesen adsorber gases de forma reversible sin colapsar. Más tarde, los esfuerzos se centraron en conseguir materiales con alta estabilidad térmica para poder competir con las zeolitas, que eran los

materiales porosos por excelencia. El número de estructuras fue creciendo a un ritmo muy alto y una vez cubiertas las principales demandas de estabilidad térmica y química, surgieron innumerables aplicaciones combinando el diseño químico que permite la composición hibrida de estos materiales y la porosidad accesible. Algunas de ellas eran la adsorción de gases como por ejemplo de efecto invernadero o tóxicos para aplicaciones relacionadas con la medicina, ya que pueden albergar grandes moléculas/medicamentos para estudiar sus propiedades electrónicas o para catálisis sirviendo como nanoreactores. Más recientemente, las tendencias actuales se dirigen hacia materiales vítreos o amorfos, propiedades mecánicas o explorar la dimensionalidad.

En el Capítulo 2 se desarrolla una nueva metodología de síntesis en ausencia de disolvente usando ferroceno, 2-metilimidazol y 4,4–bipiridina. El material obtenido es análogo al ZIF-8 con una estructura cristalina muy similar, pero reemplazando los centros metálicos de Zn(II) por Fe(II), llamado **MUV-3** (Material de la Universitat de València). Hasta ahora no había podido ser sintetizado por las rutas sintéticas clásicas debido a la facilidad de oxidarse de Fe(II) a Fe(III) durante la síntesis. Su estructura y estabilidad se caracteriza por difracción de monocristal, difracción de polvo (con la cual se detecta su inestabilidad frente al agua), análisis termogravimetrico, adsorción de gases, microscopia electrónica (SEM) y espectroscopia infrarroja. También se miden sus propiedades magnéticas. La clave de la síntesis es el uso de la 4,4–bipiridina, que actúa como ligando plantilla, el cual después no forma parte de la estructura cristalina, pero es fundamental durante la síntesis para obtener una fase pura del material. Se

pueden utilizar otro tipo de bipiridinas siempre y cuando tengan disponible el N para coordinar/interactuar durante la síntesis y sean suficiente voluminosas para favorecer el crecimiento del **MUV-3**. La particularidad de la incorporación de Fe(II) a esta estructura tipo ZIF permite una mayor adsorción de gases tóxicos como el NO. En el caso del ZIF-8, solo se produce una fisiadsorción del NO, mientras que en el MUV-3 se produce además de la fisiadsorción una quimiadsorción, siendo mucho mayor la cantidad de NO atrapado. Este método novedoso de síntesis también es ampliable a otros metales, y se puede sintetizar materiales conocidos como el ZIF-8 y el ZIF-67 utilizando ZnO o cobaltoceno, respectivamente. Esto abre la puerta a explorar nuevos materiales de tipo ZIF con diversos metales, además de la posibilidad de expandir la familia de materiales tipo ZIF de Fe(II), como los **MUV-6** (Fe(2etim)) y **MUV-7** (Fe(2mebim)).

En el Capítulo 3 se explora una vía de mejora de la estabilidad frente al agua del **MUV-3**. Siendo los materiales basados en ZIFs estables desde el punto de vista térmico y químico, recientes estudios de procesos donde el agua está presente muestran una degradación de estos materiales. Para la mejora de la estabilidad frente al agua se utiliza un método de síntesis directa pretendiendo obtener un nuevo material conservando la topología del **MUV-3**, pero incorporando ligandos más voluminosos que impidan o dificulten la entrada de agua. Este tipo de síntesis directa con mezcla de ligandos es poco usual ya que se suelen utilizar métodos post-sintéticos para intercambiar los ligandos debido a la dificultad de mantener la topología utilizando dos ligandos distintos. En este estudio se utiliza 2-etilimidazol y el 2-metilbenzimidazol junto con el anterior ligando, el 2-metilimidazol.

De las posibles mezclas, las que consiguen mantener la estructura tipo SOD son 2-metilbenzimidazol + 2-metilimidazol (**MUV-3-mixme**) y 2-metilbenzimidazol + 2-etilimidazol (**MUV-3-mixet)**. Las estructuras se estudian por difracción de monocristal y difracción de polvo. Se encuentra que solo hay una fase cristalina la cual concuerda con la del **MUV-3**, siendo materiales isoreticulares. Pero, para estar completamente seguros de la relación entre los ligandos dentro de la estructura, se hace un estudio de espectroscopia de RMN de ^{1}H para ver los porcentajes de ligandos, siendo 70 (2-metilimidazol, 2-etilimidazol) – 30 (2-metilbenzimidazol) el porcentaje más encontrado. Los análisis termogravimétricos señalan un aumento de la estabilidad térmica, lo que puede estar relacionado con una pérdida de porosidad, ya que se asemeja más a la estabilidad térmica de otros compuestos densos sintetizados anteriormente (**MUV-6** y **MUV-7**). Las medidas magnéticas de susceptibilidad en función de la temperatura muestran diferentes ordenamientos magnéticos para cada material, señalando una sola temperatura de ordenamiento en cada material, lo que confirma la existencia de un solo tipo de fase cristalina. De hecho, las temperaturas de ordenamiento de **MUV-3-mixme** (15 K) y **MUV-3-mixet** (17 K) son más próximas a las del **MUV-3** (23 K) que a la de las estructuras de ligando puro correspondientes a otras topologías (***qtz*-MUV-6** y ***dia*-MUV-7**, 34 y 39 K). Esta estructura tipo SOD con mezcla de ligandos otorga algo más de estabilidad frente al agua, unas 24-36 horas. Siendo el caso que el Fe(II) presenta una sensibilidad alta en este tipo de estructuras, se pensó en trasladar esta estrategia de síntesis directa a otros metales como el Zn(II) y el Co(II), que parten de base de una estabilidad mayor para comprobar su impacto en la resistencia frente al agua. Para ello se utilizó la

misma ruta sintética cambiando el ferroceno por cobaltoceno o ZnO. Por suerte, se consiguió obtener el mismo tipo de estructura tipo SOD con los dos metales en combinación con los ligandos, nombrando a los nuevos materiales **ZIF-8-mixme**, **ZIF-8-mixet**, **ZIF-67-mixme** y **ZIF-67-mixet**, confirmado por difracción de polvo. En el caso del Co(II) y el Zn(II) también se exploró que estructuras son accesibles mediante la síntesis en ausencia de disolvente con los ligandos puros, sin combinarlos, ya que se conocen más estructuras que con Fe(II). Se obtuvo una variedad grande de compuestos, donde suelen aparecer como mezclas de todos los sistemas conocidos, pudiéndose orientar la síntesis cambiando las condiciones de éstas. El RMN de los nuevos materiales de ligando mixto confirmó la mezcla de ligandos en las estructuras. En experimentos para comprobar la estabilidad frente al agua se utilizó una proporción del 0.006 % en peso de los materiales en agua durante 48 horas en agitación. Los materiales puros de ligando, ZIF-8 y ZIF-67, presentan una mayor descomposición en agua frente a los compuestos mixtos de ligando. Esto fue analizado por RMN del agua, para comprobar la cantidad de ligando presente en el agua, y mediante difracción de polvo para comprobar la cristalinidad y la aparición de otras fases. La adsorción de gases muestra que los compuestos de Fe(II) no adsorben prácticamente, los de Co(II) solo un 2 %, frente al 10 % y 4% de los materiales **ZIF-8-mixme** y **ZIF-8-mixet.** Estos datos concuerdan con los análisis termogravimétricos realizados.

El Capítulo 4 muestra una aproximación sintética muy distinta para controlar el crecimiento cristalino del ZIF-8. Los sistemas que se utilizaron, sistemas microfluídicos, son buenos para controlar y estudiar los procesos

de ensamblaje y cristalización ya que no presentan fenómenos turbulentos como las rutas sintéticas clásicas. Basados en los trabajos anteriores desarrollados por J. Puigmartí sobre la síntesis de MOFs en superficie denominada "In-flow MOF lithography", se adaptó esta metodología para sintetizar ZIF-8 sobre substratos de vidrio con finas capas de ZnO crecidas encima. La metodología consiste en el uso de chips microfluídicos basados en un polímero, PDMS (polidimetilsiloxano), el cual tiene un canal de dimensiones conocidas con una entrada y salida para los reactivos. En este caso, los reactivos consisten en una disolución de 2-metilimidazol en metanol (saturada). Se hace pasar esta disolución saturada sobre el sustrato con ZnO a través del chip microfluídico controlando la cantidad de volumen por minuto. Los que se observa es el crecimiento de ZIF-8 en una especia de película fuera del canal principal del chip, al contrario que en el caso reportado para otro MOF, el HKUST-1. Además, se observa la aparición de patrones con una distancia establecida y repetida. Las dos claves fundamentales de este experimento son el control de la difusión a través del chip con el flujo continuo y la propia difusión en sí misma. Por ello, se diseñaron experimentos complementarios con bloques de PDMS para ver la influencia de la difusión en el crecimiento cristalino, pero en ausencia de control sobre el flujo de la disolución de 2-metilimidazol. Lo que se observó para esta batería de experimentos es la ausencia de patrones, y una mayor tendencia a crecer en forma de cristales aislados. Por tanto, se concluye que el control sobre el flujo continuo es crucial para la aparición de patrones, lo que abre la puerta a estudiar y formar diferentes patrones y ver cómo afecta a las propiedades del material o película.

En el Capítulo 5 la motivación principal cambia de redes tridimensionales a la búsqueda de materiales laminares tipo MOF para explorar la incorporación de magnetismo en materiales estables al aire y poder llegar por primera vez a obtener materiales bidimensionales en este tipo de compuestos híbridos. Los materiales bidimensionales han cobrado protagonismo los últimos años debido al aislamiento del grafeno, el cual es una sola lamina de grafito aislada del resto de capas. La baja dimensionalidad del grafeno afecta a sus propiedades, las cuales distan de las mismas en forma de grafito (3D). La química molecular puede aportar nuevos materiales complementarios a los clásicos inorgánicos ya conocidos como el MoS_2 o el fósforo negro gracias a su composición híbrida de moléculas. Para ello, se utiliza la síntesis en ausencia de disolvente como en los primeros capítulos, pero utilizando un ligando distinto, benzimidazol y derivados, para tratar de obtener un sistema isostructural con el conocido $Zn(bim)_2$. La substitución de Zn(II) por Fe(II) en la síntesis podría permitir la presencia de propiedades magenticas, gracias a la configuración del Fe(II) en un entorno tetraédrico sien un d^6. La síntesis utilizada da lugar a cristales de gran tamaño, los cuales después de ser analizados por difracción de monocristal, presentan una estructura laminar, es decir, capas extendidas en dos dimensiones covalentemente y en una tercera dimensión solo interactuando mediante fuerzas débiles de van der Waals. Este material fue nombrado **MUV–1**–**Cl**. La pureza y estabilidad en aire fue comprobada por difracción de polvo siendo este sistema un material robusto y estable. Las imágenes de SEM corroboran la estructura laminar del **MUV–1**–**Cl**. Las medidas magnéticas muestran un ordenamiento antiferromagnético a baja temperatura 20 K. La particularidad de este ordenamiento es que los espines

no están perfectamente alineados (“spin canting”) y, por ello, se produce un momento magnético no compensado, como si fuese un ordenamiento ferromagnético muy débil. Todas estas características y propiedades promovieron la exploración del mundo bidimensional a través de su exfoliación por métodos micromecánicos (método de la cinta Scotch). Este método suele romper en exceso los materiales tipo MOF debido a su baja robustez, pero en este caso se obtuvieron magníficos resultados con monocapas de gran tamaño y haciendo posible su caracterización mediante técnicas como espectroscopia Raman o el microscopio electrónico de transmisión, para demostrar su composición química y que se mantiene la estructura cristalina original. Además, se utiliza el **MUV-1-Cl** exfoliado para construir resonadores mecánicos, lo cual solo se había conseguido hasta el momento con grafeno y MoS_2. Esto demuestra que los materiales 2D moleculares pueden ser útiles y complementarios a los clásicos inorgánicos debido a su gran versatilidad y posibilidad de diseño químico.

El Capítulo 6 se enfoca en demostrar la versatilidad de los materiales moleculares, ya que al estar construidos de una parte inorgánica (centros metálicos) y una parte orgánica (ligando), pueden presentar una gran variedad. Por ello, uno de los grandes problemas de los materiales bidimensionales es su dificultad a la hora de funcionalizarlos, tanto en control sobre la funcionalización como tener un orden de largo alcance de los grupos funcionales. La ventaja de los materiales moleculares es la posibilidad de poder implementar estos grupos funcionales en el ligando orgánico manteniendo la estructura cristalina. En el caso del **MUV-1**, se utilizaron diferentes ligandos organicos con un esqueleto común

(benzimidazol) pero con diferentes grupos funcionales: CH_3, H, NH_2, Br. Utilizando la misma síntesis que con el **MUV-1**, se sintetizó una familia de compuesto isoreticulares, lo que significa que se mantiene la estructura cristalina en todos ellos, solo cambiando los grupos funcionales. Por tanto, es posible, de una forma pre-sintetica, obtener una familia con el mismo tipo de estructura, pero con una funcionalización distinta. Estos cambios en el ligando no afectan a ninguna de sus propiedades, manteniendo la robustez y propiedades magnéticas. Este hecho permite obtener materiales moleculares bidimensionales en los cuales las propiedades magnéticas se mantienen, pero presentan diferente comportamiento en la superficie, desde la hidrofobicidad hasta la hidrofilicidad.

El Capítulo 7 nos sigue mostrando la gran versatilidad de la química de coordinación, esta vez desde el punto de vista de la parte metálica. En materiales 2D, el cambio de metal puede significar un cambio de estructura cristalina, como en el caso de grafeno o fosforo negro, o mantener una "familia" de estructuras cristalinas como en los dicalcogenuros de metales de transición. Las propiedades electrónicas suelen variar, ya que el metal es uno de los grandes responsables de estas propiedades. En compuestos de coordinación, donde los metales más usados son los metales de la primera serie de transición, también es muy importante el metal usado, ya que puede determinar las propiedades eléctricas y dirigir hace una estructura cristalina concreta. En el caso de los ZIFs, los metales pueden presentar propiedades catalíticas distintas, flexibilidad diferente incluso no favorecer las redes tipo ZIF, debido a la necesidad de estar en un entorno tetraédrico. Por ello, basándonos en la química de ZIFs, la familia del **MUV-1** se ha ampliado a

nuevos centros metálicos con el objetivo de variar sus propiedades magnéticas. Utilizando la misma ruta sintética en ausencia de disolvente, nuevas fuentes metálicas se utilizaron, como el ZnO, cobaltoceno o manganoceno, esperando obtener los análogos de Zn(II), Co(II) y Mn(II). Los materiales obtenidos son isostructurales con los compuestos **MUV-1**, manteniendo la misma estructura cristalina, comprobada por difracción de polvo. La morfología de estos materiales casa con la estructura laminar y lo observado para los **MUV-1** de Fe (II). Las propiedades magnéticas fueron medidas una vez se conocía que los materiales compartían la misma estructura. Para el Zn(II) no se observó ordenamiento magnético, debido a su naturaleza electrónica d^{10}. Para el Mn(II) se observa un ordenamiento antiferromagnetico puro, alrededor de 20 K. A diferencia de con el Fe(II), no hay rastro de un momento magnético no compensado debido al "canting". El comportamiento del Co(II) es más similar al del Fe(II), presentando un ordenamiento magnético alrededor de 11-12 K, mostrando también un momento no compensado debido a la no alineación perfecta de los espines. En estas medidas magnéticas se resalta la importancia del metal en este tipo de materiales y su influencia en las propiedades electrónicas. Aunque el metal influye en este tipo de propiedades, la resistencia mecánica no se ve alterada, y es posible exfoliar estos materiales hasta el límite bidimensional. Gracias a esto, se pudieron construir nanoresonadores con los materiales basados en Fe(II) y Co(II), para detectar el ordenamiento magnético a baja temperatura del material exfoliado. Esta parte del trabajo se realizó en colaboración dek grupo de P. Steneeken en la Universidad de Delft. A la temperatura de ordenamiento de ambos materiales (20 K y 11 K) se puede apreciar un cambio en la frecuencia del resonador y en el factor

Q, lo cual corrobora que el material exfoliado mantiene las propiedades magnéticas.

En el último capítulo, el Capítulo 8, se abordan dos nuevas estrategias para expandir la síntesis de materiales laminares con el objetivo de obtener más materiales moleculares bidimensionales más allá del **MUV-1**. La primera de las estrategias se basa en introducir un nuevo sustituyente en el ligando X-benzimidazol, ya que ese segundo grupo funcional es incompatible con la estructura del **MUV-1** por impedimento estérico. Para ello, se utilizan dos ligandos nuevos, con dos –Cl/–CH_3 en las posiciones 5–6. Gracias a la difracción de monocristal se resuelve la estructura cristalina del nuevo material, el **MUV-8**, el cual sigue siendo un material laminar, pero con otro tipo de estructura. En este caso, la red pasa de ser cuadrada (**MUV-1**) a ser hexagonal, siendo el hecho más inusual, que una lámina del material, esté formada por dos centros metálicos (Fe(II)). Es decir, una monocapa del compuesto está constituida por dos series de centros de Fe(II). En una misma serie de centros metálicos se unen a través de puentes benzimidazol (tres ligandos) y entre series de centros metálicos se conectan por un puente benzimidazol, completando el entorno tetraédrico. Entre las monocapas del **MUV-8** interactúan por fuerzas débiles de van der Waals. También se encuentran moléculas de ferroceno en el espacio entre capas, el cual no se puede retirar. El magnetismo de estos dos compuestos es muy similar al del **MUV-1**, presentando un ordenamiento magnético alrededor de 24 K con espin "canting". La segunda aproximación se basa en la síntesis de materiales con dos ligandos, los cuales suelen ser denominados pilar-laminar, debido a que están

construidos formando laminas (con uno de los ligandos) y éstas laminas a su vez unidas entre sí por el otro ligando. Utilizando el ejemplo del primer compuesto publicado con la metodología de ausencia de disolvente en nuestro laboratorio, compuesto por imidazol y bipiridina, se diseñó una nueva aproximación. El ligando tipo pilar, la bipiridina en ese caso, suele ser un ligando didentando. Para la nueva aproximación se pensó utilizar un ligando asimétrico para favorecer uno de los modos de coordinación e intentar debilitar el otro con el fin de poder delaminar un posible material pilar-laminar. Se utilizó un ligando piridina–pirazol donde el pk_a del pirazol lo hace coordinar más fuertemente. Utilizando el mismo ligando para la parte laminar, el imidazol y este nuevo ligando asimétrico, se obtuvo una estructura tridimensional densa. Observando la estructura tridimensional se apreció que un ligando más impedido estéricamente como el 2-metilimidazol no sería compatible con esta estructura, así que se decidió utilizar este otro ligando para comprobar que estructura se obtendría. En este caso, el material obtenido sí es un material laminar que gracias a la difracción de monocristal, el cual presenta las bipiridinas orientadas hacia la parte exterior de las láminas sin coordinar. Los grupos pirazolato unen centros de Fe(II) al igual que los puentes imidazol. Esto forma una red extendida en dos dimensiones. En la tercera dimensión, los grupos piridina interactúan débilmente por fuerzas de van der Waals. Los centros de Fe(II) se encuentran en entornos tetraédricos. Las imágenes de SEM muestran un material de naturaleza laminar concordando con lo observado en su estructura cristalina. El nuevo material, el **MUV-9**, puede ser exfoliado y se pueden obtener finas capas del material de largas dimensiones laterales como los anteriores **MUV-1** y **MUV-8**. Las propiedades magnéticas

presentan dos tipos de ordenamientos, lo que puede ser debido a los dos diferentes puentes entre los centros de Fe(II).